



Journal of Heat Transfer

Published Monthly by ASME

VOLUME 127 • NUMBER 2 • FEBRUARY 2005

RESEARCH PAPERS

Combustion and Reactive Flows

- 117 Fluidized Bed Combustion of a Biomass Fuel: Comparison Between Pilot Scale Experiments and Model Simulations
Francesco Miccio, Fabrizio Scala, and Riccardo Chirone
- 123 Energy Extraction From a Porous Media Reciprocal Flow Burner With Embedded Heat Exchangers
Fabiano Contarin, William M. Barcellos, Alexei V. Saveliev, and Lawrence A. Kennedy

Evaporation, Boiling, and Condensation

- 131 Wall Heat Flux Partitioning During Subcooled Flow Boiling: Part I—Model Development
Nilanjana Basu, Gopinath R. Warrier, and Vijay K. Dhir
- 141 Wall Heat Flux Partitioning During Subcooled Flow Boiling: Part II—Model Validation
Nilanjana Basu, Gopinath R. Warrier, and Vijay K. Dhir
- 149 Ultrahigh CHF Prediction for Subcooled Flow Boiling Based on Homogenous Nucleation Mechanism
Wei Liu and Hideki Nariai

Forced Convection

- 159 Calculation of Turbulent Boundary Layers Using Equilibrium Thermal Wakes
James Sucec

Heat Pipes

- 165 Investigation of a Novel Flat Heat Pipe
Yaxiong Wang and G. P. Peterson

Heat Transfer Enhancement

- 171 Heat Transfer Enhancement for Finned-Tube Heat Exchangers With Winglets
James E. O'Brien and Manohar S. Sohal

Bio-Heat and Mass Transfer

- 179 An Analytical Study of Heat Transfer in Finite Tissue With Two Blood Vessels and Uniform Dirichlet Boundary Conditions
Devashish Shrivastava, Benjamin McKay, and Robert B. Roemer

TECHNICAL BRIEFS

- 189 New Interpretation of Non-Fourier Heat Conduction in Processed Meat
Paul J. Antaki
- 194 Transpired Turbulent Boundary Layers Subject to Forced Convection and External Pressure Gradients
Raúl Bayoán Cal, Xia Wang, and Luciano Castillo

(Contents continued on inside back cover)

This journal is printed on acid-free paper, which exceeds the ANSI Z39.48-1992 specification for permanence of paper and library materials. ©™
♻️ 85% recycled content, including 10% post-consumer fibers.

HEAT TRANSFER DIVISION
Chair, R. D. SKOCYPEC
Vice Chair, M. K. JENSEN
Past Chair, Y. BAYAZITOGU
Secretary, T. W. TONG
Treasurer, CHANG H. OH
Member, RODNEY W. DOUGLASS
Editor, V. DHIR (2005)
Associate Editors,
S. ACHARYA (2006)
N. K. ANAND (2006)
G. CHEN (2005)
J. N. CHUNG (2005)
A. F. EMERY (2005)
B. FAROUK (2006)
S. V. GARIMELLA (2007)
C. P. GRIGOROPOULOS (2006)
S. G. KANDLIKAR (2007)
J. M. KHODADADI (2007)
K. KIHM (2005)
J. H. LIENHARD V (2006)
P. M. LIGRANI (2006)
R. M. MANGLIK (2006)
C. H. OH (2007)
R. PITCHUMANI (2007)
V. PRASAD (2005)
R. P. ROY (2007)
K. A. THOLE (2007)
S. THYNELL (2005)
S. PRATAP VANKA (2005)

PUBLICATIONS DIRECTORATE
Chair, ARTHUR G. ERDMAN

OFFICERS OF THE ASME
President, HARRY ARMEN
Executive Director,
VIRGIL R. CARTER
Treasurer,
R. E. NICKELL

PUBLISHING STAFF
Managing Director, Engineering
THOMAS G. LOUGHLIN
Director, Technical Publishing
PHILIP DI VIETRO
Production Coordinator
COLIN McATEER
Production Assistant
MARISOL ANDINO

Transactions of the ASME, Journal of Heat Transfer (ISSN 0022-1481) is published monthly by The American Society of Mechanical Engineers, Three Park Avenue, New York, NY 10016. Periodicals postage paid at New York, NY and additional mailing offices. POSTMASTER: Send address changes to Transactions of the ASME, Journal of Heat Transfer, c/o THE AMERICAN SOCIETY OF MECHANICAL ENGINEERS, 22 Law Drive, Box 2300, Fairfield, NJ 07007-2300. **CHANGES OF ADDRESS** must be received at Society headquarters seven weeks before they are to be effective. Please send old label and new address. **STATEMENT from By-Laws.** The Society shall not be responsible for statements or opinions advanced in papers or ... printed in its publications (B7.1, Para. 3). **COPYRIGHT** © 2005 by The American Society of Mechanical Engineers. For authorization to photocopy material for internal or personal use under those circumstances not falling within the fair use provisions of the Copyright Act, contact the Copyright Clearance Center (CCC), 222 Rosewood Drive, Danvers, MA 01923, tel: 978-750-8400, www.copyright.com. Request for special permission or bulk copying should be addressed to Reprints/Permission Department. **INDEXED** by Applied Mechanics Reviews and Engineering Information, Inc. Canadian Goods & Services Tax Registration #126148048.

- 199 A Semi-Analytical Model for Evaporating Fuel Droplets
Achintya Mukhopadhyay and Dipankar Sanyal

ERRATUM

- 204 Erratum: "Mie Scattering Theory for Phonon Transport" [ASME J. Heat Transfer, 2004, 126, pp. 793–804]
205 ASME Journal of Heat Transfer Referees — 2004

The ASME Journal of Heat Transfer is abstracted and indexed in the following:

Applied Science and Technology Index, Chemical Abstracts, Chemical Engineering and Biotechnology Abstracts (Electronic equivalent of Process and Chemical Engineering), Civil Engineering Abstracts, Compendex (The electronic equivalent of Engineering Index), Corrosion Abstracts, Current Contents, E & P Health, Safety, and Environment, Ei EncompassLit, Engineered Materials Abstracts, Engineering Index, Enviroline (The electronic equivalent of Environment Abstracts), Environment Abstracts, Environmental Engineering Abstracts, Environmental Science and Pollution Management, Fluidex, Fuel and Energy Abstracts, Index to Scientific Reviews, INSPEC, International Building Services Abstracts, Mechanical & Transportation Engineering Abstracts, Mechanical Engineering Abstracts, METADEX (The electronic equivalent of Metals Abstracts and Alloys Index), Petroleum Abstracts, Process and Chemical Engineering, Referativnyi Zhurnal, Science Citation Index, SciSearch (The electronic equivalent of Science Citation Index), Theoretical Chemical Engineering

Fluidized Bed Combustion of a Biomass Fuel: Comparison Between Pilot Scale Experiments and Model Simulations

Francesco Miccio

Fabrizio Scala¹

e-mail: scala@irc.na.cnr.it

Riccardo Chirone

Istituto di Ricerche sulla Combustione, CNR,
P.le V. Tecchio 80, 80125 Napoli, Italy

In the present work the efficiency of the fluidized bed combustion (FBC) of high-volatile fuels and the extent of volatile matter post-combustion in the splashing zone and freeboard are investigated. A typical Mediterranean biomass (pine-seed shells) has been burned in a pilot-scale bubbling FB combustor (200 kWt) at different operating conditions. Both over-and under-bed fuel feeding options have been considered. A FBC model specifically developed for high-volatile fuels has been also applied to provide a comparison with bed carbon loading, in-bed heat release and splashing region temperature experimental data. Experimental results showed that the biomass combustion efficiency is always very high as a consequence of the high reactivity of the fuel. Extensive volatile post-combustion above the bed is observed, whose extent appears to be sensitive to the over/under bed feeding option and to the excess air. Approximately 80% of the total heat is released/recirculated in the bed, the remainder leading to appreciable overheating of the freeboard with respect to the nominal bed temperature. Very low bed carbon loadings have been found. Model results compare well with the experimental temperature, heat release and carbon loading trends. However, a detailed prediction of the freeboard temperature profiles requires further improvements of the model. [DOI: 10.1115/1.1842787]

Keywords: Fluidized Bed Combustion, Biomass, Segregation, Volatile Post-Combustion

Introduction

The growing interest for exploitation of nonfossil solid fuels as an alternative energy source is a result of a number of economic and environmental issues. Among these, the increasing price of fossil fuel resources, the disposal of wastes or low-value byproducts, and issues related to the management of pollutant emissions and to the global warming concern. Most of the nonfossil fuels of practical interest, in particular biomass and wastes, are characterized by a large fraction of the heat release related to the volatile matter, so that they are often indicated as high-volatile fuels. The application of the fluidized bed combustion (FBC) technology to high-volatile fuels has been proposed as one of the most promising technological options because of its fuel flexibility and clean and efficient operation, but poses a series of relatively new problems [1–3]. Operational concerns have arisen mostly as regards two issues: the occurrence and the extent of volatile matter and fuel particles segregation with respect to the fluidized bed [4–6]; the behavior of ashes, with particular concern to agglomeration of the bed material in presence of low melting inorganic compounds [7–10]. On the other hand, the impact of fuel particle comminution and related generation of elutriable carbon fines on the FBC efficiency, which is one of the main concerns when burning fossil fuels, has been reported to be limited with high-volatile fuels [11,12].

As far as fuel segregation is concerned, it has been pointed out that the higher the volatile content of the fuel, the greater the tendency of the fuel particle to segregate at the bed surface during the devolatilization stage [13–15]. In fact, the released volatiles may form “endogenous” bubbles around the devolatilizing particles, lifting coarse fuel particles to the bed surface. As a consequence, a significant amount of volatile matter effectively by-

passes the bed and is released and burns directly in the freeboard, resulting in a considerable temperature increase in this region above the nominal bed temperature. The fraction of volatiles released in the bed is, in turn, relevant to the achievement of high fuel conversion in the bed zone, where heat transfer is more efficient. Furthermore, axial temperature profiles in the combustor affect the cleanness of flue gases and the efficiency of the process control. The assessment of whether the position of the fuel feeding system affects or not the post combustion of volatiles is still an open problem.

In the present paper results of a pilot-scale experimental study regarding the FBC of a biomass fuel with over-/under-bed fuel feeding at different operating conditions are reported. The focus is particularly on the occurrence of fuel post-combustion in the splashing zone and freeboard. A comparison with the predictions of a recently presented FBC model suitable for high-volatile fuels [6] is also proposed, as a first attempt for model validation.

Experimental

A bubbling fluidized bed combustor (FBC-370) has been used to carry out steady state combustion tests under atmospheric conditions [4]. The pilot-scale 200 kW facility is sketched in Fig. 1. The fluidization column is made of AISI 310 stainless steel. It has a circular section (370 mm ID) and a total height of 4.65 m. The lower section of the column contains the plenum chamber and the pipe type distributor equipped with 55 vertical tuyeres. The distributor sustains bed materials allocated in the intermediate section, which is also equipped with several access ports. The heat exchange is accomplished thanks to an array of horizontal bayonet-type pipes whose adjustable penetration into the bed controls the heat removal rate. The higher section of the fluidization column (freeboard) provides the disengagement of elutriated solids and is also fitted with several ports for temperature, pressure and gas concentration probes. Two cyclones, the first with medium and the second with high efficiency, are used for flue gas

¹Corresponding author. Phone: +39 081 7682969; fax: +39 081 5936936.

Manuscript received November 10, 2003; revision received September 3, 2004. Review conducted by: H. S. Lee.

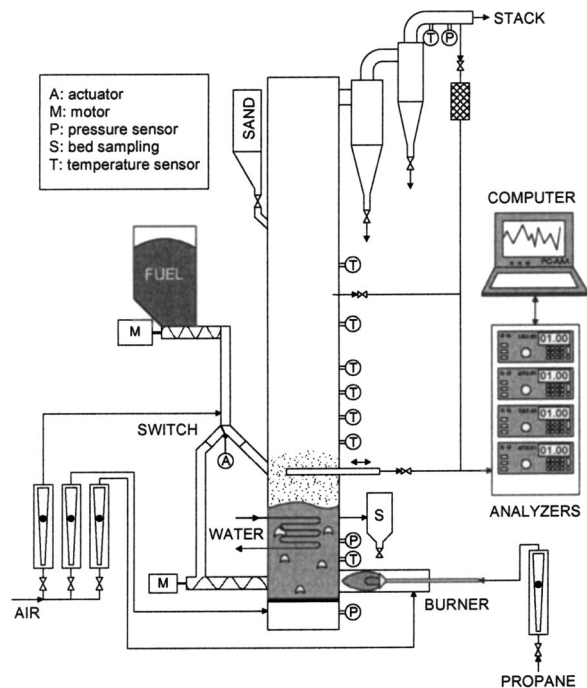


Fig. 1 Scheme of the fluidized bed combustor FBC-370

de-dusting. The entire vessel is thermally insulated by means of ceramic wool. A propane burner is used for start-up by directly heating fluidized bed materials. FBC-370 is equipped with a continuous over-bed/under-bed feeding system. Fuel particles are dosed by means of a screw type metering device. Particles fall down directly on bed surface after the passage throughout an inclined tube, under the option of O-Bed feeding. Otherwise, they are passed in sequence to a second rotating screw, which allows the entrance of particles into the bed, under the option of U-Bed feeding. Such water-cooled screw represents a significant improvement with respect to the pneumatic injection device previously adopted for under-bed feeding [4].

A horizontal cooled probe is installed at an elevation of 1024 mm from the distributor and allows gas suction for chemical analysis at a different radial penetration. The probe is equipped with a stainless steel sintered tip to prevent capture of fine particulate. The fluidization column is also provided with a device for sampling hot bed materials under inert atmosphere, located at the elevation of 0.49 m above the distributor.

The combustor start up is carried out by using a propane burner. After the bed reaches a temperature high enough to ignite fuel particles (e.g., 600°C), the feeding of fuel is started. Adjustments of operating variables are required in order to achieve the desired steady-state condition, which is maintained for at least 40 min. Temperatures, pressures and flue gas concentrations (O_2 , CO_2 , CO , N_2O and NO) are on-line monitored and recorded using a data acquisition system supervised by a personal computer. Samples of bed solids and fines collected at cyclones are taken. At the end of a combustion test, the fuel feeding is quickly switched off in order to burn out the residual char and the transient profile of O_2 , CO_2 and CO is recorded for the estimation of bed carbon loading by integration.

Materials

Shells of pine-seeds are considered for the experimental campaign. The fuel originates from seasonal agricultural manufacturing in the Mediterranean area. The yearly production in Italy is around 1000 tons. Typical fuel particles are shown in Fig. 2; they have a fairly high density, an irregular and drop like shape (ap-



Fig. 2 Photograph of biomass particles (shells of pine-seeds)

proximately 30×10 mm in size), a good mechanical resistance and anisotropic properties. Resins are also present, as revealed from the intense smell of the material. Physical properties and chemical analysis are reported in Table 1. The biomass can be considered as a typical high volatile fuel. The presence of alkalis (K, Na) in the fuel ashes is a potential source of agglomeration phenomena during fluidized bed combustion.

Silica sand with two nominal sizes (i.e., 300 and 725 μm) has been used as inert material during experiments. No sorbent has been added to the bed, the fuel being sulfur free. The bed inventory has been 45 and 85 kg, corresponding to an unexpanded bed height of about 270 and 500 mm, respectively.

Experimental Results

Table 2 reports a summary of tests performed in the FBC-370 facility. Experiments have been carried out by varying fluidization velocity, excess air ratio and sand size. The operating bed temperature was kept constant at 850°C.

Both the under-bed and over-bed fuel feeding options were tested. With the exception of tests carried out under quasi-stoichiometric conditions, emissions of carbon monoxide and nitrogen oxide are low. The volumetric concentration of CO is less than 50 ppm in the majority of tests by virtue of the high reactivity of volatile matter and residual char. NO emissions are comprised in the range of 70–140 ppm and are congruently lowered at a low excess air ratio. Of course, the result concerning NO is strictly related to the low nitrogen content of the biomass fuel. The carbon elutriation rate of the cyclones was negligible. This figure, combined with that concerning CO emissions, led to high combustion efficiencies, always greater than 99%. Bed carbon

Table 1 Properties and chemical analysis of pine-seed shells

| | |
|--|-------|
| Particle size, mm | 10–30 |
| Density, $kg\ m^{-3}$ | 1200 |
| Low Heating Value (dry basis), $kJ\ kg^{-1}$ | 15200 |
| Proximate analysis | |
| Volatiles, % | 59.6 |
| Fixed carbon, % | 26.6 |
| Ash, % | 0.8 |
| Moisture, % | 13.0 |
| Ultimate analysis (dry basis) | |
| Carbon, % | 48.5 |
| Hydrogen, % | 6.1 |
| Nitrogen, % | 0.2 |
| Sulfur, % | <0.1 |
| Oxygen, % | 44.3 |
| Ash, % | 0.9 |

Table 2 Summary of experimental tests carried out in the FBC-370 facility.^a Bed carbon load by burn-out/bed carbon load by chemical analysis

| Inert bed material: Fuel: Operating bed temperature: | | | | Silica sand Pine-seed shells 850°C | | | | | | | | |
|--|----------------------------|----------------|----------------|--|------------------|---------------------------|---------------------|----------------------|-----------|-----------|-------------------------------|--|
| Test | Sand size μm | Bed mass kg | Feeding option | Fluidization Velocity m/s | Excess air ratio | Freeboard overtemp. °C | O ₂ % | CO ₂ % | CO ppm | NO ppm | Carbon load ^d g | |
| PINE-A02 | 300 | 45 | O-BED | 0.99 | 1.25 | 45 | 3.3 | 15.9 | 175 | 74 | -/251 | |
| PINE-A04 | 300 | 45 | O-BED | 0.66 | 1.34 | 37 | 4.2 | 14.7 | <10 | 75 | -/151 | |
| PINE-A06 | 300 | 45 | U-BED | 0.67 | 1.35 | 41 | 4.3 | 15.3 | 30 | 78 | -/- | |
| PINE-A08 | 300 | 45 | O-BED | 0.68 | 1.04 | 76 | 0.7 | 20.5 | 3300 | 36 | -/- | |
| PINE-A09 | 300 | 85 | O-BED | 0.67 | 1.05 | 102 | 0.8 | 20.2 | 2040 | 39 | -/208 | |
| PINE-B01 | 725 | 85 | U-BED | 0.97 | 1.23 | 56 | 3.4 | 16.3 | 27 | 115 | 105/174 | |
| PINE-B02 | 725 | 85 | U-BED | 0.70 | 1.28 | 49 | 4.1 | 15.9 | 12 | 120 | 83/165 | |
| PINE-B03 | 725 | 85 | U-BED | 0.57 | 1.25 | 58 | 3.7 | 16.4 | 10 | 127 | 77/160 | |
| PINE-B04 | 725 | 85 | U-BED | 0.97 | 1.23 | 50 | 3.6 | 16.4 | 15 | 141 | -/- | |
| PINE-B04b | 725 | 85 | U-BED | 1.01 | 1.33 | 93 | 3.8 | 16.2 | 10 | 150 | 126/- | |
| PINE-B05 | 725 | 85 | O-BED | 0.97 | 1.23 | 113 | 3.7 | 16.7 | <10 | 130 | 105/- | |
| PINE-B06 | 725 | 85 | O-BED | 0.70 | 1.25 | 82 | 3.9 | 15.9 | <10 | 134 | 89/- | |

loading is mainly related to the presence of coarse char particles. In this respect, no differences between U-Bed and O-Bed feeding option are noted. It is worth noting that values of carbon load obtained by a chemical analysis of bed samples are always overestimated with respect to the direct evaluation of carbon load performed at the end of a single test. The explanation can be found in the tendency for char particles to float and segregate near bed surface [14], where bed sampling is performed.

Figure 3 reports a temperature profile along the combustor axis at different fluidization velocities for U-Bed and O-Bed feeding options. On the right side of the figure the approximate heights of the bed, splashing zone and freeboard are also indicated. In particular, the reported height of the splashing region represents the height required to halve the entrained solids flux according to published correlations [16]. The temperature in the freeboard was higher than that in the bed attaining a maximum at an elevation above the air distributor, which varies with operating conditions and ranges between 1.2 and 2 m. This indicates that the post-

combustion of unburned species occurred in the freeboard because of an insufficient residence time, incomplete mixing between oxygen and combustible matters in the bed region and segregation of fuel particles in the upper bed zone. In particular, it appears that an increase of the fluidization velocity leads to a higher location of the temperature peak. Higher freeboard temperatures are always observed by adopting over-bed feeding. The difference between the maximum temperature in the freeboard and the bed temperature is reported in Table 2. The maximum over-temperature equals 113°C and is obtained with the O-Bed feeding option at the condition of the highest load (i.e., $U = 0.97$ m/s corresponding to 72 kW). Figure 4 shows the temperature increase in the freeboard as a function of the excess air ratio. Two data sets are reported here for the different feeding options. Even if an effect of parallel change in other variables is present leading to data dispersion, it appears that the O-Bed feeding option causes a higher freeboard over-temperature with respect to the U-Bed option.

Figure 5 shows how the fuel heating value is distributed inside the bed (for PINE-B04 and PINE-B05 tests). The terms heat removed and heat dispersed represent the fraction exchanged with cooling tubes and with combustor walls, respectively. The sensible heat is the energy required to heat up the air flow rates up to bed temperature. The last term in the figure is the sum of the previous ones and represents the net heat exchanged by the bed. It appears that there is only a small difference between O-Bed and U-Bed options (0.80 vs. 0.82, respectively). Of course, the result is consistent with the temperature profile measured in the splashing region and the freeboard. In fact the temperature increase in

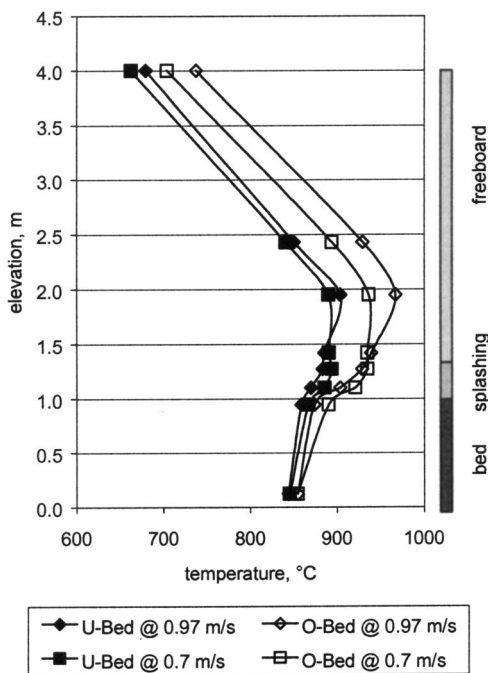


Fig. 3 Temperature profiles along combustor axis at different fluidization velocities and feeding options

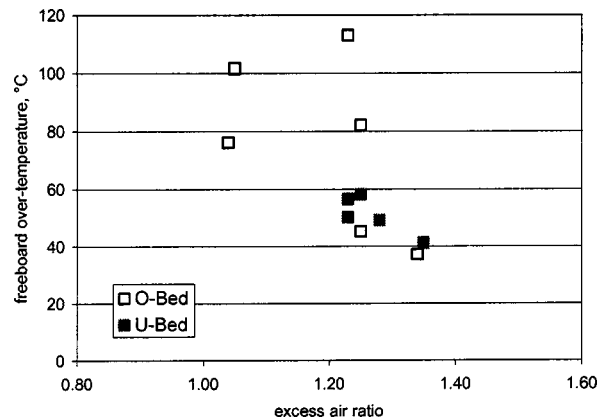


Fig. 4 Freeboard over-temperature versus excess air ratio

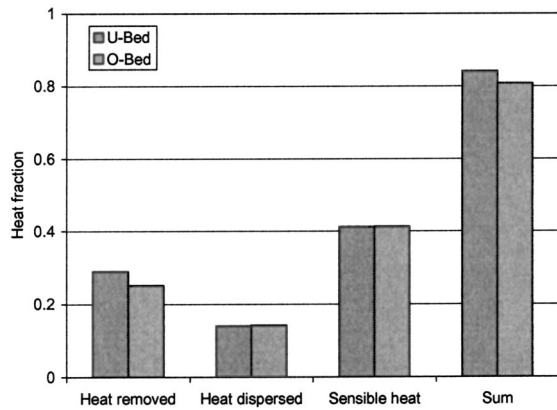


Fig. 5 Heat distribution in the bed region for U-Bed and O-Bed feeding options ($U=0.97$ m/s; $e=1.23$)

these sections, even if appreciable, is not dramatic, indicating that only a small fraction of the heating value of the biomass contributes to freeboard over-heating.

Figure 6 reports the radial profiles of oxygen and carbon monoxide obtained by means of the radial probe located in the splashing region. Two data series for U-Bed and O-Bed feeding options are reported. It appears that the average value of monitored gas concentration does not change dramatically by varying the feeding option. The average values of oxygen are 5.5% and 6.2% for the U-Bed and the O-Bed, respectively. On the contrary, the shape of the O_2 profile differs significantly. When submerged fuel feeding is adopted, the oxygen concentration increases from 4.5% to 6.2%, passing from the starting radial position, located above the fuel entry point, to the opposite side. The O_2 profile is almost flat, in the case of an O-Bed option. Carbon monoxide assumes the same average value irrespective of the adopted feeding option. Also CO radial profiles have a similar shape; in fact they monotonically decrease moving from the location close to feeding point to the opposite side. The result provides a clear confirmation that a radial segregation of combustible matters released upon particle injection occurs. The segregation mechanism appears to be en-

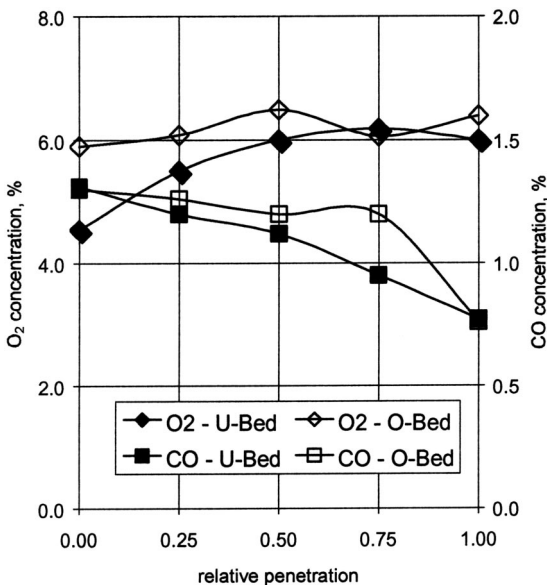


Fig. 6 Radial profiles of gaseous species in the splashing zone. The X coordinate is adimensionalized with the combustor diameter ($U=0.97$ m/s; $e=1.23$)

hanced by adopting a U-Bed option as a consequence of a less uniform spreading of fuel particles along the combustor section.

Model Description

A stationary lumped parameter model of an atmospheric bubbling fluidized bed combustor, suitable for high-volatile solid fuels, has been recently presented [6]. The combustor is modeled as a series of three reaction zones: the dense fluidized bed, the splashing region, and the freeboard. The splashing region height is calculated by solving a simplified motion equation of a single bed particle ejected by a bubble bursting at the surface of the bed. This region has been considered to be perfectly mixed because of the high turbulence that establishes above the bed surface. The model is based on material balances on fixed carbon (present both as relatively large nonelutriable char particles and as fine char particles of elutriable size), volatile matter and oxygen in each combustor section. The model takes into account phenomena that assume particular importance with high-volatile fuels, namely fuel particles fragmentation and attrition in the bed, volatile matter segregation and turbulent postcombustion above the bed. An energy balance on the splashing region is set up to account for thermal feedback from the splashing region to the bed associated to solids ejection/falling back. Volatile matter and elutriated fines postcombustion and radiative and convective heat fluxes to the bed and the freeboard are considered in the balance. Gaseous pollutants formation and emission have been neglected in the model.

The model has been applied to the prediction of the fluidized bed combustion performance of pine-seed shells. Input parameters were selected with reference to the fuel (Table 1) and to geometrical and operating conditions relative to the experiments reported in this work. In particular, the Pine-B series of experiments (Table 2) was simulated. Values of the other model parameters can be found in Scala and Salatino [6].

Model Results

Model results are reported in Table 3, together with the values of operating variables used for calculations. Results show that total combustion efficiency is always about 100%. This is a consequence of the large oxygen concentration in the bed due to an extensive bypass of volatile matter and of the large intrinsic reactivity of biomass chars that makes their combustion either as coarse or as fine particles very effective. The carbon loading of fines in the bed is much smaller than that corresponding to coarse char particles, because of the much larger burning rates of the former. Carbon loadings in the splashing region and in the freeboard are negligible. Figure 7 reports a comparison between model and experimental total carbon loadings in the bed as a function of the fluidization velocity for both under-bed and over-bed feeding options. The model computations predict satisfactorily both the values and the trend of carbon loading in the bed. It is interesting to note that for all fluidization velocities the predicted carbon loading under both feeding conditions is almost coincident, the dense phase environment being practically the same. Experimental data reported in the figure confirm this result.

The bed section represents the main location for fixed carbon conversion. Most volatile matter is converted in the splashing region of the combustor. Even when submerged fuel feeding is considered in the computations, in-bed volatile matter burning is rather limited (5–6%). Up to 40% of the volatile matter can escape the splashing region and burn in the freeboard, depending on the operating conditions. It can be noted that results of over-bed and under-bed feeding are always very close to each other. This is due to the very rapid segregation of the fuel particles during devolatilization at the top of the bed whatever the feeding option.

Table 3 reports heat generation rates in the three combustor sections for the operating conditions considered. One can estimate that about 70% of the heat release takes place within the bed during combustion of the biomass under the simulated conditions,

Table 3 Operating variables and results of model computations

| Operating variables | | | | | | |
|--|-----------------|----------------|--------|--------|--------|--------|
| Bed temperature, K | | | | | | 1123 |
| Freeboard temperature, K | | | | | | 973 |
| Pressure, kPa | | | | | | 101 |
| Bed solids mean size, mm | | | | | | 0.725 |
| Fuel feed mean size, mm | | | | | | 10.0 |
| Fuel feeding | | | | | | |
| Superficial gas velocity, m/s | | O-Bed | | | U-Bed | |
| Excess air factor, – | 0.7 | 0.97 | 0.57 | | 0.7 | 0.97 |
| | 1.25 | 1.23 | 1.25 | | 1.28 | 1.23 |
| Model results | | | | | | |
| Expanded bed height, m | | 0.84 | 0.96 | 0.78 | 0.84 | 0.96 |
| Splashing zone height, m | | 0.06 | 0.10 | 0.08 | 0.06 | 0.10 |
| Fuel feed rate, kg/s | | 0.0033 | 0.0046 | 0.0027 | 0.0032 | 0.0046 |
| Coarse char mean size, mm | | | | 6.84 | | |
| Fraction of volatiles burned in bed, % | | 0.0 | 0.0 | 6.1 | 5.4 | 4.6 |
| Frac. of volatiles burned in spl. zone, % | | 84.6 | 60.5 | 93.9 | 86.2 | 59.0 |
| Carbon loading, kg | | 0.077 | 0.119 | 0.064 | 0.075 | 0.121 |
| | Coarses in: | Bed | | | | |
| | Fines in: | Bed | 1.1e-4 | 1.6e-4 | 0.9e-4 | 1.1e-4 |
| | | Splashing zone | | ~0.0 | | 1.7e-4 |
| | | Freeboard | | ~0.0 | | |
| Oxygen mole fraction, – | | | | | | |
| | | Bed | 0.11 | 0.10 | 0.10 | 0.11 |
| | | Splashing zone | 0.052 | 0.066 | 0.042 | 0.051 |
| | | Exhaust | 0.042 | 0.039 | 0.042 | 0.039 |
| Total combustion efficiency, % | | | | 100 | | |
| Splashing zone temperature, K | | | | 1188 | 1180 | 1152 |
| Heat generation rate, kW | | | | | | |
| | Bed: | Coarse char | 17.2 | 24.2 | 14.0 | 16.7 |
| | | Fine char | 17.0 | 23.9 | 13.8 | 16.6 |
| | | Volatiles | 0.0 | 0.0 | 0.8 | 0.8 |
| | Splashing zone: | Fine char | | | ~0.0 | |
| | | Volatiles | 13.3 | 13.4 | 12.0 | 13.2 |
| | Freeboard: | Fine char | | | ~0.0 | |
| | | Volatiles | 2.4 | 8.7 | 0.0 | 1.3 |
| Splashing zone-to-bed heat fluxes (% of s.z. heat release) | | Convective | 55.4 | 57.5 | 53.1 | 55.5 |
| | | Radiative | 2.7 | 1.7 | 3.3 | 2.7 |
| | | Total | 58.1 | 59.2 | 56.4 | 58.2 |
| Splashing zone-to-freeboard heat fluxes (% of s.z. heat release) | | Convective | 13.6 | 10.5 | 13.5 | 13.4 |
| | | Radiative | 28.3 | 30.4 | 30.1 | 28.4 |
| | | Total | 41.9 | 40.8 | 43.6 | 41.8 |

the remainder being released in the splashing region (20–30%) and in the freeboard (0–10%), because of extensive volatile matter postcombustion. It is interesting to assess the magnitude of thermal fluxes that are established between the different sections of the combustor. The aim is that of determining to what extent heat released in the splashing region is fed back to the bed, and the related temperature of the splashing region. It is recalled here that in the model bed and freeboard temperatures were fixed at 850°C and 700°C, respectively. The importance of volatile matter afterburning brings about a pronounced over-temperature of the splashing region (30–65°C). However large thermal feedback to

the bed prevents overheating from being even larger. About 60% of the heat released in the splashing zone is fed back to the bed, the dominant mechanism being solids convection associated with particles ejection/fall-back.

Figure 8 reports the calculated fraction of the total heat that is directly released or recirculated in the bed for the same conditions as for Fig. 5 ($U = 0.97$ m/s; $e = 1.23$). Results show that approximately 70% of the total heat is generated in the bed by char combustion, the in-bed volatile combustion being very small (U-Bed feeding) or absent (O-Bed feeding). Part of the heat released in the splashing region by volatile combustion is recirculated to

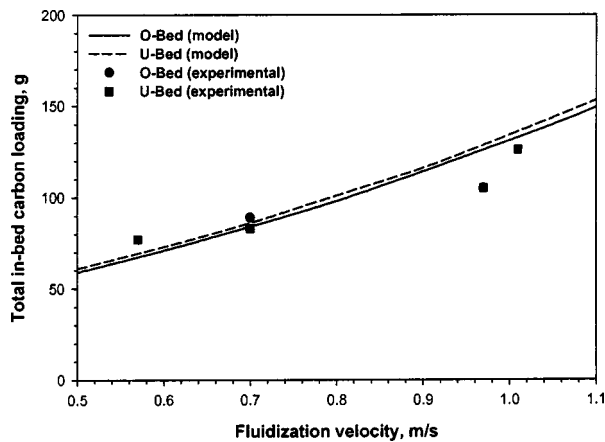


Fig. 7 A comparison of calculated and experimental carbon loadings as a function of the fluidization velocity ($e = 1.2$)

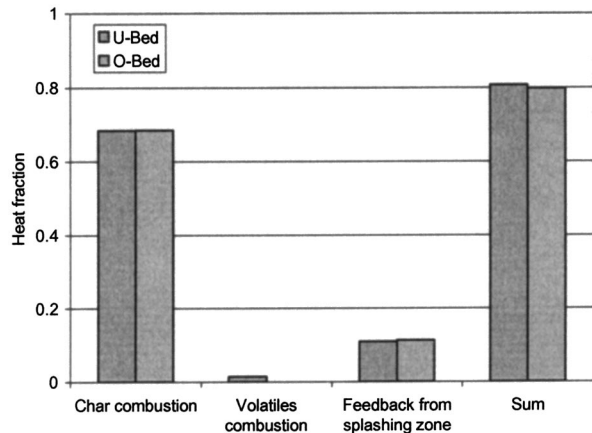


Fig. 8 Calculated fractions of the total heat released/recirculated in the bed ($U = 0.97$ m/s; $e = 1.23$).

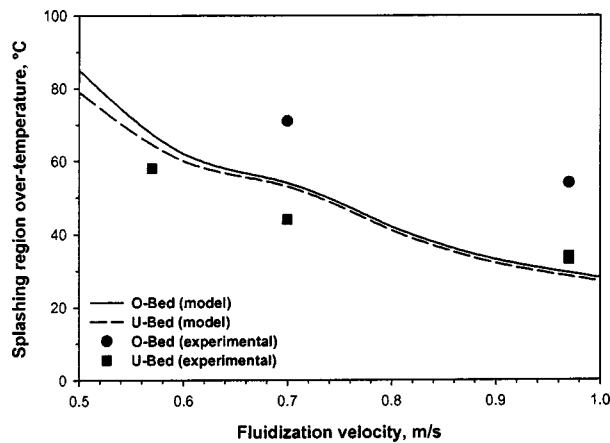


Fig. 9 A comparison of calculated and experimental splashing region over-temperature as a function of the fluidization velocity ($e = 1.2$)

the bed by the solids convection feedback mechanism ($\sim 10\%$). It is important to note that the sum of the contributions to the bed heat input is about 80% of the total heat release. This value is very close to the sum of the measured/estimated contributions to heat removed from the bed as reported in Fig. 5 for both over-bed and under-bed feeding options. This confirms the soundness of the model schematization and assumptions.

Figure 9 shows a comparison between the model and experimental data for the splashing region temperature increase above the bed one, as a function of the fluidization velocity. Agreement is fair, especially for under-bed feeding conditions. The model clearly underestimates the over-bed feeding values, which are predicted to be very close to under-bed ones. This is probably caused by a too simplified schematization of the splashing region and freeboard fluid-dynamics. It must be noted, further, that even if splashing region temperatures are fairly predicted, the model cannot simulate the freeboard temperature profiles as a consequence of the lumped-parameter nature of the schematization. Experimental data, however, show that under some operating conditions a higher peak temperature is reached in the lower section of the freeboard above the splashing region. As a consequence, the prediction of the temperature profiles along the combustor would require a more detailed distributed-parameter schematization of the freeboard section.

Conclusions

The influence of the feeding option (i.e. under-bed vs over-bed) on the combustion performance has been investigated with reference to a biomass fuel (shells of pine-seeds). Experimental tests were performed in a pilot scale bubbling FB combustor at different fluidization velocities, excess air ratios and sand sizes and at a fixed bed temperature (850°C).

Combustion efficiencies are always greater than 99% thanks to the high level of volatile matter and the high reactivity of residual char. Carbon in the bed is mainly related to the presence of coarse char particles and no significant differences between U-Bed and O-Bed feeding option are noted.

In most cases freeboard temperature is higher than bed temperature as a consequence of volatile matter post-combustion. There is experimental evidence that the freeboard over-temperature is enhanced by adopting an O-Bed feeding option. Nevertheless, the temperature increase in the freeboard is contained within 113°C , indicating that only a limited fraction of fuel is burned above the bed region. This result was also confirmed by thermal measurements, which indicate that about 80% of the energy is released/recirculated inside the bed.

Significant differences between U-Bed and O-Bed options can be also found in the analysis of radial profiles of gaseous species in the splashing zone. Changes in measured radial concentration along combustor diameter are related to the segregation of combustible matter. This segregation mechanism is enhanced by adopting the U-Bed option as a consequence of a less uniform spreading of fuel particles along the combustor section.

A FBC model specifically developed for high-volatile fuels is also applied to provide a comparison with the experimental results of bed carbon load, heat release in the bed and temperature peak in the splashing region. The model computations predict quite satisfactorily both the values and the trends of experimental data.

About 70% of the heat release takes place within the bed under the simulated conditions, the remainder being released in the splashing region (20–30%) and in the freeboard (0–10%), because of extensive volatile matter post-combustion. About 60% of the heat released in the splashing zone, however, is fed back to the bed mainly by solid convection associated with particle ejection/fall-back.

The model underestimates experimental peak temperatures with over-bed feeding, which are predicted to be very close to under-bed ones. A detailed prediction of the freeboard temperature profiles will require further improvements of the model.

Acknowledgment

Authors gratefully acknowledge A. Cante, C. Liccardi and A. Silvestre for the set-up of the experimental rig, the assistance during combustion tests and chemical analysis.

References

- La Nauze, R. D., 1987, "A Review of the Fluidized Bed Combustion of Biomass," *J. Inst. Energy*, **60**, pp. 66–76.
- Anthony, E. J., 1995, "Fluidized Bed Combustion of Alternative Solid Fuels: Status, Success and Problems of the Technology," *Prog. Energy Combust. Sci.*, **21**, pp. 239–268.
- Andersson, B. A., Leckner, B., and Amand, L. E., 1985, "Fluidized-Bed Combustion of Coals and Alternative Fuels," *Proceedings of the 8th International Conference on Fluidized Bed Combustion*, ASME, New York, pp. 1019–1029.
- Fiorentino, M., and Miccio, F., 2000, "On the Relevance of Segregation Phenomena During Bubbling Fluidized Bed Combustion and Desulfurization of Ebonite," *Combust. Sci. Technol.*, **159**, pp. 57–86.
- Chirone, R., Marzocchella, A., Salatino, P., and Scala, F., 2001, "Fluidized Bed Combustion of High-Volatile Solid Fuels," *Fluidization X*, M. Kwak, J. Li, and W. Jang, eds., Engineering Foundation, New York, pp. 645–652.
- Scala, F., and Salatino, P., 2002, "Modelling Fluidized Bed Combustion of High-Volatile Solid Fuels," *Chem. Eng. Sci.*, **57**, pp. 1175–1196.
- Grubor, B. D., Oka, S. N., Ilic, M. S., Dakic, D. V., and Arsic, B. T., 1995, "Biomass FBC Combustion—Bed Agglomeration Problems," *Proceedings of the 13th International Conference on Fluidized Bed Combustion*, ASME, New York, pp. 515–522.
- Natarajan, E., Ohman, M., Gabra, M., Nordin, A., Liljedahl, T., and Rao, A. N., 1998, "Experimental Determination of Bed Agglomeration Tendencies of Some Common Agricultural Residues in Fluidized Bed Combustion and Gasification," *Biomass Bioenergy*, **15**, pp. 163–169.
- Skrifvars, B., Backman, R., and Hupa, M., 1998, "Characterization of the Sintering Tendency of Ten Biomass Ashes in FBC Conditions by a Laboratory Test and by Phase Equilibrium Calculations," *Fuel Process. Technol.*, **56**, pp. 55–67.
- Chirone, R., Salatino, P., and Scala, F., 2000, "The Relevance of Attrition to the Fate of Ashes During Fluidized-Bed Combustion of a Biomass," *Proc. Combust. Inst.*, **28**, pp. 2279–2286.
- Salatino, P., Scala, F., and Chirone, R., 1998, "Fluidized Bed Combustion of a Biomass Char: the Influence of Carbon Attrition and Fines Postcombustion on Fixed Carbon Conversion," *Proc. Combust. Inst.*, **27**, pp. 3103–3110.
- Scala, F., Salatino, P., and Chirone, R., 2000, "Fluidized Bed Combustion of a Biomass Char (Robinia Pseudoacacia)," *Energy Fuels*, **14**, pp. 781–790.
- Fiorentino, M., Marzocchella, A., and Salatino, P., 1997, "Segregation of Fuel Particles and Volatile Matter During Devolatilization in a Fluidized Bed Reactor—I. Model Development," *Chem. Eng. Sci.*, **52**, pp. 1893–1908.
- Fiorentino, M., Marzocchella, A., and Salatino, P., 1997, "Segregation of Fuel Particles and Volatile Matter During Devolatilization in a Fluidized Bed Reactor—II. Experimental," *Chem. Eng. Sci.*, **52**, pp. 1909–1922.
- Madrali, E. S., Ercikan, D., and Ekinici, E., 1991, "Changes in Fuel Particle Structure and its Effect on Segregation in Fluidized Beds During the Initial Combustion Stages," *FBC—Technology and the Environmental Challenge*, Hilger, London, pp. 139–147.
- Kunii, D., and Levenspiel, O., 1991, *Fluidization Engineering* 2nd ed., Butterworth-Heinemann, Boston.

Energy Extraction From a Porous Media Reciprocal Flow Burner With Embedded Heat Exchangers

Fabiano Contarin
Graduate Student

William M. Barcellos
Post-Doctoral Fellow

Alexi V. Saveliev
Research Professor

Lawrence A. Kennedy¹
kennedy@uic.edu
Professor

Department of Mechanical and Industrial
Engineering,
University of Illinois at Chicago,
Chicago, IL 60607

Superadiabatic combustion in porous media allows a stable burning of ultralean methane/air mixtures, far below flammability limits. The intrinsic heat regeneration process of the porous matrix and the low degree of thermal nonequilibrium between the gas and the solid phases maintain temperatures of less than 1600 K resulting in extremely low levels of CO and NO_x production. Due to the transient nature of this phenomenon, a method to confine the combustion into a practical burner has been engineered. The Reciprocal Flow Burner (RFB) is an effective and simple system to achieve this result by arranging the reaction zone to travel back and forth along the length of the burner. This ultimately results in a relatively uniform temperature profile over the central zone of the reactor. Embedding heat exchangers into the ends of the bed makes it an appealing alternative for high-efficiency, low-emission heat generation. In the present work, experimental results are presented and compared to an earlier numerical model to provide a better understanding of heat extraction from a RFB.

Keywords: Filtration Combustion, Porous Combustion, Heat Exchanger, Process Heater
[DOI: 10.1115/1.1844539]

Introduction

As an internally self-organized process of heat recuperation, the combustion of premixed air–fuel mixtures in porous media differs significantly from homogeneous flames. This difference can be attributed to two main factors: the highly developed inner surface of the porous media results in efficient heat transfer between the gas and the solid, and the intense mixing of the gas flowing in the porous media increases effective diffusion and heat transfer in the gas phase. It is an internally self-organized process of heat recuperation.

The combustion zone in common porous burners is usually stabilized at a fixed position in a finite section of a porous matrix by the imposed boundary conditions. However, in an unrestricted uniform porous media, the combustion zone is transient and can propagate freely as a coupled reaction—a thermal wave in either the downstream or upstream directions. It is the unrestricted system that is the focus of the present study.

Strong interstitial heat transfer results in a low degree of thermal nonequilibrium between the gas and the solid phases resulting in coupling of the thermal and the reaction waves. This situation generally corresponds to the low velocity regime of wave propagation, according to the classification given by Babkin [1]. The motion of the combustion zone results in positive or negative enthalpy fluxes between the reacting gas and solid porous media. As a result, observed combustion temperatures can significantly differ from adiabatic predictions based on the enthalpy of the initial reactants and are controlled mainly by the reaction chemistry and heat transfer mechanism. Upstream wave propagation, countercurrent to the gas flow, results in subadiabatic combustion temperatures [2] while downstream propagation of the wave leads to combustion in the superadiabatic regime with temperatures much in excess of the adiabatic temperature [3]. Superadiabatic combustion significantly extends conventional flammability limits to the region of ultralow heat content mixtures in the range of equivalence ratios $0.1 \leq \Phi \leq 0.5$. The combined effect of the lean

mixtures and low combustion temperatures makes the superadiabatic burners capable of operating at ultralow emissions of NO_x and CO [4]. The modern applications of transient porous burners include combustion of low-calorific fuels, VOC emission control with the possibility of heat recovery, and fuel reforming in the ultrarich superadiabatic flames as studied by Kennedy et al. [5–9] and Drayton et al. [10].

The presence of a high-conductivity high-specific heat solid phase enables porous combustion to occur in the vicinity of heat exchangers. The porous matrix is capable of retaining the heat produced by the reaction and transferring it to a colder body (e.g., heat exchanger). This significantly enhances the efficiency of the heat extraction from the combustion zone.

Stationary and transient systems are the two major design approaches commonly employed in porous combustion. Historically, the research on heat extraction from porous media burners was directed toward the stationary approach. Radiant burners [11,12] and surface combustion heaters, where coolant tubes are embedded in the porous matrix [13–15], are characteristic examples of this approach. Nevertheless the transient approach offers advantages due to its ability to operate at superadiabatic temperatures and higher efficiencies despite its larger degree of complexity.

RFB Features

The main problem arising from the unsteady nature of this phenomenon is to engineer a method to confine the combustion in a practical burner. The reciprocal flow burner (RFB) configuration represents a simple and effective way to achieve this result. In the RFB the direction of the flow is periodically reversed with the inlet becoming the outlet and vice versa, allowing the combustion zone to be restricted in a finite reactor while maintaining its transient behavior [16]. By adjusting the period of the cycle reversal, steady temperature profiles can be achieved within the reactor. The RFB systems have been recently an object of both numerical and experimental studies [17–19].

In an earlier work by the authors [18], a numerical model investigated the possibility of using the RFB as a process heater. In the present work, this new concept of heat extraction strategy is tested utilizing a heat exchanger made of two separate components embedded in the terminal sections of a porous matrix. Tran-

¹Corresponding author.

Contributed by the Heat Transfer Division for publication in the JOURNAL OF HEAT TRANSFER. Manuscript received by the Heat Transfer Division May 9, 2003; revision received October 27, 2004. Review conducted by: B. Farouk.

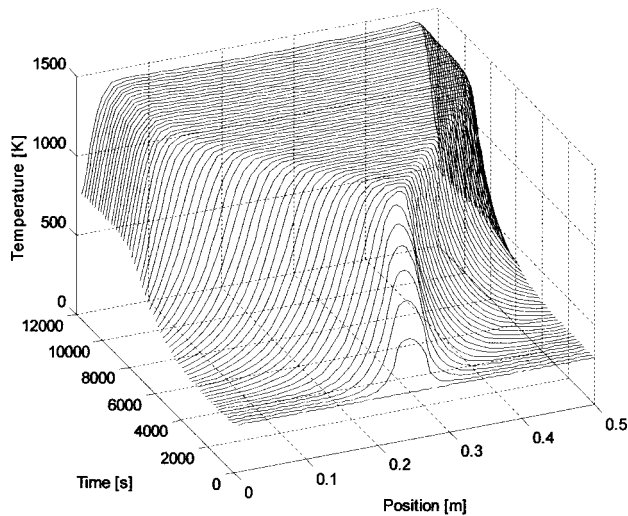


Fig. 1 Temperature profile formed in the perfectly insulated RFB: $\nu_g=0.3$ m/s, $\Phi=0.35$, $\tau=100$ s

sient combustion with alternating flow direction of the reactants makes possible the combustion of mixtures with ultra-low heat contents that lie out of the conventional flammability limits. Furthermore, the NO_x production is decreased since the combustion temperature is typically low (<1600 K).

Advantages of Using a RFB for Heat Generation. Conceptually, the use of the RFB for heat generation offers two main advantages compared to conventional (stationary) porous medium burners:

1. It can operate in the superadiabatic regime, making possible the extraction of heat from ultralean mixtures.
2. A pseudotrapezoidal temperature profile within the burner is possible because the reciprocating reaction zone is established and maintained centrally in the combustor. This favors positioning the heat exchangers at the lateral exit zones, which are relatively far from the reaction zone, resulting in the flame not being quenched and, hence, producing low amounts of CO.

Featuring the RFB, the previously developed numerical model of the RFB [18] takes into account the heat extraction. It is able to

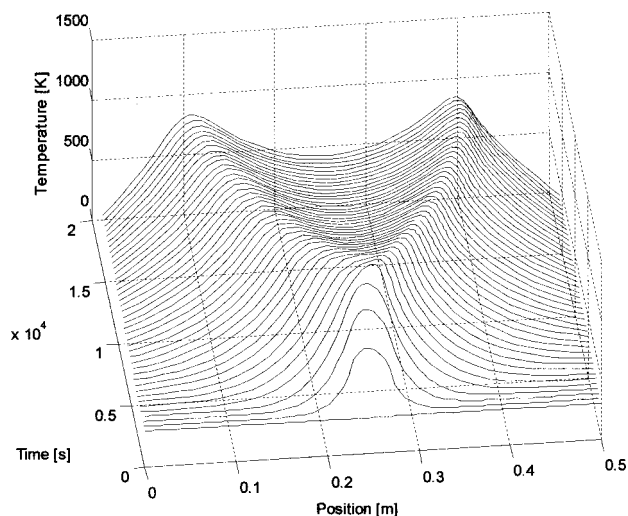


Fig. 2 Temperature profile formed in the RFB with radial heat losses: $\nu_g=0.3$ m/s, $\Phi=0.35$, $\tau=100$ s

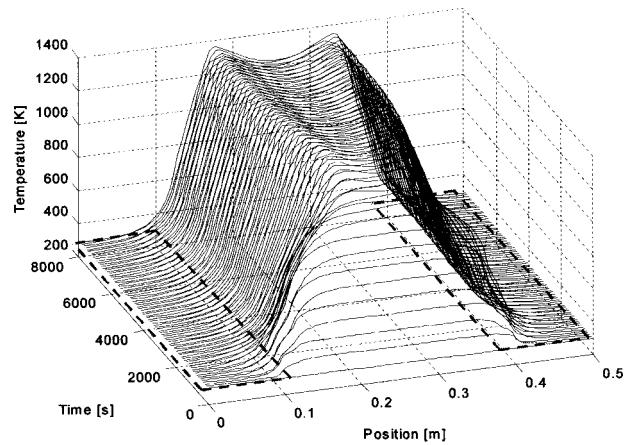


Fig. 3 Temperature profile in reactor with radial heat losses and lateral heat extraction: $\nu_g=0.3$ m/s, $\Phi=0.35$, $\tau=100$ s

predict the influence of the process parameters based on a detailed heat transfer and single-step chemical mechanism.

Briefly, the model solves three time-dependent differential equations:

- The solid phase energy conservation equation,

$$(1 - \epsilon)c_s \rho_s \frac{\partial T_s}{\partial t} = \frac{\partial}{\partial x} \left([k_s^* + k_r] \frac{\partial T_s}{\partial x} \right) + h_v(T_g - T_s) - \beta(T_s - T_{room}) \quad (1)$$

The gas phase energy conservation equation,

$$\epsilon c_g \rho_g \frac{\partial T_g}{\partial t} = \epsilon \frac{\partial}{\partial x} \left([k_g + (c_g \rho_g) D_{ax}] \frac{\partial T_g}{\partial x} \right) - \epsilon c_g \rho_g \nu_g \frac{\partial T_g}{\partial x} + h_v(T_s - T_g) + \epsilon H_{chem} W \quad (2)$$

The species conservation equation,

$$\rho_g \frac{\partial y_p}{\partial t} = \frac{\partial}{\partial x} \left([D + D_{ax}] \frac{\partial y_p}{\partial x} \right) - \rho_g \nu_g \frac{\partial y_p}{\partial x} + W \quad (3)$$

where the product mass production rate per unit volume W is given by the Arrhenius law:

$$W = \rho_g (1 - y_p) A_f \exp(-E_a/RT) \quad (4)$$

The gas phase is considered to be a mixture of only two generalized species: the reactants and the products. For full details, see Ref. [18].

Temporal evolution of temperature profiles in RFB is illustrated in Figs. 1–3 for the cases of perfectly insulated reactor (Fig. 1), reactor with radial heat loss (Fig. 2), and reactor with heat extraction (Fig. 3). Figure 1 shows a perfectly insulated reactor with heat losses through the walls considered to be zero. Fresh reactants are supplied through the inlet at ambient conditions and exhausted at the outlet to ambient conditions. After initiating the combustion wave initiated in the RFB by preheating, it propagates back and forth through the bed establishing a temperature profile with a peak near the center of the length of the reactor. As time progresses, this peak grows and broadens throughout the length of the reactor. The flat central temperature plateau that develops in this reactor is ideal for energy extraction or chemical processing.

Figure 2 shows numerical results considering uniform radial heat losses through the reactor walls at an equivalence ratio of 0.35. The evolving temperature distribution is confined within the burner forming a valley-like shape in the central zone. Figure 3 presents the results of numerical modeling showing the influence of the heat exchangers on the temperature profile as they effectively confine the reaction zone in the middle region of the burner.

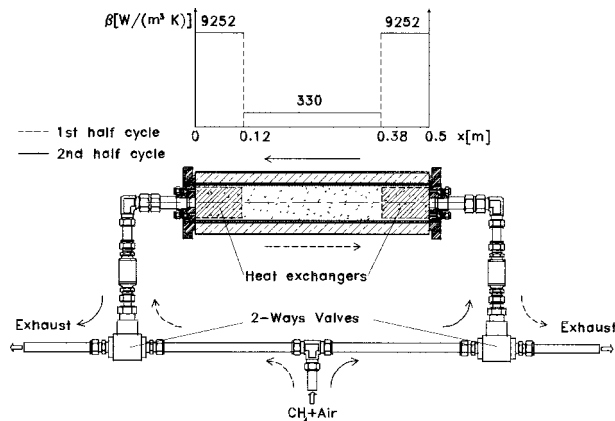


Fig. 4 Experimental RFB setup with reciprocating flow system

Experimental System

The core of the RFB consists of a 50-cm long vertical quartz tube with 7.6-cm internal diameter filled with 5.6-mm solid alumina pellets creating a loose packed bed, whose porosity is approximately 40%. A 3 mm thick layer of Kaowool insulation (ceramic fiber) is interposed between the alumina pellets and the tube wall.

At the both ends of the reactor two aluminum flanges retain the porous media inside the tube making the system hermetic and isolated from the surrounding environment. The operation of the combustor begins with the preheating of the porous media using an electrical heater that covers the outer surface of the quartz tube. The reciprocating air flow system is already operational in order to maintain a homogeneous inner temperature. The combustion

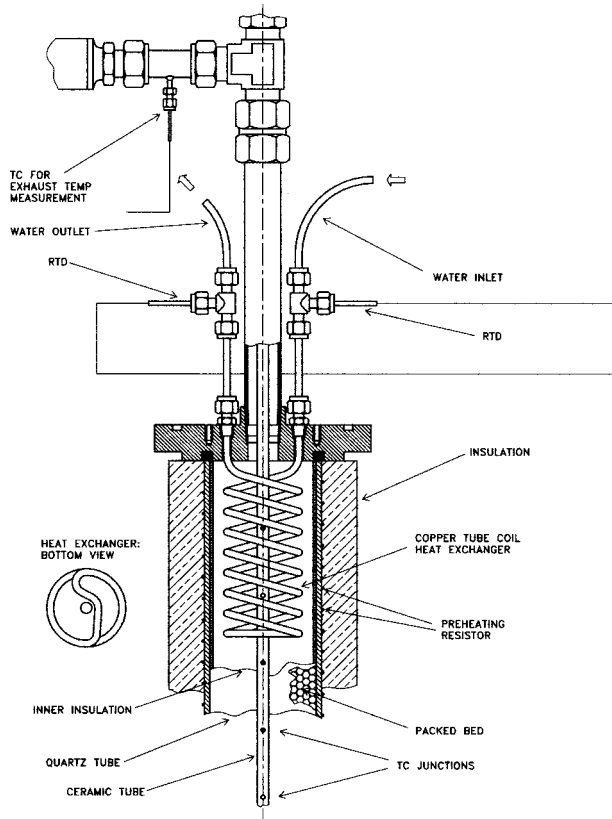


Fig. 5 Heat exchanger mounted at the terminal sections of a RFB

process automatically initiates when any point in porous media reaches a temperature above 1200 K. Subsequently, the reaction wave travels back and forth over the length of the reactor establishing a relatively stable temperature plateau at the burner middle. The gas flow velocities (filtration velocities) used in the experiments are selected in the range from 0.15 to 0.45 m/s. As mentioned previously, this range corresponds to the low velocity regime of combustion wave propagation as defined by Babkin [1].

Most of the experiments were performed with a half cycle time τ of 100 s. This switching period is found to be optimal from experimental studies on the stability of the combustion process, temperature distribution, and capability to maintain good energy storage. The heat extraction from the RFB was accomplished by placing two heat exchangers in the terminal sections of the reactor. The dimensions of the heat extraction zones are given in Fig. 4. The heat exchangers consist of copper tube coils positioned in the ends of the combustor, and embedded in the porous matrix. The reaction zone is then constrained in the central region of the reactor due to their presence. Figure 5 provides a close up view of the heat exchanger mounted at the end section of the combustor. In all experiments, the temperature measurements were performed with 0.2-mm diameter S-type thermocouples. These thermocouples were positioned axially at the inlet and outlet plus at 50 mm intervals along the axis of the reactor. Gas samples were taken at the reactor exit and analyzed with a Varian model 3600 gas chromatograph and a Thermo Environmental Instrument model 42H chemiluminescence NO_x analyzer. All thermocouple signals were digitized by a data acquisition system, as was the data from the gas analyzers. Technical grade methane was used in all conducted experiments.

Results and Discussion

The experimental and numerical results presented in this work show the influence of the important parameters: gas flow velocity, equivalence ratio, heat losses, and heat exchanger length. Also, the emissions and efficiency results are presented. The numerical predictions are compared with the experimental data. Figure 6 presents a comparison of the numerically predicted and experimentally measured temperature profiles for an equivalence ratio of 0.36, a gas flow velocity of 0.30 m/s, and a half cycle of 100 s. The developed numerical model accurately predicts the temperature inside the combustor. In the following, numerical and experimental results are presented, analyzing the influence of the RFB operating parameters on the temperature profile.

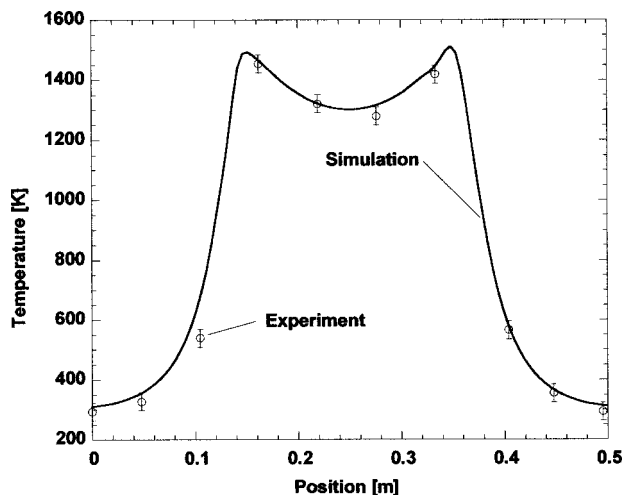


Fig. 6 Simulated and experimental temperature profiles obtained with the heat exchangers: $v_g=0.3$ m/s, $\Phi=0.36$, $\tau=100$ s

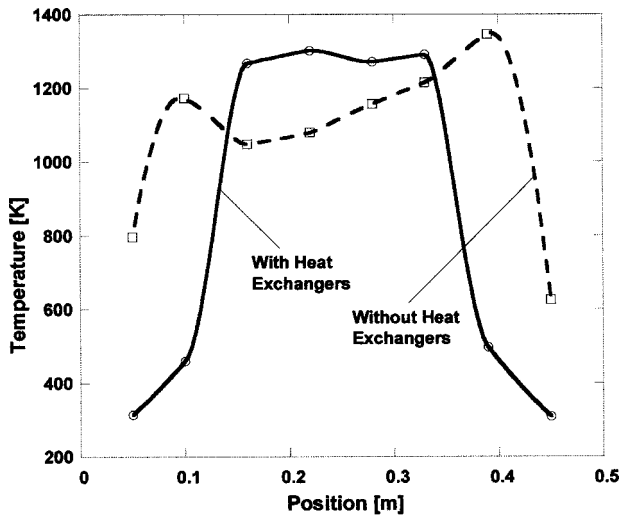


Fig. 7 Influence of the heat exchangers on the experimental temperature profiles: $\nu_g=0.2$ m/s, $\Phi=0.36$, $\tau=100$ s

Influence of Heat Exchangers on Temperature Profiles

The experimental results shown in Fig. 7 illustrates the influence of the equivalence ratio on the temperature profiles in the RFB with and without the heat exchangers. It should be noted that without heat extraction, the reaction zone can be stabilized within the reactor only for equivalence ratios less than 0.45. With a heat extraction it is possible to increase Φ up to stoichiometry. Figure 7 illustrates that the trapezoidal temperature profile is more uniform when heat exchangers are employed. The heat that would be lost by radiation and convection in the burner ends or through the exhaust is absorbed by the heat exchangers, resulting in a much reduced exhaust temperature and hence a higher thermal efficiency.

Influence of Heat Losses on Temperature Profiles.

From the numerical results presented in Fig. 8, the radial heat losses are seen to have a strong effect on the temperature profile principally in the central region of the combustor. Raising the coefficient of the heat losses to the surroundings lowers the temperature in the reactor midpoint. The maximum temperature is only slightly reduced. At the ends of the reactor, the temperature variations are small because of the presence of the heat exchangers. For the employed experimental configuration, the heat loss coefficient in the middle of the reactor is estimated to be close to $330 \text{ W}/(\text{m}^3 \text{ K})$.

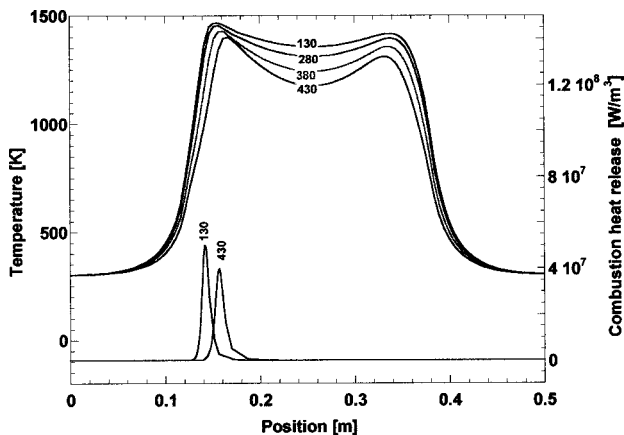


Fig. 8 Influence of heat losses on the RFB temperature distribution. Numbers show heat losses coefficient β in the central zone of RFB.

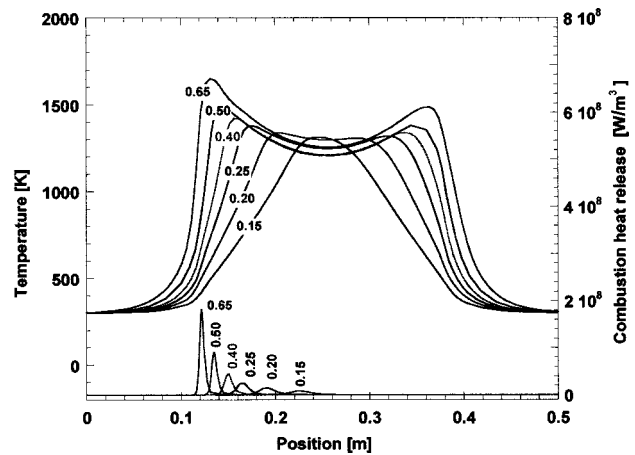


Fig. 9 Influence of the equivalence ratio (numbers on the curves) on temperature distribution in the RFB, $\nu_g=0.2$ m/s

Influence of Equivalence Ratio on Temperature Profiles.

Numerical predictions of the effect of equivalence ratio on the temperature profile for a constant gas flow velocity are shown in Fig. 9. It shows that temperature plateau widens and the peak temperatures increase with increasing equivalence ratios. The lateral thermal gradients also are large. The experimental results (Fig. 10) also show that the temperature plateau expands toward the ends of the combustor as the equivalence ratio increases and that the maximum temperatures remain almost independent of the equivalence ratio. The different trend of the predicted maximum temperatures with equivalence ratio is attributed to the simplified reaction model employed and the filtration velocity. The predicted evolution of the temperature profile from the single maximum to a trapezoidal shape is well reproduced by the model. Again it should be noted that without the radial heat losses, the temperature profile would be flat in the central region. As the value of Φ increases from an extremely low value of 0.12, the experimental steady state temperature profile evolves from a single maximum to a broadening plateau with two temperature peaks. In the absence of radial heat losses this single maximum would evolve into a broadened temperature plateau.

Influence of Gas Flow Velocity on Temperature Profiles

Varying the gas the velocity from 0.15 to 0.45 m/s, the numerical

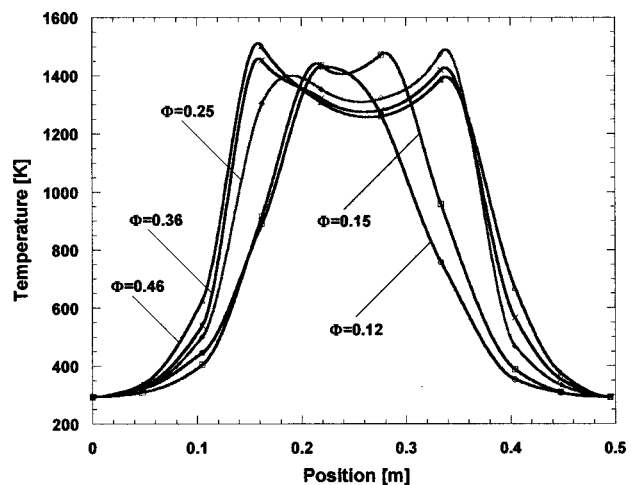


Fig. 10 Experimental temperature distributions in the RFB recorded varying equivalence ratio of the supplied mixture, $\nu_g=0.3$ m/s

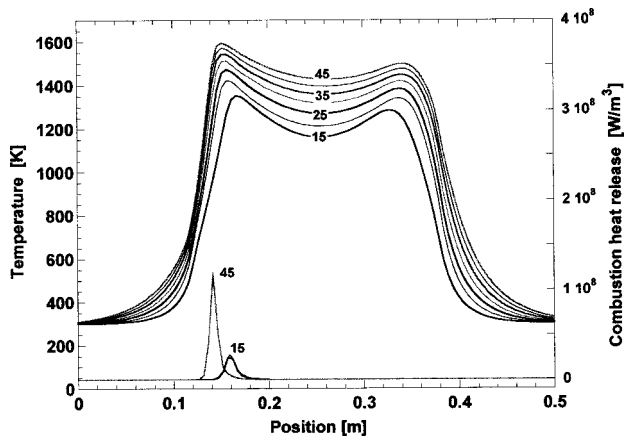


Fig. 11 Effect of gas flow velocity variation (numbers on the curves) on temperature distribution in the RFB

model predicts the raise of the maximum combustion temperature from 1350 to 1600 K, as shown in Fig. 11. Figure 12 displays the corresponding experimental results. As is seen, there is excellent agreement between the model and the experiment. The maximum values of temperature profiles are significantly increased as the gas flow velocity increases.

Figure 13 shows the exhaust gas temperatures, measured at the centerline of the exit from the bed, increase linearly with the equivalence ratio, but are always lower than 60°C. The relevant convective heat losses account for less than 1% of the total power available.

NO_x and CO Emissions. During the process cycle, the CO and NO_x oscillates around very low average values, as shown in Fig. 14. The oscillation period is equal to the full cycle instead of just one half cycle, due to asymmetries in the temperature distribution. Figures 15 and 16 separately demonstrate the effect of the equivalence ratio on the production of CO and NO_x. The NO emission grows with the equivalence ratio from less than 1 ppm at $\Phi=0.15$, to 16 ppm at $\Phi=1$. A higher NO production is observed for the higher gas flow velocity. For $0.2 < \Phi < 0.7$, CO emissions are in the range from 4 to 10 ppm. The CO level increases approaching the extinction limit ($\Phi < 0.1$) and the stoichiometry ($\Phi = 1.0$). Increasing the gas flow velocity results in a higher CO production. It should be noted that this burner is expected to op-

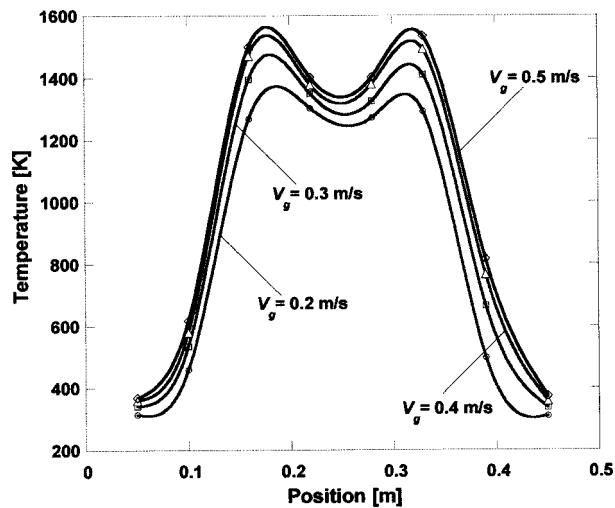


Fig. 12 Experimental temperature distributions in the RFB recorded varying the input gas flow velocities, $\Phi=0.35$

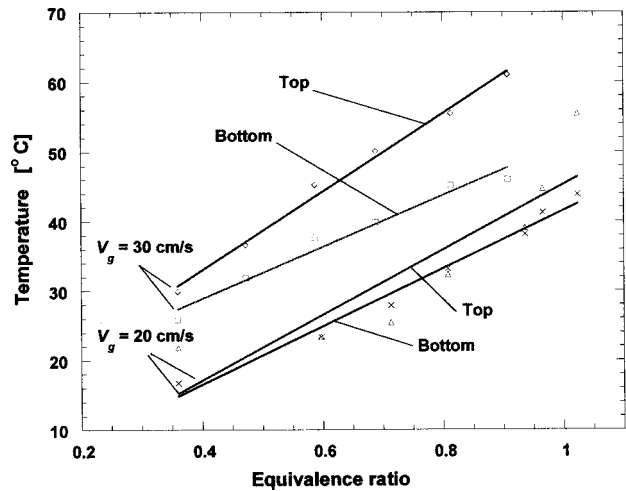


Fig. 13 Experimental exhausts temperatures as a function of equivalence ratio

erate at very low equivalence ratios, $0.2 \leq \Phi \leq 0.5$ that has NO_x and CO emission levels of less than 3 and 8 ppm, respectively.

Heat Extraction Efficiency. Figure 17 illustrates the power output of the heat exchangers oscillates with amplitudes of up to 75% of the maximum values. The instant power extracted from a single heat exchanger was measured as the product of a water mass flow rate, a water heat capacity, and a temperature increase. The hot gas flows from the high temperature plateau heats the heat exchanger located at the reactor end. At the same time, the incoming cold mixture cools the other heat exchanger. The out of phase heat exchange power outputs compensate each other when the heated water streams are combined. As a result the overall extracted power, P_{extr} , demonstrate fluctuations close to 20%. The efficiency of the heat extraction in the RFB can be determined as a ratio of the average power transferred to the water stream and the total chemical power provided by the flowing fuel/air mixture. The actual heat efficiency of the burner is defined as

$$\eta_{act} = \frac{\bar{P}_{extr}}{P_{chem}}, \quad (5)$$

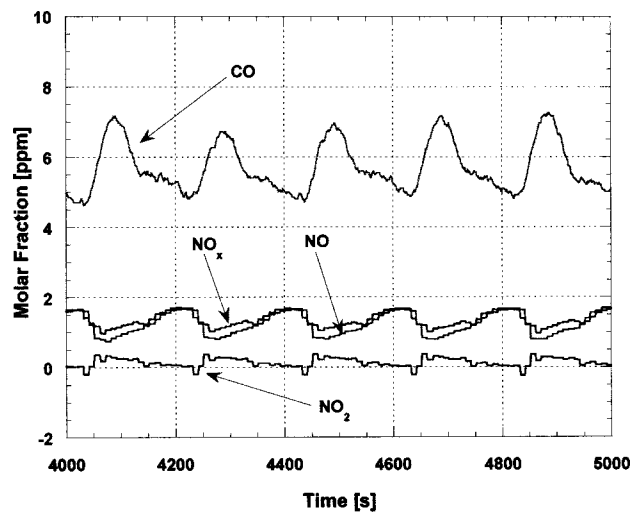


Fig. 14 Experimental pollutant emissions as a function of time, $\Phi=0.15$, $v_g=20$ cm/s

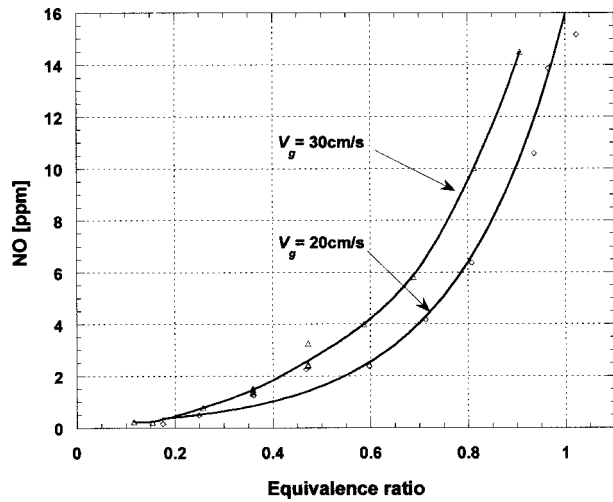


Fig. 15 Experimental NO emissions as a function of equivalence ratio

where chemical power P_{chem} is proportional to the mass fuel flow rate and the Low Heating Value (LHV) of the fuel and \bar{P}_{extr} is an average extracted power:

$$P_{chem} = \dot{m}_{CH_4} LHV \quad (6)$$

The experimentally measured actual heat extraction efficiencies are in the range from 70% to 80% (Fig. 18). The efficiencies show only a small increase with the equivalence ratio and small sensitivity to the variation of the gas flow velocity from 0.2 to 0.3 cm/s. At the same time the chemical and extracted power are varied in the range from 100 to 4000 W (Fig. 18) showing high heat extraction stability to the power load variation. A high turn-down ratio is an intrinsic feature of RFB due to the internal self-adjustment of the reaction zone and temperature profile to the combustion load. As a result, high operating efficiencies are sustained over a wide range of equivalence ratios and gas flow velocities.

In Fig. 19, the measured actual efficiency is compared with numerical predictions for a range of equivalence ratios from 0.15 to 0.7. While the experimental efficiency increases from ~70% to ~80%, the numerical predictions show a much stronger variation. The partial explanation is that the numerical predictions are per-

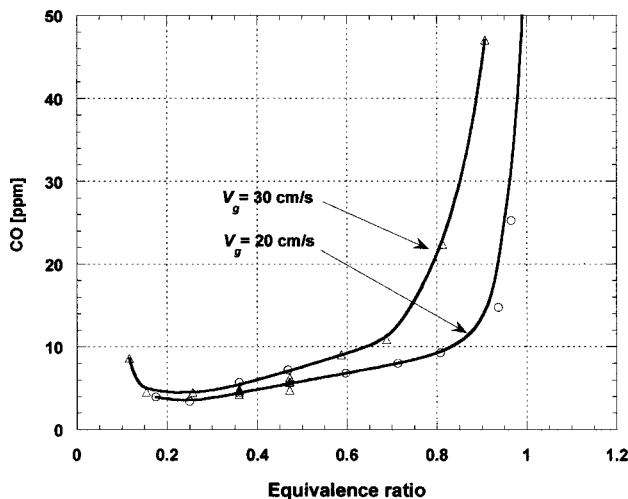


Fig. 16 Experimental CO emissions as a function of equivalence ratio

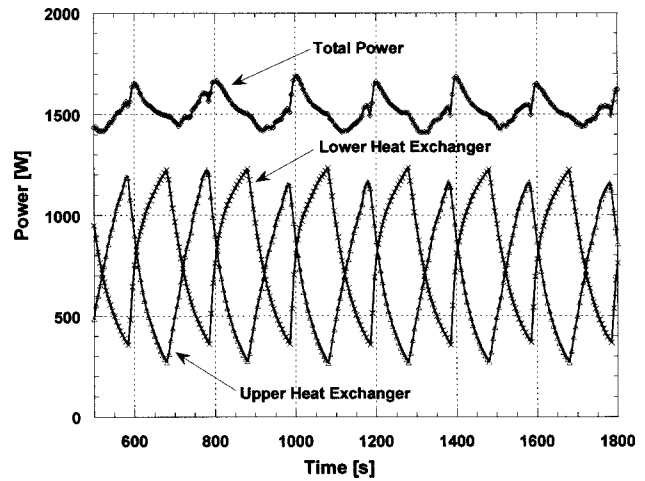


Fig. 17 Experimental power output as a function of time

formed for a constant radial heat loss coefficient, β , while the actual value of β is changed depending on experimental parameters, e.g., the maximum temperature attained at the specific equivalence ratio. Alternatively, the power lost through the walls and coefficient β can be determined at each experiment. The use of variable $\beta = \beta(T)$ allows us to correct the numerical prediction resulting in a much better agreement between experimental and numerical efficiencies (Fig. 19).

Besides, it should be noted that the actual heat extraction efficiency recorded experimentally is strongly affected by the presence of the strong radial heat losses. This effect is especially strong for the small experimental setup with high area-to-volume ratio. The ideal heat extraction efficiency defined as a theoretical limit of actual efficiency in the absence of radial heat losses can be estimated from the experimental data using the following expression:

$$\eta_{id} = \frac{P_{chem} - P_{conv}}{P_{chem}}, \quad (7)$$

where P_{conv} represents the convective heat losses determined product flow rate and exhaust gas temperature as

$$P_{conv} = \dot{m}_p (h_p(T_{exhaust}) - h_p(T_{room})) \quad (8)$$

The ideal heat extraction efficiencies for the RBF operating in the ultralean range with an input gas velocity of 0.3 m/s and the outlet water temperature of 325 K were evaluated from our data. These

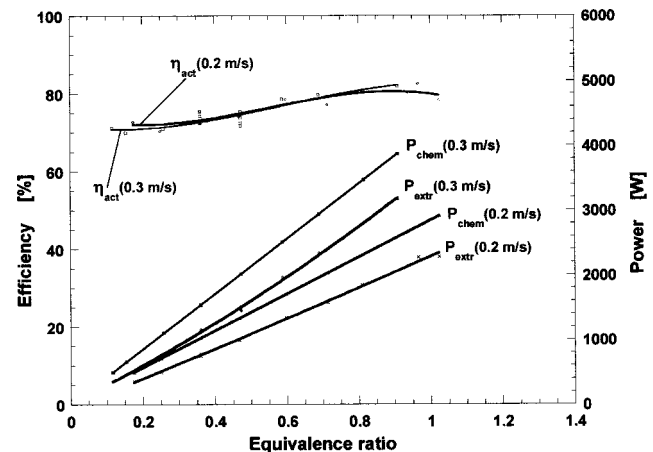


Fig. 18 Experimental efficiency of the heat extraction as a function of equivalence ratio

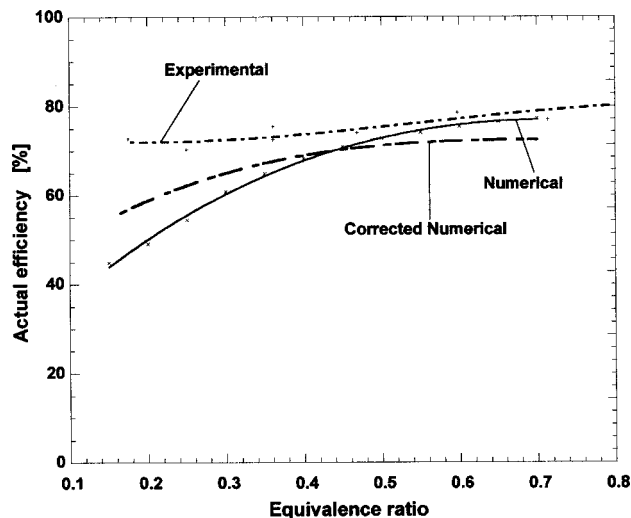


Fig. 19 Experimental and simulation results on the RFB efficiency

measured efficiencies exceed 90% for all experimental conditions at equivalence ratios well below the conventional flammability limits. The high ideal efficiency values show that most of the combustion energy release can be effectively transferred through the packed bed to the heat extraction system.

Another way of evaluating the energy transfer inside the RFB is to measure the heat recuperation efficiency that can be defined through the following expression:

$$\eta_{rec} = \frac{T_{water} - T_{exhaust}}{T_{water} - T_{room}} \quad (9)$$

This efficiency shows how close the temperature of the exhaust gas is to the temperature of the environment. The recuperation efficiency of 100% corresponds to the exhaust gas temperature equal to the room temperature. The measured recuperation efficiencies are in the range from 70% to 90%. In contrast with ideal and actual efficiencies, the recuperation efficiency drops with the increase of equivalence ratio and gas flow velocity due to the higher exhaust temperatures.

Conclusions

A new concept of porous reciprocal flow burner for heat generation was developed and tested. The main results are summarized below:

1. Stable combustion in RFB can be obtained in the range $0.10 < \Phi < 1$.
2. The heat exchanger employment is advantageous in the RFB, not only because of the efficient energy extraction and low emissions but also due to the high degree of stability and the extended operational range of the burner.
3. The RFB is characterized by very low NO and CO emissions. The NO molar fraction in the products grows from less than 1 ppm at $\Phi=0.15$ to 15 ppm at $\Phi=1$. The CO molar fraction in the products spans from 4 to 10 ppm for $0.2 < \Phi < 0.7$.
4. A single step model was developed and compared with experiments. The simulated numerical temperature profiles accurately predict the experimental data.
5. The equivalence ratio and the gas flow velocity exhibits the strongest influence on the temperature profiles of all the process parameters experimentally examined.
6. The efficiency increases from 70% to 80%, as the equivalence ratio increases in the range $0.10 < \Phi < 1.0$.

Acknowledgment

The authors wish to acknowledge the National Science Foundation support through Grant No. CTS-9812905. The work of William M. Barcellos was supported by CNPq, the Brazilian Government's Scientific and Technological Development Institution.

Nomenclature

- A_f = Arrhenius pre-exponential factor
 c = porous media specific heat
 D_{ax} = axial dispersion coefficient
 D_g = gas diffusion coefficient
 E_a = activation energy
 H_{chem} = heat of chemical reaction
 h_p = specific enthalpy of the products (kJ/mol)
 h_v = volumetric heat transfer coefficient
 k = thermal conductivity
 k_s^* = effective thermal conductivity of solid matrix
LHV = Low Heating Value
 \dot{m} = mass flow rate
 P = power
 R = universal gas constant
 T = temperature
 v = velocity
 x = axial coordinate
 y_p = product mass fraction
 \dot{W} = volumetric products production rate

Greek Symbols

- β = heat loss coefficient
 ϵ = porosity
 Φ = equivalence ratio
 ρ = density
 τ = flow reversal time

Subscripts

- conv* = convective
exhaust = exhaust
extr = extracted
g = gas
r = radiative
room = room
s = solid
water = water

References

- [1] Babkin, V. S., 1993, "Filtration Combustion of Gases, Present State of Affairs and Prospects," *Pure Appl. Chem.*, **65**, pp. 335–344.
- [2] Laevskii, Yu. M., and Babkin, V. S., 1982, "Filtration Combustion of Gases," in *Propagation of Heat Waves in Heterogeneous Media*, Yu. Matros, Ed., Nauka, Novosibirsk, pp. 108–145.
- [3] Zhdanok, S. A., Kennedy, L. A., and Koester, G., 1995, "Superadiabatic Combustion of Methane Air Mixtures Under Filtration in Packed Bed," *Combust. Flame*, **100**, pp. 221–231.
- [4] Bingue, J. P., Saveliev, A. V., Fridman, A. A., and Kennedy, L. A., 1998, "NO_x and CO Emissions of Lean and Ultra-Lean Filtration Combustion of Methane/Air Mixtures in Inert Porous Media," *Proc. 5th International Conference on Technologies and Combustion for a Clean Environment*, Lisbon, Portugal, pp. 1361–1367.
- [5] Kennedy, L. A., Fridman, A. A., and Saveliev, A. V., 1995, "Superadiabatic Combustion in Porous Media: Wave Propagation, Instabilities, New Type of Chemical Reactor," *Fluid Mech. Res.*, **22**, pp. 1–26.
- [6] Bingue, J. P., Saveliev, A. V., Fridman, A. A., and Kennedy, L. A., 2002, "Hydrogen Production in Ultra-Rich Filtration Combustion of Methane and Hydrogen Sulfide," *Int. J. Hydrogen Res.*, **27**(6), 643–649.
- [7] Bingue, J. P., Saveliev, A. V., Fridman, A. A., and Kennedy, L. A., 2002, "Hydrogen Sulfide Filtration Combustion: Comparison of Theory and Experiments," *J. Exp. Ther. Fluid Sci.*, **26**, 409–415.
- [8] Slimane, R. B., Lau, F. S., Bingue, J. P., Saveliev, A. V., Fridman, A. A., and Kennedy, L. A., 2002, "Production of Hydrogen by Superadiabatic Decomposition of Hydrogen Sulfide," *Proc. 14th World Hydrogen Energy Conference*.
- [9] Kennedy, L. A., Saveliev, A. V., Bingue, J. P., and Fridman, A. A., 2003, "Filtration Combustion of a Methane Wave in Air for Oxygen Enriched and Depleted Environments," *Proc. The Combustion Institute*, pp. 1835–1842.

- [10] Drayton, M. K., Saveliev, A. V., Kennedy, L. A., and Fridman, A. A., 1998, "Syngas Production Using Superadiabatic Combustion of Ultra-Rich Methane-Air Mixtures," *Proc. Combust. Inst.*, Vol. 27, pp. 1361-1367.
- [11] Mohamad, A. A., Viskanta, R., and Ramadhyani, S., 1994, "Numerical Predictions of Combustion and Heat Transfer in a Packed Bed With Embedded Coolant Tubes," *Combust. Sci. Technol.*, **96**, pp. 387-407.
- [12] Rumminger, M. D., Dibble, R. W., Heberle, N. H., and Crosley, D. R., 1996, "Gas Temperature Above a Radiant Porous Burner: Comparison of Measurements and Model Predictions," *Proc. Combust. Inst.*, **26**, pp. 1755-1762.
- [13] Tong, T. W., and Sathe, S. B., 1991, "Heat Transfer Characteristics of Porous Radiant Burners," *ASME J. Heat Transfer*, **113**, pp. 387-407.
- [14] Xiong, T. Y., Khinkis, M. J., and Fish, F. F., 1995, "Experimental Study of a High-Efficiency, Low Emission Porous Matrix Combustor-Heater," *Fuel*, **74**, pp. 1641-1647.
- [15] Xuan, Y., and Viskanta, R., 1999, "Numerical Investigation of a Porous Matrix Combustor-Heater," *Numer. Heat Transfer, Part A*, **36**, pp. 359-374.
- [16] Hannamura, K., Echigo, R., and Zhdanok, S., 1993, "Superadiabatic Combustion in Porous Media," *Int. J. Heat Mass Transfer*, **36**, pp. 3201-3209.
- [17] Kennedy, L. A., Saveliev, A. V., and Fridman, A. A., 1995, "Transient Filtration Combustion," *Proc. Mediterranean Combustion Symposium*, Antalya, Turkey, pp. 105-138.
- [18] Contarin, F., Saveliev, A. V., Fridman, A. A., and Kennedy, L. A., 2003, "A Reciprocal Flow Filtration Combustor With Embedded Heat Exchangers: Numerical Study," *Int. J. Heat Mass Transfer*, **36**, pp. 949-961.
- [19] Contarin, F., Barcellos, W. B., Saveliev, A. V., and Kennedy, L. A., 2003, "A Porous Media Reciprocal Flow Burner With Embedded Heat Exchanger," *Proc. ASME Summer Heat Transfer Conf.*, Paper No. HT2003-47098.

Wall Heat Flux Partitioning During Subcooled Flow Boiling: Part 1—Model Development

Nilanjana Basu¹

Gopinath R. Warrier

Vijay K. Dhir²

e-mail: vdhir@seas.ucla.edu

Mechanical and Aerospace Engineering
Department,
Henry Samueli School of Engineering and
Applied Science,
University of California, Los Angeles,
Los Angeles, CA 90095-1597

In this work a mechanistic model has been developed for the wall heat flux partitioning during subcooled flow boiling. The premise of the proposed model is that the entire energy from the wall is first transferred to the superheated liquid layer adjacent to the wall. A fraction of this energy is then utilized for vapor generation, while the rest of the energy is utilized for sensible heating of the bulk liquid. The contribution of each of the mechanisms for transfer of heat to the liquid—forced convection and transient conduction, as well as the energy transport associated with vapor generation has been quantified in terms of nucleation site densities, bubble departure and lift-off diameters, bubble release frequency, flow parameters like velocity, inlet subcooling, wall superheat, and fluid and surface properties including system pressure. To support the model development, subcooled flow boiling experiments were conducted at pressures of 1.03–3.2 bar for a wide range of mass fluxes (124–926 kg/m² s), heat fluxes (2.5–90 W/cm²) and for contact angles varying from 30° to 90°. The model developed shows that the transient conduction component can become the dominant mode of heat transfer at very high superheats and, hence, velocity does not have much effect at high superheats. This is particularly true when boiling approaches fully developed nucleate boiling. Also, the model developed allows prediction of the wall superheat as a function of the applied heat flux or axial distance along the flow direction. [DOI: 10.1115/1.1842784]

Keywords: Mechanistic Model, Heat Flux, Subcooled Flow Boiling

Introduction

Prediction of location of onset of significant voids (OSV) and void fraction along the flow direction during subcooled flow boiling is very important for nuclear reactors. As the void fraction increases, the reactivity in the reactor core decreases and vice versa. Thermal hydraulic codes (like RELAP-5) available for the nuclear industry compute the void fraction value from the interaction of three constitutive models. These models are for: (i) the source term for voids, which comes from the model for wall nucleation or wall heat flux partitioning (which gives the fraction of wall heat flux that goes to vapor generation), (ii) the sink term, given by the interfacial heat and mass transfer from the condensation of the vapor (bubbles lifting off) in the subcooled fluid, and (iii) interfacial friction.

A number of wall heat flux prediction models have been proposed in the past. These previous studies can be broadly classified into two categories: (i) those that partition the given wall heat flux into the various heat flux components and (ii) those that predict the overall heat flux. Correct partitioning of the wall heat flux is important for accurate prediction of void fraction in subcooled flow boiling process.

In the subcooled flow boiling process, before inception occurs, the heat from the wall is transferred to the liquid by single-phase forced convection. After the onset of nucleate boiling (ONB), different heat transfer mechanisms come into play. Some of the past studies for the wall heat flux partitioning downstream of ONB, as well as two-phase heat transfer models, are discussed in the following.

The wall heat flux models differ from one another on the various wall heat transfer mechanisms considered and in the way the total heat flux is partitioned (i.e., what fraction of the total heat is

transferred by the various mechanisms). Griffith et al. [1] assumed that once nucleation begins all of the wall energy is utilized for vapor generation. Bowring [2] was the first to identify different heat transfer mechanisms. He proposed that q_w has three components—single-phase heat transfer (q_{sp}), evaporation (q_{ev}), and the sensible heating of the liquid that occupies the volume vacated by a departing bubble (q_{pump}). Thus, the wall heat flux could be expressed as

$$q_w = q_{sp} + q_{ev} + q_{pump} = q_{sp} + (1 + \varepsilon)q_{ev} \\ = h_{sp}(T_{sat} - T_l) + (1 + \varepsilon)q_{ev}, \quad (1)$$

where $\varepsilon = q_{pump}/q_{ev}$ and is found empirically. The evaporation heat flux (q_{ev}) was given by the expression

$$q_{ev} = \rho_v h_{fg} V_b f N_a, \quad (2)$$

where f is the frequency of the bubbles and N_a is the active nucleation site density. The single-phase component can be calculated from standard correlations. The ratio ε was then correlated by the following expression:

$$\varepsilon = \frac{1 + 3.2 \frac{\rho_l c_{p_l} \Delta T_{sub}}{\rho_v h_{fg}}}{2.3} \quad 1 \leq p \leq 9.5 \\ \frac{2.6}{p \geq 50} \quad 9.5 \leq p \leq 50 \quad (3)$$

where p is pressure in bars. From Eq. (1) knowing q_{ev} and q_{sp} , q_{pump} can be calculated. Bowring used experimental data available in the literature for vertical upflow in rectangular channels with pressures varying from 11 to 136 bar, heat fluxes varying from 30 to 160 W/cm², and velocities varying from 0.8 to 2.0 m/s, and for all ranges of subcooling. Rouhani and Axelsson [3] extended Bowring's model. In their study q_{sp} was expressed in terms of wall voidage, meaning that this mechanism only works until the surface is fully covered with vapor bubbles. Also, unlike Bowring they expressed q_{pump} independently, proposing that the liquid re-

¹Present address: Fluent Inc., 10 Cavendish Court, Lebanon, NH 03766.

²To whom correspondence should be addressed.

Manuscript received December 12, 2003; revision received August 31, 2004. Review conducted by: M. Jensen.

placing the departing vapor bubble would be heated through a temperature gradient equal to the mean liquid subcooling. Dix [4] also used Bowring's model in his study. Dix used R-114 as the working fluid for his experiments while the pressures varied from 3.5 to 8 bar and mass fluxes was varied from 50 to 820 kg/m² s.

Several other studies have used Bowring's model. However, most of them have ignored the contribution of heat transfer due to liquid circulation caused by bubbles disrupting the boundary layer, and have only considered q_{sp} and q_{ev} as the two components of the wall heat flux. The models of Larsen and Tong [5], Ahmad [6], Hancox and Nicoll [7], Maroti [8], Lahey [9], Chatoorgoon et al. [10], and Zeitoun [11] fall into this category. Most of these models do not calculate q_{ev} directly but do so indirectly by knowing the supplied q_w and calculating q_{sp} . For example, Maroti [8] calculated q_{ev} by assuming the fraction of wall heat flux utilized for vapor generation to be proportional to the superheated part of the liquid thermal layer and applied his model for water, for pressures ranging from 27 to 138 bar. Assuming a linear temperature profile in the liquid, he derived an expression for the evaporation heat flux as

$$q_{ev} = q_w \left(\frac{\Delta T_w}{\Delta T_w + \Delta T_{sub}} \right)^2 \quad (4)$$

$$q_b = \begin{cases} 0.0 & he_l \leq he_{l,OSV} \\ q_w(z) - q_{sp} = q_w(z) \left\{ 1 - \left[\frac{he_{l,sat} - he_l(z)}{he_{l,sat} - he_{l,OSV}(z)} \right] \right\} & he_l > he_{l,OSV} \end{cases} \quad (7)$$

where $he_{l,OSV}$ is the enthalpy of the liquid at OSV while $he_l(z)$ denotes the enthalpy of the liquid at any axial location.

Chatoorgoon et al. [10] developed a model for q_{ev} using the evaporation heat flux at the OSV location as the datum. Their relationship was expressed as

$$q_{ev} = q_w \xi \left(\frac{he_l - he_{l,OSV}}{he_l - he_{l,sat}} \right) + q_{ev,OSV} \quad (8)$$

where ξ is a function chosen such that it is zero at OSV and $q_{ev,OSV}$ is determined from the assumption that at the OSV location the slope of the void fraction profile is approximately zero (i.e., the condensation rate from the bubbles in the bulk liquid balances the evaporation rate). Based on this assumption, $q_{ev,OSV}$ was expressed as

$$q_{ev,OSV} = h_c \alpha^{2/3} \quad (9)$$

where h_c is the condensation heat transfer coefficient (calculated using Akiyama's [12] correlation and assuming a constant bubble size of 2.5 mm) and α is the void fraction at OSV (calculated using the correlation of Rogers et al. [13]). The correlation was applied to flow boiling of water for pressures ranging from 1.52 to 2.1 bar and velocities ranging from 0.3 to 0.4 m/s.

Kandlikar [14] assumed that, for saturated flow boiling, the two-phase heat transfer coefficient is made up of two components, single-phase convection and nucleate boiling and empirically can be expressed as

$$\frac{h_{tp}}{h_{sp}} = C_1 Co C_2 (25 Fr_l)^{C_5} + C_3 (Bo^C F_{fl})^4, \quad (10)$$

where Co is the convection number indicating whether nucleate boiling or convection is dominant, $C_1 - C_5$ are empirical constants, Fr_l is the Froude number, and F_{fl} is a fluid-surface parameter. The correlation was developed using experimental data available in the literature for saturated boiling in horizontal and vertical tubes, for both water and refrigerants.

The wall heat flux was assumed to be given by

$$q_w = h_{boil} \Delta T_w \quad (5)$$

where $h_{boil} = K \Delta T_w^N$, with $K = 22 p^{0.58}$ and $N = 3.33$. In Eq. (5), the pressure (p) is in atmospheres.

Lahey [9] expressed the boiling heat flux (q_b) as the sum of the evaporation and pumping heat fluxes (q_{pump}) which occur due to heating of the liquid filling up the area evacuated by the bubbles lifting off from the heater surface. The total wall heat flux can then be expressed as

$$q_w = q_{sp} + q_{ev} + q_{pump} = q_{sp} + (1 + \varepsilon) q_{ev} = q_{sp} + q_b \quad (6)$$

In the earlier equation the boiling heat flux (q_b) = $q_{ev} + q_{pump}$ and $\varepsilon = q_{pump}/q_{ev} = \rho_l (he_{l,sat} - he_l) / \rho_v h_{fg}$, where he denotes enthalpy of the liquid and the subscripts l and sat denote the liquid and saturation, respectively.

In the earlier model it was assumed that the OSV location coincides with the point where fully developed nucleate boiling begins. Based on this assumption, upstream of OSV, $q_w = q_{sp}$ and downstream of OSV, $q_w = q_{sp} + q_b$. The boiling heat flux was expressed as

Liu and Winterton [15] proposed that the presence of the bubbles enhances single-phase heat transfer while suppressing the pool nucleate boiling heat transfer mechanism. They expressed the saturated flow boiling heat transfer coefficient (h_{TP}) as,

$$h_{TP}^2 = (F h_{sp})^2 + (S h_{pool})^2. \quad (11)$$

The heat transfer coefficients for single-phase (h_{sp}) was calculated using the Dittus-Boelter correlation, while the pool boiling heat transfer coefficient (h_{pool}) was determined using Cooper's [16] pool boiling correlation as

$$h_{pool} = 55 \left(\frac{p}{p_{crit}} \right)^{0.12} q_w^{2/3} \left[-\log \left(\frac{p}{p_{crit}} \right) \right]^{-0.55} M^{-0.5} \quad (12)$$

where p_{crit} is critical pressure and M is molecular weight. F and S are the enhancement and suppression factors, respectively, and are given as

$$F = \left[1 + x Pr_l \left(\frac{\rho_l}{\rho_v} - 1 \right) \right]^{0.35} \quad (13)$$

$$S = [1 + 0.055 F^{0.1} Re_l^{0.16}]^{-1} \quad (14)$$

where x is the quality, Pr_l is the liquid Prandtl number and Re_l is the liquid Reynolds number.

For subcooled flow boiling, Liu and Winterton proposed the following expression for the q_w :

$$q_w = \sqrt{[(F h_{sp} \Delta T_{sub})^2 + (S h_{pool} \Delta T_w)^2]}, \quad (15)$$

where $F = 1.0$ with all other parameters calculated as before for saturated boiling. These correlations were developed based on experimental data covering a range of mass fluxes varying from 12.4 to 8180 kg/m² s, pressures varying from 0.5 to 200 bar and liquid subcoolings varying from 0 to 173.0°C.

Wadekar [17] assumed that the single-phase convective component was suppressed during subcooled flow boiling. Noting the trends of the asymptotic addition of nucleate boiling and convective heat transfer, he obtained

$$q_w = (1 - A_{nb})q_{sp} + q_{nb}, \quad (16)$$

where A_{nb} is the time-averaged fraction of the total area over which nucleate boiling occurs. From the available data, the functional form of A_{nb} was determined to be

$$A_{nb} = 1 - \exp \left[- \left(\frac{K(\Delta T_w)^{2.5} \left(\frac{P}{P_{crit}} \right)}{Re_{2p}} \right) \right], \quad (17)$$

where Re_{2p} is the two-phase Reynolds number ($= Re F^{1.25}$), and K is a dimensional constant obtained from experimental data and is equal to $177C$, where C is the lead constant in Cooper's correlation given in Eq. (12).

Lellouche et al. [18] introduced a purely empirical wall heat flux model applicable to the entire range, i.e., single-phase forced convection to post dry-out. Their general correlation is of the form

$$q_w = q_{wg} + q_{wl}e^{-\lambda_B \Delta z} + q_N e^{-\lambda_B \Delta z} + q_{wd} + q_{wl,p}(1 - e^{-\lambda_{tp} \Delta z}) \quad (18)$$

where q_{wl} is the heat flux to the liquid, q_{wg} is the heat flux to the vapor, q_N is the nucleation heat flux, q_{wd} is the heat flux to the liquid near the wall (post-CHF), $q_{wl,p}$ is the heat flux to the dispersed liquid (post-CHF), $\Delta z = z - z_0$, where z_0 is the CHF location, and λ_B and λ_{tp} are functions that describe the restructuring of the fluid field from continuous liquid to continuous vapor. In the nucleate boiling regime, the wall heat flux was partitioned according to the following expression:

$$q_w = q_{conv} + q_N \quad (19)$$

where the convection heat flux can be broken down into two separate terms, one going to the liquid and the other to the vapor, and was expressed as

$$q_{conv} = q_{wl} + q_{wg} = h_{spf_l}(T_w - T_l) + h_{spf_g}(T_w - T_g) \quad (20)$$

where $f_l + f_g = 1$. The single-phase heat transfer coefficient was evaluated from the Dittus-Boelter correlation, while the factors f_l and f_g were determined from available experimental data.

From the earlier literature review of the available models for prediction of wall heat flux in flow boiling, it is evident that in most cases all the mechanisms for heat transfer have not been taken into account. In almost all of them, one or more of the heat flux components were obtained as ratios of other components. The dependencies were obtained by curve fitting the experimental data. Hence, the models have become too data specific and furthermore the empiricism built into them does not always represent the physics of the process. The comparison of these models with the experimental data show discrepancies at low pressures, as most of these correlations were developed for high pressure, high velocity conditions. A number of these models were developed as a part of the modeling for void fraction and though the overall model validation for void fraction prediction has been justified in most studies, an independent validation of the wall heat flux partitioning has never been carried out.

From the literature review it is evident that a model is yet to be developed in which each and every component of the wall heat flux is identified and then computed independently. The modeling should be such that the empirical relations used represent the subprocesses involved in the subcooled flow boiling phenomenon. A bottom-up approach is taken here, rather than the top-down approach that has been employed in the past. Validation of the model is carried out with low pressure data obtained in this study and that available in the literature.

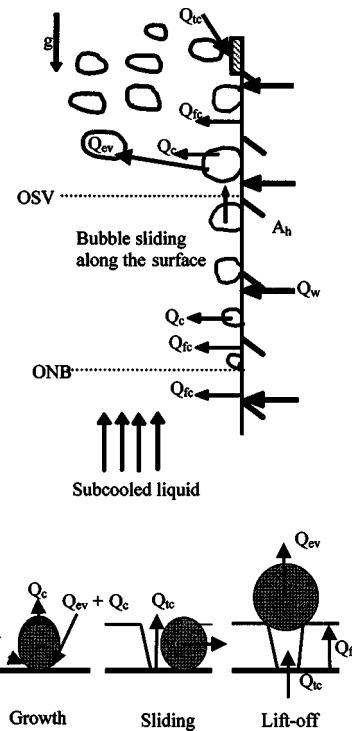


Fig. 1 Mechanisms of heat transfer at and near the wall

Proposed Model

The first step in modeling wall heat flux is to identify the ONB and OSV locations. Thereafter, each of the mechanisms by which energy is transferred from or near the wall has to be identified and quantified. The fundamental idea behind the model proposed in this work is that energy from the wall is first transferred to the liquid layer adjacent to the heated wall and thereafter from this superheated liquid layer, energy is transferred to the vapor bubble by evaporation while the remainder goes to the bulk liquid.

Upstream of ONB, heat is transferred from the wall to the bulk liquid by single-phase forced convection. Standard heat transfer correlations, depending on flow geometry and fluid properties, can be used for this purpose.

Region Between ONB and OSV. In the region, which is upstream of OSV and downstream of ONB, the bubbles remain attached to the heated surface as shown in Fig. 1. Energy transfer by single-phase forced convection (Q_{fc}) from the wall occurs in regions not occupied by bubbles as shown in Fig. 1, and results in the sensible heating of the liquid. A portion of this energy is utilized for evaporation from the superheated liquid layer adjacent to the wall. Condensation heat transfer (Q_c) occurs from the top of the attached bubbles, which is exposed to the subcooled liquid. Since the bubbles do not grow in size with time and remain attached to the heated wall, the energy lost by the bubbles due to condensation to the subcooled liquid, is equal to the energy input to the bubbles by evaporation from the superheated liquid layer. As such, the bubbles attached to the surface provide an alternate route for heat transfer from the wall to the liquid. However, the presence of bubbles on the surface enhances forced convection heat transfer coefficient by increasing the roughness of the surface. In this region, the entire wall heat energy is assumed to be transferred by enhanced forced convection to the liquid and, hence, the wall heat flux can be expressed as

$$q_w = \frac{Q_w}{A_h} = \frac{Q_{fc}}{A_h} = \frac{Q_l}{A_h} \quad (21)$$

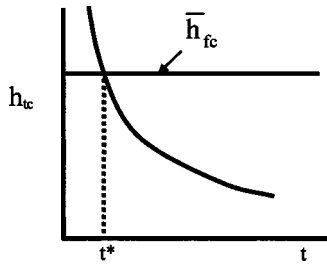


Fig. 2 Transient conduction time

$$\frac{Q_{fc}}{A_h} = \bar{h}_{fc}(T_w - T_l) \quad (22)$$

where q_l is the energy transferred to the bulk subcooled liquid, A_h is the heater surface area and \bar{h}_{fc} is the enhanced forced convection heat transfer coefficient. Enhancement in single-phase heat transfer occurs because of the presence of protrusions on the heater surface and oscillations in the bubble interface. Also, in regions 1–2 shown in Fig. 1, the rate at which heat is added to the liquid leads to the enthalpy rise of the liquid, i.e.:

$$q_l \equiv \frac{Q_l}{A_{h(1-2)}} = \dot{m} c_{pl}(T_{l,2} - T_{l,1}) \quad (23)$$

where \dot{m} is the total mass flow rate, $T_{l,1}$ and $T_{l,2}$ are the mean liquid temperatures at locations 1 and 2, respectively, c_{pl} is the liquid specific heat, and $A_{h(1-2)}$ is the heater surface area between locations 1 and 2.

Region Downstream of OSV. Further downstream, with decrease in liquid subcooling, the bubbles grow in size and lift off from the surface. Typically the bubbles slide before they lift-off. The diameter at which a bubble departs from its site of origin and begins to slide a measurable distance along the heater surface is called the departure diameter (D_d), while the diameter at which the bubble lifts off from the heater surface is called the lift off diameter (D_l). Various heat transfer mechanisms that come into play in the region of detached bubbles are also shown in Fig. 1. Each of the mechanisms occurs on different areas and over different time periods. This has to be taken into account in the modeling.

When a bubble slides, or lifts off, the boundary layer gets disrupted and cold liquid comes in contact with the heated wall, which results in transient conduction (Q_{tc}) occurring on these areas. The conduction process is modeled as a simple one-dimensional transient heat conduction into a semi-infinite medium, with the liquid at a temperature T_l and the heater surface at a temperature T_w . Based on the error function solution of the transient temperature profile, the transient conduction heat flux at the wall can be expressed as

$$q_w = \frac{k_l(T_w - T_l)}{\sqrt{\pi \alpha_l t}} \quad (24)$$

From Eq. (24), the transient conduction heat flux decreases as the inverse square root of time whereas the steady-state forced convection component is independent of time, as shown in Fig. 2. The time period, t^* , over which transient conduction is dominant over convection can be found by equating the two heat transfer rates [Eqs. (22) and (24)] and is expressed as

$$t^* = \left(\frac{k_l}{h_{fc}} \right)^2 \frac{1}{\pi \alpha_l} \quad (25)$$

where α_l is the liquid thermal diffusivity. Thus, for $t < t^*$, transient conduction will dominate and for $t > t^*$, forced convection

will dominate. In other words, q_{fc} is the lowest heat flux that the heater surface will experience; when transient conduction occurs, the local heat flux will be higher.

As mentioned earlier, the fundamental idea of the proposed model is that all the energy from the wall is transferred to the superheated liquid layer immediately adjacent to the wall by transient conduction and convection, and then a portion of this energy goes to the bubbles by means of vaporization at the vapor-liquid interface. In the post OSV region, bubbles lift-off from the heater surface and carry with them the evaporation energy (Q_{ev}). Condensation occurs at the vapor-liquid interface of the bubbles attached to the heater surface. Thus the total energy input to the bubble from the superheated liquid layer is equal to ($Q_{ev} + Q_e$), while the rest of the heat from the superheated layer goes towards heating of the bulk liquid (Q_{bulk}). Condensation is again just an alternate path for heat transfer to the liquid. So the total energy loss from the wall equals to ($Q_{tc} + Q_{fc}$), which in turn equals ($Q_{ev} + Q_l$), with $Q_l = Q_{bulk} + Q_c$. The wall heat flux in the post OSV region, can thus be expressed as

$$q_w = \frac{Q_w}{A_h} = \frac{Q_{fc}}{A_h} + \frac{Q_{tc}}{A_h} = \frac{Q_{bulk}}{A_h} + \frac{Q_c}{A_h} + \frac{Q_{ev}}{A_h} = \frac{Q_l}{A_h} + \frac{Q_{ev}}{A_h} \quad (26)$$

As can be seen from Eq. (26) since condensation need not be an independent component of the wall heat flux, this information is not necessary for modeling the wall heat flux. Also note that Q_l is the heat gained by the liquid from the wall, but there will be an additional heat gain due to condensation of vapor bubbles lifting from the wall and moving into the bulk liquid. A model for the interfacial heat transfer in the bulk liquid, during subcooled flow boiling, has been developed by Warriar et al. [19].

Further downstream, with the increase in the number density of bubbles on the heater surface, bubbles begin to merge without sliding, while growing at their sites of origin. We call this fully developed nucleate boiling. The heat transfer mechanisms discussed above along with Eq. (26) are still valid, but the time periods and area considerations for each component are different. In the post OSV region, modeling has to take into account the cases where the bubbles slide and the cases where the bubbles do not slide. A detailed discussion of this is given in the following paragraphs. In this model, it is assumed that the nucleation sites are distributed in a square grid and that the bubbles slide only in the direction of the flow. As such, the spacing between nucleation sites (s) is equal to $1/\sqrt{N_a}$, where N_a is the active nucleation site density. In pool boiling, Wang and Dhir [20] found that the average spacing between sites is given by $0.84/\sqrt{N_a}$.

Sliding Bubble Case. Sliding typically occurs when D_d and D_l are less than the spacing, s . Let l_0 represent the distance that a bubble slides while growing from D_d to D_l , when no other sites are present or the sites are widely spaced. If $s > l_0$, a bubble while sliding will not encounter bubbles nucleating at other sites. On the other hand, for $s < l_0$, a sliding bubble will encounter bubbles from other sites along its sliding path and merge with them. Hence, a smaller number of bubbles will lift off per unit area of the heater surface into the bulk liquid than the actual number of active nucleation sites. Also, a bubble, while sliding and encountering other sites, gains vapor volume from these sites. Thus such a sliding bubble grows faster and, hence, will gain the lift-off diameter earlier. In such situations, the actual sliding distance (l) will be shorter than l_0 .

Bubble sliding cases are shown in Fig. 3(a) for a no merger case and Fig. 3(b) for a case where the bubbles merge. The bubble departs from its site of origin (primary site) and slides for a distance l and merges with the other [two shown in Fig. 3(b)] sites (the secondary sites) encountered along its sliding path, and grows while sliding until it attains the lift-off diameter, D_l . The ratio of the actual number of bubbles lifting off per unit area of the heater surface to the number of active nucleation sites per unit area is called the reduction factor (R_f) and is given by

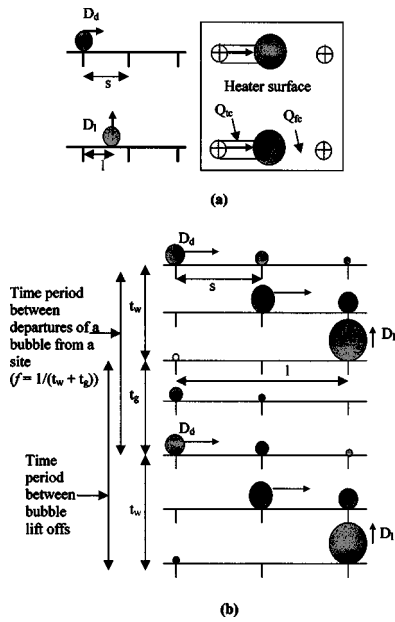


Fig. 3 Bubble sliding cases (a) sliding without merger (b) sliding with merger

$$R_f = \frac{1}{l/s} = \frac{1}{l\sqrt{N_a}} \quad (27)$$

For $s > l_0$, the actual sliding length $l = l_0$ and $R_f = 1$.

As shown in Fig. 3, the waiting time (t_w) is the time period between bubble departure and the next bubble inception at a given site. Also, the growth time (t_g) is the time required for bubble growth from inception to the maximum size (D_d) at its site of origin. Though the bubble continues to grow while sliding, it is to be noted that the time of growth at the site of origin along with the waiting time represents the periodicity, as can be seen from Fig. 3, and this time period ($t_w + t_g$) will be used for averaging all the heat transfer components. The frequency of bubble release (f) is then given by $1/(t_w + t_g)$. Since in steady state a continuous train of bubbles are sliding and lifting off, f represents both the bubble departure rate as well as the bubble lift-off rate from the heater surface.

For finding l , it is assumed that when a sliding bubble encounters a secondary site along its sliding path, it gains the volume corresponding to D_d , or in other words the time lag in sliding a distance, s , equal to the spacing between adjacent sites, is equal to the growth time t_g for a bubble at its site of origin. Hence, bubbles at a secondary site will grow to D_d before being hit by a bubble sliding from an upstream site. If D_{sl} is the size a bubble grows to while sliding a distance s , then the total size of a bubble after gaining volume due to interaction with a bubble at a secondary site is given by

$$D_{\text{total}}^3 = D_{sl}^3 + D_d^3 \quad (28)$$

If the value of $D_{\text{total}} \geq D_l$, the bubble will lift-off, otherwise the bubble will slide further and merge with bubbles at additional secondary sites till it reaches the size D_l . The actual sliding distance (l) can be determined if one keeps track of the bubble growth rate during sliding and the sudden increase in bubble volume following every encounter with secondary bubbles. For example, consider a bubble that departs from its site of origin and merges with N_{merg} number of bubbles spaced a distance s apart. The distance that the bubble has traveled so far is then given by $N_{\text{merg}}s$. Now if the current size (D_N) of the bubble is less than D_l and if the size of the bubble after one more merger will be greater than D_l , then the bubble only needs to travel a fraction of the

spacing (s) before it attains the lift off size D_l . In this case the total distance traveled by the bubble can be calculated (provided the bubble growth rate during sliding is known) as

$$l = N_{\text{merg}}s + l_{D_N - D_l} \quad (29)$$

Transient conduction occurs in regions swept by sliding bubbles, and the time period for which it will occur is governed by the magnitude of t^* . The transient conduction component is given by

$$\frac{Q_{\text{tc}}}{A_h} = \frac{1}{t_w + t_g} \int_0^t \frac{k_l}{\sqrt{\pi \alpha_l t}} (\Delta T_w + \Delta T_{\text{sub}}) (A_{sl}) R_f N_a dt \quad (30)$$

where $t = t^*$ when $t^* < (t_w + t_g)$ and $t = (t_w + t_g)$ when $t^* \geq (t_w + t_g)$. Sliding area (A_{sl}) is the area swept by the sliding bubble and is given as $A_{sl} = CDl$, where C represents the ratio of bubble base diameter to that of the bubble diameter, D , which represents an average diameter of a sliding bubble, and the product $R_f N_a$ represents the number of bubbles sliding per unit area. During sliding, since the bubble grows from D_d to D_l , the average bubble diameter is given by

$$D = D_d + 0.5(D_l - D_d) \quad (31)$$

In the present study, the ratio D_l/D_d was found to be approximately two. Dividing Eq. (31) by D_d , substituting $D_l/D_d = 2$ and rearranging yields

$$D = 1.5D_d = 0.75D_l \quad (32)$$

Hence, in this study, the average bubble diameter during sliding was assumed to be $0.75D_l$.

Forced convection will prevail for all times in the areas of the heater surface, which are not influenced by sliding bubbles. The fraction of the heater area devoid of bubble sliding is given by $(1 - A_{sl}R_fN_a)$. The heater area influenced by sliding will have transient conduction followed by forced convection, if $t^* < (t_w + t_g)$. As such, the forced convection component can be expressed as

$$\frac{Q_{\text{fc}}}{A_h} = \overline{h_{\text{fc}}} (\Delta T_w + \Delta T_{\text{sub}}) [1 - A_{sl}R_fN_a] + \overline{h_{\text{fc}}} (\Delta T_w + \Delta T_{\text{sub}}) A_{sl}R_fN_a \left(1 - \frac{t^*}{t_w + t_g} \right) \quad (33)$$

The evaporative component of the wall heat transfer is given by the energy carried away by the bubbles lifting off from the heater surface and is the energy of vaporization required to produce a bubble of size D_l . Evaporative heat flux is the product of this energy, bubble release rate (f) and the number of bubbles released per unit area of the heater surface ($R_f N_a$) and is expressed as

$$\frac{Q_{\text{ev}}}{A_h} = \rho_v h_{\text{fg}} \frac{\pi}{6} D_l^3 R_f N_a f \quad (34)$$

Energy going to the liquid from the wall is given by the total wall heat flux minus the evaporative component.

Bubble Merger Without Sliding. Typically at high superheats, with the increase in N_a (i.e., decrease in s) and increase in D_d and D_l , bubbles tend to merge with each other in all directions, while growing at their site of origin. This is shown in Fig. 4. Here the maximum size the bubble grows to is the average spacing distance, s , between sites and thereafter they merge together to form a bubble of size D_l , which then lifts off from the heater surface. In this case, the growth time (t_g) corresponds to the time required for a bubble to grow to size s . The number of bubbles merging together to give one lift off diameter bubble is obtained from volume considerations. The reduction factor can, hence be expressed as

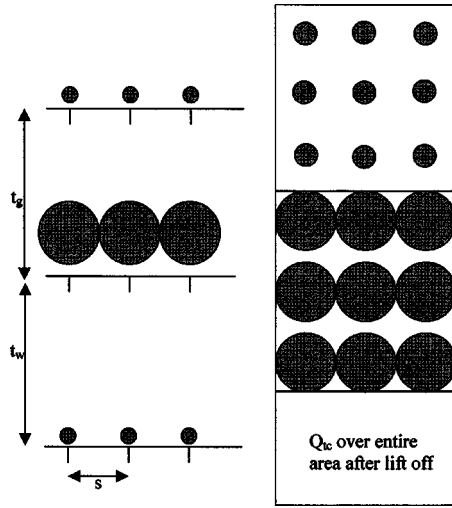


Fig. 4 Sliding without merger

$$R_f = \frac{s^3}{D_l^3} \quad (35)$$

As can be seen from Fig. 4, the entire heater surface undergoes transient conduction after the bubbles merge and lift-off. There can be several possibilities as to the area and time period for which transient conduction and forced convection occur on the heater surface depending on the relative values of t_w , t_g , and t^* . These possibilities are discussed later.

(i) $t^* \leq t_w$. When $t^* \leq t_w$, transient conduction will occur on the entire heater surface for time t^* and is given by

$$\frac{Q_{tc}}{A_h} = \frac{1}{t_w + t_g} \int_0^{t^*} \frac{k_l}{\sqrt{\pi \alpha_l t}} (\Delta T_w + \Delta T_{sub}) dt \quad (36)$$

Following transient conduction, forced convection will take place on the entire heater surface area till t_w and thereafter in regions not occupied by bubbles during t_g . This can be expressed as

$$\frac{Q_{fc}}{A_h} = \overline{h_{fc}} (\Delta T_w + \Delta T_{sub}) \frac{t_w - t^*}{(t_g + t_w)} + \overline{h_{fc}} (\Delta T_w + \Delta T_{sub}) [1 - A_b N_a] \frac{t_g}{(t_g + t_w)} \quad (37)$$

where A_b is the base area of the bubble and can be written as $A_b = \pi(Cs)^2/4$.

(ii) $t^* > t_w$. When $t^* > t_w$, transient conduction will occur over the entire heater surface for time t_w and will continue during the growth period in regions not occupied by bubbles on the heater surface till t^* or $(t_w + t_g)$, whichever is smaller. Transient conduction in this case can be expressed as

$$\frac{Q_{tc}}{A_h} = \frac{1}{t_w + t_g} \left[\int_0^{t_w} \frac{k_l}{\sqrt{\pi \alpha_l t}} (\Delta T_w + \Delta T_{sub}) dt + \int_{t_w}^{t^*} \frac{k_l}{\sqrt{\pi \alpha_l t}} (\Delta T_w + \Delta T_{sub}) [1 - A_b N_a] dt \right] \quad (38)$$

where $t = t_w + t_g$, if $t^* > t_w + t_g$, else $t = t^*$. Forced convection will occur after transient conduction only if $t^* < t_w + t_g$. For the case when $t^* > (t_w + t_g)$, forced convection will be zero (i.e., transient conduction will prevail at all times). The forced convection component can be expressed as

$$\frac{Q_{fc}}{A_h} = \overline{h_{fc}} (\Delta T_w + \Delta T_{sub}) [1 - A_b N_a] \frac{t_w + t_g - t^*}{(t_w + t_g)} \quad t_w < t^* < (t_w + t_g)$$

$$0 \quad t^* \geq (t_w + t_g) \quad (39)$$

Also, in this case the evaporative component (q_{ev}) is given by Eq. (34), with the R_f term obtained from Eq. (35). Thus the evaporative component is given by

$$\frac{Q_{ev}}{A_h} = \rho_v h_{fg} \frac{\pi}{6} D_l^3 R_f N_a f = \rho_v h_{fg} \frac{\pi}{6} s^3 N_a f \quad (40)$$

The total wall heat flux can then be partitioned into that going into the liquid and vapor phases using Eq. (26).

Parameters Required for Modeling

From the previous discussion it is clear that for modeling wall heat flux, one needs to know the location of ONB and OSV and for finding each of the wall heat flux components information regarding N_a , D_d , D_l , t_w , t_g , and $\overline{h_{fc}}$ are required apart from the flow parameters v , ΔT_w , ΔT_{sub} , and the fluid and solid properties. Additionally, literature review (see Warriar and Dhir [21]) indicated scarcity of flow boiling data at low pressure and lack of information and models for each of the earlier mentioned parameters. Hence the necessity of low-pressure flow boiling experiments was identified.

Experiments

To support the model development, subcooled flow boiling experiments were conducted at pressures varying from 1.03 to 3.2 bar for a wide range of mass fluxes (124–926 kg/m² s), heat fluxes (2.5–113 W/cm²), and for contact angles varying from 30° to 90°. These experiments were conducted using a vertical Copper plate (30.5 cm long and 3.175 cm wide) and a Zircalloy-4 nine-rod bundle arranged in a 3 × 3 square grid (91.44 cm long, 1.11 cm outer diameter with a pitch to diameter ratio of 1.288). Details of the experimental set up and procedure can be found in Basu [22] and Basu et al. [23].

Correlations/Models for Required Parameters

From the experiments conducted as part of this study and the data available in the open literature, correlations/models were developed for the various parameters identified above. Since the details of the correlations are reported elsewhere (see Basu [22]) only a brief discussion is given in the following section.

Onset of Nucleate Boiling. In determining the wall superheat at the onset of nucleate boiling, it is proposed that the probability of finding an unflooded cavity of the size corresponding to the minimum wall superheat calculated from Hsu's [24] criterion diminishes as the wettability of the surface increases. However, since the size of the available cavity is proportional to that obtained from the minimum superheat criterion, the available cavity size can be expressed as

$$D_c = D_c^0 F \quad (41)$$

where the reduction factor F [which depends on the static contact angle (ϕ)] is given as,

$$F = 1 - \exp \left[- \left(\frac{\pi \phi}{180} \right)^3 - 0.5 \left(\frac{\pi \phi}{180} \right) \right] \quad (42)$$

while D_c^0 is obtained by invoking the minimum superheat criterion

$$D_c^0 = \left[\frac{8 \sigma T_{sat} k_l}{\rho_v h_{fg} q_w} \right]^{1/2} \quad (43)$$

The reduction factor F was obtained empirically by correlating the data available in the literature (see Basu et al. [23]).

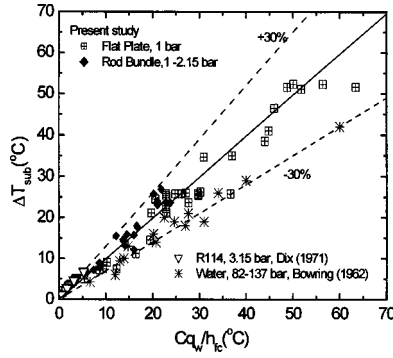


Fig. 5 Comparison of experimental $\Delta T_{\text{sub,OSV}}$ with predicted values

Under the assumption that the nucleating cavity is much smaller than the thermal boundary layer thickness (δ_t), the wall temperature at inception corresponding to D_c is obtained by using the following set of equations:

$$p_v - p_l = \frac{4\sigma}{D_c} \quad (44)$$

$$\Delta T_{w,\text{ONB}} = T_{\text{sat}}(p_v) - T_{\text{sat}}(p_l) \quad (45)$$

When the calculated wall superheat is not too high, $\Delta T_{w,\text{ONB}}$ in terms of D_c can be approximated as

$$\Delta T_{w,\text{ONB}} \cong T_{w,\text{ONB}} - T_{\text{sat}} = \frac{4\sigma T_{\text{sat}}}{D_c \rho_v h_{fg}} \quad (46)$$

Otherwise the complete equation of state must be used.

Prior to ONB, single-phase flow prevails on the heater surface, an expression for wall heat flux in terms of the single-phase heat transfer coefficient (which may or may not depend on the axial location) can be written as

$$q_{w,\text{ONB}} = h_{fc}(z) \Delta T_{w,\text{ONB}} + h_{fc}(z) (T_{\text{sat}} - T_l(z)) \quad (47)$$

The ONB correlation is strictly valid for static contact angles varying from 1° to 85° . The comparison of the predicted and experimental $\Delta T_{w,\text{ONB}}$ and $q_{w,\text{ONB}}$ values can be found in Basu et al. [23].

Onset of Significant Voids. Though in the past, different definitions of OSV have been used (see Bowring [2]; Zeitoun [11]; Unal [25]), in this study, the onset of significant void is defined as the axial location where the bubbles begin to lift off from the heater surface. Based on the experimental data obtained in the present study, the local liquid subcooling at which OSV is observed could be correlated by the expression

$$\Delta T_{\text{sub,OSV}} = C_{\text{OSV}} \frac{q_w}{h_{sp}} \quad (48)$$

where the factor C_{OSV} is a function of the ratio of the bubble departure diameter to the thermal boundary layer thickness ($\delta_t = k_l/h_{sp}$). It must be noted that the h_{sp} value used is the value without any enhancement due to the presence of the bubble. The factor C_{OSV} represents the fact that for a thicker boundary layer, a bubble could sustain a higher liquid subcooling while growing and detaching itself from the surface and vice versa, and is given by the following empirical relation:

$$C_{\text{OSV}} = 0.7 \exp\left(-0.065 \frac{D_d}{\delta_t}\right) \quad (49)$$

Figure 5 shows a comparison of the $\Delta T_{\text{sub,OSV}}$ values predicted using Eq. (48) with those obtained experimentally. It can be seen that the predicted values compare quite well with most of the

experimental values (within $\pm 30\%$). In the literature, the location of OSV is not typically given, and the lack of this information, leads one to use the fully developed heat transfer coefficient values when predicting the OSV location. This often results in the $\Delta T_{\text{sub,OSV}}$ values being predicted incorrectly.

Nucleation Site Density. The active nucleation site density (N_a) is given by the following correlations:

$$N_a = 0.34[1 - \cos(\phi_s)] \Delta T_w^{2.0} \quad \Delta T_{w,\text{ONB}} < \Delta T_w < 15^\circ \quad (50)$$

$$N_a = 3.4 \times 10^{-5} [1 - \cos(\phi_s)] \Delta T_w^{5.3} \quad \Delta T_w \geq 15^\circ \quad (51)$$

The predicted N_a values were found to be within $\pm 30\%$ of the data and is given in Basu et al. [23].

Bubble Departure and Lift-Off Diameters. Based on the data obtained in the current experiments and those available in the literature, the following observations can be made regarding D_d and D_l .

- Aside from the fluid properties, the variables that influence D_d and D_l are ΔT_w , ΔT_{sub} , v , and ϕ .
- Both D_d and D_l increase with increase in ΔT_w (i.e., D_d , $D_l \sim \text{Ja}_{\text{sup}}^{0.45}$) for given ΔT_{sub} , v , and ϕ .
- Both D_d and D_l decrease weakly with increase in ΔT_{sub} [i.e., D_d , $D_l \sim \exp(-0.0065 \text{Ja}_{\text{sub}})$] for constant ΔT_w , v , and ϕ .
- Both D_d and D_l decrease with increase in v [i.e., $D_d \sim \exp(-1.75 \times 10^{-4} \text{Re}_l)$ and $D_l \sim \exp(-1.28 \times 10^{-4} \text{Re}_l)$] for given ΔT_w , ΔT_{sub} , and ϕ , and
- Both D_d and D_l increase with increase in ϕ [i.e., D_d , $D_l \sim (\sin \phi)^{0.4}$] for given ΔT_w , ΔT_{sub} , and v .

The resulting correlations for D_d and D_l are given as follows:

$$\frac{D_d}{l_c} = 1.3 (\sin \phi)^{0.4} [0.13 \exp(-1.75 \times 10^{-4} \text{Re}_l) + 0.005] \text{Ja}_{\text{sup}}^{0.45} \exp(-0.0065 \text{Ja}_{\text{sub}}) \quad (52)$$

$$\frac{D_l}{l_c} = 1.3 (\sin \phi)^{0.4} [0.20 \exp(-1.28 \times 10^{-4} \text{Re}_l) + 0.005] \text{Ja}_{\text{sup}}^{0.45} \exp(-0.0065 \text{Ja}_{\text{sub}}) \quad (53)$$

where l_c is the characteristic length scale ($l_c = \sqrt{\sigma/g(\rho_l - \rho_v)}$), $\text{Ja}_{\text{sup}} = \rho_l c_{pl} \Delta T_w / \rho_v h_{fg}$, $\text{Ja}_{\text{sub}} = \rho_l c_{pl} \Delta T_{\text{sub}} / \rho_v h_{fg}$, $\text{Re}_l = \rho_l v_l / \mu_l$.

Due to the difficulty in obtaining reliable bubble diameter information because of the presence of multiple bubbles on the heating surface, the range of the earlier correlations are quite limited. Hence, the earlier correlations are valid only in the following range of parameters: $14 \leq \text{Ja}_{\text{sup}} \leq 56$, $1 \leq \text{Ja}_{\text{sub}} \leq 138$, $0 \leq \text{Re}_l \leq 7980$, and $30^\circ \leq \phi \leq 90^\circ$. Figure 6 shows a comparison of the D_d and D_l values predicted using Eqs. (52) and (53) with the data obtained in the present experiments. From Fig. 6 it can be clearly seen that there is large scatter in the experimentally obtained bubble diameters. Also included in Fig. 6 is the single bubble data obtained by Maity [26].

Bubble Waiting Time and Bubble Growth Time. Only limited information regarding the bubble waiting time and growth time could be obtained from the present experiments due to the fact that there are too many bubbles present on the heater surface. Based on the limited data available, the correlation for the bubble growth time (time taken for a bubble to grow from its initial size to its departure size) is given as

$$\frac{D_d^2}{\alpha_l \text{Ja}_{\text{sup}} t_g} = 45 \exp(-0.02 \text{Ja}_{\text{sub}}) \quad (54)$$

where the dimensionless parameter ($D_d^2 / \alpha_l \text{Ja}_{\text{sup}} t_g$) was chosen based on the analysis that the heat input to the bubble over its growth time (t_g), from the superheated liquid layer contributes to

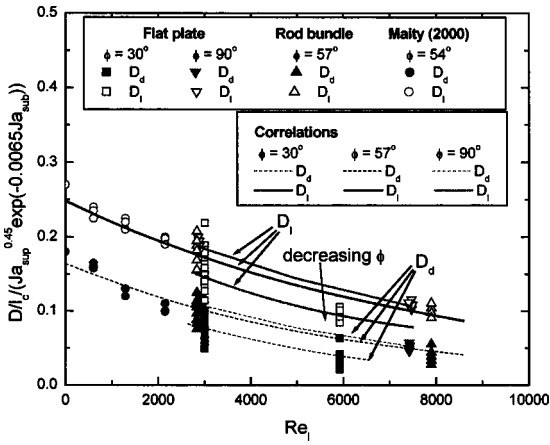


Fig. 6 Variation of D_d and D_l with Re_l

evaporation and the growth of the bubble to D_d . Figure 7 shows the variation of the dimensionless parameter ($D_d^2 / \alpha_l Ja_{sup} t_g$) as a function of Ja_{sub} . It is seen that an increase in ΔT_{sub} or a decrease in ΔT_w reduces the growth rate of the bubbles thereby increasing the time taken for the bubbles to grow to a given size D_d . It should be noted that the effect of v and ϕ on t_g comes in implicitly through their effect on D_d .

The correlation for the bubble waiting time is given by the following expression:

$$t_w = 139.1(\Delta T_w^{-4.1}) \quad (55)$$

where t_w is in seconds and ΔT_w is in $^{\circ}C$. Figure 8 shows t_w as a function of ΔT_w for various values of ΔT_{sub} . The data shows that t_w decreases with an increase in ΔT_w . Also, from Fig. 8, it can be seen that there is no clear dependence of t_w on ΔT_{sub} . Hence,

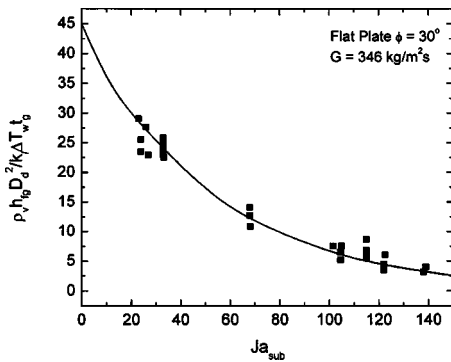


Fig. 7 Bubble growth information

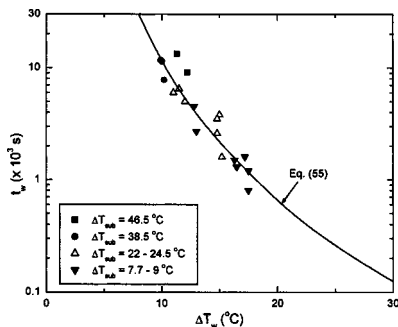


Fig. 8 Variation of t_w with ΔT_w for various values of ΔT_{sub}

t_w is assumed to be independent of ΔT_{sub} . Once t_g and t_w are known, the bubble release frequency (f) can be calculated using the following relationship:

$$f = \frac{1}{t_g + t_w} \quad (56)$$

The data were obtained on the flat plate heater and is very limited in scope as the waiting time is influenced by the solid properties, method of heating, and the thickness of the heated surface.

Enhanced Forced Convection Coefficient. The enhanced forced convection component (\bar{h}_{fc}) values used in this model are the experimentally measured values of the single-phase heat transfer coefficient (h_{sp}) with an enhancement factor of 30% to account for the presence of bubbles. The enhancement factor was obtained by comparing the fully developed single-phase heat transfer coefficients with those measured in the presence of bubbles at the OSV condition (see Basu [22]).

Sliding Distance. This parameter could not be measured from our experimental data due to the presence of too many bubbles on the surface. Information was obtained from Maity's [26] study of single bubble in flow boiling. An estimate of the sliding distance (l_0) for a single bubble is obtained as

$$l_0 = \int_0^{t_s} v_b dt = \int_0^{t_s} C_v t_{sl}^{1/2} dt = \frac{2}{3} C_v t_{sl}^{3/2} \quad (57)$$

where v_b is the bubble velocity, t_{sl} is the sliding time, and C_v is an acceleration coefficient which can again be correlated in terms of bulk velocity as

$$C_v = 3.2v + 1 \quad (58)$$

where v is the imposed liquid velocity in m/s. Equation (57) reflects the increase in bubble velocity with time after it begins to slide away from a nucleation site. Depending on the length l_0 and s , one can determine whether or not a bubble will interact with other sites while sliding. The number of mergers that will occur before lift-off will then govern the sliding distance. For the estimation of the growth of the bubble, while sliding for a distance s , from an initial size D_{in} at the beginning of sliding to a final size D_{sl} at the end of a sliding distance, again Maity's data for a bubble sliding on a vertical surface has been used. The resulting correlation is given as

$$\frac{(D_{sl}^2 - D_{in}^2)}{(t_{sl}) \alpha_l Ja_{sup}} = \frac{1}{15(0.015 + 0.0023 Re_{D_b}^{0.5})(0.04 + 0.023 Ja_{sub}^{0.5})} \quad (59)$$

where Re_{D_b} is the Reynolds number based on the bubble diameter. Equation (59) computes the growth of the sliding bubble in between nucleation sites, whereas the additional volume gain of the bubble due to merger at a site is given by Eq. (28). As described earlier these two factors for the growth of the bubble have to be considered to determine l as given in Eq. (29). In using Eq. (59) care must be taken in using the correct value for D_{in} . If the bubble departs from its site of origin and begins sliding, then $D_{in} = D_d$. On the other hand, if the bubble has already merged with bubbles at secondary sites then $D_{in} = D_{total}$ [as given by Eq. (28)].

Ratio of Bubble Base Diameter to Bubble Diameter. The ratio of the bubble base diameter to the bubble diameter is given by the following empirical correlation:

$$C = 1 - \exp(-2\phi^{0.6}) \quad (60)$$

where ϕ is the static contact angle in degrees. The earlier expression gives values of C as 0.75, 0.85, and 0.93 for ϕ values of 30 $^{\circ}$, 57 $^{\circ}$, and 90 $^{\circ}$, respectively. This correlation was developed based on the experimental data of Maity [26].

Summary

In this work a mechanistic model has been developed for prediction of wall heat flux, as a function of wall superheat, for subcooled flow boiling. The basic difference of this model from the existing ones is that in the present model a bottom-up approach is used and it is proposed that all the wall energy is first transferred to the superheated liquid layer adjacent to the wall, from where a fraction of it goes to vaporization. The evaporative component has been found independently in this model and not as an empirically determined ratio of other wall heat flux components as has been the case in most of the past studies. Also, in the modeling of the wall heat flux partitioning, the dynamics of the bubbles on the heater surface, like sliding and merger, have been considered.

The model shows that the transient conduction component can become the dominant mode of heat transfer at very high superheats and hence velocity does not have much effect at high superheats. This is particularly true when boiling approaches fully developed nucleate boiling. Also note that from this model it is possible to predict the ΔT_w as a function of an applied q_w for a given geometry and flow conditions.

Acknowledgment

This work received support from the United States Nuclear Regulatory commission (USNRC).

Nomenclature

| | |
|------------|--|
| A_i | = interfacial area, m^2 |
| A_b | = base area of influence of a bubble, m^2 |
| A_{sl} | = sliding area swept by a sliding bubble, m^2 |
| Bo | = boiling number, q/Gh_{fg} |
| C_d | = drag coefficient |
| C | = ratio of bubble base diameter to bubble diameter |
| Co | = Convection number $\{[(1-x)/x]^{0.8}(\rho_v/\rho_l)^{0.5}\}$ |
| D | = diameter, m |
| Fr | = Froude number, $v/\sqrt{g_l}$ |
| G | = mass flux, $kg/m^2 s$ |
| h | = heat transfer coefficient, $(W/m^2 K)$ |
| he | = enthalpy, J/kg |
| h_{fg} | = latent heat of vaporization, J/kg |
| Ja | = Jakob number, $\rho_l C_{pl} \Delta T / \rho_v h_{fg}$ |
| k | = thermal conductivity W/mK |
| l | = sliding distance, m |
| l_0 | = sliding distance for a single cavity on the surface, m |
| N_a | = nucleation site density, $1/m^2$ |
| Nu | = Nusselt number hl/k , where l is the length scale |
| p | = pressure, bar |
| Q | = energy, W |
| q | = heat flux, $W/m^2 K$ |
| r | = radius, m |
| Re | = Reynolds number $\rho v D / \mu$ |
| T | = temperature, $^{\circ}C$ or K |
| ΔT | = temperature difference, $^{\circ}C$ or K |
| v | = bulk velocity, m/s |
| x | = quality |
| y | = normal distance from the wall, m |
| z | = axial direction (along flow direction), m |

Greek

| | |
|----------|--|
| α | = thermal diffusivity m^2/s or void fraction |
| δ | = boundary layer thickness, m |
| ϕ | = contact angle (static, if not mentioned otherwise) deg |
| ρ | = density kg/m^3 |
| σ | = surface tension, N/m |
| τ | = shear stress, N/m^2 |
| μ | = viscosity, kg/ms |
| ν | = kinematic viscosity, m^2/s |

Subscripts

| | |
|--------|---|
| b | = bubble |
| c | = condensation |
| d | = departure diameter, dynamic contact angle when used with ϕ |
| ev | = evaporation |
| fc | = forced convection |
| g | = gas |
| in | = inlet |
| l | = liquid, lift-off diameter when used with D |
| nb | = nucleate boiling |
| ONB | = onset of nucleate boiling |
| OSV | = onset of significant void |
| $pool$ | = pool boiling |
| sat | = saturation |
| sl | = sliding |
| sp | = single phase |
| sub | = subcooled |
| tc | = transient conduction |
| v | = vapor |
| w | = wall |

References

- [1] Griffith, P., Clark, J. A., and Rohsenow, W. M., 1958, "Void Volumes in Subcooled Boiling," ASME Paper 58-HT-19, U.S. National Heat Transfer Conference, Chicago.
- [2] Bowring, R. W., 1962, "Physical Model Based on Bubble Detachment and Calculation of Steam Voidage in the Subcooled Region of a Heated Channel," HPR-10, Institutt for Atomenergi, Halden, Norway.
- [3] Rouhani, S. Z., and Axelsson, E., 1970, "Calculation of Void Volume Fraction in the Subcooled and Quality Boiling Regions," Int. J. Heat Mass Transfer, **13**, 383–393.
- [4] Dix, G. E., 1971, "Vapor Void Fraction for Forced Convection with Subcooled Boiling at Low Flow Rates," Ph.D. thesis, University of California, Berkeley.
- [5] Larsen, P. S., and Tong, L. S., 1969, "Void Fractions in Subcooled Flow Boiling," ASME J. Heat Transfer, **91**, 471–476.
- [6] Ahmad, S. Y., 1970, "Axial Distribution of Bulk Temperature and Void Fraction in a Heater Channel with Inlet Subcooling," ASME J. Heat Transfer, **92**, 595–609.
- [7] Hancox, W. T., and Nicoll, W. B., 1971, "A General Technique for the Prediction of Void Distributions in Non-Steady Two-Phase Forced Convection," Int. J. Heat Mass Transfer, **14**, 1377–1394.
- [8] Maroti, L., 1977, "Axial Distribution of Void Fraction in Subcooled Boiling," Nucl. Technol., **34**, 8–17.
- [9] Lahey, R. T., 1978, "A Mechanistic Subcooled Boiling Model," Proceedings of the 6th International Heat Transfer Conference, pp. 293–297.
- [10] Chatoorgoon, V., Dimmick, G. R., Carver, M. B., Selander, W. N., and Shoukri, M., 1992, "Application of Generation and Condensation Models to Predict Subcooled Boiling Void at Low Pressures," Nucl. Technol., **98**, 366–378.
- [11] Zeitoun, O., 1994, "Subcooled Flow Boiling and Condensation," Ph.D. thesis, McMaster University, Hamilton, Ontario, Canada.
- [12] Akiyama, M., 1973, "Bubble Collapse in Subcooled Boiling," Bull. JSME, **16**, 570–575.
- [13] Rogers, J. T., Salcudean, M., Abdullah, Z., McLeod, D., and Poirier, D., 1987, "The Onset of Significant Void in Up-Flow Boiling of Water at Low Pressure and Velocity," Int. J. Heat Mass Transfer, **30**, 2247–2260.
- [14] Kandlikar, S. G., 1987, "General Correlation for Saturated Two-Phase Flow Boiling Heat Transfer Inside Horizontal and Vertical Tubes," HTD (Am. Soc. Mech. Eng.), **85**, 9–19.
- [15] Liu, Z., and Winterton, R. H. S., 1991, "General Correlation for Saturated and Subcooled Flow Boiling in Tubes and Annuli Based on a Nucleate Pool Boiling Equation," Int. J. Heat Mass Transfer, **34**, 2759–2766.
- [16] Cooper, M. G., 1984, "Saturation Nucleate Boiling: A Simple Correlation," 1st U.K. National Conference on Heat Transfer, Vol. 2, pp. 785–793.
- [17] Wadekar, V. V., 1996, "An Alternative Model for Flow Boiling Heat Transfer," Convective Flow Boiling, Chen, J. C., Ed., Taylor and Francis, Washington, D. C., pp. 187–192.
- [18] Lellouche, G., Harrison, J., and Chexal, B., 1996, "A Full Range Wall Heat Flux Model," personal communication.
- [19] Warrior, G. R., Basu, N., and Dhir, V. K., 2002, "Interfacial Heat Transfer of Subcooled Boiling at Low Pressures," Int. J. Heat Mass Transfer, **45**(19), 3947–3959.
- [20] Wang, C. H., and Dhir, V. K., 1993, "Effect of Surface Wettability on Active Nucleation Site Density During Pool Boiling of Water on a Vertical Surface," ASME J. Heat Transfer, **115**, 659–669.
- [21] Warrior, G. R., and Dhir, V. K., 1999, "Review of Experimental and Analytical Studies on Low Pressure Subcooled Flow Boiling," Proceedings of the 5th ASME/JSME Joint Thermal Engineering Conference, Paper AJTE99-6233, CD-ROM ed.

- [22] Basu, N., 2003, "Modeling and Experiments for Wall Heat Flux Partitioning During Subcooled Flow Boiling of Water at Low Pressures," Ph.D. thesis, University of California, Los Angeles.
- [23] Basu, N., Warriar, G. R., and Dhir, V. K., 2002, "Onset of Nucleate Boiling and Active Nucleation Site Density during Subcooled Flow Boiling," *ASME J. Heat Transfer*, **124**(4), 717–728.
- [24] Hsu, Y. Y., 1962, "On the Size Range of Active Nucleation Cavities on a Heating Surface," *ASME J. Heat Transfer*, **84**, 207–216.
- [25] Unal, H. C., 1975, "Determination of the Initial Point of Net Vapor Generation in Flow Boiling Systems," *Int. J. Heat Mass Transfer*, **18**, 1095–1099.
- [26] Maity, S., 2000, "Effect of Velocity and Gravity on Bubble Dynamics," MS thesis, University of California, Los Angeles.

Wall Heat Flux Partitioning During Subcooled Flow Boiling: Part II—Model Validation

Nilanjana Basu¹

Gopinath R. Warrier

Vijay K. Dhir²

e-mail: vdhir@seas.ucla.edu

Mechanical and Aerospace Engineering
Department,
Henry Samueli School of Engineering and
Applied Science,
University of California, Los Angeles,
Los Angeles, CA 90095-1597

A mechanistic model for wall heat flux partitioning during subcooled flow boiling proposed in Part I of this two-part paper, is validated in this part. As the first step of the validation process, the developed model was applied to experimental data obtained as part of this study. Comparison of the model predictions with the present data shows good agreement. In order to further validate/exercise the model, it was then applied to several data sets available in the literature. Though the data in the literature were for experimental conditions vastly different from those from which the model was originally developed, reasonable agreement between the model predictions and the experimental data were observed. This indicates that the proposed model can be extended to other flow conditions provided the submodels cover the conditions of the experiments. Future work should be directed towards improvement of the various submodels involved to extend their range of applicability, especially the ones related to bubble dynamics. Additionally, it must be kept in mind that the model as proposed is strictly only applicable to vertical up-flow and may not be applicable to other orientations. [DOI: 10.1115/1.1842785]

Keywords: Mechanistic Model, Heat Flux, Subcooled Flow Boiling

Introduction

For prediction of void fraction in nuclear reactors, the source term for voids is wall vapor generation, which in turn can only be obtained from the wall heat flux partitioning model. In Part I of this paper [1], it is shown that the existing wall heat flux models are mainly applicable for high-pressure applications. These models have too much empiricism built into them such that their application to low pressure situations such as those in passively cooled nuclear reactors is suspect. Hence, a mechanistic model taking a bottom-up approach considering each of the heat transfer mechanisms at the wall has been proposed in Part I. The submodels required for the overall model have been discussed in the companion paper. This paper deals with the validation of the model. All the heat transfer components at the wall are calculated as per the procedure already outlined in Part I, and the overall wall heat flux predictions are validated with experimentally measured values of the wall heat flux.

For a given geometry, the basic approach taken was to find the wall heat flux components—transient conduction component (q_{tc}) and forced convection component (q_{fc}). The wall heat flux is further subdivided into that going for evaporation (q_{ev}) and that going to heat the bulk liquid (q_l). These component were evaluated for imposed mass flux (G), liquid subcooling (ΔT_{sub}), single-phase heat transfer coefficient (h_{fc}), static contact angle (ϕ), and fluid properties for each test case. Thus, the predicted wall heat flux ($q_{w,pred}$) can be expressed as

$$q_{w,pred} = \frac{Q_w}{A_h} = \frac{Q_{fc}}{A_h} + \frac{Q_{tc}}{A_h} = q_{fc} + q_{tc} = \frac{Q_l}{A_h} + \frac{Q_{ev}}{A_h} = q_l + q_{ev} \quad (1)$$

Details of Eq. (1) can be found in Part I [1]. The predicted q_w value is then compared with the corresponding applied q_w for the same test case.

Also, q_{ev} is calculated and then q_l is obtained by subtracting q_{ev} from $q_{w,pred}$. The wall temperature can be found iteratively when

¹Present address: Fluent Inc., 10 Cavendish Court, Lebanon, NH 03766.

²To whom correspondence should be addressed.

Manuscript received December 12, 2003; revision received August 31, 2004. Review conducted by: M. Jensen.

the input used is q_w instead of ΔT_w , while all other inputs remain the same. In this case, the predicted value of ΔT_w is found iteratively by matching $q_{w,pred}$ with the input q_w .

As this model is only applicable in the region downstream of the onset of significant (OSV) location, one needs to be specific about the experimental conditions downstream of OSV. In the post OSV region, the model distinguishes between these two situations—one where the bubbles slide and another where they do not. Additionally, the bubbles can also merge with each other either at their site of origin or along their sliding path. Details of how these different situations are handled are given in Part I.

As part of the model validation process, three different computer programs were written (in FORTRAN)—one for predicting q_w given ΔT_w , another for predicting ΔT_w given q_w , and a third one for predicting the ΔT_w profile in the axial direction given a q_w profile. Details of these programs can be found in Basu [2]. As mentioned earlier, the other inputs required are the geometry, G , ΔT_{sub} , h_{fc} , ϕ , and the fluid properties. Figure 1 shows a flow-chart with the sequence of steps involved in predicting q_w , for a given ΔT_w .

In the code for the prediction of q_w , there is a provision to check if the inputs do indeed correspond to post onset of nucleate boiling (ONB) and OSV conditions (calculated from the models developed for these two conditions in the present work). Only if these conditions are satisfied does the calculation of q_w proceed. A similar check is also performed when predicting ΔT_w . When calculating the ΔT_w profile, location of ONB as well as OSV along with the corresponding ΔT_w values are first found from the models for ONB and OSV. Then, downstream of OSV, using the wall heat flux partitioning model, ΔT_w is obtained using an iterative procedure.

Experiments

Subcooled flow boiling experiments were conducted for vertical up flow in vertical Copper plate (30.5 cm long and 3.175 cm wide) and a Zircalloy-4 nine-rod bundle arranged in a 3×3 square grid (91.44 cm long, 1.11 cm outer diameter with a pitch to diameter ratio of 1.288). Experiments were conducted at pressures varying from 1.03 to 3.2 bar for a wide range of mass fluxes (124–926 kg/m²s), heat fluxes (2.5–113 W/cm²) and for contact

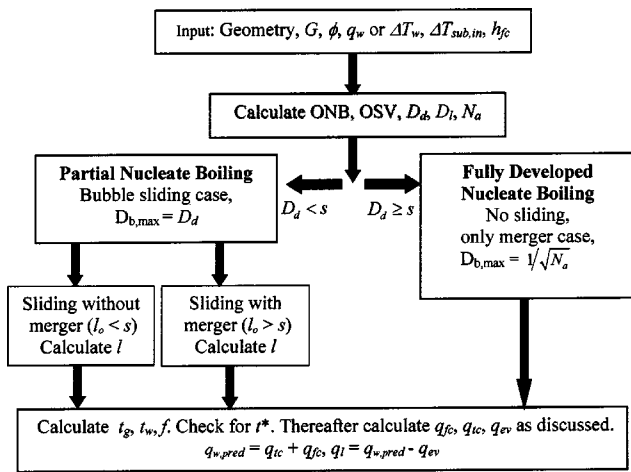


Fig. 1 Flowchart showing the sequence of calculations

angles varying from 30° to 90°. Details of the experimental set up and procedure can be found in Basu [2] and Basu et al. [3].

Validation of the Model

Application to Present Data (Low Pressures)

Flat Plate Test Cases. For validation of the model, the flat plate test results, downstream of OSV and at mid-plane ($z = 15.24$ cm) are used. In these set of experiments, the pressure, static contact angle, mass flux, and liquid subcooling were kept constant at 1.03 bar, 31°, 346 kg/m²s, and 7.4°C, respectively, while the heat flux was increased from 12.3 to 94.3 W/cm². The resulting wall superheats recorded varied from 11.7 to 25°C. Table 1 lists these experimental conditions. Based on these values, the heat flux components were calculated based on the model developed. In order to give a sense of the magnitude of the various parameters calculated from the submodels, the results of the sample calculations are given in Table 2. A brief discussion of these results is given in the following: As the wall superheat increases from 11.7 to 25°C, the nucleation site density (N_a) increases from about 6 to 127 sites/cm², which in turn results in the bubble spacing (s) decreasing from 3.85 to 0.89 mm. Values of the bubble departure diameter (D_d), bubble lift off diameter (D_l), and bubble sliding distance (l) are also listed in Table 2. It can be seen that as ΔT_w increases, D_d increases. When $\Delta T_w \sim 23.6^\circ\text{C}$, $D_d > s$ and as such the bubbles merge at their site of origin (hence, $l=0$). This also indicates the onset of fully developed nucleate boiling. The magnitudes of both the waiting time (t_w) and the growth time (t_g) decrease with increasing ΔT_w , resulting in an increase in the bubble release frequency (f). The variation of the various flux components is discussed later.

Figure 2 shows a plot of the heat flux component q_{tc} and q_{fc} as a function of ΔT_w for two different flow rates. Note that the heat fluxes have been normalized with $q_{w,pred}$, while the wall superheat has been normalized with the ΔT_w at OSV. Figure 2(a) is for $G = 346$ kg/m²s (data listed in Table 2) while Fig. 2(b) is for $G = 868$ kg/m²s. The plot clearly shows that as ΔT_w (or applied q_w) increases, the q_{tc} component continues to increase while the q_{fc} component decreases. Initially $q_{fc}/q_{w,pred}$ is unity but it approaches zero when $\Delta T_w/\Delta T_{w,OSV} \sim 2.5$, indicating that initially (at low all superheats) forced convection is the only mode of heat transfer from the wall but as the wall superheat increases, the forced convection contribution decreases steadily and finally goes to zero at a high enough wall superheat. Conversely, $q_{tc}/q_{w,pred}$ is initially zero but then increases to unity. As such, at high wall superheats, transient conduction to liquid (q_{tc}) becomes the only mode of heat transfer from the wall to the superheated liquid. This typically occurs when the nucleation site density is so high that bubbles merge without sliding. Similar results are obtained at higher flow rates ($G = 868$ kg/m²s). For $G = 868$ kg/m²s [see Fig. 2(b)], the forced convection component is higher and as a result the intersection point between q_{tc} and q_{fc} shifts to the right indicating for the same ratio of superheats, the $q_{fc}/q_{w,pred}$ ratio is higher for higher mass fluxes. As listed in Table 2, the maximum difference between $q_{w,exp}$ and $q_{w,pred}$ varies between -15.7% and +17.6%.

Table 2 Predicted parameters for the flat plate test case

| Parameter | Run No. | | | | | |
|-----------------------------------|---------|--------|--------|--------|--------|--------|
| | BC3d | BC3e | BC3f | BC3g | BC3h | BC3i |
| N_a (sites/cm ²) | 6.73 | 10.06 | 21.47 | 51.34 | 92.93 | 126.93 |
| D_d (mm) | 1.01 | 1.11 | 1.23 | 1.34 | 1.42 | 1.47 |
| D_l (mm) | 1.53 | 1.68 | 1.86 | 2.03 | 2.15 | 2.23 |
| t_g (ms) | 5.25 | 5.14 | 5.02 | 4.90 | 2.58 | 1.74 |
| t_w (ms) | 4.25 | 2.98 | 1.95 | 1.37 | 0.57 | 0.34 |
| f (Hz) | 105.27 | 123.28 | 143.59 | 159.39 | 318.03 | 480.66 |
| s (mm) | 3.85 | 3.15 | 2.16 | 1.40 | 1.04 | 0.89 |
| l (mm) | 5.94 | 5.91 | 4.32 | 2.79 | 0.00 | 0.00 |
| q_{tc} (W/cm ²) | 7.05 | 14.00 | 20.23 | 39.94 | 72.00 | 91.90 |
| q_{fc} (W/cm ²) | 7.62 | 7.42 | 7.08 | 5.13 | 0.00 | 0.00 |
| q_{ev} (W/cm ²) | 0.82 | 1.90 | 4.30 | 14.69 | 21.32 | 27.57 |
| q_l (W/cm ²) | 13.64 | 19.19 | 23.56 | 30.37 | 44.96 | 64.33 |
| $q_{w,pred}$ (W/cm ²) | 14.46 | 21.09 | 27.86 | 45.07 | 66.27 | 91.90 |
| $q_{w,exp}$ (W/cm ²) | 12.30 | 18.30 | 33.00 | 53.50 | 70.50 | 94.30 |
| Error (%) | 17.59 | 15.22 | -15.58 | -15.76 | -5.99 | -2.55 |

Figures 3(a) and 3(b) show the q_{ev} and q_l components as a function of ΔT_w for two different flow rates. The heat fluxes and wall superheats are normalized as in Fig. 2. The plots show that at OSV all the energy goes to the liquid ($q_l/q_{w,pred} = 1$), and hence, the evaporative component is zero ($q_{ev}/q_{w,pred} = 0$). Gradually, with the increase in the wall superheat, q_{ev} increases and q_l decreases. In the cases shown, the bulk liquid is subcooled even at very high superheats—hence there is still considerable energy going to the heating of the liquid. For $G = 346$ kg/m²s, the maximum value q_{ev} reaches is about 30% of $q_{w,pred}$ for the highest heat flux [Fig. 3(a)] and about 25% of $q_{w,pred}$ for the higher flow rate [Fig. 3(b)]. Thus even at a heat flux exceeding 90 W/cm², not all the energy is going into phase change. The rate of increase in q_{ev} or decrease in q_l with increase in ΔT_w is slower at higher heat fluxes.

From the model it is also possible to predict the boiling curve. This is shown in Fig. 4 where the predicted wall heat flux value

Table 1 Experimental conditions for the flat plate test case

| Run No. | G (kg/m ² s) | p (bar) | ΔT_{sub} (°C) | ΔT_w (°C) | q_{exp} (W/cm ²) | ϕ (deg) |
|---------|---------------------------|-----------|-----------------------|-------------------|--------------------------------|--------------|
| BC3d | 346 | 1.03 | 7.4 | 11.7 | 12.3 | 31 |
| BC3e | 346 | 1.03 | 7.4 | 14.3 | 18.3 | 31 |
| BC3f | 346 | 1.03 | 7.4 | 17.9 | 33.0 | 31 |
| BC3g | 346 | 1.03 | 7.4 | 21.1 | 53.5 | 31 |
| BC3h | 346 | 1.03 | 7.4 | 23.6 | 70.5 | 31 |
| BC3i | 346 | 1.03 | 7.4 | 25 | 94.3 | 31 |

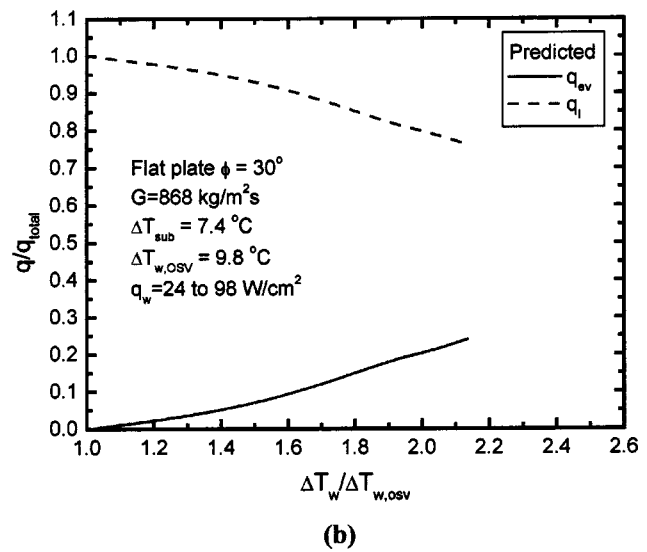
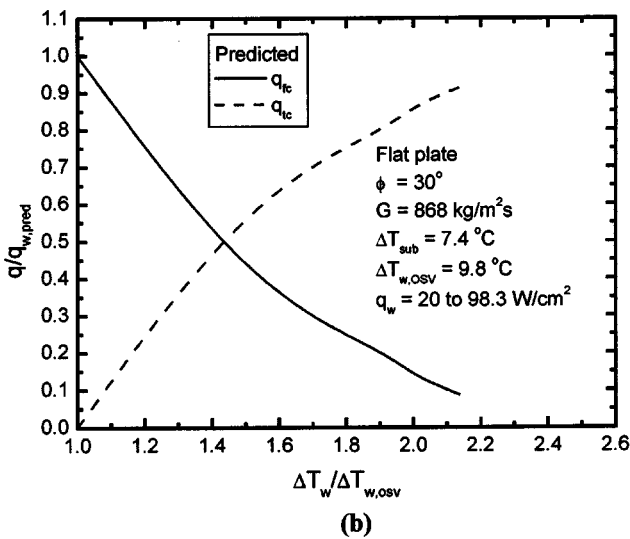
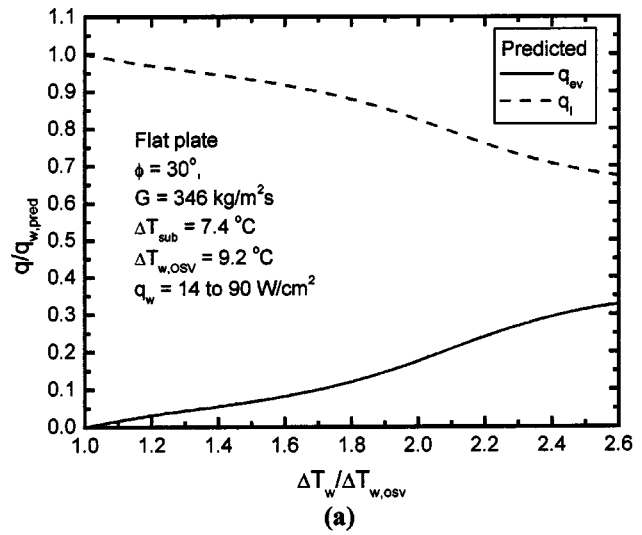
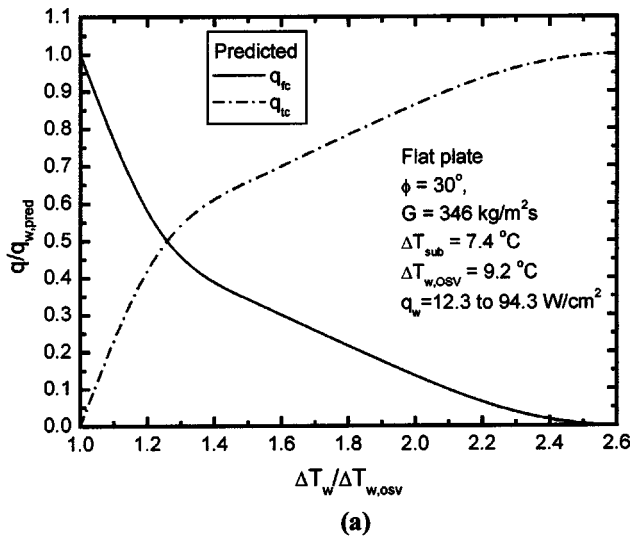


Fig. 2 Predicted q_{ic} and q_{fc} components of wall heat flux for two different flow rates for the flat plate test case

Fig. 3 Predicted q_{ev} and q_l components of wall heat flux for two different flow rates for the flat plate test case

($q_{w, pred} = q_{fc} + q_{ic}$) is plotted as a function of the ΔT_w for the flat plate test case ($z = 15.2$ cm and $\Delta T_{sub, in} = 7.4$ °C). The $\Delta T_{w, ONB}$ is obtained iteratively from the model developed and is described here. The ONB condition corresponds to the limit of single-phase heat transfer. So by choosing a q_w value and checking whether $\Delta T_{w, ONB}$ obtained from this q_w also corresponds to the single-phase value given by $\Delta T_w = q_w / h_{fc} - \Delta T_{sub}$, one can find $\Delta T_{w, ONB}$. Next the wall heat flux at OSV is obtained as per the model developed. Thereafter the corresponding ΔT_w at OSV is calculated. The experimental data obtained are also shown and clearly show very good agreement.

Rod Bundle Test Cases. Figure 5 shows the predicted axial variation of q_{ic} and q_{fc} for the rod bundle case for $G = 336$ kg/m² s. For the rod bundle case, since the liquid subcooling changes rapidly along the axial direction, the plots are shown with the heat flux components as a function of axial location (z), for the same applied wall heat flux. The figure shows that q_{ic} increases along the z direction with increase in ΔT_w , and decrease in ΔT_{sub} , while q_{fc} decreases monotonically along the axial direction. However, since the condition that exists at the end of the channel is still that of a sliding bubble (the wall superheat not being as high as that for most of the flat plate cases, the bubble

spacing is still large enough for sliding to occur), forced convection still contributes. The difference between the predicted and imposed wall heat fluxes varies between -2.5% and $+5.5\%$. Figure 6 shows the corresponding q_{ev} and q_l components. The q_{ev} component increases rapidly and reaches about 80% of $q_{w, pred}$ close to the outlet. The bulk liquid has already attained saturation at this location. However about 20% of the heat is going into superheating the liquid. The experimentally observed location of OSV, as well as the location where the bulk liquid attains saturation is also been marked in Fig. 6.

The wall temperature can also be predicted as a function of axial distance, for given heat flux profile. Figure 7 shows the predicted wall temperature for the rod bundle test case. The experimental conditions were the following: $G = 336$ kg/m² s, $\Delta T_{sub, in} = 26.5$ °C, and applied constant $q_w = 14.5$ W/cm². Here also, the location of ONB and OSV is found as described previously. In the region upstream of OSV, the local subcooling at each axial location can be obtained from the energy balance (all the energy goes to heating the liquid). Downstream of OSV, the heat flux partitioning model is applied and T_w is found iteratively by matching the predicted q_w with the applied value. Also, note that all the energy is not going to the liquid and as such the q_{ev} component calculated needs to be subtracted from the total q_w to

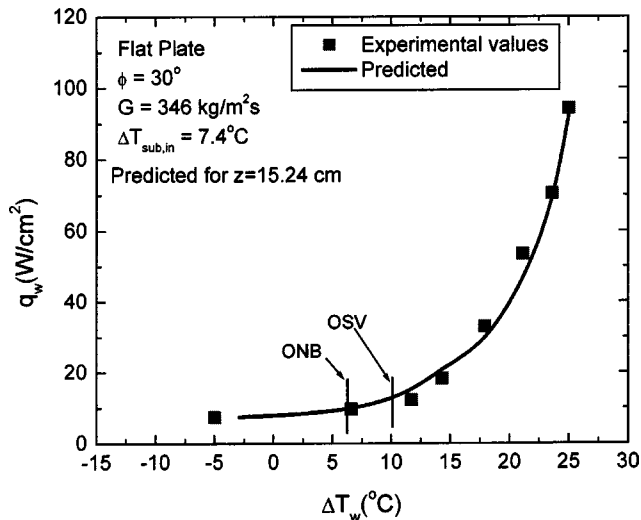


Fig. 4 Predicted boiling curve for the flat plate test case

obtain the fraction of energy going to the liquid. The temperature increase of the bulk liquid has to be updated accordingly. It must be noted that in this study, the local subcooling is determined using only the q_l component computed from Eq. (1). This ap-

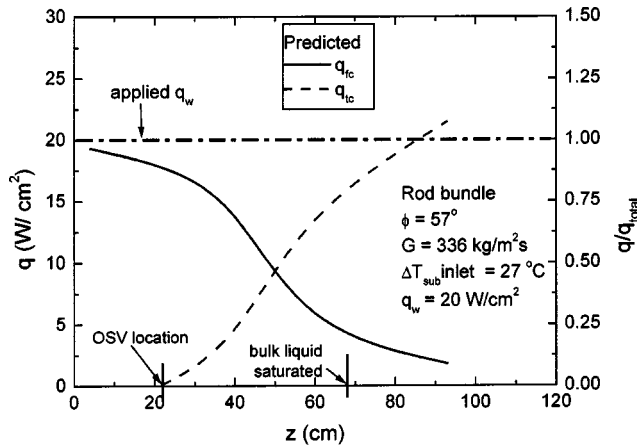


Fig. 5 Predicted q_{tc} and q_{fc} components of wall heat flux for a constant wall heat flux for the rod bundle test case

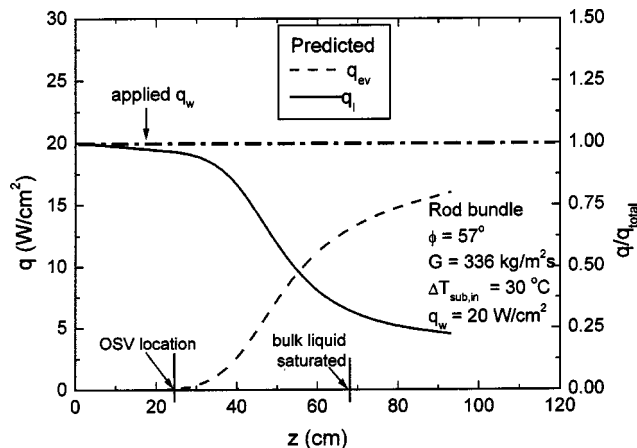


Fig. 6 Predicted q_{ev} and q_l components of wall heat flux for a constant wall heat flux for the rod bundle test case

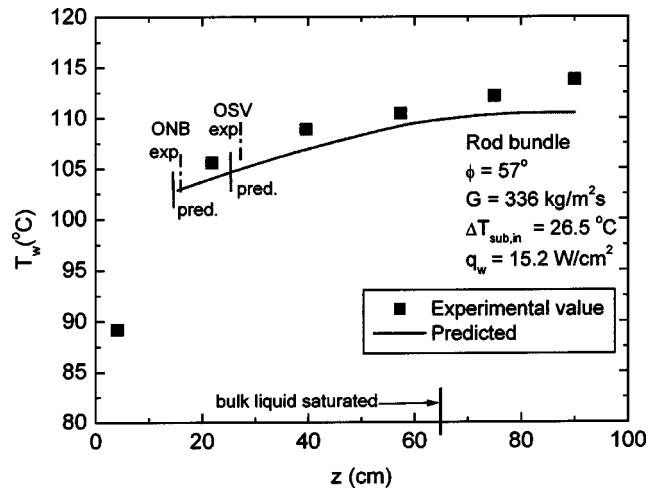


Fig. 7 Predicted wall temperature profile for the rod bundle test case

proach does not account for the additional energy that would be added to the liquid when the all or part of the vapor (generated at the wall) condenses in the bulk liquid. Figure 7 shows that though the wall temperatures are slightly under predicted; the overall agreement between the predicted and experimental values is good.

Figure 8 shows a comparison of all the predicted and experimentally measured heat fluxes (for post OSV conditions) for different flow rates, liquid subcooling, wall superheats and contact angles, for both the flat plate and rod bundle test cases. Almost all of the predicted heat fluxes lie within $\pm 30\%$ of the experimental values.

Application to Data in Literature (Low to Medium Pressures). In our attempts to check the model and validate/extend it for different pressures and flow rate conditions, the model was applied to some of the data available in the literature. The data considered included those from Bergles and Rohsenow [4] for water boiling on a stainless steel surface at 2.8 bar, McAdams [5] data for water boiling on a stainless steel surface at a pressure of 4.13 bar, Morozov [6] for water boiling on a stainless steel at 31–41 bar, and Hodgson [7] for water boiling on a stainless steel surface at 7.9–38.9 bar. Since the contact angle data was not

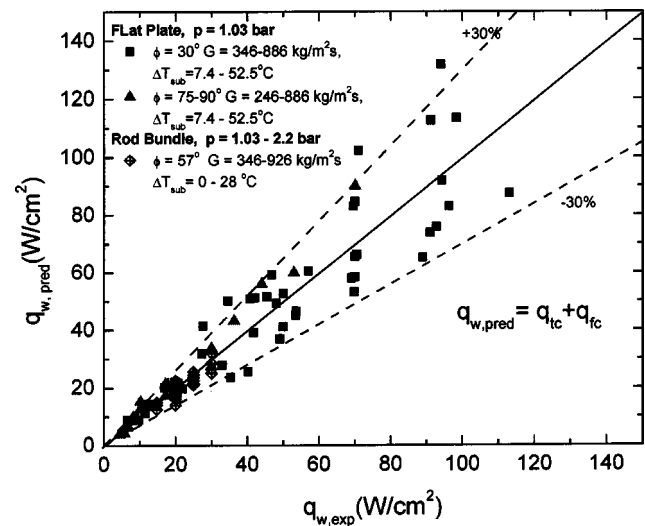


Fig. 8 Comparison of predicted wall heat flux with experimental value from present study

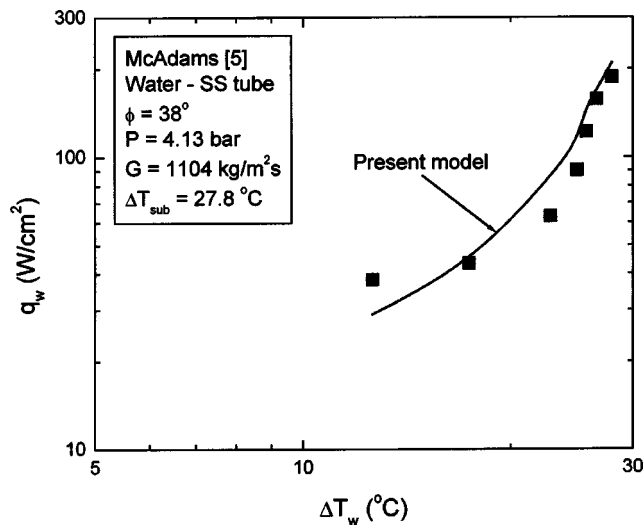


Fig. 9 Boiling curve comparison with McAdams's [5] data

explicitly given in the literature, for most sets of data a contact angle of 38° was assumed, which is a typical value for water boiling on a stainless steel surface.

Figure 9 shows a comparison between the experimental boiling curve from McAdams [5] and the predicted boiling curve. The experimental conditions were the following: $p=4.13$ bar, $G=1104$ kg/m² s, $\Delta T_{\text{sub}}=27.8^\circ\text{C}$, and $\phi=38^\circ$. Good agreement is observed between the experimental and predicted values. Boiling curves obtained by Morozov [6] for two different system pressures are shown in Fig. 10. Figure 10(a) shows a comparison between experimental and predicted values for $p=31$ bar, while Fig. 10(b) shows the comparison for $p=41.4$ bar. For $p=31$ bar, the agreement is good, while at $p=41.4$ bar, the heat fluxes are consistently underpredicted by about 14%–20%.

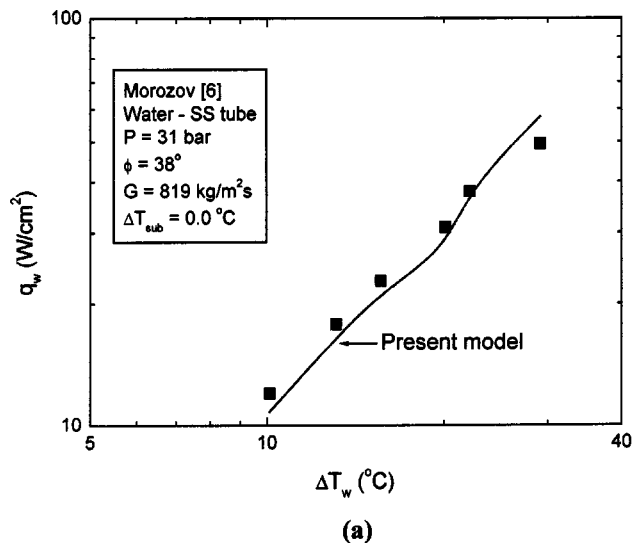
Figure 11 shows a comparison of the predicted ΔT_w with the experimentally measured values of Hodgson [7], for two different heat flux values: 191 and 242 W/cm². For all the cases shown in Fig. 11, the inlet liquid subcooling is about 55°C . Other experimental conditions for the various cases shown are as follows:

- i. Fig. 11(a): $G=21,148$ kg/m² s, $v=23.4$ m/s, $p=7.9$ bar;
- ii. Fig. 11(b): $G=20,738$ kg/m² s, $v=23.9$ m/s, $p=14.8$ bar;
- iii. Fig. 11(c): $G=20,348$ kg/m² s, $v=25.4$ m/s, $p=38.9$ bar; and
- iv. Fig. 11(d): $G=14,578$ kg/m² s, $v=16.8$ m/s, $p=14.8$ bar.

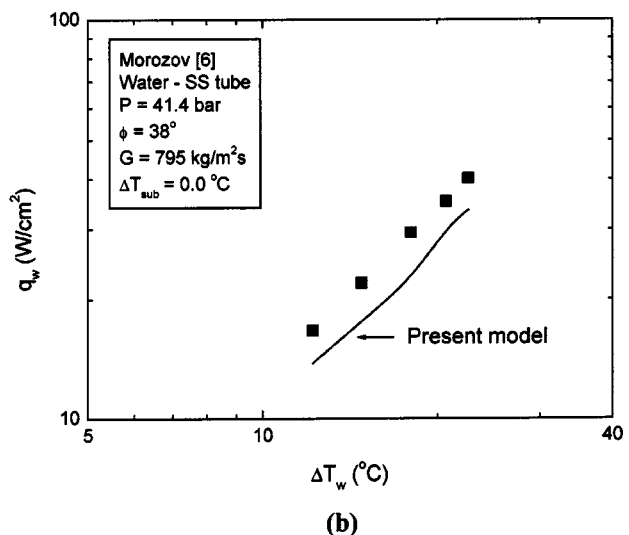
Figure 11(a)–11(c), which are for pressures varying from 7.9 to 38.9 bar with all other parameters constant, show that the model predicts the wall superheat profile very well. Reasonable agreement is also seen in Fig. 11(d), which is for a lower flow rate than that in Fig. 11(b), but for a pressure of 14.8 bar.

Application to Data in Literature (High Pressures). The high pressure data available in the literature are that of Rohsenow and Clark [8] for water boiling on a nickel surface at 138 bar. In this case too, since the static contact angle was not explicitly given it was assumed to be 38° , which is a typical value for water boiling on a nickel surface. Comparisons with the high pressure data of Rohsenow and Clark [8] are included in Fig. 12, which is discussed later.

Figure 12 shows an overall comparison of predicted q_w values with all of the data obtained from the literature (Bergles and Rohsenow [4]; McAdams [5]; Morozov [7]; Rohsenow and Clark [8]). The data plotted in Fig. 10 cover a wide range of pressures (2.8–138 bar), velocities (0.1–17 m/s), liquid subcoolings (0.0–110°C), and wall superheats (9.5–120°C). The comparison of the predicted value with the data shows good agreement (typically



(a)



(b)

Fig. 10 Boiling curve comparisons for Morozov's [6] data

within $\pm 30\%$). It clearly indicates that the model can be extended to higher pressures and velocities, and wall superheats and liquid subcoolings with proper extension of the submodels for the various parameters used in the overall heat flux partitioning model.

Finally, the results from the present model were compared with Lahey's [9] model, which is used in codes such as RELAP 5. In making this comparison, flow in a 360 cm long vertical tube made of stainless steel ($\phi=38^\circ$), with an assumed heat flux profile [$q_w(z)=5+20\sin(z/2)$ W/cm²], was considered. The inlet liquid subcooling is taken to be 50°C and the system pressure is assumed to be 70 bar. The single-phase heat transfer coefficient for this test case was assumed to be constant and was calculated using the Dittus–Boelter correlation [10]. The aim of this exercise was to determine the wall superheat profile and hence the axial variation in the various heat flux components. Figure 13(a) shows the calculated axial variation of ΔT_w . Note that the calculations are only performed from the ONB location onwards. The calculated ONB ($z=93$ cm, $\Delta T_{w,\text{ONB}}=0.75^\circ\text{C}$) and OSV ($z=116$ cm, $\Delta T_{w,\text{OSV}}=3.4^\circ\text{C}$) locations are also indicated in Fig. 13(a). After ONB, ΔT_w increases rapidly and reaches a maximum value of about 23.0°C at $z=198$ cm. Thereafter, ΔT_w decreases monotonically.

Figure 13(b) shows the variation of the q_l and q_{ev} components as a function of the axial distance, calculated from the present model and Lahey's [9] model. In addition to the ONB and OSV

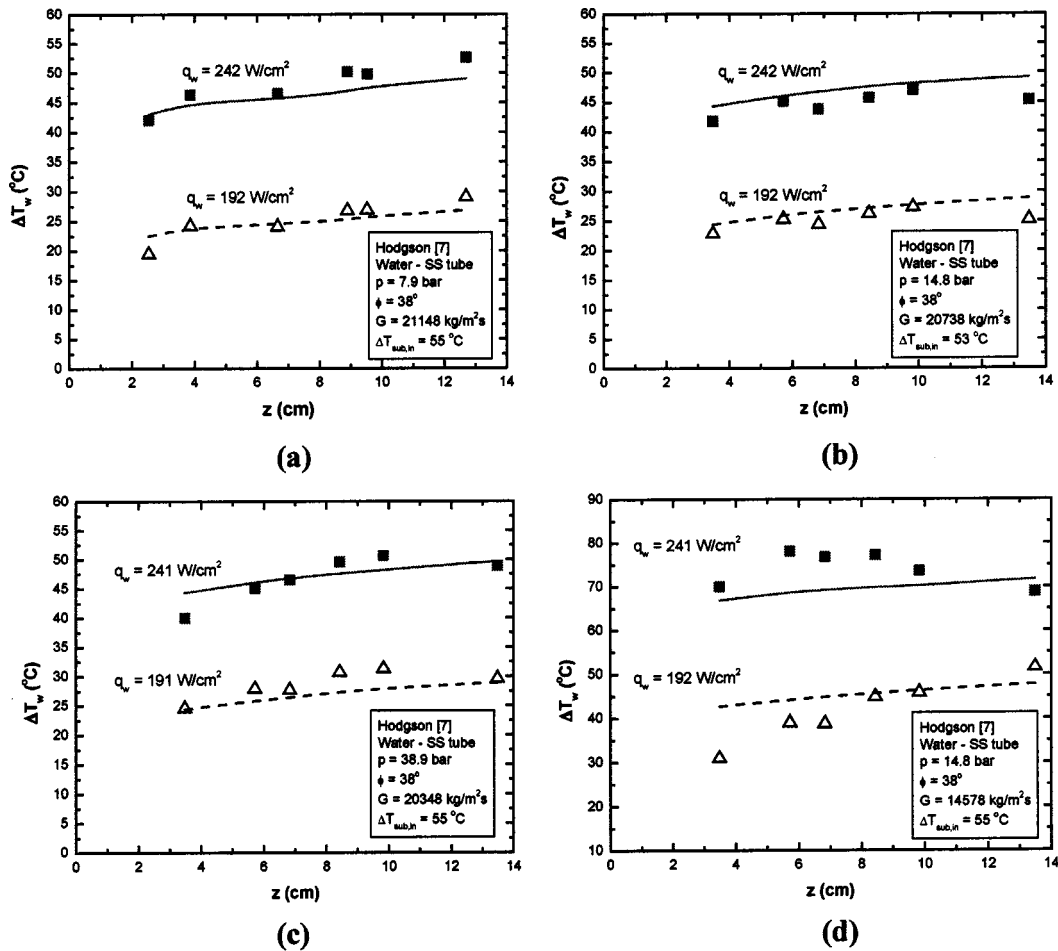


Fig. 11 Wall superheat prediction for Hodgson's [7] data

locations, the location where the bulk liquid is saturated ($z = 198 \text{ cm}$) is also indicated in Fig. 13(b). From Lahey's model it can be seen that as long as the bulk liquid is subcooled, almost all of the energy from the wall goes to the liquid ($q_l \approx q_w$, $q_{ev} \approx 0$). However, once the liquid is saturated, q_{ev} becomes the only mode of heat transfer ($q_{ev} \approx q_w$, $q_l \approx 0$). As mentioned earlier, in the present model, q_l is calculated by subtracting q_{ev} from q_w . In the

present model, upstream of OSV, all the energy goes to the liquid. However, downstream of OSV, the q_{ev} component increases rapidly (because of the increase in ΔT_w with q_w), while q_l decreases rapidly. The q_{ev} component reaches a maximum at $z = 198 \text{ cm}$ (since this is the location of maximum ΔT_w and where the bulk liquid is saturated) and thereafter decreases monotonically (because ΔT_w is decreasing). It is interesting to note that even in the region where the bulk liquid is saturated, the q_l component plays a significant role, unlike Lahey's model where $q_l = 0$. This basically indicates that there is still energy being transferred from the wall to the liquid and that not all of the energy at the wall is used to generate vapor. However, downstream of a given location some excess energy from the superheated liquid may revert back to the vapor.

The validation of the model based on experimental data from the present study indicates good agreement between the predicted and experimental values. The model also seems to work well when applied to other data sets in the literature. This gives us confidence that the present model can be extended to other flow conditions. As a word of caution, it must, however, be mentioned that occasionally we have encountered flow conditions where the model predicts incorrect results, when applied to some of the data obtained from the literature. These situations were encountered at high heat fluxes (or wall superheats) for medium to high pressures ($31 < p < 138 \text{ bar}$) or high velocities ($v > 6 \text{ m/s}$). Analysis of the incorrect results showed that in all cases, the predicted q_{ev} component was greater than $q_{w,pred}$. The reason for this is as follows: For medium to high pressures or high velocities, as q_w (or ΔT_w) increases, the bubble release frequency (f) increases rapidly (because t_g and t_w decrease sharply). Since q_{ev} is sensitive to f , q_{ev}

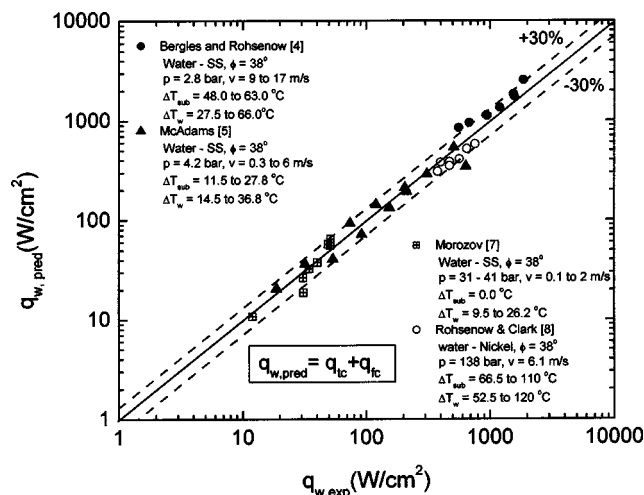
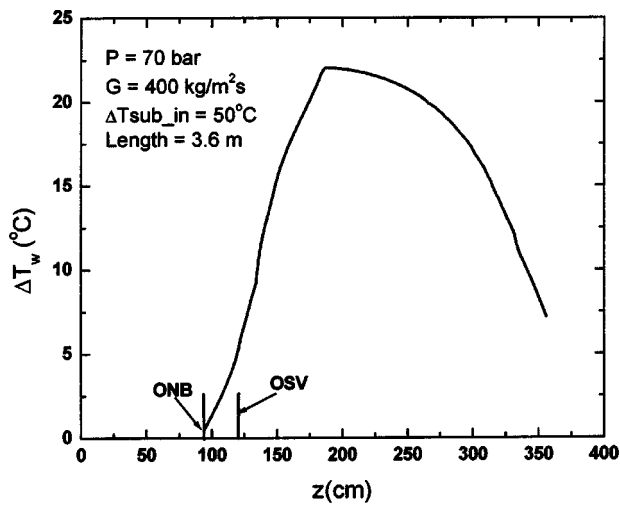
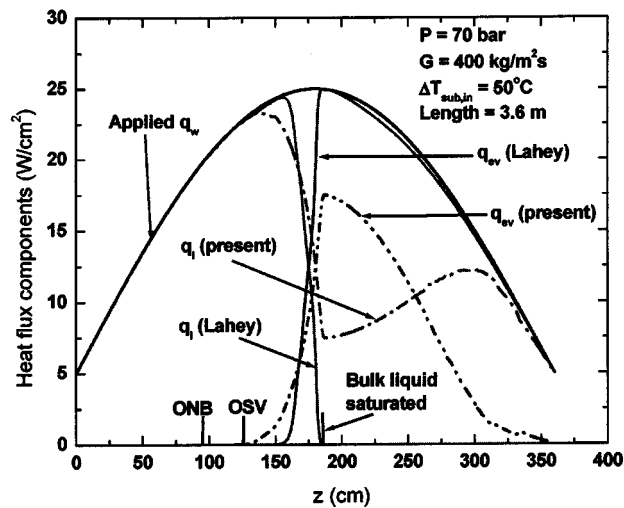


Fig. 12 Application of model to data available in the literature



(a)



(b)

Fig. 13 Comparison between the present model and Lahey's [9] model

increases rapidly with increasing values of f , and for particular flow conditions exceeds $q_{w,pred}$. The increase in f is due to the decrease in both t_g and t_w , with t_w decreasing more rapidly than t_g , with increasing p , v , and q_w (or ΔT_w).

The critical submodels, we believe, are those relating to the bubble diameters (D_d and D_l) and bubble release frequency (f). It must be kept in mind that the submodels for these parameters were developed from low pressure, low velocity experiments performed using a copper test surface (properties of the solid affect t_w and, hence, f). For extension of these submodels to a much broader range of conditions, it would be essential to acquire additional experimental data covering those conditions.

Summary

Validation of the mechanistic model developed earlier for the prediction of wall heat flux has been carried out. In the first step in the validation process, the model was applied to experimental data from the present study for both a flat plate test section and a nine-rod bundle geometry. The data covered in the present study are for vertical up-flow for following range of parameters: (i) p : 1–3.1 bar, (ii) G : 124–926 kg/m²s, (iii) ϕ : 30°–90°, (iv) ΔT_{sub} :

0–52.5°C, and (v) q_w : 2.5–113 W/cm². Good agreement was observed between the model predictions and the experimental data.

Additionally, the model was also applied to several data sets available in the literature. In spite of the data in the literature being for experimental conditions vastly different [higher pressures, velocities, liquid subcoolings, and wall superheats (or heat fluxes)] from those for which the model was originally developed, good agreement between the model predictions and the experimental data were observed (within $\pm 30\%$).

Future work should be directed towards improvement of the various submodels involved, specially the ones related to bubble dynamics and bubble release frequency, at high heat flux or fully developed nucleate boiling conditions. The bubble release frequency is affected by the waiting time, which depends on the thermal response of the solid to the imposed heat flux condition on the liquid side. Additionally, it must be kept in mind that the model as proposed is strictly only applicable to vertical up-flow and may not be applicable to other orientations.

Acknowledgment

This work received support from the United States Nuclear Regulatory Commission (USNRC).

Nomenclature

- D = diameter, m
- G = mass flux, kg/m²s
- h = heat transfer coefficient, W/m²K
- l = sliding distance, m
- N_a = nucleation site density, 1/m²
- p = pressure, bar
- Q = energy, W
- q = heat flux, W/m²
- s = spacing between nucleation sites, m
- t = time, s
- T = temperature, °C
- ΔT = temperature difference, °C
- v = bulk velocity, m/s
- z = axial direction (along flow direction), m

Greek

- ϕ = contact angle (static, if not mentioned otherwise)

Subscripts

- b = bubble
- c = condensation
- ev = evaporation
- fc = forced convection
- in = inlet
- l = liquid, lift off diameter when used with D
- ONB = onset of nucleate boiling
- OSV = onset of significant void
- sat = saturation
- sub = subcooled
- tc = transient conduction
- v = vapor
- w = wall

References

- [1] Basu, N., Warriar, G. R., and Dhir, V. K., 2005, "Wall Heat Flux Partitioning During Subcooled Flow Boiling—Part I: Model Development," *ASME J. Heat Transfer*, **127**(2), pp. 131–140.
- [2] Basu, N., 2003, "Modeling and Experiments for Wall Heat Flux Partitioning During Subcooled Flow Boiling of Water at Low Pressures," Ph.D. thesis, University of California, Los Angeles.
- [3] Basu, N., Warriar, G. R., and Dhir, V. K., 2002, "Onset of Nucleate Boiling and Active Nucleation Site Density During Subcooled Flow Boiling," *ASME J. Heat Transfer*, **124**(4), 717–728.

- [4] Bergles, A. E., and Rohsenow, W. M., 1964, "The Determination of Forced Convective Surface Boiling Heat Transfer," *ASME J. Heat Transfer*, **86**, 365–372.
- [5] McAdams, W. H., 1954, *Heat Transmission*, McGraw-Hill, New York.
- [6] Morozov, V. G., 1969, "Convective Heat Transfer in Two Phase Flow," V. M. Borishanskii and I. I. Paleev, eds., Israel Program for Scientific Transactions.
- [7] Hodgson, A. S., 1966, "Forced Convection, Subcooled Boiling in Water," Ph.D. thesis, University of London, London.
- [8] Rohsenow, A. E., and Clark, J. A., 1951, "Heat Transfer and Pressure Drop Data for High Heat Flux Densities to Water at High Subcritical Pressure," *Heat Transfer and Fluid Mechanics Institute*, Stanford University Press, Stanford.
- [9] Lahey, R. T., 1978, "A Mechanistic Subcooled Boiling Model," Proceedings of the 6th International Heat Transfer Conference, pp. 293–297.
- [10] Dittus, W. F., and Boelter, L. M. K., 1930, University of California Publications on Engineering, Vol. 2, p. 443, Berkeley, CA.

Ultrahigh CHF Prediction for Subcooled Flow Boiling Based on Homogenous Nucleation Mechanism

Wei Liu

Department of Energy Systems, Japan Atomic
Energy Research Institute, Tokai, Ibaraki,
319-1195, Japan
Tel: 81-29-2826428
e-mail: liuwei@hflwing.tokai.jaeri.go.jp

Hideki Nariai

Japan Nuclear Energy Safety Organization,
Tokyo, 105-0001, Japan
e-mail: nariai-hideki@jnes.go.jp

Homogeneous nucleation, although being discounted as a mechanism for vapor formation for water in most conditions, is found to possibly occur under some extreme conditions in subcooled flow boiling. Under the conditions, vapor bubbles of molecular dimensions generated in the superheated liquid adjacent to channel wall from homogeneous nucleation due to the local temperature exceeds homogeneous nucleation temperature. The condition is called in this paper as homogeneous nucleation governed condition. Under the condition, conventional flow pattern for subcooled flow boiling, which is characterized by the existence of Net Vapor Generation (NVG) point and the followed bubble detachment, movement and coalescence processes, cannot be established. Critical heat flux (CHF) triggering mechanism so far proposed, which employs a premise assumption that the conventional flow pattern has been established, such as liquid sublayer dryout model, is no more appropriate for the homogeneous nucleation governed condition. In this paper, first, the existence of the homogeneous nucleation governed condition is indicated. In the following, a criterion is developed to judge a given working condition as the conventional one or the homogeneous nucleation governed one. With the criterion, subcooled flow boiling data are categorized and typical homogeneous nucleation governed datasets are listed. The homogeneous nucleation governed data are characterized by extreme working parameters, such as ultrahigh mass flux, ultralow ratio of heated length to channel diameter (L/D) or ultrahigh pressure. CHF triggering mechanism for the homogeneous nucleation governed condition is proposed and verified. Parametric trends of the CHF, in terms of mass flux, pressure, inlet subcooling, channel diameter, and the ratio of heated length to diameter are also studied. [DOI: 10.1115/1.1844536]

Keywords: Critical Heat Flux, Boiling, Flow, Heat Transfer, Modeling, Two-Phase

1 Introduction and Basic Consideration

Subcooled flow boiling is the boiling that begins and develops even though the mean enthalpy of liquid phase is less than saturation. As is well known, this forced convective boiling is one of the most efficient ways for the removal of high heat flux. It is widely used in high heat flux component such as nuclear reactor cores, accelerator targets, and fusion reactor components. The operating conditions of these systems are restricted to be lower than a heat flux called as Critical Heat Flux (CHF).

The CHF triggering mechanism is considered tightly associated with the flow pattern developed before CHF. For subcooled flow boiling, the most often encountered flow pattern, as shown in Fig. 1(a), is called "conventional flow pattern." The conventional flow pattern is characterized by the existence of the so-called Net Vapor Generation (NVG) point, which is the first bubble detaching point, and the following bubble detachment, movement, and coalescence processes.

However, it does not seem that all the subcooled flow boiling can definitely develop to the conventional flow pattern. As we know, to have the NVG point established, a heat flux that is high enough is needed to be exerted on the tube. With the increase of mass flux, increase of inlet subcooling, decrease of inner diameter or decrease of ratio of heated length to inner diameter (L/D), this heat flux may be so high that under a heat flux that is lower than the heat flux, the wall temperature even reaches homogeneous

nucleation temperature. This will lead to the formation of vapor bubbles due to homogeneous nucleation in the liquid adjacent to the heating wall. The condition is called "homogeneous nucleation governed condition." The corresponding flow pattern is shown in Fig. 1(b). The threshold of the conventional condition and the homogeneous nucleation governed condition is whether the homogeneous nucleation occurs or not at the NVG point, i.e., whether the temperature in the superheated liquid layer adjacent to the channel wall at the first appearance of the NVG point (which occurs at tube exit) reaches homogeneous nucleation temperature or not.

The two conditions imply two different triggering mechanisms for the CHF occurrence. At present, for the subcooled flow boiling, liquid sublayer dryout mechanism [1–5] is the popular CHF triggering mechanism and receiving significant attention. Liquid sublayer dryout mechanism employs a premise assumption that the CHF happens in the downstream region of the NVG point, and is therefore considered being fit only for the conventional flow pattern. Actually, although being very successful, liquid sublayer dryout mechanism was found not being able to give good CHF prediction under some extreme condition, such as extremely high mass flux condition, extremely high pressure condition [5] or low L/D condition (especially when pressure is high) [5–7]. Why the deficiencies occur under these conditions puzzled the present authors greatly in the past several years. Although several reasons were attributed to the deficiencies, the main and basic reason now is considered being due to the conventional flow pattern, which is the base of the liquid sublayer dryout model, cannot be established under those extreme conditions. Far by now, no report on

Contributed by the Heat Transfer Division for publication in the JOURNAL OF HEAT TRANSFER. Manuscript received by the Heat Transfer Division November 24, 2003; revision received November 2, 2004. Review conducted by: M. K. Jensen.

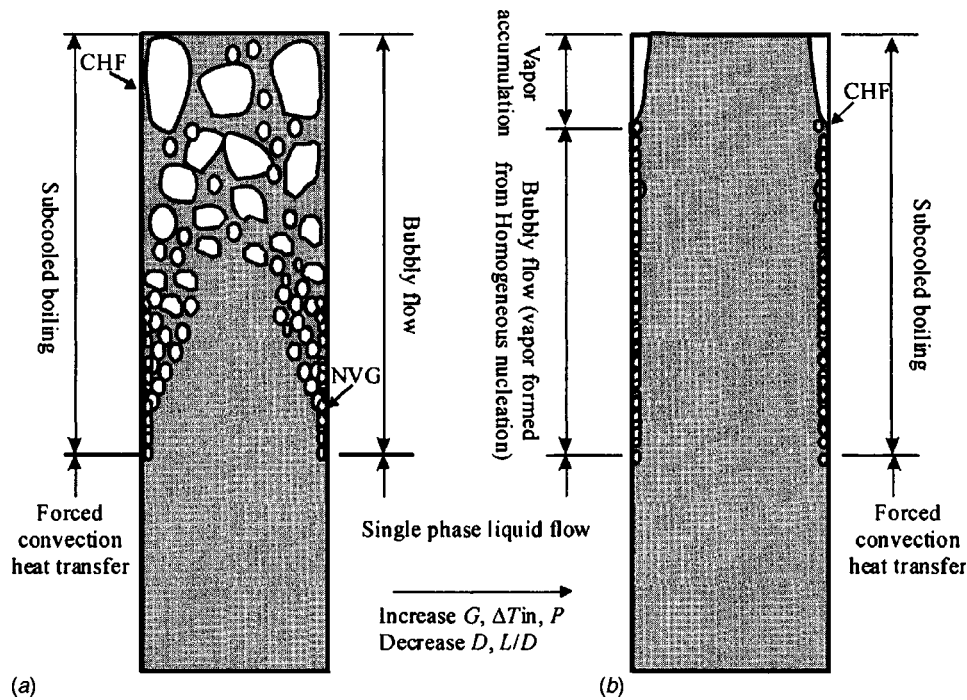


Fig. 1 Flow patterns for subcooled flow boiling. (a) The conventional flow pattern. (b) The homogeneous nucleation governed flow pattern.

the existence of the homogeneous nucleation governed subcooled flow boiling is found and the CHF triggering mechanism for the condition has never been studied separately.

Therefore, the objectives of present paper are:

1. Indicating the existence of the homogeneous nucleation governed condition in subcooled flow boiling. Developing a criterion to judge whether a given working condition is of the conventional flow pattern or the homogeneous nucleation governed one.
2. Proposing the CHF triggering mechanism and prediction method for the homogeneous nucleation governed condition. Verifying the proposed model and studying parametric trends of mass flux, pressure, inlet temperature and L/D on CHF for the homogeneous nucleation governed condition.

2 Criterion for the Judgement of Flow Pattern Development

For the conventional flow pattern, under low heat fluxes up to that needed for the onset of nucleate boiling, single phase liquid flows through the channel. Then, with the increase of heat flux, vapor bubbles due to heterogeneous nucleation appear. However, the formed vapor bubbles, due to high degrees of subcooling, only grow and collapse whilst still attached to the heating surface. This process continues until the NVG point is reached. As shown in Fig. 1(a), the conventional flow pattern is characterized by the existence of the NVG point, and the followed bubble detachment, movement and coalescence processes.

Here we note the heat flux needed for the first appearance of the NVG point (at tube exit) with q_{NVG} . The heat flux is only determined by the given working condition (mass flux G , pressure P , inner diameter D , ratio of heated length to inner diameter L/D , and inlet temperature T_{in}) and can be seen as a characteristic parameter for subcooled flow boiling.

The calculation to q_{NVG} is shown in Appendix A. The q_{NVG} increases with the increase of mass flux, increase of inlet subcooling, decrease of inner diameter, and decrease of L/D .

Under some extreme conditions, the q_{NVG} may be so high that under which, the wall temperature even exceeds (reaches) homogeneous nucleation temperature. This, according to foam limit theory (also called “limit of liquid superheat” or “ultraheat” by Spiegler et al. [8]), will lead to the explosive-like generation of vapor bubbles of molecular dimensions in the liquid adjacent to channel wall. In other words, homogeneous nucleation occurs under a heat flux lower than q_{NVG} at the channel exit due to local temperature of superheated liquid adjacent to the channel wall exceeds homogeneous nucleation temperature. The condition is called the homogeneous nucleation governed condition. The threshold of the two conditions is whether the homogeneous nucleation occurs or not at the NVG point. In other words, whether the temperature of the liquid adjacent to channel wall at q_{NVG} reaches homogeneous nucleation temperature or not.

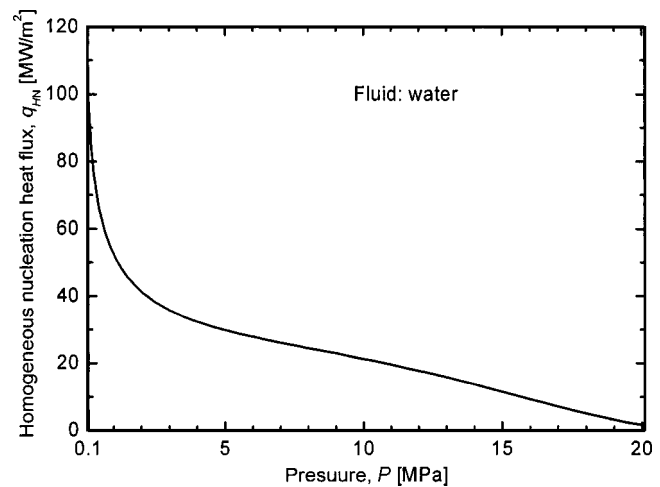


Fig. 2 Relationship between homogeneous nucleation heat flux and pressure

Table 1 Theoretical value of the threshold mass flux that would induce the occurrence of the homogeneous nucleation governed condition (calculated at $D=0.001$ m, $\Delta T_{in}=80^\circ$ C)

| Pressure (MPa) | $L/D=40$ | $L/D=5$ |
|----------------|--|--|
| | Threshold mass flux G_{tr} (kg/m ² s) | Threshold mass flux G_{tr} (kg/m ² s) |
| 0.1 | 198.72×10^3 | 138.37×10^3 |
| 3.1 | 43.32×10^3 | 25.22×10^3 |
| 8.1 | 26.57×10^3 | 15.27×10^3 |
| 15.1 | 9.59×10^3 | 4.96×10^3 |
| 19.1 | 1.74×10^3 | 0.67×10^3 |

The temperature of the liquid adjacent to channel wall, T_1 , is assumed being equal to the wall temperature. That is:

$$T_l = T_w \quad (1)$$

Wall temperature at the NVG point is roughly calculated from Thom correlation [9] [Eq. (2)], which is for the wall temperature estimation for the fully developed boiling (FDB) region. The correlation is reported being good accuracy even under high mass flux and high subcooling condition [10].

$$T_w = T_{SAT} + 22.65 \times (q/1,000,000)^{0.5} \times \exp(-P/8.7) \quad (2)$$

The pressure P in Eq. (2) is in [MPa].

The homogeneous nucleation temperature is calculated from Lienhard [11] correlation [Eq. (3)], where T_{cr} is thermodynamic critical temperature.

$$T_{HN} = T_{SAT} + T_{cr} \times \left(0.923 - \frac{T_{SAT}}{T_{cr}} + 0.077 \left(\frac{T_{SAT}}{T_{cr}} \right)^9 \right) \quad (3)$$

Combining Eqs. (1)–(3), under a certain pressure, there exists a heat flux, under which the temperature of the liquid adjacent to the channel wall just reaches the homogeneous nucleation tempera-

ture. Here we call the heat flux as homogeneous nucleation heat flux and note it with q_{HN} . q_{HN} is calculated from Eq. (4). By rewriting Eq. (4), we get q_{HN} in Eq. (5).

$$T_l = T_{HN} \quad (4)$$

$$q_{HN} = \left(T_{cr} \times \left[0.923 - \frac{T_{SAT}}{T_{cr}} + 0.077 \times \left(\frac{T_{SAT}}{T_{cr}} \right)^9 \right] \times \exp(P/8.7)/22.63 \right)^2 \times 10^6 \quad (5)$$

As we can find from Eq. (5), q_{HN} is only a function of pressure. The relation between q_{HN} and pressure is shown in Fig. 2. q_{HN} decreases significantly with the increase of pressure. If a working condition possesses a q_{NVG} higher than (equal to) the corresponding q_{HN} under the working pressure, wall temperature reaches homogeneous nucleation temperature before (at) the first appearance of the NVG point. The condition then is the homogeneous nucleation governed condition. On the other hand, if a working condition possesses a q_{NVG} lower than the corresponding q_{HN} , at q_{NVG} , wall temperature is lower than the homogeneous nucleation temperature, no vapor bubble due to homogeneous nucleation is generated, and the conventional flow pattern can be established and developed.

Thereby, the following procedures are proposed to judge a given working condition is of the conventional one or the homogeneous nucleation governed one:

1. For the given working condition, calculate q_{NVG} from Appendix A.
2. Compare the calculated q_{NVG} with the corresponding q_{HN} . If $q_{NVG} < q_{HN}$, no homogeneous nucleation occurs and the given working condition is the conventional one. Otherwise, if $q_{NVG} \geq q_{HN}$, homogeneous nucleation occurs before (once) the NVG point is reached. The given working condition is the homogeneous nucleation governed one.

Table 2 Data used for categorization

| Reference | No. of data | $G \times 10^{-3}$ [kg/m ² s] | P [MPa] | D [mm] | L/D | T_{in} [°C] | CHF_{exp} [MW/m ²] |
|---------------------------|-------------|--|------------|----------|---------|---------------|----------------------------------|
| Ornatskii [14] | 68 | 20–90 | 1.0–3.2 | 0.5 | 28 | 1.5–153.7 | 42–224.5 |
| Ornatskii–Vinyarskii [15] | 125 | 10–90 | 1.1–3.2 | 0.4–2.0 | 28 | 6.7–155.6 | 27.9–228 |
| Mayersak et al. [16] | 1 | 44.4 | 2.9 | 11.7 | 50 | 18.0 | 42.8 |
| Schaefer–Jack [17] | 2 | 61.2–61.7 | 1.3–1.5 | 3.05 | 6.25 | 15.6–18.9 | 125–130 |
| Celata et al. [18] | 268 | 2.0–40.0 | 0.1–5.0 | 2.5–8.0 | 12.5–40 | 18.6–80.7 | 4.0–60.6 |
| Vanderfort et al. [19] | 210 | 8.4–42.7 | 0.1–2.3 | 0.3–2.6 | 2.5–26 | 6.4–84.9 | 18.7–124 |
| Mudawar et al. [20] | 174 | 5–134 | 0.34–17.24 | 0.4–2.5 | 2.36–34 | 18–70 | 9.4–276 |
| Inasaka–Nariai [21] | 29 | 4.3–30.0 | 0.3–1.1 | 3 | 33.3 | 25.0–78.0 | 7.3–44.5 |
| Nariai et al. [22] | 95 | 6.7–20.9 | 0.1 | 1.0–3.0 | 3–50 | 15.4–64.0 | 4.6–70.0 |
| Boyd [23–25] | 10 | 4.4–40.5 | 0.77–1.66 | 3 | 96.57 | 20.0 | 6.0–41.5 |
| Achilli et al. [26] | 35 | 4.6–14.9 | 1.0–5.5 | 8.0–15 | 15–20 | 26.4–158 | 11.0–35.6 |
| Gambill–Greene [27] | 7 | 13.0–26 | 0.1 | 7.8 | 9–20 | 4.9–35.8 | 15.8–33.0 |
| Loosmore–Skinner [28] | 202 | 3.0–2.0 | 0.1–0.7 | 0.6–2.4 | 3–50 | 3.2–130.9 | 6.7–44.8 |
| Ornatskii–Kichigan [29] | 117 | 5.0–30.0 | 1.0–2.5 | 2 | 28 | 2.7–204.5 | 6.4–66.6 |
| Knoebel et al. [30] | 376 | 3.9–13.7 | 0.2–0.7 | 9.5 | 64 | 0.3–104.8 | 3.3–11.4 |
| Mirshak et al. [31] | 56 | 4.7–12.2 | 0.2–0.6 | 6.0–11.9 | 41–96 | 4.7–12.2 | 3.9–10.0 |
| Babcock [32] | 57 | 2.4–11.4 | 0.4–8.4 | 7.9–25.4 | 27–75 | 20–242.7 | 4.9–11.8 |
| Burck et al. [33] | 143 | 0.9–3.8 | 1.1–3.1 | 10 | 35 | 16.7–60.8 | 4.5–12.2 |
| Thorgerson [34] | 42 | 4.2–13.4 | 0.5 | 7.8–8.4 | 72.3–78 | 1.1–79.2 | 4.2–12.4 |
| Zeigarnik et al. [35] | 21 | 4.8–20.6 | 0.5–3.0 | 4 | 62.5 | 0.6–134.1 | 9.4–32.6 |
| Gambill et al. [36] | 23 | 7.0–53.0 | 0.1–0.5 | 3.2–7.8 | 6–54 | 8.8–23.9 | 7.0–48.7 |
| Bortoli [12] | 153 | 1.2–10.6 | 3.5–19.3 | 1.9–5.7 | 20–365 | 27–354 | 1.7–13.3 |
| Matzner [37] | 76 | 1.36–18.6 | 7 | 13–37.5 | 26–151 | 116–270 | 3.1–8.1 |
| Lee et al. [38] | 23 | 2.0–4.1 | 3.9–11.3 | 5.6–10.8 | 20–82 | 181–254 | 3.9–7.2 |
| Thompson [39] | 146 | 3.7–10.4 | 3.5–10.5 | 10.3 | 74–77.3 | 201.5–251 | 4.19–9.4 |
| Weatherhead [40] | 9 | 6.5–9.3 | 2.17 | 1.1 | 100 | 102–173 | 4.26–7.3 |
| Weatherhead [41] | 76 | 0.9–2.7 | 14 | 7.7–11.1 | 41.3–59 | 66.5–302 | 2.52–5.3 |
| Hood [42] | 3 | 1.7–2.4 | 7 | 12–23.5 | 26–49 | 162–252 | 3.4–4.9 |
| Chen et al. [43] | 109 | 1.4–13 | 0.16–1.3 | 10–16 | 18–40 | 19–114 | 4.17–10.4 |
| Total | 2656 | 0.9–134 | 0.1–19 | 0.3–37.5 | 2.4–365 | 0.3–354 | 3.3–276 |

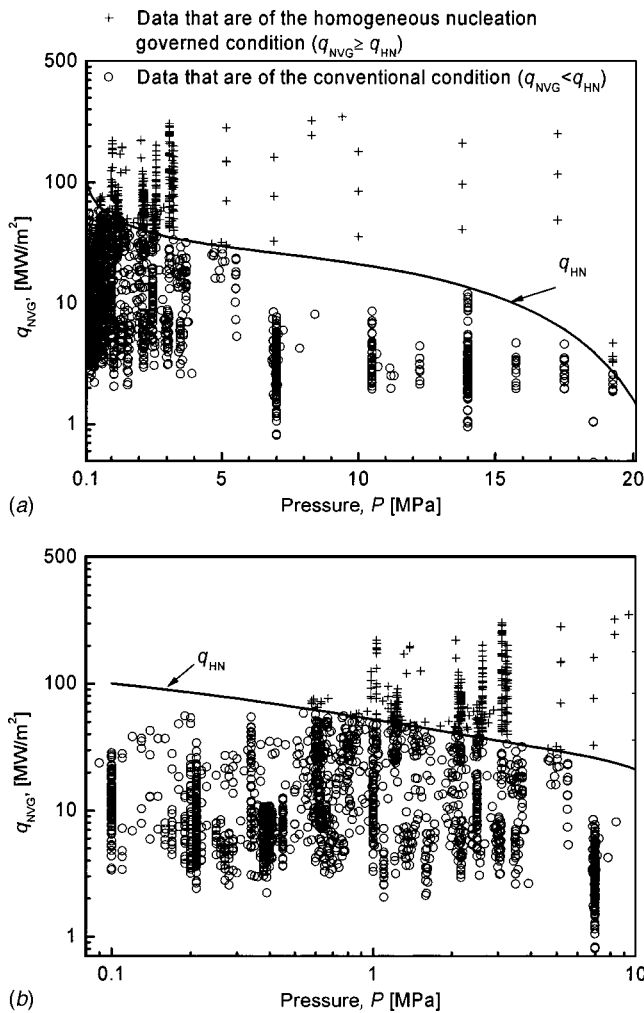


Fig. 3 Categorization to the data shown in Table 2. (a) View to the whole data. (b) Magnification view for the $P < 10$ MPa data.

From the above criterion, any condition that makes q_{NVG} higher (such as increasing G , increasing ΔT_{in} , decreasing L/D or D) or makes q_{HN} lower (such as increasing P) can make the homogeneous nucleation governed condition easily occur. Therefore, the homogeneous nucleation governed subcooled flow boiling is generally characterized by high mass flux, high subcooling, low L/D or high pressure.

As an example, when tube inner diameter $D = 1$ mm and inlet subcooling $\Delta T_{in} = 80^\circ\text{C}$, theoretical order of the threshold mass flux that will induce the occurrence of the homogeneous nucleation governed condition is calculated. The calculation method and the result are shown in Appendix B and Table 1, respectively. At low pressure condition, because q_{HN} is very high (Fig. 2), the homogeneous nucleation governed condition can not be reached until mass flux is extremely high enough (to increase q_{NVG} to reach q_{HN}). As shown in Table 1, in the column that L/D is 40, at low pressure ($P = 0.1$ MPa), the threshold mass flux G_{tr} is as high as $198.72 \times 10^3 \text{ kg/m}^2 \text{ s}$, which is very difficult to be achieved in experiment. This may be the reason why the homogeneous nucleation governed condition is seldom observed and attracts little attention. With the increase of pressure, due to the significant decrease of q_{HN} (Fig. 2), a working condition that is of not so high mass flux, not so high inlet subcooling, and not so low L/D can make the q_{NVG} reach the q_{HN} . In other words, compared to low pressure condition, the homogeneous nucleation governed condition is much easily achieved under high pressure. As shown in Table 1, under a certain L/D , threshold mass flux decreases sig-

nificantly with the increase of pressure. Especially when pressure is near to the critical pressure, the threshold mass flux is very easily reached. This is why some of Bortoli data ([12], up to 19.25 MPa), although being comparatively low mass flux and high L/D (shown in detail in Table 3), are typical homogeneous nucleation governed data.

Besides pressure, inlet subcooling and L/D also play significant roles. Higher inlet subcooling and lower L/D ask for a higher heat flux for the establishment of the NVG point and then result in a higher q_{NVG} . The influence of L/D on the flow pattern development is also observed in Table 1. With pressure maintained unchanged, the decrease of L/D from 40 to 5 decreases the threshold mass flux greatly, which means the homogeneous nucleation governed condition is much easily established at low L/D .

With the criterion, we carried out data categorization to a big database (Table 2). The result is shown in Fig. 3. In the total 2656 data points, with Levy model [13] used for the NVG point calculation, predominant 2252 data possess q_{NVG} lower than the corresponding q_{HN} and fall in the region lower than the q_{HN} curve (region of the conventional condition). And 404 data points are found possessing q_{NVG} higher than q_{HN} and falling in the region above the q_{HN} curve (region of the homogeneous nucleation governed condition). In the data listed in Table 2, several datasets are typical homogeneous nucleation governed data. They are Bortoli data ([12], extremely high pressure (up to 19.25 MPa) data), Ornatkii et al. data ([14,15], extremely high mass flux (up to 90,000 $\text{kg/m}^2 \text{ s}$) data), Mayersak data ([16], high mass flux data) and Schaefer-Jack data ([17], high mass flux and low L/D data). Besides, some of Celata [18] and Vanderfort [19] data are also found being the homogeneous nucleation governed data. Recently, Mudawar's experiment for achieving ultrahigh CHF [20] [extremely high mass flux (up to 134,000 $\text{kg/m}^2 \text{ s}$) and high pressure (up to 17.24 MPa) data] also supplies us with a homogeneous nucleation governed data source.

Pressurized water reactor (PWR) and high heat flux components of fusion reactors are very important components that use the characteristics of subcooled flow boiling CHF. Operating conditions of experimental CHF research relevant to the PWR, i.e. intermediate to high pressure (7–15 MPa), low to intermediate mass velocity (up to 10 m/s), low to intermediate inner diameter (1–35 mm), and high L/D , are found generally being the conventional one, whose CHF can be well predicted from liquid sublayer dryout model [5]. While operating conditions of experimental CHF research relevant to the fusion reactor, i.e. low to intermediate pressure (up to 5 MPa), high mass velocity (up to 130 m/s), high liquid subcooling (up to 200 K), small to intermediate channel diameter (0.3–3 mm), and low L/D (2–20), which always results in ultrahigh CHF (30–276 MW/m^2), are found easily falling in the homogeneous nucleation governed region. The CHF triggering mechanism and prediction for the conditions will be discussed in the next section.

One thing needs specifying here is that, because the Thom correlation is only an empirical approximation for the prediction of channel wall temperature, the curve q_{HN} shown in Figs. 2 and 3 is considered only giving an approximate conception for distinguishing the conventional and the homogeneous nucleation governed conditions. Actually, the CHF of some points near the curve with falling in the region just above the q_{HN} curve (Fig. 3) can be predicted quite well from the liquid sublayer dryout model [5]. Therefore, only the data that falling in the region above the q_{HN} curve with enough surpluses are considered being typical homogeneous nucleation governed data.

3 CHF Triggering Mechanism and Prediction for the Homogeneous Nucleation Governed Subcooled Flow Boiling Condition

In Sec. 2, a criterion has been developed to judge a subcooled flow boiling working condition is of the conventional one or the homogeneous nucleation governed one. For the conventional one,

CHF triggering mechanism can be well explained from liquid sublayer dryout model [3,5]. The liquid sublayer dryout model assume CHF occurring in the afterward region of the NVG point and being triggered by the complete dryout of liquid sublayer beneath a vapor blanket, which is formed as a consequence of coalescence of small bubbles rising along the near wall region. The CHF for the condition, then is characterized by the observations to obvious net vapor generation region and comparatively big vapor bubbles.

This section will focus on the research to the CHF triggering mechanism and CHF prediction for the homogeneous nucleation governed condition.

As mentioned in Sec. 2, the homogeneous nucleation governed condition is the condition that homogeneous nucleation occurs before the conventional NVG point is ever established in the channel. The vapor bubbles formed from homogeneous nucleation, just like those formed from conventional heterogeneous nucleation, are affected greatly by its surrounded fluid's thermohydraulic condition. As the homogeneous nucleation governed condition is generally accompanied by high mass flux and high degree of subcooling, vapor bubbles are easily condensed and collapse on its originating point. The process corresponds to the bubbly flow region shown in Fig. 1(b). It continues until a point (axial elevation), whose thermohydraulic condition allows vapor bubbles of molecular dimensions surviving and growing, is reached. Whereas once this point is reached, a quick accumulation of vapor bubbles that formed explosively from the homogeneous nucleation will occur. As the high-density vapor bubble accumulation consequently results in the deterioration of the heat transfer coefficient, the occurrence of the vapor bubble accumulation is assumed being the CHF triggering mechanism.

In other words, CHF for the homogeneous nucleation governed condition is triggered when the following two conditions are met:

1. The highest wall temperature (usually at tube exit) exceeds the homogeneous nucleation temperature. This guarantees vapor bubbles of molecule dimensions can be formed from homogeneous nucleation. This asks a heat flux that is higher than q_{HN} is exerted on tube:

$$CHF \geq q_{HN} \quad (6)$$

2. The formed vapor bubbles of molecule dimensions are in the region whose thermohydraulic condition allows them surviving and growing to cause bubble accumulation. In the conventional flow pattern, this region is identified as the downstream region of the NVG point. Because the homogeneous nucleation occurs only in a very thin liquid superheated layer adjacent to channel wall and the bubble generated from homogeneous nucleation is much smaller than that generated from the heterogeneous one, homogeneous nucleated bubbles at the traditional NVG point then locate in a more near wall superheated layer than heterogeneous nucle-

ated bubbles do, and thereby are considered being able to survive and grow. In other words, the region that the homogeneous nucleated bubbles can survive and grow is roughly taken as that for the heterogeneous nucleated vapor bubbles in the conventional condition: the downstream region of the NVG point. With this assumption, the CHF is confined being not lower than q_{NVG} :

$$CHF \geq q_{NVG} \quad (7)$$

Combining Eqs. (6) and (7), CHF for the homogeneous nucleation governed condition is calculated from:

$$CHF = \max(q_{HN}, q_{NVG}) \quad (8)$$

As for the homogeneous nucleation governed condition, $q_{HN} \leq q_{NVG}$ is always working, CHF then can be calculated from:

$$CHF = q_{NVG} \quad (9)$$

From the above assumed mechanism, the CHF for the homogeneous nucleation governed condition should be characterized by (1) not obvious net vapor generation; (2) very small vapor bubbles. These are in good agreements with that observed in ultrahigh mass flux (up to 134,000 kg/m²s) CHF [20].

4 Verification of the Proposed Model

To calculate CHF for a given subcooled flow boiling working condition, we need first determine the condition is a conventional one or a homogeneous governed one. For the conventional one, calculate CHF from liquid sublayer dryout model [3,5]. Otherwise, for the homogeneous nucleation governed working condition, calculate CHF from Eq. (9).

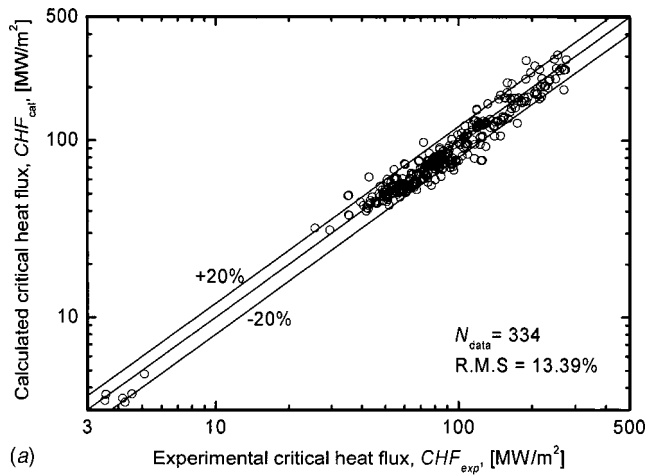
Table 3 lists datasets that are used for the verification of the new model for the homogeneous nucleation governed working condition. The data are gathered through a selection to ensure they are typical homogeneous nucleation governed data.

Verification results are shown in Fig. 4. Figure 4(a) shows calculated CHF versus experimental CHF and Fig. 4(b) shows the percentages of data points within a given error band (%) against error band. Here error band is defined as $(CHF_{cal}/CHF_{exp} - 1)$. About 98% of data are predicted within the error band of $\pm 35\%$.

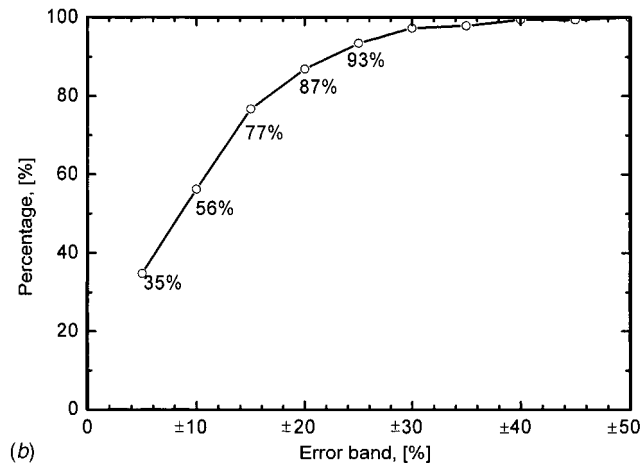
The average and standard deviation of ECHFR (Experimental Critical Heat Flux Ratio, $= CHF_{cal}/CHF_{exp}$) to the whole data (334 data points) are 0.96 and 12.8%, respectively. The RMS is 13.4%.

Table 3 Data used for the verification of the CHF model proposed for the homogeneous nucleation governed condition

| Reference | No. of data | $G \times 10^{-3}$ [kg/m ² s] | P [MPa] | D [mm] | L/D | T_{in} [°C] | CHF [MW/m ²] |
|-----------------------|-------------|--|--------------|-----------------------------------|------------|---------------|--------------------------|
| Bortoli [12] | 6 | 2.05–3.78 | 19.25 | 1.9 | 80, 365 | 215–288, 35 | 3.53–5.11 |
| Ornatskii et al. [14] | 50 | 40, 50, 60, 90 | 0.98–3.25 | 0.5 | 28 | 18–153 | 41.9–224.5 |
| Ornatskii et al. [15] | 100 | 30, 40, 50, 60, 90 | 1.14–3.2 | 0.4, 0.5, 0.6, 0.8, 1.0, 1.5, 2.0 | 28 | 15.8–155.6 | 35.5–227 |
| Mayersak [16] | 1 | 44.4 | 2.89 | 11.7 | 50 | 18 | 48.24 |
| Schaefer–Jack [17] | 2 | 61.2, 61.7 | 1.52, 1.34 | 3.0, 3.0 | 6.25, 6.25 | 15.6, 18.9 | 130, 126 |
| Celata [18] | 19 | 10–40 | 1.2–5.0 | 2.5–8 | 12.5–40 | 30–70 | 25.7–54.4 |
| Vandervort [19] | 55 | 21.4–41.8 | 0.59–2.28 | 0.3–2.4 | 2.34–25 | 7–81 | 48–123 |
| Mudawar [20] | 5 | 5, 15, 40 | 13.79, 17.24 | 0.9 | 5.76–6.54 | 25–28 | 35–159 |
| | 33 | 16.1–134 | 1.03–10 | 0.4, 0.9 | 6.32–25.86 | 23–40 | 47.5–270 |
| | 58 | 20–130 | 3.1 | 0.5, 1.1, 2.5 | 2.36–30 | 22–29 | 46–276 |
| Ornatskii [29] | 5 | 20, 30 | 2.5 | 2.0 | 28 | 17.3–80.5 | 51–63 |
| Total | 334 | 2.05–134 | 0.98–19.25 | 0.4–11.7 | 2.36–365 | 15.6–288 | 3.53–276 |



(a)



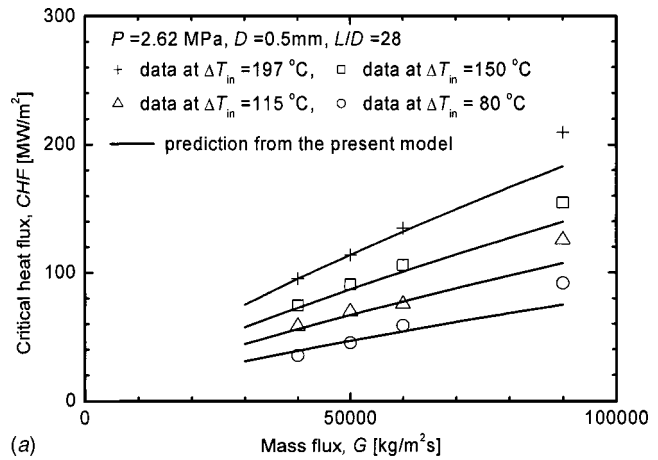
(b)

Fig. 4 Verification to the proposed CHF model for the homogeneous nucleation condition. (a) Calculated CHF versus exp. CHF for the data shown in Table 3. (b) Predicted data percentage versus error band.

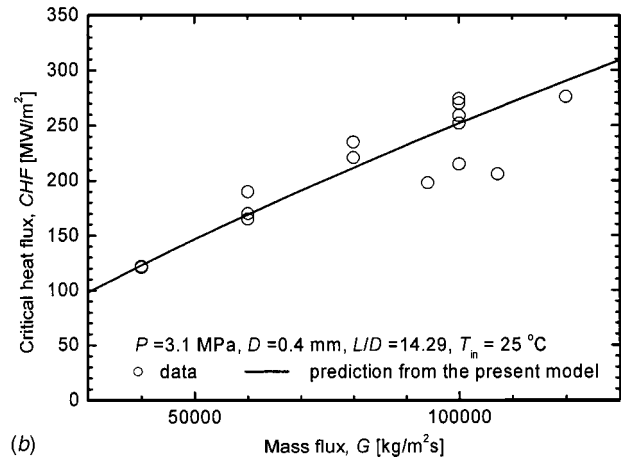
5 Parametric Trends for the Homogeneous Nucleation Governed Subcooled Flow Boiling

Due to the different CHF triggering mechanisms, parametric trends on CHF exhibited in the conventional condition and homogeneous nucleation governed condition should be somewhat different. At low-pressure (for example, at atmospheric pressure) condition, because the homogeneous nucleation governed condition is very difficult to be reached, observed parametric trends are almost all those for the conventional one. But at high pressure, especially when pressure is near to the critical one, parametric trends of the homogeneous nucleation governed condition show out.

Parametric trends for the conventional condition have been researched a lot [3,5]. Except the L/D effect, the parametric trends for the homogeneous nucleation governed condition are found quite similar to those for the conventional one. As shown in Figs. 5–9, where solid lines are predicted CHF from the present new model and discrete points are experimental CHF, the trends can be concluded as follows: The CHF is an increasing (almost linear) function of mass flux and coolant subcooling. The influence of the pressure on the CHF is found being very small when inlet subcooling is used as a parameter. The effects of the inner diameter and L/D are to decrease the CHF as they increase. But unlike the effect of L/D for the conventional condition (which shows a threshold effect that inside the threshold the effect of L/D is very significant while beyond the threshold the influence of L/D is



(a)



(b)

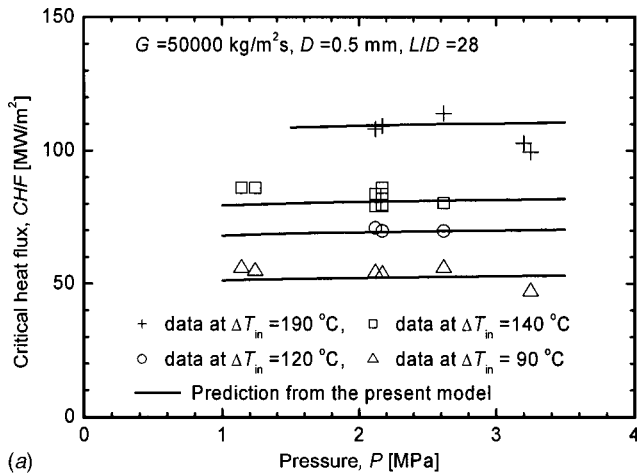
Fig. 5 Comparison of prediction with experimental data (effect of mass flux on CHF). (a) Compared with Ornatkii data [15]. (b) Compared with Mudawar data [20].

small [3,5]), for the homogeneous nucleation governed condition, L/D affect CHF almost inverse linearly. In Fig. 9, L/D effects are shown in a comparatively low value range. This is due to the homogeneous nucleation governed condition is generally accompanied by low L/D condition. The comparison of the new model with experimental data through Figs. 5–9 also show the proposed model being significant CHF prediction accuracy for the homogeneous nucleation governed condition.

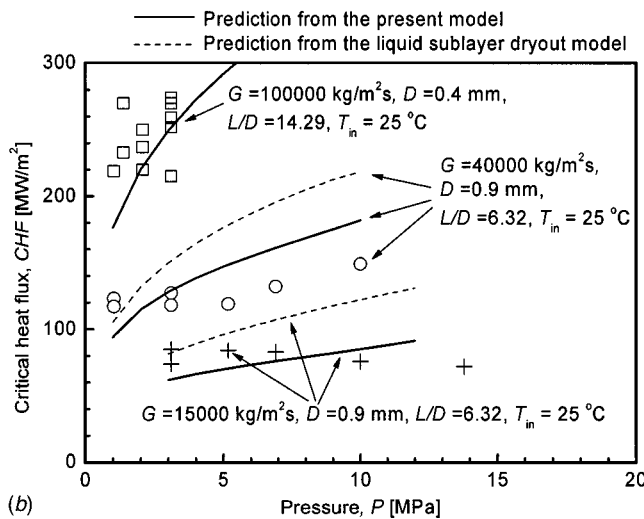
In the above figures, the prediction from the liquid sublayer dryout model [5], if it is predictable, is shown by a broken line as well. The liquid sublayer dryout model, as that shown in Fig. 6(b) (two cases) and Fig. 9(a) (1 case), shows very high CHF predictions for the typical homogeneous nucleation governed condition. This trend turns more obvious with the increases of pressure and the decrease of the L/D ratio (more typical homogeneous nucleation governed condition).

6 Discussion on the Relationship Between the Popular Liquid Sublayer Dryout Mechanism and Present Homogeneous Nucleation Mechanism

(1) The liquid sublayer dryout model by the present authors [5], although has succeeded a lot in CHF prediction, was also reported deficiencies under some extreme operating condition [5]. Concretely, at low L/D , it shows an overprediction tendency,



(a)



(b)

Fig. 6 Comparison of prediction with experimental data (effect of pressure on CHF). (a) Compared with Ornatskii data [14,15]. (b) Compared with Mudawar data [20].

which turns much obvious with the increase of pressure. And at some ultrahigh mass flux or ultrahigh pressure conditions, it is unable to predict the CHF unless some modification is done to D_B , the equivalent diameter of vapor blanket. As reported in Ref. [5], with the modification, the predicted CHF is actually the heat flux needed for the establishment of the NVG point at the tube exit, i.e., q_{NVG} . The predicted accuracy from q_{NVG} was found being astonishingly good.

As we can find, the data for which the liquid sublayer dryout model shows deficiency have almost the same characteristics as the homogeneous nucleation governed condition. The reason why the CHF for some high mass flux or high pressure data cannot be predicted from the liquid sublayer dryout model is due to the conventional flow pattern, which is the base for applying the liquid sublayer dryout model, can not be established under those conditions. On the other hand, the reason that the CHF under the conditions can be well predicted from the liquid sublayer dryout model by doing a modification to D_B , is due to the predicted CHF is q_{NVG} , which, in Sec. 3, is reported can be used for CHF calculation for the homogeneous nucleation governed condition. Thereby, the deficiencies reported in Ref. [5] are not due to the deflection of the liquid sublayer dryout model itself, but due to the base of the model, the conventional subcooled flow pattern, can not be established. Actually, at the time the model [5] was proposed, the present authors still had no knowledge on the existence of the homogeneous nucleation governed condition. Therefore no

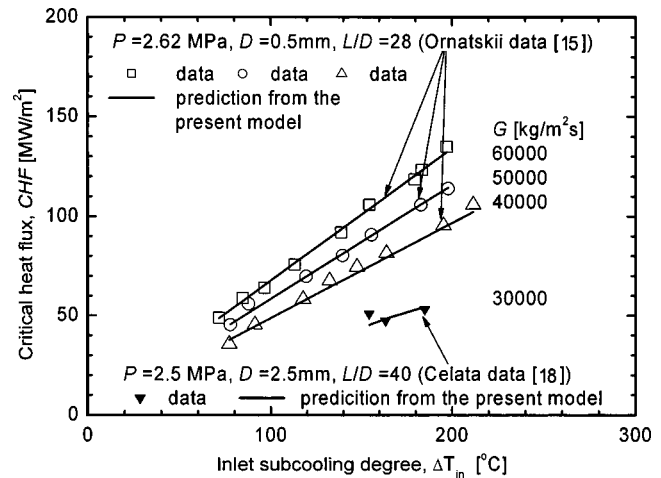


Fig. 7 Comparison of prediction with experimental data (Ornatskii data [15], Celata data [18]). (Effect of inlet subcooling on CHF.)

data categorization was carried out to ensure that the data used in the verification were of the conventional condition.

Therefore, indicating the existence of the homogeneous nucleation governed condition and proposing the new CHF model is not a contradiction to the liquid sublayer dryout model. From another side, it supports and complements the liquid sublayer dryout model, while reminding us of the existence of the homogeneous nucleation governed area, for which the liquid sublayer dryout model is no longer fit.

(2) In Sec. 3, we took the downstream region of the traditional NVG point as the region where homogeneous nucleated vapor bubbles can survive and grow. Actually, this may be a very rough modeling for the real condition. In future, a stricter model for the accumulation of the homogeneous nucleated bubbles, based on present popular near wall bubble crowding model [6,44–47], is considered being necessary.

7 Concluding Remarks

Homogeneous nucleation governed condition, which is characterized by the occurrence of homogeneous nucleation before the NVG point can be ever established, is found to theoretically exist for the subcooled flow boiling. In this paper, first, the existence of the homogeneous nucleation governed condition was indicated. Then, a criterion was developed to judge a given working condi-

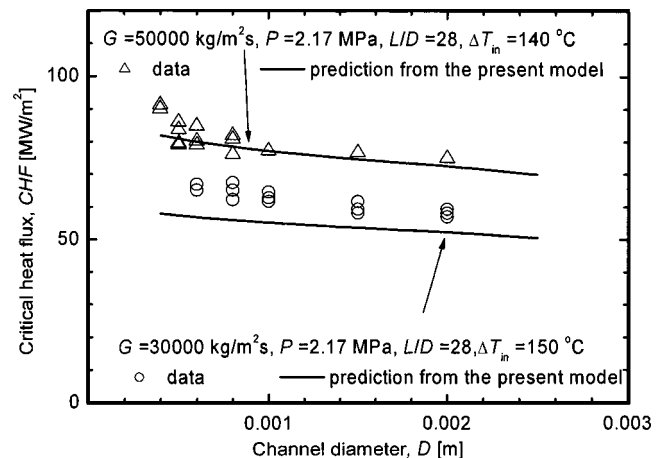
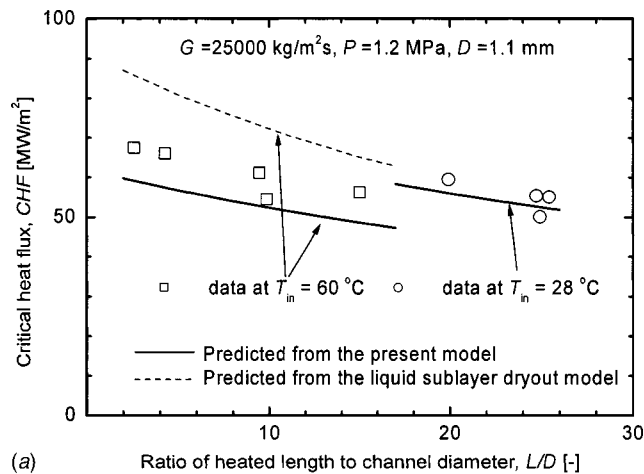
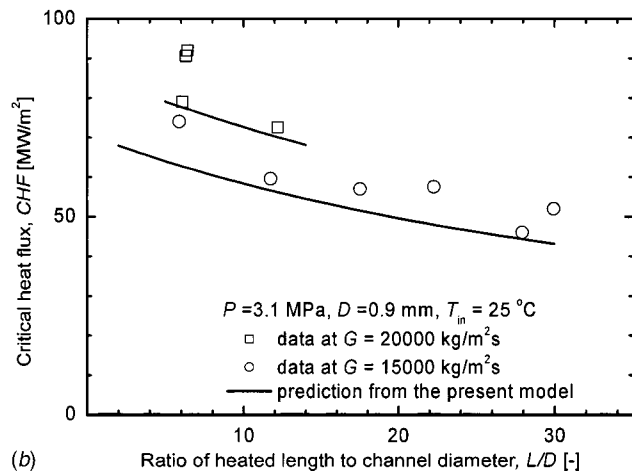


Fig. 8 Comparison of prediction with experimental data (Ornatskii data [15]). (Effect of inner diameter on CHF.)



(a) Ratio of heated length to channel diameter, L/D [-]



(b) Ratio of heated length to channel diameter, L/D [-]

Fig. 9 Comparison of prediction with experimental data. (Effect of L/D on CHF.) (a) Compared with Vandervort data [19]. (b) Compared with Mudawar data [20].

tion was the conventional one or the homogeneous nucleation governed one. With the criterion, subcooled flow boiling data were categorized. In the total 2656 data points, predominantly 2252 data points were found being the conventional condition and 404 data points were of homogeneous nucleation governed condition. The homogeneous nucleation governed data were characterized by extreme working parameters, such as ultrahigh mass flux (up to 134,000 kg/m² s), ultralow L/D (down to 2.36) or ultrahigh pressure (up to 19.25 MPa).

For the homogeneous nucleation governed condition, a new CHF triggering mechanism was proposed: the vapor bubbles generated from homogeneous nucleation, if locating in a thermohydraulic environment that the bubbles could survive, would cause quick and explosive-like high-density vapor accumulation. This occurrence of accumulation of high-density vapor bubbles was assumed being the new CHF triggering mechanism. The downstream region of the traditional NVG point was roughly taken as the region where the homogeneous nucleated vapor bubbles could survive and grow. The value of the CHF could be approximately calculated from q_{NVG} , which is the heat flux that is needed for the first appearance of the NVG point at the tube exit. The model was verified with typical homogeneous nucleation governed datasets. The R.M.S. to the whole collected data (334 points) was 13.4%. The average and standard deviation of ECHFR to the whole data were 0.96 and 12.8%, respectively.

Parametric trends of the CHF for the homogeneous nucleation governed condition, in terms of mass flux, pressure, subcooling, channel diameter, and ratio of heated length to diameter (L/D), were studied with compared to experimental data. Except the effect of L/D , the parametric trends of the CHF for the homogeneous nucleation governed condition were quite similar to those for the conventional condition. The trends could be concluded as that: the CHF is an increasing (almost linear) function of mass flux and coolant subcooling. The influence of pressure on CHF, when inlet subcooling is used as a parameter, is very small. The effect of inner diameter is to decrease the CHF as it increases. Unlike the effect of L/D for the conventional condition, which shows a threshold effect that inside the threshold the effect of L/D is very significant while beyond the threshold the influence of the L/D is small, for the homogeneous nucleation governed condition, L/D affects CHF almost inverse linearly.

Nomenclature

Latin Symbols

- C_P = specific heat at constant pressure, [J/kg K]
- CHF = critical heat flux, [W/m²]
- D = channel inner diameter, [m]
- D_B = equivalent diameter of vapor blanket in liquid sublayer dryout model, [m]
- ECHFR = Experimental Critical Heat Flux Ratio, = CHF_{cal}/CHF_{exp}
- f = friction factor
- FDB = Fully Developed Boiling region
- g = gravitational acceleration, [m/s²]
- G = mass flux, [kg/m² s]
- G_{tr} = threshold mass flux that will induce the occurrence of the homogeneous nucleation governed condition, [kg/m² s]
- H_{ld} = liquid enthalpy at the NVG point, [J/kg]
- H_{in} = liquid enthalpy at channel inlet, [J/kg]
- H_f = liquid saturation enthalpy, [J/kg]
- H_{fg} = latent heat of vaporization, [J/kg]
- h_1 = Dittus-Boelter turbulent heat transfer coefficient
- k = thermal conductivity, [W/mK]
- L = heated length, [m]
- L/D = ratio of heated length to inner diameter
- NVG = Net Vapor Generation point, which is the point that the first bubble detaches
- P = system pressure, [Pa]
- Pr = Prandtl number
- q = heat flux exerted on tube, [W/m²]
- q_{HN} = homogeneous nucleation heat flux, [W/m²]
- q_{NVG} = heat flux needed for the NVG established at channel exit, [W/m²]
- T_{in} = liquid temperature at channel inlet, [°C]
- T_B = temperature at the tip of the bubble in Levy NVG model, [°C]
- T_B^+ = nondimensional temperature at the tip of the vapor bubble in Levy NVG model
- T_{cr} = thermodynamic critical temperature, [°C]
- T_{HN} = homogeneous nucleation temperature, [°C]
- T_1 = temperature of liquid adjacent to channel wall, [°C]
- T_{SAT} = saturation temperature, [°C]
- T_w = wall temperature, [°C]
- ΔT_d = liquid subcooling at the NVG point, [°C]
- ΔT_{in} = liquid subcooling at channel inlet, [°C]
- ΔT_{sat} = wall superheat, $\Delta T_{\text{sat}} = T_w - T_{\text{SAT}}$, [°C]
- u^* = friction velocity, [m/s]
- Y_B = distance from wall to the tip of the vapor bubble in Levy NVG model, [m]
- Y_B^+ = nondimensional distance to the tip of the vapor bubble in Levy NVG model
- Z_0 = distance from channel inlet to the NVG point, [m]

Greek Symbols

- ρ = density, [kg/m³]
 σ = surface tension, [N/m]
 τ_w = wall shear stress, [Pa]
 μ = viscosity, [kg/ms]

Subscripts

- d = at net vapor generation point
in = channel inlet
l = liquid at subcooled condition
f = liquid at saturation
SAT = at saturation

Appendix A: Calculation to q_{NVG}

q_{NVG} , the heat flux needed for the NVG establishment at channel exit, is calculated from the following iterative procedures:

(1) Assume a heat flux q . At the heat flux, calculate ΔT_d from Levy [17] model.

$$\Delta T_d = q \left(\frac{1}{h_l} - \frac{T_B^+}{C_{pf} \rho_f u^*} \right) \quad (10)$$

where h_l is calculated from:

$$h_l = 0.023 \times \left(\frac{k_f}{D} \right) \left(\frac{GD}{\mu_f} \right)^{0.8} \left(\frac{C_{pf} \mu_f}{k_f} \right)^{0.4} \quad (11)$$

T_B^+ is calculated from:

$$\begin{cases} T_B^+ = \text{Pr}_f Y_B^+ & 0 \leq Y_B^+ \leq 5 \\ T_B^+ = 5 \left\{ \text{Pr}_f + \ln \left[1 + \text{Pr}_f \left(\frac{Y_B^+}{5} - 1 \right) \right] \right\} & 5 \leq Y_B^+ \leq 30 \\ T_B^+ = 5 \left[\text{Pr}_f + \ln(1 + 5 \text{Pr}_f) + 0.5 \ln \left(\frac{Y_B^+}{30} \right) \right] & Y_B^+ > 30 \end{cases} \quad (12)$$

$$Y_B^+ = \frac{Y_B u^* \rho_f}{\mu_f}, \quad \text{where } u^* = \sqrt{\tau_w / \rho_f}$$

$$Y_B = 0.015 \left(\frac{\sigma D}{\tau_w} \right)^{1/2}, \quad \text{where } \tau_w = \frac{f G^2}{8 \rho_f}$$

(2) Calculate Z_0 , the length from channel inlet to the NVG point, from:

$$Z_0 = \frac{G \times (H_{\text{ld}} - H_{\text{lin}}) \times D}{4 \times q} \quad (13)$$

where H_{ld} and H_{lin} are liquid enthalpy at the NVG point and inlet, respectively.

(3) Compare Z_0 with heated length L :

If Z_0 is close enough to L , stop calculation. The calculated q is q_{NVG} .

Else increase (if $Z_0 > L$) or decrease (if $Z_0 < L$) the heat flux q and repeat the above (1)–(3) procedures.

Appendix B: Calculation to Threshold Mass Flux G_{tr}

Under a given pressure, inlet temperature, inner diameter, and L/D ratio, threshold mass flux is calculated from the following iterative procedures:

1. Assume a threshold mass flux G_{tr} ;
2. Under G_{tr} , calculates q_{NVG} from Appendix A;
3. Calculate q_{HN} from Eq. (5);
4. If q_{NVG} is close enough to q_{HN} , the assumed G_{tr} is the calculated threshold mass flux.

Else increase (if $q_{\text{NVG}} < q_{\text{HN}}$) or decrease (if $q_{\text{NVG}} > q_{\text{HN}}$) G_{tr} and repeat the above (1)–(4) procedures.

References

- [1] Lee, C. H., and Mudawar, I., 1988, "A Mechanism Critical Heat Flux Model for Subcooled Flow Boiling on Local Bulk Flow Conditions," *Int. J. Multiphase Flow*, **14**, pp. 711–728.
- [2] Katto, Y., 1992, "A Prediction Model of Subcooled Water Flow Boiling CHF for Pressure in the Range 0.1–20.0 MPa," *Int. J. Heat Mass Transfer*, **35**, pp. 1115–1123.
- [3] Celata, G. P. et al., 1994, "Rationalization of Existing Mechanistic Models for the Prediction of Water Subcooled Flow Boiling Critical Heat Flux," *Int. J. Heat Mass Transfer*, **37**, Suppl. 1, pp. 347–360.
- [4] Sudo, Y., 1996, "Analytical Study on Characteristics of Critical Heat Flux Under High Subcooling and High Velocity Condition," *Trans. Jpn. Soc. Mech. Eng.*, Ser. B, **62**, pp. 311–318 (in Japanese).
- [5] Liu, W., Nariai, H., and Inasaka, F., 2000, "Prediction of Critical Heat Flux for Subcooled Flow Boiling," *Int. J. Heat Mass Transfer*, **43**, pp. 3371–3390.
- [6] Kinoshita, H., Nariai, H., and Inasaka, F., 1998, "Modeling of the Subcooled Flow Boiling CHF in Short Tubes," *ICONE6-6420*.
- [7] Kureta, M., Mishima, K., and Nishihara, H., 1995, "Critical Heat Flux for Flow Boiling of Water in Small Diameter Tubes Under Low-Pressure Condition," *Trans. Jpn. Soc. Mech. Eng.*, Ser. B, **61**, pp. 4109–4116 (in Japanese).
- [8] Spiegler, P. et al., 1963, "Shorter Communications: Onset of Stable Film Boiling and the Form Limit," *Int. J. Heat Mass Transfer*, **6**, pp. 987–989.
- [9] Thom, J. R. S., Walker, W. M. et al., 1965, "Boiling in Subcooled Water During Flow Up Heated Tubes or Annuli. Paper 6 Presented at the Symposium on Boiling Heat Transfer in Steam Generation Units and Heat Exchangers Held in Manchester," *IMECHE (London)*.
- [10] Celata, G. P. et al., 1997, "Experimental Evaluation of the Onset of Subcooled Flow Boiling at High Liquid Velocity and Subcooling," *Int. J. Heat Mass Transfer*, **40**, pp. 2879–2885.
- [11] Lienhard, J. H., 1986, "Corresponding States Correlations of the Spindale and Homogeneous Nucleation Limits," *ASME J. Heat Transfer*, **104**, pp. 379–381.
- [12] Bortoli, D. et al., 1958, "Forced Convection Heat Transfer Burnout Studies for Water in Rectangular Channels and Round Tubes at Pressures Above 500 psia," *WAPD-188*.
- [13] Levy, S., 1967, "Forced Convection Subcooled Boiling Prediction of Vapor Volumetric Fraction," *Int. J. Heat Mass Transfer*, **10**, pp. 951–965.
- [14] Ornatkii, A. P., 1960, "The Influence of Length and Tube Diameter on Critical Heat Flux for Water With Forced Convection and Subcooling," *Teploenergetika*, **4**, pp. 67–69.
- [15] Ornatkii, A. P., and Vinyarskii, L. S., 1965, "Heat Transfer Crisis in a Forced Flow of Underheated Water in Small-Bore Tubes," *High Temp.*, **3**, pp. 444–451.
- [16] Mayersak, J., Raezer, S. D., and Bunt, E. A., 1964, "Confirmation of Gambill-Greene Straight Flow Burnout Heat Flux Equation at High Flow Velocity," *ASME J. Heat Transfer*, **86**, pp. 420–425.
- [17] Schaefer, J. W., and Jack, J. R., 1962, "Investigation of Forced-Convection Nuclear Boiling of Water for Nozzle Cooling at Very High Flux," *Technical Note D-1214, NASA*.
- [18] Celata, G. P. et al., 1994, "Assessment of Correlation and Models for the Prediction of CHF in Subcooled Flow Boiling," *Int. J. Heat Mass Transfer*, **37**, pp. 237–255.
- [19] Vandervort, C. L., Bergles, A. E., and Jensen, M. K., 1992, "The Ultimate Limits of Forced Convective Subcooled Boiling Heat Transfer," *RPI Interim Report No. HTL-9 DE-FG02-89ER 14019*.
- [20] Mudawar, I. et al., 1999, "Ultra-high Critical Heat Flux (CHF) for Subcooled Water Flow Boiling-I: CHF Data and Parametric Effects for Small Diameter Tubes," *Int. J. Heat Mass Transfer*, **42**, pp. 1405–1428.
- [21] Inasaka, F., and Nariai, H., 1989, "Critical Heat Flux of Subcooled Flow Boiling With Water," *Proceedings of the NURETH-4*, Vol. 1, pp. 115–120.
- [22] Nariai, H., Inasaka, F., and Shimura, T., 1987, "Critical Heat Flux of Subcooled Flow Boiling in Narrow Tube," in *Proceedings of the 1987 ASME-JSME Thermal Engineering Joint Conference*, pp. 455–462.
- [23] Boyd, R. D., 1988, "Subcooled Water Flow Boiling Experiments Under Uniform High Flux Conditions," *Fusion Technol.*, **13**, pp. 121–142.
- [24] Boyd, R. D., 1989, "Subcooled Water Flow Boiling at 1.66 MPa Under Uniform High Flux Conditions," in *Proceedings of the ASME Winter Annual Meeting, HTD*, Vol. 119, pp. 9–15.
- [25] Boyd, R. D., 1990, "Subcooled Water Flow Boiling Transition and the L/D Effect on CHF for a Horizontal Uniformly Heated Tube," *Fusion Technol.*, **18**, pp. 317–324.
- [26] Achilli, A., Cattadori, G., and Gaspari, G. P., 1992, "Subcooled Burnout in Uniformly and Nonuniformly Heated Tubes," *European two-phase flow group meeting, paper C2, Stockholm, June*, pp. 1–3.
- [27] Gambill, W. R., and Greene, N. D., 1958, "Boiling Burnout With Water in Vortex Flow," *Chem. Eng. Prog.*, **54**, pp. 68–76.
- [28] Loosmore, C. S., and Skinner, B. C., 1965, "Subcooled Critical Heat Flux for Water in Round Tube," *S.M. thesis, Massachusetts Institute of Technology, Cambridge, Massachusetts*.
- [29] Ornatkii, A. P., and Kichigan, A. M., 1962, "Critical Heat Loads in High-Pressure Boiling of Underheated Water in Small Diameter Tubes," *Teploenergetika*, **9**(6), pp. 44–47.
- [30] Knobel, D. H., Harris, S. D., Jr., Crain, B., and Biderman, R. M., 1973, "Forced-Convection Subcooled Critical Heat Flux," *DP-1306, E.I. Dupont de Nemours and Company, February*.
- [31] Mishak, S., Durant, W. S., and Towell, R. H., 1959, "Heat Flux at Burnout," *DP-35, E.I. Dupont de Nemours and Company*.

- [32] Babcock, D. F., 1962, "Heavy Water Moderated Power Reactors," DP-725, E.I. Dupont de Nemours and Company.
- [33] Burck, E., and Hufschmidt, W., 1965, EUR-2432 d, Euratom.
- [34] Thorgerson, E. J., 1969, "Hydrodynamic Aspect of the Critical Heat Flux in Subcooled Convection Boiling," Ph.D. thesis, University of South Carolina.
- [35] Zeigarnik, Y. A., Privalov, N. P., and Klimov, A. L., 1981, "Critical Heat Flux With Boiling of Subcooled Water in Rectangular Channels With One-Sided Supply of Heat," *Teplotenergetika*, **28**(1), pp. 48–51; *Thermal Engineering*, **28**, pp. 40–43.
- [36] Gambill, W. R., Bundy, R. D., and Wansbrough, R. W., 1961, "Heat Transfer, Burnout and Pressure Drop for Water for Swirl Flow Through Tubes With Internal Twisted Tapes," *Chem. Eng. Prog., Symp. Ser.*, **57**, pp. 127–137.
- [37] Matzner, B., 1963, "Basic Experimental Studies of Boiling Fluid Flow and Heat Transfer at Elevated Pressure," T.I.D. 18978.
- [38] Lee, D. H., and Obertelli, J. D., 1963, "An Experimental Investigation of Forced Convection Burnout in High Pressure Water," Part 1, Round tube with uniform flux distribution, AEEW-R213.
- [39] Thompson, R. V., 1964, "Boiling Water Heat Transfer Burnout in Uniformly Heat Round Tubes: A Compilation of World Data With Accurate Correlation," AEEW-R356.
- [40] Weatherhead, R. J., 1963, "Heat Transfer Flow Instability and Critical Heat Flux in a Small Tube at 200 psia," A.N.L. 6715.
- [41] Weatherhead, R. J., 1963, "Nucleate Boiling Characteristics and Critical Heat Flux Occurrence in Sub-Cooled Axial-Flow Water Systems," A.N.L.6675.
- [42] Hood, R. R., and Isakoff, L., 1962, "Heavy Water Moderate Power Reactors Progress Report for June 1962," D.P.755.
- [43] Chen, Y. Z., Zhou, R. B., Hao, L. M., and Chen, H. Y., 1997, "Critical Heat Flux With Subcooled Boiling of Water at Low Pressure," Eighth International Topical Meeting on Nuclear Reactor Thermal-Hydraulics, Vol. 2, pp. 958–964.
- [44] Weisman, J., and Pei, B. S., 1983, "Prediction of Critical Heat Flux in Flow Boiling at Low Qualities," *Int. J. Heat Mass Transfer*, **26**, pp. 1463–1477.
- [45] Weisman, J., and Ying, S. H., 1983, "Theoretically Based CHF Prediction at Low Qualities and Intermediate Flows," *Trans. Am. Nucl. Soc.*, **45**, pp. 832–843.
- [46] Weisman, J., and Ileslamlous, S., 1988, "A Phenomenological Model for Prediction of Critical Heat Flux Under Highly Subcooled Conditions," *Fusion Technol.*, **13**, pp. 654–659.
- [47] Kwon, Y. M., Suk, S. D., and Chang, S. H., 1999, "Prediction of Critical Heat Flux in Highly Subcooled Convective Boiling," 9th International Meeting on Nuclear Reactor Thermal Hydraulics.

Calculation of Turbulent Boundary Layers Using Equilibrium Thermal Wakes

James Sucec¹

e-mail: RME700@MAINE.EDU

University of Maine,
Department of Mechanical Engineering,
5711 Boardman Hall, Room 202,
Orono, ME 04469

The combined thermal law of the wall and wake is used as the approximating sequence for the boundary layer temperature profile to solve an integral thermal energy equation for the local Stanton number distribution. The velocity profile in the turbulent boundary layer was taken to be the combined law of the wall and wake of Coles. This allows the solution of an integral form of the x -momentum equation to give the skin friction coefficient distribution. This, along with the velocity profile, is used to solve the thermal energy equation using inner coordinates. The strength of the thermal wake was found by analysis of earlier research results, in the literature, for equilibrium, constant property, turbulent boundary layers. Solutions for the Stanton number distribution with position are found for some adverse pressure gradient boundary layers as well as for those having zero pressure gradient. The zero pressure gradient results cover both fully heated plates and those with unheated starting lengths, including both isothermal surfaces and constant flux surfaces. Comparison of predictions of the present work is made with experimental data in the literature. [DOI: 10.1115/1.1844538]

Keywords: Forced Convection, Boundary Layers, Turbulent, Heat Transfer

Introduction

One approach to the calculation of the heat transfer in turbulent thermal boundary layers in a pressure gradient is to use the combined thermal law of the wall and wake, namely, $T^+ = (\text{Pr}_t/K) \ln y^+ + C_t(\text{Pr}) + (\Pi_t/K)[W(y/\delta_t)]$. $W(y/\delta_t)$ is Coles' wake function. As pointed out by So [1], values of the thermal wake strength parameter, Π_t , unlike the velocity wake strength, Π , are not well established even for the simplest case of a flat plate with zero pressure gradient. Kader and Yaglom [2] recommend $\tilde{A}_\theta = 2 \text{Pr}_t \Pi_t / K = 2.35$ which gives $\Pi_t = 0.57$ when using $\text{Pr}_t = 0.85$ and $K = 0.41$. However, in later work, Kader [3], implies that $\Pi_t = 0.43$ for zero pressure gradient and still later, Kader [4] uses $\Pi_t = 0.31$. Subramanian and Antonia [5] have experimental evidence indicating that $\Pi_t \text{Pr}_t \approx 0.50 \Pi$ or $\Pi_t \approx 0.31$. Fridman [6] predicts values of $\Pi_t \approx 0.61$. Faraco-Medeiros and Silva-Freire [7] examine experimental results that point toward $\Pi_t \approx 0.52$ while Bell and Ferziger [8] say the few experimental measurements of Π_t in air suggest that it ranges from about 0.5 Π to Π .

The present work uses the solution, of So [1], for equilibrium turbulent thermal boundary layers, that is, boundary layers for which the Clauser parameter, $\beta = \delta^* (dP/dx) / \tau_w$, is independent of x . Based on the results of So [1], the thermal wake strength, Π_t , is found as a function of β and of the turbulent Prandtl number, Pr_t . Using these values of Π_t , the laws of the wall and wake, for both the velocity field and the temperature field, will be used in the integral forms of the x -momentum equation and the thermal energy equation to solve for the Stanton number distribution, St_x . These predicted St_x values will be compared to experimental data for the zero pressure gradient cases as well as to data for two adverse pressure gradient boundary layers. Some evidence will be offered, as indeed it was by So [1], for the possible values of the thermal wake strength, Π_t , for the case of $dP/dx = 0$.

Analysis

The work of So [1] is for steady, constant property, high Reynolds number, equilibrium turbulent boundary layers over an isothermal planar body. From his results, it can be shown that the following is true:

$$\tilde{A}_\theta = \frac{2 \text{Pr}_t \Pi_t}{K} = A_\theta - \frac{\text{Pr}_t}{K} \ln \left(\frac{\delta_t}{\Delta} \right) \quad (1)$$

$A_\theta = f(\beta, \text{Pr}_t)$ is given in Table 1 of So. The values of δ_t/Δ could not be accurately read from the graphs, so an alternate method was used here in estimating the value of δ_t/Δ at various values of β . After some rearrangement, it can be shown that δ_t/Δ can be written as follows:

$$\frac{\Delta}{\delta_t} = \frac{1 + \Pi}{K} \left(\frac{\delta}{\delta_t} \right) \quad (2)$$

With this, Eq. (1) becomes

$$\frac{2 \Pi_t \text{Pr}_t}{K} = A_\theta + \frac{\text{Pr}_t}{K} \ln \left[\frac{1 + \Pi}{K} \left(\frac{\delta}{\delta_t} \right) \right] \quad (3)$$

The values of the hydrodynamic wake strength, Π , that were used in the present work for the various different values of β came from Mellor and Gibson [9] and are very close to those predicted by So [1] when $\beta \geq 0$. The values of Π so determined differ by about 9%–15% from the modified experimental correlation of Das and White [10] for $\Pi(\beta)$ given in Sucec and Oljaca [11]. The reason for the difference is that the experimental correlation includes values of Π from both nonequilibrium and equilibrium boundary layers. The needed ratio δ_t/δ in Eq. (3) was estimated from the experimental results of Blackwell [12] and Orlando et al. [13]. The value of δ_t/δ used for $dP/dx = 0$, namely 1.10, is also supported by the DNS results of Bell and Ferziger [8]. For $0 \leq \beta \leq 6.5$, these estimates could be adequately represented by the following equation:

$$\delta_t/\delta = 1.10 - 0.0292\beta \quad (4)$$

Using the values of δ_t/δ and of Π along with So's predicted A_θ in Eq. (3), Π_t was obtained for various values of β and Pr_t . These results are given in graphical form as Fig. 1.

¹Presented at the IMECE2002, New Orleans.

Contributed by the Heat Transfer Division for publication in the JOURNAL OF HEAT TRANSFER. Manuscript received by the Heat Transfer Division June 3, 2004; revision received November 2, 2004. Review conducted by: J. H. Lienhard V.

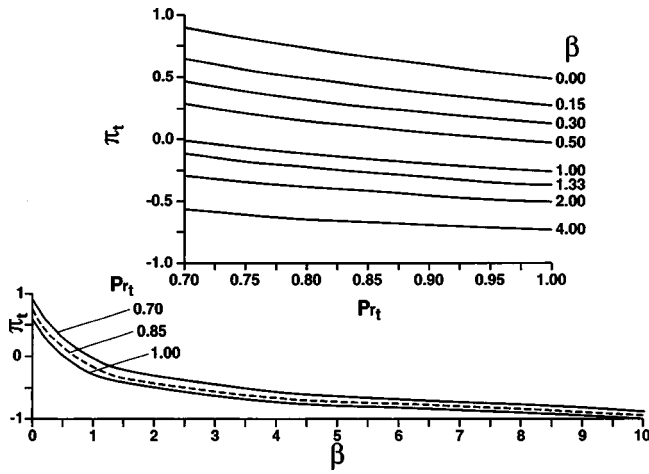


Fig. 1 Predicted thermal wake strength, Π_t , variation with Pr_t and β

Solution for the Stanton Number. To solve for St_x , the integral forms of the x -momentum equation and the low speed thermal energy equation will be used. Introducing the following inner variables,

$$u^+ = u/u^*, \quad y^+ = u^*y/\nu, \quad T^+ = \frac{T_w - T}{q_w/\rho c_p u^*},$$

where

$$u^* = \sqrt{\tau_w/\rho} = u_s \sqrt{C_f/2},$$

the integral thermal energy equation can be written as shown next (Sucec and Lu [14]).

$$\frac{d}{dx} \left[\frac{\nu q_w(x)}{u^*(x)} \int_0^{\delta_t^+} u^+(T_s^+ - T^+) dy^+ \right] = q_w(x) \quad (5)$$

We will now treat the case of specified surface heat flux, $q_w(x)$. This allows easy integration of Eq. (5) from x_0 , where all quantities are known, to the general position x at which the value of $\delta_t^+(x)$ is to be predicted. The result of this is shown next.

$$\begin{aligned} & \int_0^{\delta_t^+} u^+(T_s^+ - T^+) dy^+ \\ &= \frac{u^*(x)}{\nu q_w(x)} \int_{x_0}^x q_w dx + \frac{u^*(x) q_w(x_0)}{u^*(x_0) q_w(x)} \int_0^{\delta_{t_0}^+} u^+(T_s^+ - T^+) dy^+ \end{aligned} \quad (6)$$

The velocity profile, u^+ , needed in Eq. (6) is given by the combined law of the wall and wake due to Coles as shown below.

$$\begin{aligned} u^+ &= \frac{1}{K} \ln y^+ + B + \frac{2\Pi(x)}{K} \left[3 \left(\frac{y^+}{\delta^+} \right)^2 - 2 \left(\frac{y^+}{\delta^+} \right)^3 \right], \\ & 0 < y^+ \leq \delta^+, \\ u^+ &= u_s^+ = 1/\sqrt{C_f/2} \quad \text{for } y^+ > \delta^+ \end{aligned} \quad (7)$$

The temperature profile T^+ is given by the combined thermal law of wall and wake, as,

$$T^+ = \frac{Pr_t}{K} \ln y^+ + C_t(Pr) + \frac{2 Pr_t \Pi_t(x)}{K} \left[3 \left(\frac{y^+}{\delta_t^+} \right)^2 - 2 \left(\frac{y^+}{\delta_t^+} \right)^3 \right] \quad (8)$$

In the calculations, the following values and expressions needed in Eqs. (7) and (8), were used. $B=5.0$, $K=0.41$ and $C_t(Pr)=13.2 Pr - 5.34$, from Kays and Crawford [15].

The hydrodynamic solution is required in order to calculate the values of δ^+ and $C_f/2$ needed in Eqs. (6) and (7). This was found by using Eq. (7) as the velocity profile in the integral form of the x -momentum equation after transforming it into the inner variables y^+ and u^+ . The solution details are given in Sucec and Oljaca [11].

Solution for δ_t^+ . For the case of specified surface heat flux, $q_w(x)$, Eq. (6) must be solved for $\delta_t^+(x)$. The procedure is to insert the velocity and temperature profiles, Eqs. (7) and (8), into Eq. (6) along with the flux. T_s^+ is given by Eq. (8) evaluated at $y^+ = \delta_t^+$. The integrations of these profiles, required by Eq. (6), were made analytically for the two situations possible, namely, $\delta_t^+ \leq \delta^+$ and $\delta_t^+ > \delta^+$. This yielded a nonlinear algebraic equation for δ_t^+ . The solution begins at $x=x_0$, where the known initial conditions are the values of Stanton number, St , and skin friction coefficient, C_f . These are then used in Eqs. (7) and (8) evaluated at $y^+ = \delta^+$ and $y^+ = \delta_t^+$, respectively, to give the starting values of δ^+ and δ_t^+ at x_0 . Next, the nonlinear ordinary differential equation for δ^+ (Sucec and Oljaca [11]), is solved for δ^+ at $x_0 + \Delta x$. With this now available, Eq. (6) can be solved for δ_t^+ at $x_0 + \Delta x$. This is accomplished using Newton's method. The derivative needed in this method was found analytically and a short computer program was used to solve for δ_t^+ as a function of position, x . The first approximation to δ_t^+ at x was taken to be the converged value of δ_t^+ at the previous x position. Since the hydrodynamic solution came from an ordinary differential equation solved by a Runge-Kutta procedure, δ_t^+ was also calculated at each small finite increment in x . Hence, taking the first approximation to δ_t^+ at $x + \Delta x$ to be the value found at position x was found to be close enough to the correct value at $x + \Delta x$ so that no convergence problems were encountered.

The solution procedure described above is for cases where the heat flux, $q_w(x)$, is specified as was the case for some of the experimental data (Taylor et al. [16]), to which the solution was compared. However, other experiments were run for isothermal surfaces, in both Taylor et al. [16] and in other references. For an isothermal surface, in the absence of a pressure gradient, $q_w(x)$ is approximately proportional to $x^{-0.2}$ (Kays and Crawford [15]). Hence, this variation with x was used in the solution for the isothermal surfaces. However, the proportionality, $q_w \sim x^{-0.20}$, is strictly true for fully heated surfaces or for x locations not too near the end of an unheated starting length. To some degree, this concern with the use of the proper surface condition may not be warranted. As is known, for a turbulent boundary layer, if Pr is not low, the specific surface condition may not have very much effect on the Stanton number distribution. Therefore, the results for constant flux surfaces are practically the same as for constant wall temperature surfaces, the difference in St_x being about 4% when $dP/dx=0$ (Kays and Crawford [15]).

To calculate the value of the Stanton number, the predicted $\delta_t^+(x)$ is used to evaluate T_s^+ by setting $y^+ = \delta_t^+$ in Eq. (8). Now, using the definition of T_s^+ gives the heat transfer law shown next.

$$\frac{\sqrt{C_f/2}}{St_x} = \frac{Pr_t}{K} \ln \delta_t^+ + C_t(Pr) + 2 \frac{Pr_t}{K} \Pi_t \quad (9)$$

The value of the turbulent Prandtl number, Pr_t , in the log layer is needed in some of the previous equations. In this work, the greatest number of experimental data sets available were for the plate with $dP/dx=0$. The consensus, at this time, is that Pr_t lies between about 0.85 and 0.90. Kader and Yaglom [2] indicate that the evidence is for $Pr_t=0.85$ and Kader [3] uses $Pr_t=0.85$. The DNS results of Bell and Ferziger [8] give $Pr_t=0.90$ while the DNS results of Kong et al. [17] predict $Pr_t=0.85$ in the log region. In

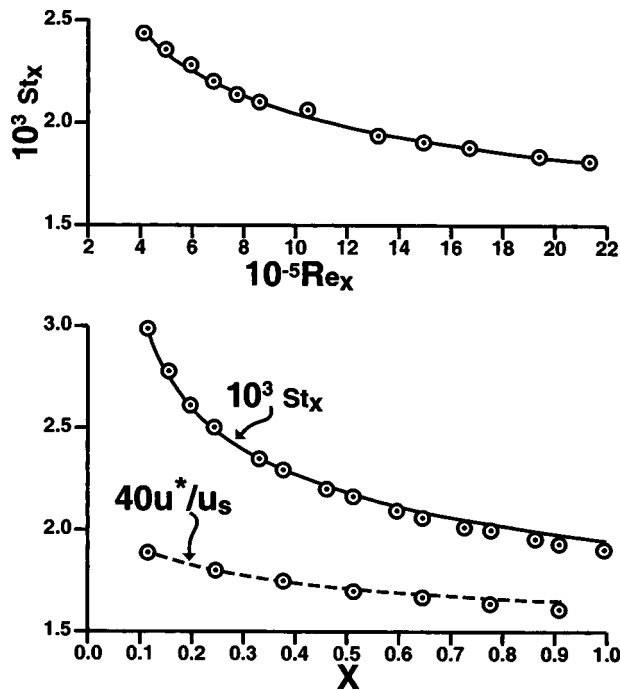


Fig. 2 Predictions and experimental data for constant u_s and isothermal surface. Data, \circ , predictions —. Upper curve data, Moffat and Kays [18]. Lower curves' data, Blackwell [12]. $L = 2.286$ m (7.5 ft).

finite difference solutions, Taylor et al. [16] uses 0.90 while Fridman [6] uses 0.85. There is evidence in Blackwell [12] that Pr_t decreases with positive pressure gradient, that is, for $\beta > 0$, decelerating flows.

In the present work, calculations were made both using $Pr_t = 0.85$ and 0.90 with their respective Π_t values at these turbulent Prandtl numbers. Also, at this time, the same two values were used for the decelerating flows rather than modeling the decrease in Pr_t below the $dP/dx = 0$ values.

Discussion and Results

Figure 1 displays the dependence of Π_t upon β and Pr_t that was calculated using the results of So [1] for high Reynolds number, turbulent, equilibrium thermal boundary layers with adverse and zero pressure gradients. Although So [1] gives information needed to calculate Π_t for $0.7 \leq Pr_t \leq 7$, it was felt that, realistically, only the range $0.7 \leq Pr_t \leq 1.0$ was useful for $\beta \geq 0$. We see, from the figure, that Π_t is significantly dependent upon Pr_t at a given β and varies close to linearly with Pr_t . The bottom three curves show that the thermal wake strength, Π_t , decreases with increasing β and quickly takes on negative values. This is in accord with the experimental results shown in Kays and Crawford [15].

In Fig. 2 is shown a comparison of the predicted St_x results with experimental data. All predictions and experimental data are for air, $Pr \approx 0.71$. The upper curve uses the data of Moffat and Kays [18] while the lower curve uses the data of Blackwell [12]. Both data sets are for constant free stream velocity and an isothermal surface. The agreement between the present predictions, the solid curves, and the experimental data, the circles, is very good for these data sets. The calculations were made using $Pr_t = 0.85$ which, for $\beta = 0$, gives the thermal wake strength $\Pi_t = 0.672$ from Fig. 1. It was found that the results using $Pr_t = 0.90$, with its associated $\Pi_t = 0.608$, were not as good as when $Pr_t = 0.85$ was used. In general, this was found to be true for most of the other data sets as well. For example, the average difference between predictions and the data of Moffat and Kays [18] is 0.9% for $Pr_t = 0.85$ and is 2.3% using $Pr_t = 0.90$. For most of the other data

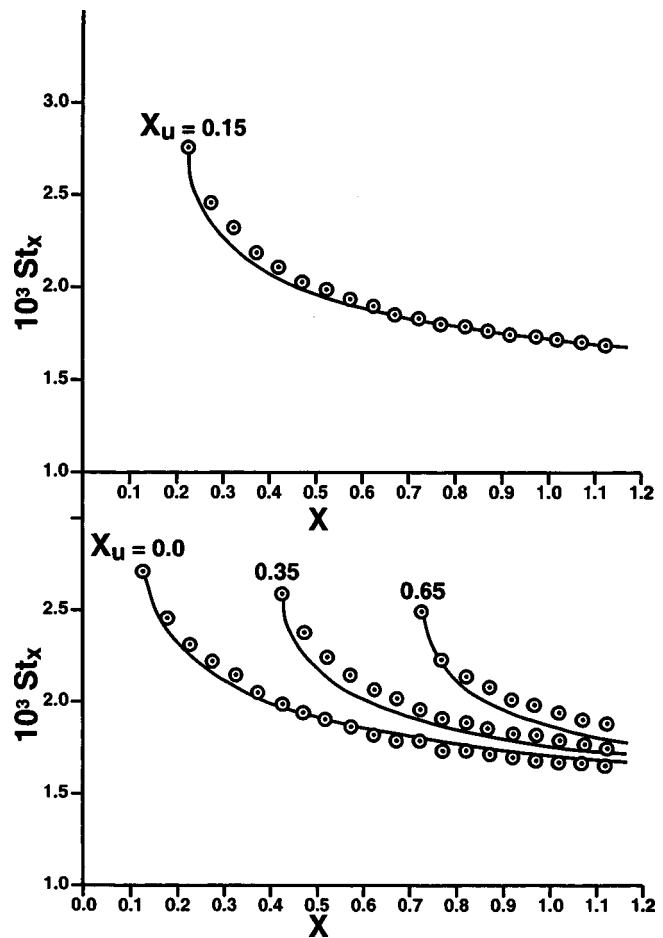


Fig. 3 Predictions —, and data \circ , for constant u_s and constant flux. Nondimensional unheated lengths of 0.0, 0.35, and 0.65 bottom curves, 0.15 top curve. Data from Taylor et al. [16]. $L = 2.00$ m.

sets used in Figs. 3–6, the $Pr_t = 0.90$ predictions are 3% farther from the data than are the $Pr_t = 0.85$ predictions. The $Pr_t = 0.90$ predictions are closer to the data only for some of the isothermal surfaces of Taylor et al. [16], but not for their constant flux surfaces.

Computations were also made using $\Pi_t = 0.300$, the value of Π_t suggested by some authors, Kader [4], as the value for constant free stream velocity. In all cases considered, the results using $\Pi_t = 0.672$ were superior, sometimes much better than the predictions which used 0.300. For the data of Blackwell [12] in Fig. 2, the use of $\Pi_t = 0.300$ gave results that, on the average, are 4% farther from the data than are the predictions using 0.672. The maximum difference between predictions and data in Fig. 2 is 2.1%.

Finally, to illustrate the dependence of St_x on the flat plate wake strength Π_t , some calculations were made using $\Pi_t = 0.0$. This led to predictions which, on the average, differed from the data of Blackwell [12] and Taylor et al. [16] by 8.3% with a maximum difference of 10.8%. On the other hand, use of $\Pi_t = 0.672$ and $Pr_t = 0.85$ led to a maximum difference from data of the order of 2.5%.

Comparison of the predictions in Fig. 2 to an older integral method, that of Kays and Crawford [15], was also made. Their equation for the isothermal, constant u_s , plate is, for $Pr = 0.71$,

$$St_x = 0.0329 Re_x^{-0.20} \quad (10)$$

For the data of Blackwell [12], Eq. (10) is about 3.5% further

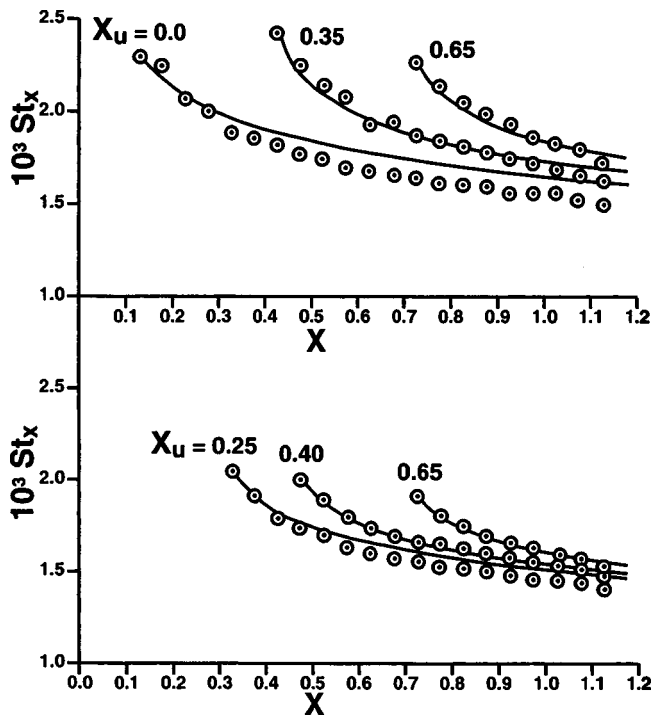


Fig. 4 Predictions —, and data \circ , for constant u_s and isothermal surface. Nondimensional unheated lengths of 0.25, 0.40, and 0.65, lower half, and 0.0, 0.35, and 0.65 upper half. Bottom curves' Reynolds numbers twice as large as for upper curves. Data from Taylor et al. [16]. $L=2.00$ m.

away from the data than are the present predictions, while for the data of Moffat and Kays [18], Eq. (10) virtually coincides with the present work.

The lowest curve in Fig. 2 is a comparison of predictions, the dashed line, with the data for u^*/u_s . This was done because of the need to use u^* in Eqs. (6) and (9). The agreement is very close between them.

Predictions of St_x are compared to the constant flux experimental results of Taylor et al. [16] in Fig. 3. The four curves shown are the predictions for unheated lengths of 0 m, the lowest curve, 0.3 m, the curve in the upper half of the figure, 0.7 m and 1.30 m, the second and third lowest curves, respectively. Although predictions are not as close to the data as in the previous figure, the present integral solution results have accuracy comparable to the numerical finite difference solution given in Taylor et al. [16]. The largest error in present predictions is 4.9%, while the average error is much less than this for all curves. The unheated starting length of 1.30 m is the only data set for which the use of $\Pi_1=0.300$ gave better results than the $\Pi_1=0.672$ used in the predictions.

Results and data for constant surface temperature, from Taylor et al. [16], are presented in Fig. 4. The three curves in the lower portion of the figure are for $u_s=67.3$ m/s and unheated lengths of 0.50 m, 0.80 m, and 1.30 m, respectively. The upper half curves are for $u_s=27.9$ m/s with unheated portions of 0.0 m, 0.70 m, and 1.30 m. For the lower curves, predictions agree well with data with the greatest deviation coming, somewhat surprisingly, for the shortest unheated length. The same trends are observed for the upper three curves with agreement between predictions and data being good for the unheated lengths of 0.70 m and 1.30 m and worst for the 0.0 m case.

Constant surface flux results from Taylor et al. [16] are presented in Fig. 5, $u_s=67.4$ m/s for all curves in the figure. The upper three curves are for unheated lengths of 0.0 m, 0.5 m, and 1.3 m from bottom to top. The predictions are seen to be very

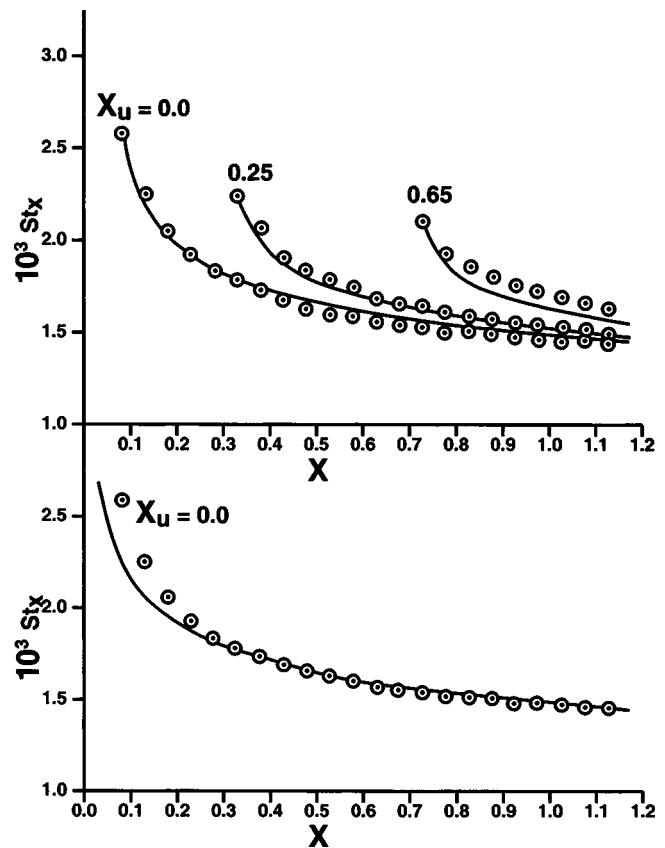


Fig. 5 Predictions —, and data \circ , for constant u_s and constant flux. Nondimensional unheated lengths of 0.0, 0.25, and 0.65, upper half. Lower figure has 0.0 unheated length and calculations start at $X=0.0$. Data from Taylor et al. [16]. $L=2.00$ m.

good for the 0.0 m and 0.5 m cases and worse for the 1.30 m unheated length. The accuracy is about the same as the numerical solution in Taylor et al. [16]. The curve and data points in the lower half of this figure are for the same case as the lowest curve in the upper half, namely, the fully heated plate, so the data points are the same. However, the predictions in the upper half start by matching the measured St_x at the first data point while the lower half predictions start at $x=0.0$ m (actually the start was at $x=10^{-5}$ m.). The values of St_x and $C_f/2$ at this location were assigned as 0.00942 and 0.00858, namely, very large values. This arbitrary assignment of starting values was checked by rerunning this case with higher and lower values as well. It was found that the downstream solution for St_x was independent of starting values even smaller than the ones used. It can be seen that the results coming from the start at $x=0.00$ m are not as good, at low x values, as when the starting value of St_x was the measured value at the first data point as was done for the corresponding curve in the upper half. However, beginning at $X=0.25$, the results of the two different ways of starting the calculation are essentially the same along the rest of the surface.

As was done earlier for Fig. 2, some of the present predictions and data of Taylor et al. [16] will be compared to those from one of the older integral methods given in Kays and Crawford [15] for isothermal surfaces with an unheated starting length, x_u . This relation is Eq. (10) with a function that is dependent upon x_u/x , namely, for $Pr=0.71$,

$$St_x = 0.0329 Re_x^{-0.20} [1 - (x_u/x)^{0.9}]^{-1/9} \quad (11)$$

Calculations using Eq. (11) were made for $x_u=0.5, 0.7, 0.8$, and 1.3 m for four of the cases of Fig. 4. For $x_u=0.5$ and 0.7 m, Eq.

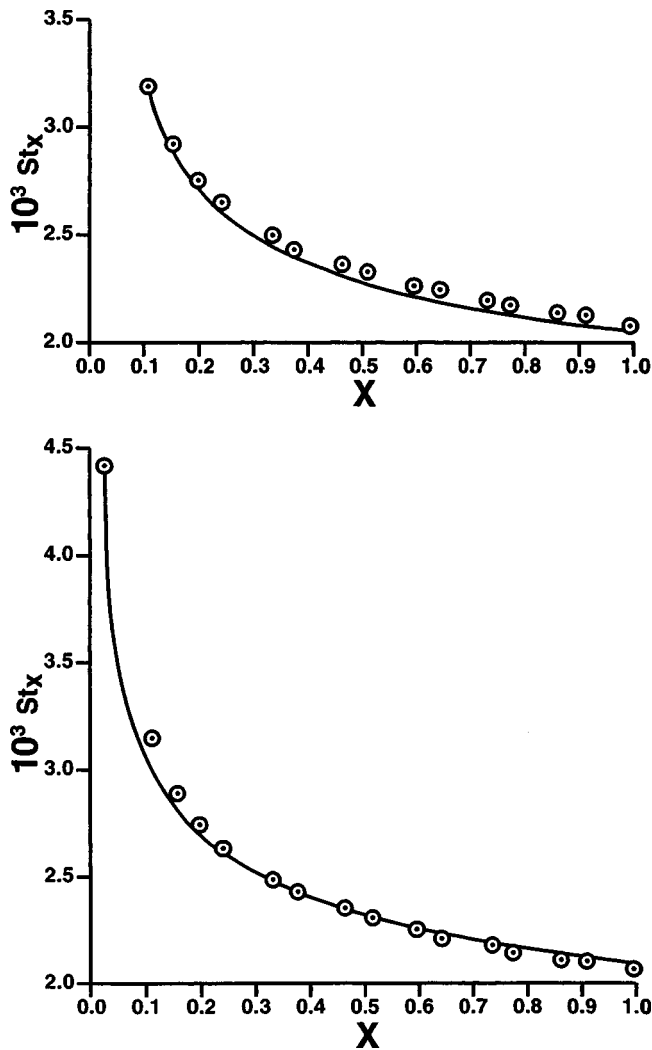


Fig. 6 Predictions —, and data ○, for isothermal surface. Upper curve has $u_s \sim x^{-0.20}$. Lower curve has $u_s \sim x^{-0.15}$. Data from Blackwell [12]. $L = 2.286$ m (7.5 ft.).

(11) and present computations were within 1% of each other while for $x_u = 0.8$ and 1.3 m, present calculations were 3.5% closer to the experimental data than was Eq. (11).

In addition, some comparisons were made for two constant flux cases in Figs. 5 and 3. For the case of no unheated starting length, Kays and Crawford [15] give an equation similar to Eq. (10) for constant temperature surfaces, except the coefficient is about 4% higher. This equation practically coincides with the present predictions in Fig. 5. For the case of a step change at $x_u = 1.3$ m to a constant flux condition, the appropriate relation is developed from the general solution in Kays and Crawford [15] and is given in terms of Beta functions in Taylor et al. [16]. Present predictions were found to be about 1.5% closer to the experimental data in Fig. 3 than is the older integral method of Kays and Crawford [15].

The experimental data in Fig. 6 come from Blackwell [12] and are for decelerating flows over constant temperature surfaces. The upper curve and data points are for $u_s(x) \sim x^{-0.20}$, a strong adverse pressure gradient. First the velocity field solution was obtained to find the predicted β values. It turned out that this data set was close to being for an equilibrium turbulent boundary layer since the β predictions were between +1.0 and +1.18 over the entire surface. From Fig. 1, this value at $Pr_t = 0.85$ gave $\Pi_t = -0.25$ which was then used to make the heat transfer predictions.

As can be seen, agreement between predictions of the present integral method and the data points is good with a maximum difference of 2.5%.

The lower portion of this figure is for a flow which decelerates as $u_s(x) \sim x^{-0.15}$, a milder adverse pressure gradient than that of the upper data set. This lower data set was not as close to belonging to an equilibrium boundary layer as the upper set was. Predicted β values ranged from +0.36 to +0.52, a 30% increase in β based on the ending value. To account for this variation in β , the following curve fit was made to the Π_t values found from Fig. 1 when $Pr_t = 0.85$.

$$\Pi_t = 0.51 - 0.805\beta \quad (12)$$

Using Eq. (12), predictions of St_x agreed well with the experimental values.

Concluding Remarks

Calculations were made of the thermal wake strength, Π_t , as a function of turbulent Prandtl number and the Clauser pressure gradient parameter for high Reynolds number, equilibrium, turbulent thermal boundary layers. The results of these calculations are presented in graphical form. Π_t decreases with both increasing values of Pr_t and increasing values of β and eventually Π_t takes on negative values.

Predictions made of the Stanton number distributions, using this thermal wake strength, Π_t , in an inner variable integral method, compare well with experimental data for zero pressure gradients as well as for some adverse pressure gradients.

Use of the thermal wake strength value of $\Pi_t = 0.672$ yielded predicted Stanton numbers that were in better agreement with experiment than predictions with the, sometimes recommended, lower values close to 0.300 for the zero pressure gradient case. On the basis of this, as well as the evidence of other investigations, it is concluded that Π_t probably lies between about 0.60 and 0.67 for the, somewhat controversial, case of a flat plate with zero pressure gradient.

Nomenclature

- A_θ = temperature outer law log layer parameter when y/Δ is used
- \tilde{A}_θ = temperature outer law log layer parameter when y/δ_t is used
- B = a constant in the velocity profile, Eq. (7)
- C_f = $2\tau_w/\rho u_s^2$, skin friction coefficient
- C_p = constant pressure specific heat
- C_t = Prandtl number function in temperature profile, Eq. (8)
- DNS = direct numerical simulation
- K = von Karman constant, 0.41
- L = reference length
- P = local pressure
- Pr = molecular Prandtl number
- Pr_t = turbulent Prandtl number
- q_w = surface heat flux
- Re_x = $u_s x/\nu$, local Reynolds number
- St_x = $h_x/\rho c_p u_s$, local Stanton number
- T, T_w, T_s = local, wall, and freestream temperature, respectively
- T^+ = $(T_w - T)\rho C_p u^*/q_w$
- T_s^+ = value of T^+ in freestream
- u, u_s = local and freestream x velocity component
- u^* = $\sqrt{\tau_w/\rho}$, friction velocity
- u^+ = u/u^* , inner velocity
- u_s^+ = freestream value of u^+
- $W(y/\delta_t)$ = Coles' wake function
- X = x/L , nondimensional x coordinate
- X_u = x_u/L , nondimensional unheated length

- x = space coordinate along surface
- x_0 = x value at start of calculations
- x_u = length of unheated section
- y = space coordinate normal to surface
- y^+ = yu^*/ν , inner coordinate

Greek Symbols

- β = $\delta^*(dP/dx)/\tau_w$, Clauser parameter
- δ, δ_t = local thickness of velocity and thermal boundary layer, respectively
- δ^* = displacement thickness
- δ^+, δ_t^+ = value of y^+ at $y = \delta$ and δ_t
- Δ = $\delta^*/\sqrt{C_f/2}$, velocity defect thickness
- ν = kinematic viscosity
- Π, Π_t = wake strength for velocity and temperature profiles, respectively, Eqs. (7) and (8)
- ρ = mass density
- τ_w = surface shear stress

References

- [1] So, R. M. C., 1994, "Pressure Gradient Effects on Reynolds Analogy for Constant Property Equilibrium Turbulent Boundary Layers," *Int. J. Heat Mass Transfer*, **37**, pp. 27–41.
- [2] Kader, B. A., and Yaglom, A. M., 1972, "Heat and Mass Transfer Laws for Fully Turbulent Wall Flows," *Int. J. Heat Mass Transfer*, **15**, pp. 2329–2351.
- [3] Kader, B. A., 1981, "Temperature and Concentration Profiles in Fully Turbulent Boundary Layers," *Int. J. Heat Mass Transfer*, **24**, pp. 1541–1544.
- [4] Kader, B. A., 1991, "Heat and Mass Transfer in Pressure Gradient Boundary Layers," *Int. J. Heat Mass Transfer*, **34**, pp. 2837–2857.
- [5] Subramanian, C. S., and Antonia, R. A., 1981, "Effect of Reynolds Number on a Slightly Heated Turbulent Boundary Layer," *Int. J. Heat Mass Transfer*, **24**, pp. 1833–1846.
- [6] Fridman, E., 1997, "Heat Transfer and Temperature Distribution in a Turbulent Flow Over a Flat Plate With an Unheated Starting Length," *HTD—Vol. 346, Proceedings of the 1997 National Heat Transfer Conference*, **8**, pp. 127–132.
- [7] Faraco-Medeiros, M. A., and Silva-Freire, A. P., 1992, "The Transfer of Heat in Turbulent Boundary Layers With Injection or Suction: Universal Laws and Stanton Number Equations," *Int. J. Heat Mass Transfer*, **35**, pp. 991–995.
- [8] Bell, D. M., and Ferziger, J. H., 1993, "Turbulent Boundary Layer DNS With Passive Scalars," *Near-Wall Turbulent Flows*, edited by So, R. M. C., Speziale, C. G., and Launder, B. E., pp. 327–336.
- [9] Mellor, G. L., and Gibson, D. M., 1966, "Equilibrium Turbulent Boundary Layers," *J. Fluid Mech.*, **24**, pp. 255–274.
- [10] Das, D. K., and White, F. M., 1986, "Integral Skin Friction Prediction for Turbulent, Separated Flows," *ASME J. Fluids Eng.*, **108**, pp. 476–482.
- [11] Sucec, J., and Oljaca, M., 1995, "Calculation of Turbulent Boundary Layers With Transpiration and Pressure Gradient Effects," *Int. J. Heat Mass Transfer*, **38**, pp. 2855–2862.
- [12] Blackwell, B. F., 1972, "The Turbulent Boundary Layer on a Porous Plate: An Experimental Study of the Heat Transfer Behavior With Adverse Pressure Gradients," Ph.D. thesis, Stanford University, Stanford California.
- [13] Orlando, A. F., Moffat, R. J., and Kays, W. M., 1974, "Turbulent Transport of Heat and Momentum in a Boundary Layer Subject to Deceleration, Suction and Variable Wall Temperature," *Thermosciences Division Report No. HMT-17*, Stanford University, Stanford, CA.
- [14] Sucec, J., and Lu, Y., 1990, "Heat Transfer Across Turbulent Boundary Layers With Pressure Gradient," *ASME J. Heat Transfer*, **112**, pp. 906–912.
- [15] Kays, W. M., and Crawford, M. E., 1993, *Convective Heat and Mass Transfer*, 3rd ed., McGraw-Hill, New York, pp. 278–284.
- [16] Taylor, R. P., Love, P. H., Coleman, H. W., and Hosni, M. H., 1989, "The Effect of Step Changes in the Thermal Boundary Condition on Heat Transfer in the Incompressible Flat Plate Turbulent Boundary Layer," *HTD—Vol. 107*, in *Proceedings of the 1989 National Heat Transfer Conference*, pp. 9–16.
- [17] Kong, H., Choi, H., and Sik Lee, J., 2000, "Direct Numerical Simulation of Turbulent Thermal Boundary Layers," *Phys. Fluids*, **12**, pp. 2555–2568.
- [18] Moffat, R. J., and Kays, W. M., 1968, "The Turbulent Boundary Layer on a Porous Plate: Experimental Heat Transfer With Uniform Blowing and Suction," *Int. J. Heat Mass Transfer*, **11**, pp. 1547–1566.

Investigation of a Novel Flat Heat Pipe

Yaxiong Wang

Senior Engineer,
ASME Member
Foxconn Thermal Technology,
Austin, TX 78758

G. P. Peterson¹

Professor of Mechanical Engineering,
ASME Fellow
Department of Mechanical, Aerospace and
Nuclear Engineering,
Rensselaer Polytechnic Institute,
Troy, NY 12180

A novel flat heat pipe has been developed to assist in meeting the high thermal design requirements in high power microelectronics, power converting systems, laptop computers and spacecraft thermal control systems. Two different prototypes, each measuring 152.4 mm by 25.4 mm were constructed and evaluated experimentally. Sintered copper screen mesh was used as the primary wicking structure, in conjunction with a series of parallel wires, which formed liquid arteries. Water was selected as the working fluid. Both experimental and analytical investigations were conducted to examine the maximum heat transport capacity and optimize the design parameters of this particular design. The experimental results indicated that the maximum heat transport capacity and heat flux for Prototype 1, which utilized four layers of 100 mesh screen were 112 W and 17.4 W/cm², respectively, in the horizontal position. For Prototype 2, which utilized six layers of 150 mesh screen, these values were 123 W and 19.1 W/cm², respectively. The experimental results were in good agreement with the theoretical predictions for a mesh compact coefficient of $C=1.15$. [DOI: 10.1115/1.1842789]

Keywords: Flat Heat Pipe, Heat Transport Capacity, Sintered Mesh, Cooling

Introduction

Flat heat pipes have wide-ranging applications in many areas related to the thermal control of spacecraft, cooling of high power-density electronics, medical treatment and therapy, electronic appliances and power converters. Because of the lightweight, geometric flexibility, and extremely high effective thermal conductivities, these devices are excellent candidates for heat spreaders, especially for high performance computer applications where size, weight and geometry are of significant importance.

Flat heat pipes can typically be divided into two categories according to the design of the wicking structures, those that use a traditional porous wicking structure and those with noncircular micro channels, which act as liquid arteries. Flat heat pipes with micro-channels or axial grooves have many advantages, such as high heat fluxes and low manufacturing costs [1,2].

In addition to being fabricated within separate devices, the micro grooves or channels can be made as an integrated part of microelectronic devices to enhance the heat spreading capabilities by allowing the structure of the microelectronic devices to serve as the actual heat spreader [3]. The micro grooves that comprise the heat spreader, are typically parallel and provide one-dimensional heat transfer. Because this may restrict the heat spreading capability and limit the amount of heat that is transferred orthogonal to the grooves, additional transverse grooves or two-dimensional porous wicking structures may be used to transfer liquid across the individual channels and allow two-dimensional heat transfer. This two-dimensional heat transport capacity, along with the ease of manufacture, lightweight, and higher transport capacities, make these devices ideal for a wide range of applications in the cooling of high power-density microelectronic devices, medical devices or equipment, spacecraft, power converters, and wide band radar devices.

Similar to conventional heat pipes, the operation of flat micro heat pipes is subject to a number of performance limitations, including the capillary, boiling, entrainment, viscosity and sonic limits [4,5]. Past research, however, has indicated that the capillary limitation, defined as the point where there is insufficient capillary pumping to return the working fluid back to the evap-

orator area, is the dominant factor in low or moderate temperature devices. The second most significant limitation is the boiling limit which may result from the high localized heat flux, characteristics of the application shown above. In this later limit, nucleation within the capillary wick obstructs the liquid circulation, resulting in a significant reduction in the capillary limit and localized hot spots on the heated surface [2,6].

Both theoretical and experimental investigations have been conducted previously on flat micro heat pipes, in order to evaluate the heat transfer performance and study the fundamental mechanisms of the various limitations [2,7–11]. Wick structures that have been investigated previously include sintered powder and fibers, screen meshes, and micro grooves or channels. For each of these different wicking structures, the fabrication processes and characteristic properties must be identified and known.

In the present investigation flat heat pipes fabricated by bonding an array of parallel wires between two layers of screen mesh and enclosing this in a solid case, have been developed, fabricated and tested experimentally. The array of the parallel wires serves two functions: First is to provide support for the internal structure so as to withstand the variations in the operating pressure, and second, to assist in the return of the working fluid. Because the physical properties of the sintered screen mesh wicks are significantly different from those typically reported for wrapped screen mesh wick, it is necessary to identify and investigate these differences, in order to provide an accurate method by which the heat transfer performance can be analyzed and modeled.

The objectives of the present investigation are threefold: First, to develop an analytical model that can be used to predict the heat transport limitations of the flat heat pipes developed herein; second, to develop the fabrication process necessary to construct the test articles; and third, to determine the effect of variations in the geometric shape and operational parameters on the heat transport capacity in order to optimize the design.

Experimental Investigation

The Novel Flat Heat Pipe. A novel flat heat pipe, illustrated in Fig. 1 was developed, and two prototypes were fabricated using a high temperature sintering process. Those prototypes were evaluated experimentally to determine the operational and performance characteristics. The screen mesh and the sharp corners formed between the wire and mesh combined to serve as the cap-

¹Please address all correspondence to G. P. Peterson, Office of the Provost, Room 3018, Troy Building, Rensselaer Polytechnic Institute, Troy, NY 12180.

Manuscript received February 5, 2004; revision received May 10, 2004. Review conducted by: J. H. Lienhard V.

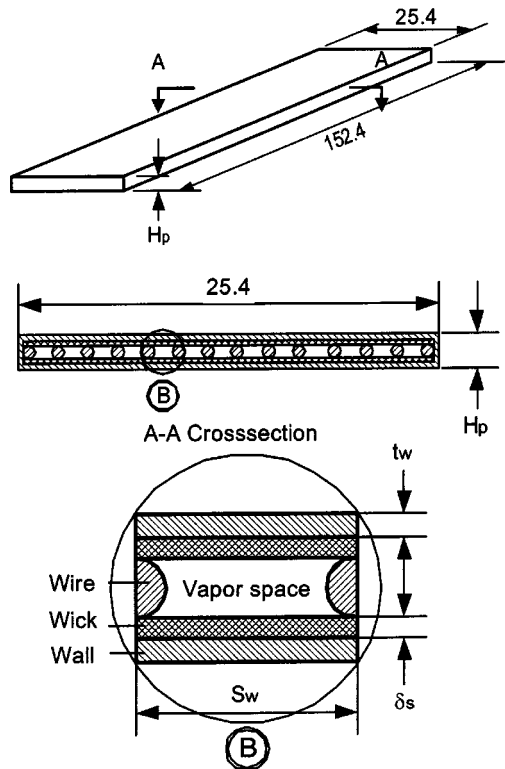


Fig. 1 Schematic of the flat heat pipe

illary structure to circulate the working fluid in the axial and transverse directions, respectively. In addition, the array of parallel wires improved the capacity of the heat pipe to withstand variations in operating pressure occurring due to the transient operating conditions. Pure water was used as the working fluid.

The test articles measured 152.4 mm long and 25.4 mm wide, with a 25.4 mm evaporator and a 50.8 mm condenser, were fabricated from copper. The detailed configuration of the test articles is presented in Table 1.

Experimental Setup. The experimental test facility shown in Fig. 2 was developed and experiments were conducted to evaluate the heat transfer performance of the two test articles described above, over a wide range of test conditions. The experimental system was composed of a cooling system, the test section, a power supply and measurement system, and a data acquisition system. A PC was used to monitor, log, and process the experimental data. The cooling system included a constant-temperature thermal bath and a cooling chamber. The condenser section of the flat heat pipe was inserted horizontally into the cooling chamber. The coolant circulated through the cooling chamber, where heat was removed from the condenser section by forced convection, and then to a constant-temperature bath. The constant-temperature bath was set to the required temperature and held at a constant

Table 1 Physical specification of the flat heat pipes

| Flat heat pipe | Prototype 1 | Prototype 2 |
|----------------|-------------|-------------|
| L , mm | 152.4 | 152.4 |
| L_e , mm | 25.4 | 25.4 |
| L_c , mm | 50.8 | 50.8 |
| t_w , mm | 0.254 | 0.254 |
| Wick structure | #100 screen | #150 screen |
| Layers | 4 | 6 |
| d_s , mm | 0.813 | 0.813 |
| S_w , mm | 2.5 | 2.5 |
| H_p , mm | 2.71 | 2.52 |

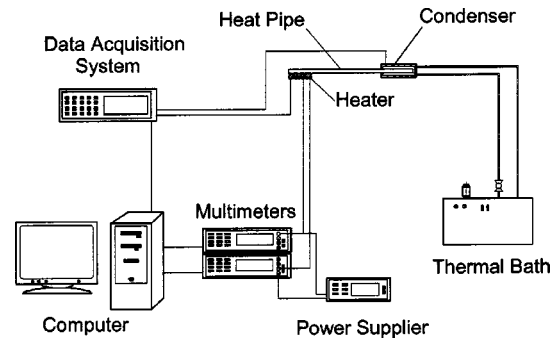


Fig. 2 Schematic of the experimental setup

temperature through the tests. The temperature variation of the cooling fluid was held to within $\pm 1^\circ\text{C}$, and the operating temperature was varied over a range of 30°C – 90°C within an uncertainty of $\pm 0.71^\circ\text{C}$.

The power supply and measurement system utilized an electrical resistance heater powered by a DC power supplier, and two multimeters (HP3498A) used to measure the voltage and current through the heater. The electric heater which measured 25.4×25.4 mm was attached to one side of the evaporator section with Omega 201 thermal grease to reduce the contact thermal resistance between the heater and the heat pipe surface. This approach resulted in an experimental uncertainty of less than 0.1 mW.

The test section was thermally insulated to minimize the convective losses from the outer surface of the heat pipe. In order to monitor the temperature variations along the heat pipe, ten thermocouples were attached to the outer surface of the flat heat pipe along the centerline as illustrated in Fig. 3. Those thermocouples were directly connected to an HP data acquisition system (34970A), controlled and processed by a PC. In addition, two thermocouples were placed in the cooling chamber to monitor the cooling fluid temperature and ensure a constant condenser temperature.

Test Procedures. The test procedure utilized here was similar to that previously described by Wang and Peterson [11]. Prior to each test, the system was allowed to equilibrate for approximately one hour. The power supply was then turned on and the power incremented. At this point in the tests, it took approximately 15 to 20 minutes to reach steady-state, which was defined as no change in temperature of more than $\pm 0.5^\circ\text{C}$ in any of the thermocouples within a given ten minute period. Once the steady-state condition had been reached, the temperature distribution along the heat pipe was measured and recorded, along with the other experimental parameters. The power input was then increased incrementally, and the process repeated until dryout occurred as determined by rapid spikes in the evaporator thermal couple farthest from the condenser. Once dryout was reached, the temperature difference between the evaporator and condenser rapidly increased. The power input at this point was assumed to be the maximum heat transport capacity of the heat pipe at this power level and operating temperature, which is defined as the adiabatic vapor temperature. Changing the temperature of the condenser coolant by changing the set point on the constant temperature bath, and fol-

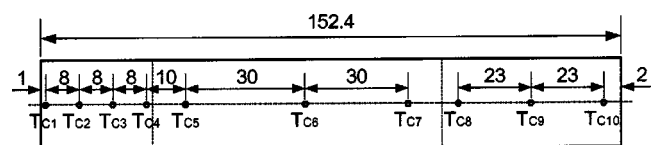


Fig. 3 Thermocouple distributions on the tested flat heat pipes

lowing the procedure described above, allowed the maximum heat transport capacity to be determined for various operating temperatures.

Utilizing an energy balance, the measured heat loss was determined to be less than 6.6% of the input power for all of the tests. The overall experimental uncertainty was determined to be approximately 0.71°C.

Analysis

As described previously [12], the operation of a flat heat pipe is subject to a number of limitations and the maximum heat transport capacity at a given operating temperature is determined by the smallest of these values at the specified operating temperature. For high heat flux heat pipes operating in a low to moderate temperature range, the capillary and boiling limits are typically the dominant factors that govern the operation of these devices [4,5]. The calculation of the operational limitations for flat heat pipes of this type can be found as follows.

Capillary Limit. In order to maintain the continuity of the interfacial evaporation, the total pressure drop in the heat pipe must be less than or equal to the maximum capillary pumping pressure [12]. When the overall pressure drop is equal to the capillary pumping pressure, the evaporation heat transfer reaches maximum value, and

$$\Delta P_{total} = \Delta P_{cap} \quad (1)$$

The total pressure drop resulting from the frictional viscous pressure drop of the liquid and vapor, the pressure drop due to the phase-change and gravitational body force induced pressure drop can be expressed as [4]

$$\Delta P_{total} = \Delta P_v + \Delta P_l + \Delta P_{ph,e} + \Delta P_{ph,c} + \Delta P_g \quad (2)$$

The capillary pressure can be estimated by the Young–Laplace equation and expressed as

$$\Delta P_{cap} = 2\sigma \cos \alpha \left(\frac{1}{r_{m,e}} - \frac{1}{r_{m,c}} \right) \quad (3)$$

Combining Eq. (1) and Eq. (3) and neglecting the phase-change pressure drop, the maximum capillary heat transport capacity of the flat heat pipe can be estimated as [4]

$$Q_{max} = \left(\frac{2\sigma \cos \alpha}{L_{eff} r_{m,e}} - \rho_l g \sin \theta \right) \cdot \left[\frac{2(f Re)_v \mu_v}{\rho_v D_{h,v}^2 A_{c,v} h_{fg}} + \frac{\mu_l}{KA_{c,l} \rho_l h_{fg}} \right]^{-1} \quad (4)$$

where the effective length of the flat micro heat pipe, L_{eff} , can be defined as

$$L_{eff} = 0.5L_e + L_a + 0.5L_c \quad (5)$$

and the hydraulic diameter of the vapor phase can be expressed as

$$D_{h,v} = \frac{4A_{c,v}}{p_v} \quad (6)$$

The vapor-phase frictional factor, $(f Re)_v$ can be calculated as previously described [13,14]. The cross-sectional area of the vapor flow, $A_{c,v}$, and the wetted perimeter, p_v , in Eq. (4) for this special case have been obtained from the derivation by Wang and Peterson [11].

For the sintered multi-layer screen mesh, the permeability will be affected by the sintering and other fabrication processes. In the absence of extensive experimental data, the formula for wrapped screen wicks, which is described in Eq. (7), can be used to estimate the permeability by modifying the porosity

$$K = \frac{d_w^2 \epsilon^3}{122(1 - \epsilon)^2} \quad (7)$$

through a change in the porosity of the sintered screen mesh which is defined as

$$\epsilon = 1 - \frac{C\pi N d_w}{4} \quad (8)$$

where C is the compact coefficient. Using experimental data from the tests conducted here, it was determined that this value ranged from 1.05 to 1.33 depending on the sintering conditions and the configuration of the mesh used. This compares very well with previous results obtained by other investigators.

Boiling Limit. Nucleation within the capillary wick is undesirable for wicked heat pipe operation since the bubbles can obstruct the liquid circulation and cause hot spots on the heated wall [15]. Though there are always some vapor nuclei or small vapor domes on the heated wall of wick structure, significant superheat is required essentially for those bubbles to grow. Evaporation heat transfer on the wick layer is different from pool boiling on a surface with and without a porous layer. The evaporation in the thin wick layer occurs at the liquid–vapor interface and the liquid pressure is affected by the capillary structure of the wick. Bubble formation within the wick layer is dominated by the porous structure and the superheat between the heated wall and the liquid-phase. As a result, only those bubbles larger than a critical value can exist and grow in the superheated liquid. It is very difficult to accurately estimate the critical bubble size, but a method for approximating the critical bubble radius, required for bubble formation and growth can be found in Ref. [16] as

$$r_b = \frac{2\sigma}{P_{sat}(T_l) \exp\{v_l [P_l - P_{sat}(T_l)] / R_g T_l\} - P_l} \quad (9)$$

where the liquid pressure, P_l , in the wick layer can be expressed as

$$P_l = P_v - (P_{cap} + P_d) \quad (10)$$

and

$$P_{cap} = \frac{2\sigma}{r_{m,e}} \quad (11)$$

$$P_d = -\frac{\bar{A}}{\delta^3} \quad (12)$$

For an ideal gas

$$P_d = \rho_l R_g T_{lv} \ln(a \delta^b) \quad (13)$$

In the capillary wick, the size of the bubble is constrained by the pore size on the heated wall. The bubble cannot form, nor will it grow when the critical bubble size is less than the effective pore size in capillary structure, therefore, no boiling occurs. The interfacial temperature is affected by the disjoining and capillary pressures, and also depends on the value of the interfacial resistance. Because the interfacial resistance is very small, it was not considered in the current study.

The heat transfer through the wick-fluid layer occurs mainly by conduction and as a result, the critical boiling limitation in the wick layer can be estimated as [4]

$$q_b = \frac{k_{eff} T_{v,sat}}{\delta_s h_{fg} \rho_v} \left(\frac{2\sigma}{r_b} - P_{cap} \right) \quad (14)$$

where δ_s is the average thickness of the wick layer. For a thicker homogenous wick layer, this process provides reasonable accuracy. It should be noted that the effective thermal conductivity of the wick-fluid layer of the sintered mesh is different from that of the wrapped screen mesh. The correct value can be best estimated using the formula for sintered metal fibers presented by Peterson [4]

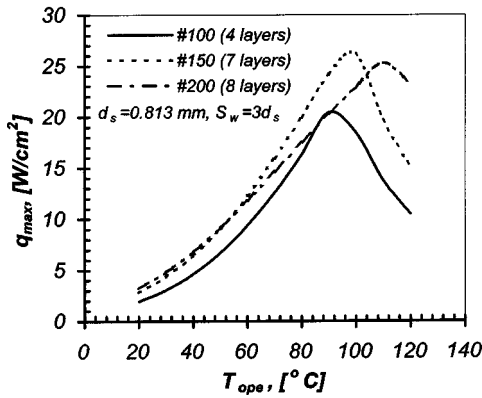


Fig. 4 Modeling results of the effect of mesh number on the maximum heat transport capacities of flat heat pipes

$$k_{\text{eff}} = \frac{(k_f - k_s) + (1 - \varepsilon)(k_f - k_s)}{(k_f - k_s) - (1 - \varepsilon)(k_f + k_s)} \quad (15)$$

Entrainment Limit. When a heat pipe operates at high heat fluxes, the counter-current vapor flow may entrain liquid droplets and carry these droplets back towards the condenser. This short-circuits the liquid return path and causes premature dryout in the evaporator. When this occurs it is referred to as the entrainment limit and for an axial heat pipe can be expressed as [5]

$$q_e = A_{c,v} h_{fg} \left(\frac{\sigma \rho_v}{2r_{h,w}} \right)^{0.5} \quad (16)$$

for screen mesh wick surfaces, the hydraulic radius can be estimated to be one half of the distance between the wires. Other limits can be estimated as described by Peterson [4].

The maximum heat transfer capacity of the heat pipe can be determined by evaluating the different limits at various operating conditions and can be expressed as

$$Q_{\text{max}} = \text{Min}\{Q_{c,\text{max}}, Q_{b,\text{max}}, Q_{e,\text{max}}, Q_{s,\text{max}}, Q_{v,\text{max}}\} \quad (17)$$

Results and Discussion

A thorough investigation of the heat transport capacity at various operating temperatures and the effects of variations in the design parameters helps us to understand the operation of heat pipes and allows the design parameters to be optimized. The analytical and experimental results described above are presented and compared in this section.

Effect of the Mesh Number. Variations in the mesh number of the screen have a reverse effect on the capillary pumping pressure and the frictional pressure drop occurring in the liquid phase in different ways, and as a result, there may exist an optimum mesh number for a given heat pipe at a specific operating temperature. The analytical results of the effect of variations in the wick design on the maximum transport capacity is presented in Fig. 4 for the flat heat pipes developed and evaluated here. The diameter of the supporting wires was 0.813 mm. The results indicated that for the three screen mesh combinations investigated here, the maximum heat transport capacity of the heat pipe with a mesh number of 150 was higher than others in most operating temperature ranges.

Effect of Wire Diameter. Variations in the diameter of the wires can change the size of the vapor space, which in turn affects the heat transport capacity of the flat heat pipe. As presented in Fig. 5 for the flat heat pipe with 6 layers of 150 screen mesh, the

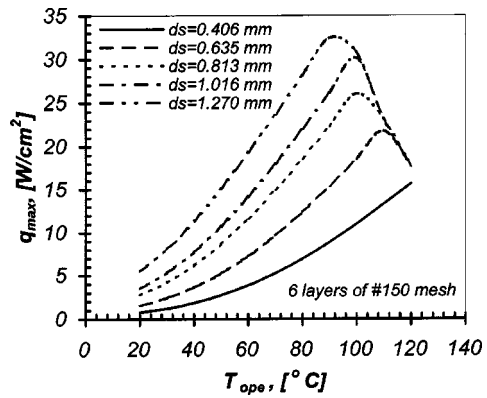


Fig. 5 Modeling results of the effect of the wire diameter on the maximum heat transport capacities of flat heat pipes

analytical results indicated that the maximum heat transfer capacity increased considerably by very small increases in the wire diameter.

Effect of the Wick Thickness. The thickness of the wick layer (in layers) is very important in the design and manufacture of the heat pipes. An increase of the layer of the mesh wick can reduce the liquid frictional pressure drop proportionally by increasing the liquid flow area, resulting in improved heat transfer capacity. However, the increase in the layer of the screen mesh results in significant increases in superheat through the wick layer, and therefore, in premature boiling limitations as indicated in Fig. 6.

The modeling results are presented in Fig. 6 for three flat heat pipes with the screen mesh number of 100, 150, and 200. The results indicate that there exist an optimum number of layers for each screen mesh structure. In addition, this optimum number of layers of screen (or thickness) is larger for the screen with larger mesh numbers. The highest maximum heat transport capacities are obtained for the optimum number of layers. The flat heat pipe with multiple layers of denser mesh wick has a much higher heat transport capacity than the one with a lower mesh number wick.

Effect of the Orientation. As mentioned previously, the tilt angle of the heat pipe has a considerable effect on the heat transport capacity by assisting or suppressing the return of the working fluid. However, the sensitiveness to the orientation is much different for various wick structures. Both model the analytical and experimental evaluation of the flat heat pipes were conducted and the results are presented in Fig. 7. Results indicated that the maximum heat transport capacity is reduced by increasing the tilt

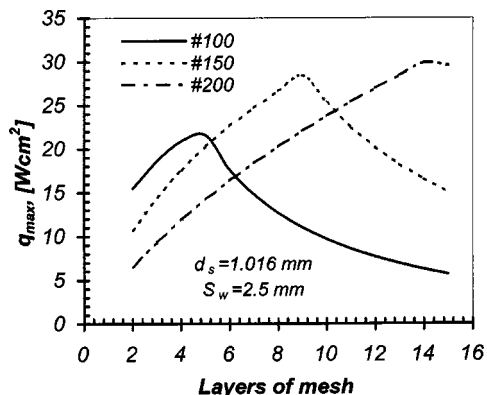


Fig. 6 Modeling results of the effect of layers of the wick on the maximum heat transport capacities of flat heat pipes

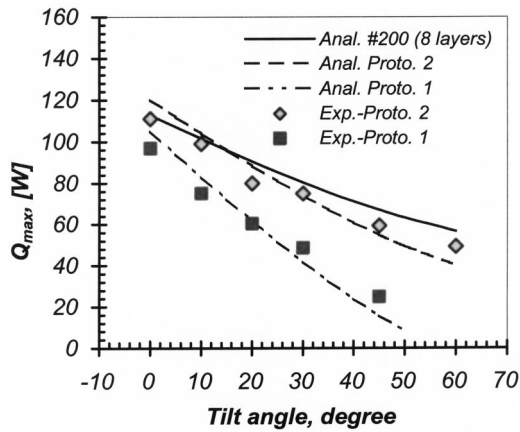


Fig. 7 Effect of the tilt angle on the maximum heat transport capacities of the flat heat pipes

angle, but that this effect is moderate, even for the wicks with larger mesh numbers. The trends of experimental results are agreeable with the analytical results. However, the experimental results both for prototype 1 and 2 were higher than the modeling results for larger tilt angles. The performance of the sintered mesh wick is better than the wrapped one because of the better effective thermal conductivity and smaller cell structure.

Effect of Length. It is apparent that longer heat pipes have lower heat transport capacities due to the larger frictional pressure drop. The effects of variations in the length on the heat transfer are illustrated in Fig. 8 for different mesh numbers. For shorter heat pipes, the boiling limit is dominant, while the capillary limit is the major limiting factor for the longer heat pipes.

Comparison of Experimental and Modeling Results. As described in the experimental investigation, two prototypes whose configurations are summarized in Table 1, were fabricated, charged, and tested in order to determine the maximum heat transport capacity and verify the modeling results. The results of this comparison are illustrated in Fig. 9 and Fig. 10 for Prototype 1 and Prototype 2, respectively. The predicted maximum heat transport capacities were in very good agreement with the experimental results when the compact coefficient of the sintered screen mesh wick was equal to 1.15. The maximum heat transport capacity of Prototype 1 was 112 W at an operating temperature of 85°C and 123 W for Prototype 2.

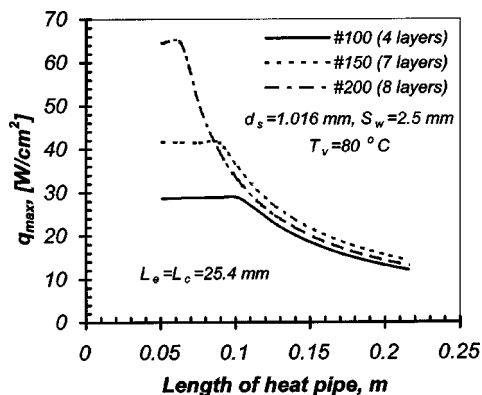


Fig. 8 Modeling result of the variation of the maximum heat flux with the length of the flat heat pipes

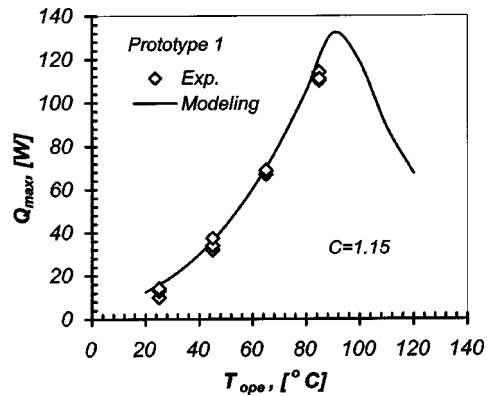


Fig. 9 A comparison of the experimental and modeling results of the Prototype 1 flat heat pipe

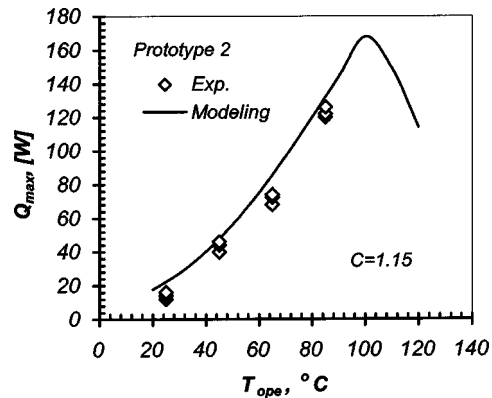


Fig. 10 A comparison of the experimental and modeling results of the Prototype flat heat pipes

Conclusions

A novel flat heat pipe has been developed and investigated both experimentally and analytically. Two prototypes with different wick configurations were evaluated. The results indicated that the maximum heat transfer capacity of the flat heat pipe was affected by the mesh number, wire diameter, number of layers, and tilt angle, as well as the sintering process utilized, i.e., the compact coefficient of the sintered screen mesh wick. Increasing the wire diameter resulted in an increase in the maximum heat transport capacity. The mesh number had opposing effects on the capillary pumping capacity and the frictional pressure drop, such that there exists a set of optimum design parameters. Similar to the mesh number, the layer number of the screen mesh also has an opposing effect on the capillary and boiling heat transfer, with the larger mesh number having a higher heat transfer capacity with more layers. The tilt angle had the greatest effect on the maximum heat transfer capacity and the impact of tilt, decreases with increasing mesh number. At higher operating temperatures, the boiling limit, which is related to the physical properties of the porous wick may be exceeded. The sintering process determined the compact coefficient, which ranged from 1.05 to 1.33, and significantly changed the properties of the screen mesh, thereby influencing the optimum design for various thermal loads.

The experimental results indicated that the maximum heat transport capacity and heat flux for Prototype 1, which utilized four layers of 100 mesh screen and a compact coefficient, of 1.15, were 112 W and 17.4 W/cm², respectively, in a horizontal position. For Prototype 2, which utilized six layers of 150 mesh screen and a compact coefficient of 1.15, these values were 123 W and

19.1 W/cm², respectively. In both cases, the experimentally obtained values compared quite well with those obtained analytically.

Acknowledgment

The authors would like to acknowledge the support of the National Science Foundation through grant CTS-0312848.

Nomenclature

| | |
|------------|---|
| \bar{A} | = Constant |
| A_c | = Cross-section area, m ² |
| a | = Constant |
| b | = Constant |
| C | = Compact coefficient |
| D_e | = Equivalent diameter, m |
| D_h | = Hydraulic diameter, m |
| d_s | = Diameter of the supporting wires, m |
| d_w | = Wire diameter of the mesh, m |
| f | = Frictional coefficient |
| g | = Gravity acceleration, m/s ² |
| H_p | = Height of the heat pipe, m |
| h_{fg} | = Latent heat of vaporization, J/kg |
| K | = Permeability, m ² |
| k | = Thermal conductivity, W/m K |
| L | = Length of the heat pipe, m |
| N | = Number of the mesh |
| P | = Pressure, Pa |
| p | = Perimeter, m |
| P_d | = Disperse pressure, Pa |
| ΔP | = Pressure drop, Pa |
| Q | = Heat load, W |
| Q_b | = Boiling heat flux, W/m ² |
| Q_c | = Capillary heat flux, W/m ² |
| Q_e | = Entrainment heat flux, W/m ² |
| r_b | = Radius of vapor bubble, m |
| r_{cap} | = Radius of liquid meniscus, m |
| S_w | = Space between wires, m |
| T | = Temperature, K |
| T_l | = Liquid-phase temperature, K |
| T_{lv} | = Liquid-vapor interface temperature, K |
| T_v | = Vapor-phase temperature, K |
| T_{ope} | = Operating temperature, K |
| t_w | = Thickness of the wall, m |
| W | = Width of the heat pipe, m |

Greek Alphabet

| | |
|---------------|--|
| α | = Contact angle, degree |
| δ | = Thickness of the film on the porous surface, m |
| δ_s | = Thickness of the screen wick, m |
| ε | = Porosity, % |
| θ | = Tilt angle, degree |
| μ | = Viscosity, N ⁻⁵ /m ² |
| ρ | = Density, kg/m ³ |
| σ | = Surface tension, N/m |

Subscripts

| | |
|-------|----------------------------|
| a | = Adiabatic, air |
| b | = Boiling |
| c | = Condensation, capillary |
| cap | = Capillary |
| e | = Evaporation, entrainment |
| eff | = Effective |
| f | = Fluid |
| g | = Gravity |
| l | = Liquid phase |
| m | = Meniscus |
| ph | = Phase-change |
| s | = Sonic |
| sat | = Saturated |
| v | = Vapor phase |

References

- [1] Plesch, D., Bier, W., Seidel, D., and Schubert, K., 1991, "Miniature Heat Pipes for Heat Removal from Microelectronic Circuits," *Proceedings of ASME Annual Meeting*, Atlanta, GA.
- [2] Hopkins, R., Faghri, A., and Khrustalev, D., 1999, "Flat Miniature Heat Pipes With Micro Capillary Grooves," *ASME J. Heat Transfer*, **121**, pp. 102–109.
- [3] Peterson, G. P., Duncan, A. B., and Weichold, M. H., 1993, "Experimental Investigation of Micro Heat Pipe Fabricated in Silicon Wafers," *ASME J. Heat Transfer*, **11**, pp. 751–756.
- [4] Peterson, G. P., 1994, *An Introduction to Heat Pipes—Modeling, Testing, and Applications*, John Wiley & Sons Inc., New York.
- [5] Faghri, A., *Heat Pipe Science and Technology*, Taylor & Francis, PA, 1995, pp. 240–245.
- [6] Wang, Y. X., and Peterson, G. P., 2003, "Investigation of the Heat Transfer Limits in Thin Capillary Wicks of Phase-Change Cooling Devices," *The 6th ASME-JSME Thermal Engineering Joint Conference*, March 16–20, Kohala, Hawaii.
- [7] Van Ooijen, H., and Hoogendoorn, C. J., 1981, "Experimental Pressure Profiles Along the Vapor Channel of a Flat-Plate Heat Pipe," *Advances in Heat Pipe Technology*, Pergamon Press, Oxford, pp. 121–129.
- [8] Mallik, A. K., and Peterson, G. P., 1992, "On the Use of Micro Heat Pipes As an Integral Part of Semiconductor Devices Arrays" *ASME J. Electron. Packag.*, **114**, pp. 436–442.
- [9] Mallik, A. K., and Peterson, G. P., 1995, "Steady-State Investigation of Vapor Deposited Micro Heat Pipe Arrays," *ASME J. Electron. Packag.*, **117**, pp. 75–87.
- [10] Peterson, G. P., Duncan, A. B., and Weichold, M. H., 1993, "Experimental Investigation of Micro Heat Pipe Fabricated in Silicon Wafers," *ASME J. Heat Transfer*, **11**, pp. 751–756.
- [11] Wang, Y. X., and Peterson, G. P., 2002, "Investigation of Wire-Bonded Micro Heat Pipes," *AIAA J.*, **16**, pp. 346–355.
- [12] Wang, Y. X., and Peterson, G. P., 2003, "Flat Heat Pipe Cooling Devices for Laptop/Mobile Computers," *ASME INTERPACK03 Int'l Electronic Packaging Conf. and Expo.*, July 6–11, Maui, Hawaii.
- [13] Bejan, A., 1985, *Convection Heat Transfer*, John Wiley & Sons, New York, pp. 77–82.
- [14] Shah, R. K., and Bhatti, M. S., 1987, "Laminar Convective Heat Transfer in Ducts," *Handbook of Single-Phase Convective Heat Transfer*, Wiley, New York, pp. 3.45–3.70.
- [15] Wang, Y. X., and Peterson, G. P., 2002, "Investigation of h_{tin} Film Evaporation Limit in Single Screen Mesh Layer," *Proceedings of the 2002 ASME Int'l Mechanical Enr. Conf. and Expo.*, November 17–22, New Orleans, LA.
- [16] Cary V. P., 1992, *Liquid-Vapor Phase-Change Phenomena: An Introduction to the Thermophysics of Vaporization and Condensation Process in Heat Transfer Equipment*, Hemisphere Publishing Corporation, Washington, p. 140.

Heat Transfer Enhancement for Finned-Tube Heat Exchangers With Winglets

James E. O'Brien
Manohar S. Sohal

Idaho National Engineering and Environmental
Laboratory,
Idaho Falls, ID 83415

This paper presents the results of an experimental study of forced convection heat transfer in a narrow rectangular duct fitted with a circular tube and/or a delta-winglet pair. The duct was designed to simulate a single passage in a fin-tube heat exchanger. Heat transfer measurements were obtained using a transient technique in which a heated airflow is suddenly introduced to the test section. High-resolution local fin-surface temperature distributions were obtained at several times after initiation of the transient using an imaging infrared camera. Corresponding local fin-surface heat transfer coefficient distributions were then calculated from a locally applied one-dimensional semi-infinite inverse heat conduction model. Heat transfer results were obtained over an airflow rate ranging from 1.51×10^{-3} to 14.0×10^{-3} kg/s. These flow rates correspond to a duct-height Reynolds number range of 670–6300 with a duct height of 1.106 cm and a duct width-to-height ratio, W/H , of 11.25. The test cylinder was sized such that the diameter-to-duct height ratio, D/H is 5. Results presented in this paper reveal visual and quantitative details of local fin-surface heat transfer distributions in the vicinity of a circular tube, a delta-winglet pair, and a combination of a circular tube and a delta-winglet pair. Comparisons of local and average heat transfer distributions for the circular tube with and without winglets are provided. Overall mean fin-surface Nusselt-number results indicate a significant level of heat transfer enhancement associated with the deployment of the winglets with the circular cylinder. At the lowest Reynolds numbers (which correspond to the laminar operating conditions of existing geothermal air-cooled condensers), the enhancement level is nearly a factor of 2. At higher Reynolds numbers, the enhancement level is close to 50%. [DOI: 10.1115/1.1842786]

Introduction

Air-cooled condensers used in binary-cycle geothermal power plants require the use of finned tubes in order to increase heat transfer surface area on the air side. Air is forced through several rows of these finned tubes by large fans. The condenser units can be very large, representing approximately 50% of the overall capital cost of these plants. In addition, the power required to operate the fans represents a significant parasitic house load, reducing the net power production of the plant. The research presented in this paper has been undertaken with the aim of devising viable heat transfer enhancement strategies for application to geothermal air-cooled condensers and similar applications. An effective strategy can result in a reduction in condenser size (and plant capital cost) and/or power consumption.

One heat transfer enhancement strategy that has been studied in some detail is the exploitation of longitudinal vortices to increase heat transfer coefficients with only small increases in pressure-drop penalty. Longitudinal vortices are generated naturally in fin-tube heat exchanger passages by the interaction of the flow with the heat exchanger tube. In this case, the vortices are called horse-shoe vortices. Longitudinal vortices can also be created intentionally through the use of winglet vortex generators mounted or punched into the fin surfaces. Jacobi and Shah [1] provide an excellent review of heat transfer enhancement through the use of longitudinal vortices. Various winglet shapes have been studied. Results presented in the present paper are restricted to delta winglets, both as a delta-winglet pair (no tube) and in conjunction with a circular tube. Heat transfer enhancement with double rows of longitudinal vortex-generators (delta-winglet pairs) in a channel flow without tubes has been evaluated experimentally by

Tiggelbeck et al. [2]. An investigation of the mechanisms of heat transfer enhancement associated with delta-wing vortex generators was performed by Torii et al. [3]. The specific configuration of vortex generators plus circular tube used in the present study was based on recommendations provided by Fiebig et al. [4]. We are also investigating the usage of oval tubes instead of circular tubes with or without winglets [5,6] for the geothermal application. Base line local heat transfer measurements for both circular and oval tubes without winglets were obtained previously by the present authors and are presented in Ref. [7].

In order to assess the heat transfer effectiveness of various combinations of tube and vortex-generator geometries, a heat transfer measurement technique that allows for high-resolution visualization and measurement of local heat transfer was chosen for this work. The focus of the work presented in this paper was to document local heat transfer distributions for two cases: a delta-winglet pair with no tube, and a delta-winglet pair positioned in the downstream wake region of a circular tube. During the next phase of the research, delta-winglet vortex generators will be placed in the test section in various configurations with an oval tube. Subsequent research will involve measurement of local heat transfer and pressure drop in single-channel, multiple-tube geometries with winglets. Finally, overall heat transfer and pressure drop will be evaluated for a multiple-channel, multiple-tube-row prototype heat exchangers. Concurrent numerical studies are under way. The numerical studies should allow for evaluation of many more configurations than can be studied experimentally. The ultimate goal is to devise optimal heat exchanger geometries for the geothermal air-cooled condenser application.

Apparatus

The experiments were performed in a narrow rectangular duct designed to simulate a single passage of a fin-tube heat exchanger. A drawing of the test section is shown in Fig. 1. Dimensions of

Manuscript received November 7, 2003; revision received April 21, 2004. Review conducted by: P. M. Ligrani.

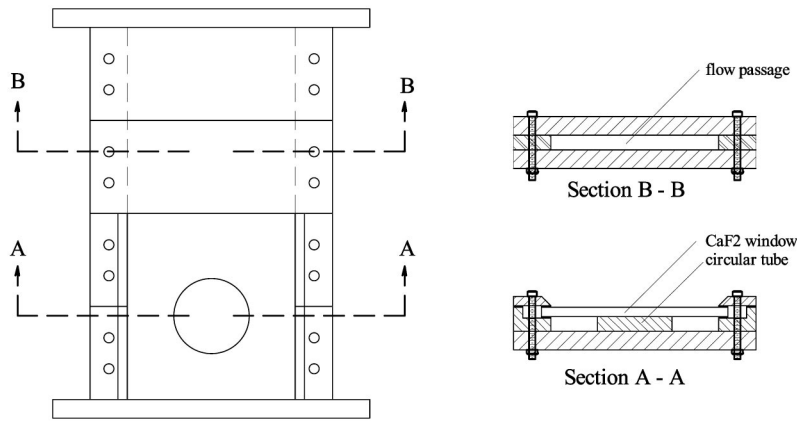


Fig. 1 Test section

the flow channel were width, $W=11.4$ cm, height, $H=1.0$ cm (4.5 in. \times 0.4 in.). It is scaled up to approximately double-size compared to a typical fin-tube condenser heat exchanger. The duct was fabricated primarily out of lexan polycarbonate. For the circular-tube tests, a 5.08 cm (2.0 in.) diameter circular disk, representing the tube of a fin-tube heat exchanger, also fabricated from lexan, was positioned in the center of the duct as shown. The test section length was 27.94 cm (11.0 in.), yielding $L/H=27.5$. A flow-development section with $L/H=30$ was located upstream of the test section. Consequently, depending on Reynolds number, the flow is approximately hydrodynamically fully developed as it enters the test section.

In order to enable thermal visualization of the test section bottom surface (representing the fin surface), the top wall of the flow duct in the vicinity of the circular tube was formed by calcium fluoride (CaF_2) windows. Initial testing (single circular tube, delta-winglet pair) was performed using two CaF_2 windows, each 12.7 cm \times 6.35 cm \times 6 mm (5 in. \times 2.5 in. \times 0.24 in.). Subsequent testing with the circular tube plus winglets was performed using a single larger window, 12.7 cm \times 12.7 cm \times 6 mm (5 in. \times 5 in. \times 0.24 in.). The CaF_2 windows enabled viewing of test section bottom surface with an imaging infrared camera. Lexan is opaque in the sensitive wavelength range of the camera (3.6–5 μm). The transmissivity of the CaF_2 windows is very high (>95%) in this wavelength range. The test section bottom surface (polycarbonate) was painted black using ultraflat black paint in order to achieve a

surface emissivity very close to 1.0. This emissivity value was verified over a wide temperature range in separate camera-calibration tests by comparing camera-indicated temperatures with surface temperatures measured using a precision thin-foil flush-mounted thermocouple bonded to a black-painted polycarbonate test surface. Therefore no emissivity corrections were required for the infrared temperature measurements.

A transient heat transfer measurement technique was employed for obtaining detailed local heat transfer measurements on the model fin surface. A schematic of the flow loop is shown in Fig. 2. Inlet air is heated to a desired setpoint temperature using an in-line feedback-controlled finned-element air heater (350 W). The heated air initially flows through a bypass line until the desired air temperature and flow rate is established. The air is then suddenly diverted through the test section by changing the position of a three-way valve. Using this technique, the room-temperature fin/tube model is suddenly exposed to a uniformly heated airflow, thereby inducing a heat conduction transient in the lexan substrate. Local surface temperatures on the substrate increase at a rate that is dependent on the value of the local heat transfer coefficient. This transient localized heating is quantitatively recorded using an imaging infrared camera. Values of local heat transfer coefficients can then be determined from an inverse heat conduction analysis.

The bypass flow is diverted from the main flow duct through a

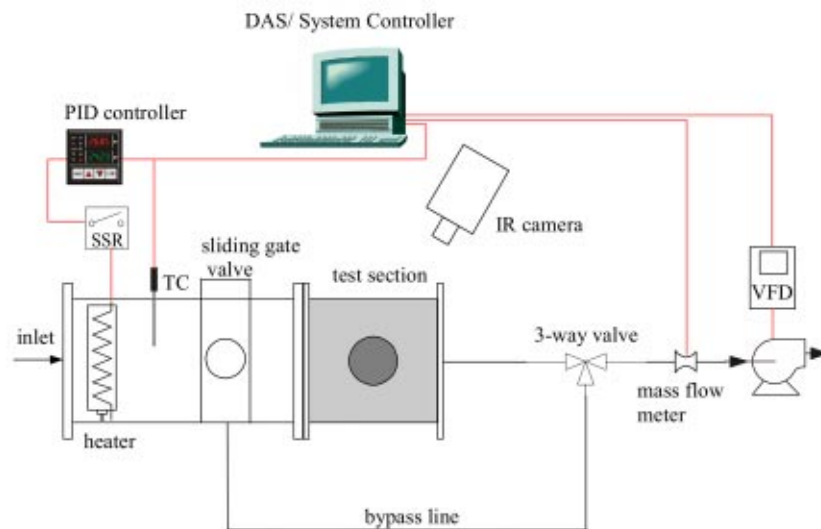


Fig. 2 Schematic of flow loop

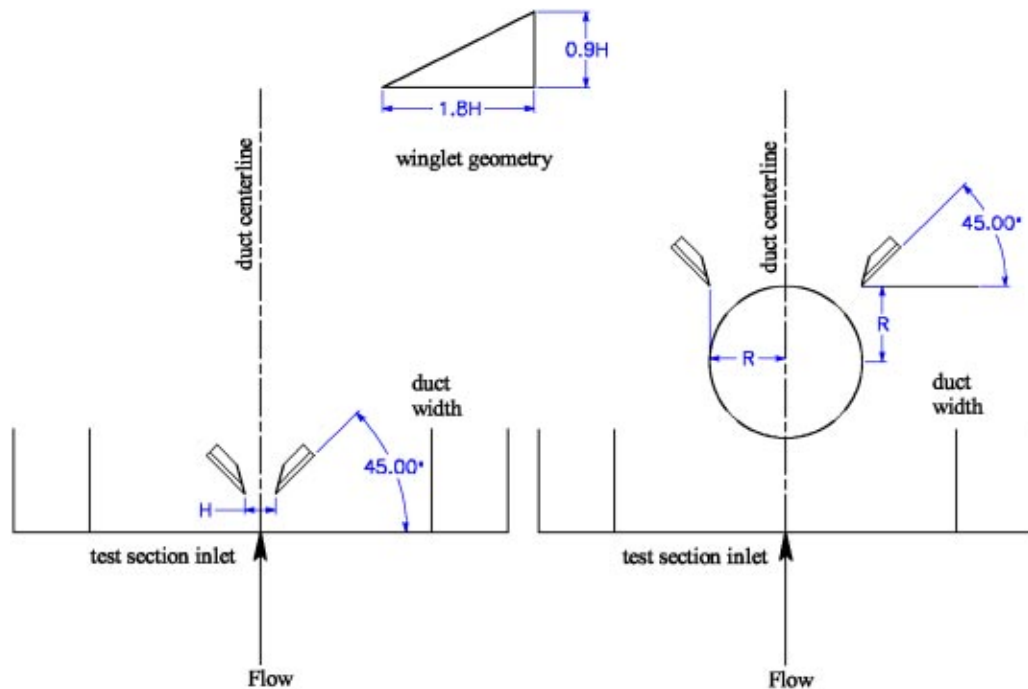


Fig. 3 Winglet locations and geometry: (a) winglet-only case, (b) circular cylinder plus winglets

circular hole (4.85 cm diameter) cut into the bottom of the flow-development section. The center of the hole is located 8.25 cm (3.25 in.) upstream of the test section entrance. The duct walls downstream of this location are not preheated during the flow establishment period. Therefore, this distance represents a thermal entry length. When flow is suddenly initiated through the test section by changing the position of the three-way valve, the flow bypass hole in the bottom of the flow development section is covered by sliding a flat lexan cover (sliding gate valve) over the hole. This procedure provides a continuous flat smooth flow surface, eliminating any concerns about a cavity-type flow disturbance associated with the hole.

Heater control is accomplished using a PID controller (Yokogawa model 514) coupled to a solid-state relay with a pulsed relay output. A thermocouple mounted inside the duct measures the process variable. Air temperature uniformity across the duct was verified via infrared imaging of the test surface during preliminary tests with no test cylinder in place. Airflow rate is monitored through the use of an in-line precision mass-flow meter (Kurz model 504FT) plumbed into the exhaust line. Test-section mass-average velocities and Reynolds numbers were calculated based on the SCM values obtained from the mass-flow meter. Air is drawn through the system by a centrifugal blower (1/3 HP, 240 V three-phase) located at the flow exit. Blower speed is controlled by a sub-micro inverter variable-frequency drive (AC Tech model SF215), which in turn is controlled by a computer-generated 4–20 mA control signal. System flow rate varies linearly with blower speed over the range used in this study from about 1.51×10^{-3} to 14.0×10^{-3} kg/s. These flow rates correspond to a duct-height Reynolds number ($Re_H = \rho UH / \mu = \dot{m} / \mu W$) range of 670–6300 with a duct height of 1.106 cm and a duct width-to-height ratio, W/H , of 11.25.

Two flush-mounted thin-foil thermocouples were bonded to the bottom surface of the test section near the test section inlet. These thermocouples provide a continuous indication of surface temperature at two locations and are used to help determine the exact start time of each test, which occurs when the heated airflow is diverted through the test section.

Heat transfer results will be presented for three experimental configurations: circular tube, delta-winglet pair, and circular tube

plus delta-winglet pair. The test section geometry for the circular tube was presented in Fig. 1. The specific geometries for the delta-winglet pair and the circular tube plus delta-winglet pair are presented in Fig. 3. The winglets had a 1:2 height/length aspect ratio and were oriented at a 45 deg angle to the flow. The height of the winglets was 90% of the channel height. This height was chosen rather than the full channel height in order to avoid damage to the CaF_2 windows. The winglets were machined from lexan polycarbonate and were bonded to the test surface. The test configuration for the winglet-only tests is shown in Fig. 3(a). For these tests, the winglets were located near the test section inlet and were spaced one channel height apart. The test configuration for the circular tube plus delta-winglet pair tests is shown in Fig. 3(b). The location of the winglets for these tests was based on the geometry recommended in Ref. [4]. The winglet tips are located downstream of the test cylinder at the intersection of the horizontal and vertical cylindrical-tube tangent lines. The angular orientation with respect to the flow was again 45 deg.

Quantitative thermal visualization images are obtained using a precision imaging infrared camera (FLIR PRISM DS). This camera uses a fully calibrated 320×244 platinum-silicide infrared (IR) charge coupled device focal plane array detector which operates at a temperature of 77 K. The detector temperature is maintained by a mechanical split-stirling-cycle helium cryocooler. In its base mode of operation, the camera can be used to measure infra-red intensities corresponding to temperatures in the -10 – 250°C range, with extended ranges available through the use of filters up to 1500°C . The camera detector has a 12-bit digital dynamic range and a minimum discernible temperature difference of 0.1°C at 30°C . It is equipped with a 25 mm standard lens, which provides a $17^\circ \times 13^\circ$ field of view. All radiometric information is stored in binary digital files on PCMCIA flash memory cards for subsequent analysis. Infra-red thermography has several advantages over thermochromic liquid crystals for surface temperature mapping, including wide available temperature range, high spatial resolution, excellent thermal resolution, and full-field direct digital data acquisition and processing.

The thermal image binary data files created by the camera on-board processor are stored in a specialized 16-bit TIFF gray-scale format (file extension.ana). These files include not only the image

pixel values, but also a large amount of camera and test-specific information such as camera and firmware identifiers, date and time of image acquisition, camera settings at image acquisition, and temperature/pixel calibration data points. This information is included in the TIFF file in the form of "private tags" [8]. Specific file-format information provided by FLIR was used in conjunction with general information about the TIFF standard found in Ref. [8] to fully decode the binary data files for subsequent thermal analysis using a Labview program created for this purpose.

Signals from loop instrumentation were fed into a modular multiplexing data-acquisition system (Hewlett Packard 3852A) which in turn was interfaced to a system-controller computer via an IEEE-488 bus. For this experiment, the data acquisition unit was configured with a 20-channel field-effect transistor (FET) multiplexer with thermocouple compensation, a 5 1/2 digit integrating voltmeter, and a four-channel voltage/current digital-to-analog converter (DAC). The DAC module was used to provide control signals (4–20 mA) to the variable-frequency blower drive. The mass-flow meter was configured to communicate directly with the computer using an RS-232 interface. Data-acquisition and instrument-control system programming was accomplished using Labview (National Instruments version 5.1) software. The data files included time histories of the thermocouple and mass-flow meter signals with updates at 0.7 s intervals.

Experimental Procedure

As mentioned previously, a transient heat transfer technique was employed in order to obtain measurements of local heat transfer coefficients on model fin surfaces. Details of the experimental procedure will now be provided. After the IR camera is powered up and the detector array has reached its 77 K operating temperature, the camera is positioned above the test section at an appropriate height for observing either the entire portion of the test section or a close-up view. In order to avoid IR reflections of the warm camera body off the CaF₂ windows, the camera is positioned at a small angle off the vertical. The camera gain and level adjustments are set such that the minimum observable temperature corresponds to the initial temperature with a temperature range of 10–15°C. The software clock on the camera is synchronized with the clock on the data acquisition computer to within ±0.5 s. The three-way valve is set to the bypass position and the sliding gate valve is opened. Flow is initiated through the bypass line by adjusting the blower RPM until the desired flow rate is observed. The air temperature is established by adjusting the PID controller set-point value to the desired level, typically 45°C. Before diverting heated air through the test section, a pretest thermal image of the test section is acquired. At this time, the data acquisition system is set to begin writing data to disk. The three-way valve position is then changed and the sliding gate valve is closed to divert the heated airflow through the test section, initiating the thermal transient. A number of thermal images of the test section (typically 5) are acquired during the first 5–60 s of the transient. These images are stored on PCMCIA flash memory cards and are transferred to the system controller computer after each test.

Data Reduction

The objective of the tests is to obtain detailed maps of local heat transfer coefficient. The IR images provide local surface temperatures at specified times after initiation of the transient. In order to obtain heat transfer coefficients from the measured surface temperatures, the bottom surface of the test section is assumed to behave locally as a one-dimensional semi-infinite solid undergoing a step change in surface heat transfer coefficient. For the 1.27 cm thickness of the lexan test surface, the semi-infinite assumption is valid for at least 88 s after initiation of the transient. The time-dependent surface ($x=0$) temperature for a semi-infinite solid subjected to this boundary condition is given by [9]

$$\frac{T(0,t) - T_i}{T_\infty - T_i} = 1 - \exp\left(\frac{h^2 \alpha t}{k^2}\right) \operatorname{erfc}\left(\frac{h\sqrt{\alpha t}}{k}\right) \quad (1)$$

and if we let

$$\theta = \frac{T(0,t) - T_i}{T_\infty - T_i}; \gamma = \frac{h\sqrt{\alpha t}}{k} = \frac{h\sqrt{t}}{\sqrt{\rho c k}} \quad (2)$$

the equation reduces to

$$\theta = 1 - \exp(\gamma^2) \operatorname{erfc}(\gamma) \quad (3)$$

This equation represents the relationship between heat transfer coefficient and surface temperature measured at a specific time after the start of the test. It must be solved iteratively for γ . However, since the camera pixel array includes over 78,000 pixels, it is not practical to directly solve the equation at every pixel. Instead, a look-up-table approach was used in the data-reduction scheme. The measured temperature range for each thermal image is divided into 100 increments and a value of heat transfer coefficient is obtained for each of these 100 temperatures by iteratively solving Eq. (3). Each actual pixel temperature is then converted to a heat transfer coefficient by linear interpolation among the 100 increments.

Experimental Uncertainty

Estimates of the experimental uncertainties of the Reynolds numbers and heat transfer coefficients presented in this paper have been obtained based on constant-odds, 95% confidence level [10]. For Reynolds number, the uncertainties associated with the mass-flow meter and the viscosity need to be considered. The accuracy specification for the mass-flow meter was stated by the manufacturer (and independently verified at the INEEL calibration laboratory) as ±2% of reading plus 0.5% of full scale. The uncertainty in the viscosity is very small, since it is calculated quite accurately for each run at the measured duct air temperature as part of the data reduction procedure. Total relative uncertainty in Reynolds number was estimated to be about 9% at $Re_H=670$ and 2.5% at $Re_H=6300$. For the heat transfer coefficients, individual uncertainties in image-capture time, surface temperature, air temperature, and substrate thermal product were considered. Results indicated that the relative uncertainty in heat transfer coefficient ranges from 20% at $h \sim 10$ W/m² K to 10% at $h \sim 120$ W/m² K.

Results

Local surface heat transfer contour plots for the delta-winglet-pair configuration are presented in Fig. 4. Heat transfer results are presented as a function of Reynolds number based on channel height, H . Heat transfer coefficients are based on the test section inlet temperature. The results presented in Fig. 4 reveal the heat transfer effects of a double-vortex system associated with each winglet [3]. The vortices are swept downstream as longitudinal vortices. The main vortex, located directly downstream of the vortex generators, is formed by flow separation along the leading edge of the winglets. The corner vortex, located outside of the main vortex, develops like a horseshoe vortex on the upstream-facing pressure side of the winglets. The heat transfer effects of the vortices persist for many channel heights (at least 15) downstream of the winglet location. The horizontal line near the center of each heat transfer distribution is an artifact caused by the boundary between two of the CaF₂ windows. The small circular white region in the center of each image just below the horizontal window boundary is a bolt hole used to attach a circular disk for the fin/tube studies to be discussed later in this paper. This hole was covered with tape on the outside substrate surface to avoid any flow disturbance. Apparent heat transfer coefficient values on the winglets themselves are not valid since the one-dimensional semi-infinite assumption does not apply at this location.

At low Reynolds numbers, maximum fin-surface heat transfer coefficients are observed in the main vortex downstream of the

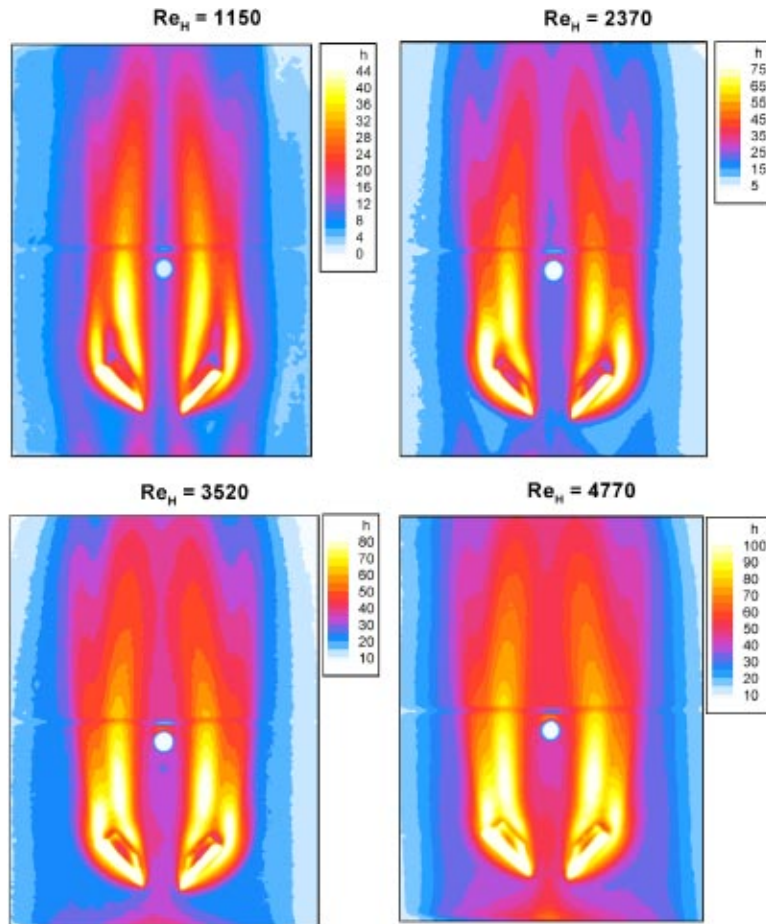


Fig. 4 Local fin-surface heat transfer coefficients for a delta-winglet pair

winglets. At higher Reynolds numbers, maximum values are associated with the corner vortex, very close to the outer corner of the winglets. The magnitudes of these peak values are similar to the peak values observed in the same duct in the stagnation region of a circular cylinder, as reported in Ref. [7]. The peak values are about 4–5 times larger than corresponding fully developed duct values. However, mean surface heat transfer coefficient values for the configuration displayed in Fig. 4 are just about equal to the corresponding fully developed duct values, as predicted using the Dittus–Boelter correlation, with Reynolds number based on the

hydraulic diameter of the rectangular duct. The individual vortices appear to be most well defined at the lowest Reynolds number shown. Lowest heat transfer coefficients occur in the corner regions of the rectangular duct, which are at the sides of the images shown in Fig. 4.

The spanwise variation in local fin-surface heat transfer coefficient for the delta-winglet-pair configuration is presented in Fig. 5 at two different axial measurement locations. The coordinate system used is defined in the figure. These plots clearly show the heat transfer effects of the winglet-induced double-vortex system. The

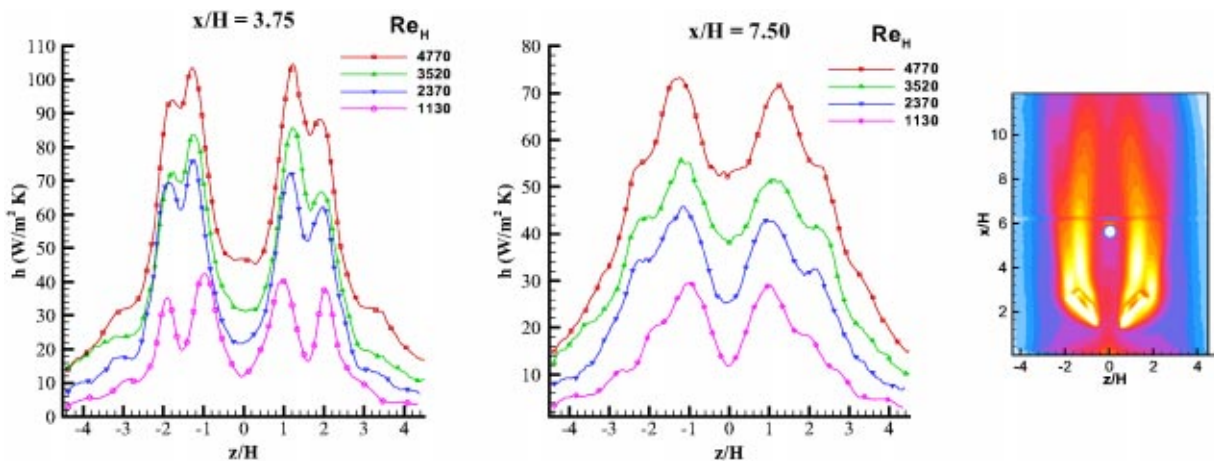


Fig. 5 Spanwise variation of local heat transfer coefficient for delta-winglet-pair configuration

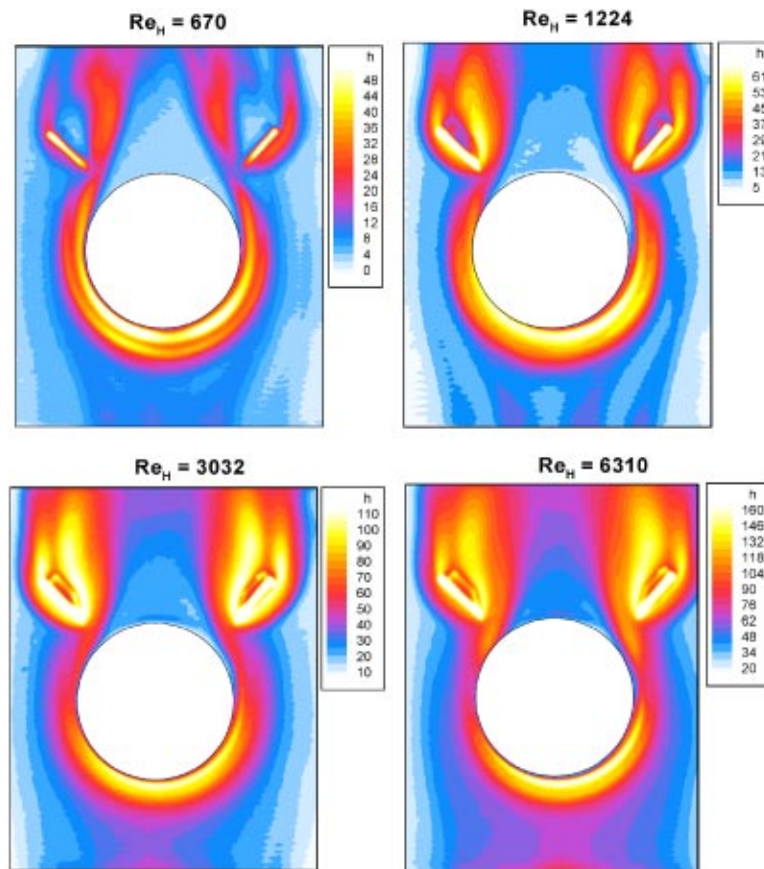


Fig. 6 Local fin-surface heat transfer distributions for circular cylinder plus winglets

local spanwise variation in heat transfer coefficient at $x/H = 3.75$, which is just downstream of the winglets, shows very sharp double peaks in local heat transfer associated with each vortex generator. For all of the Reynolds numbers shown, the highest heat transfer coefficients at each axial location are associated with the primary vortex. The magnitude of the local heat transfer coefficient decreases sharply from the peak values to a minimum near the sides of the rectangular duct. At $y/H = 7.50$, the spanwise heat transfer variations are broader, and the peak associated with the corner vortex is visible, but indistinct.

The second configuration considered for this study was the case of a circular cylinder plus winglets (see Fig. 3 for geometry specifics). Local fin-surface heat transfer results for this configuration are presented in Fig. 6 for four Reynolds numbers. The addition of winglets yields a reduction in the size of the low-heat-transfer wake region and also provides localized heat transfer enhancement in the vicinity of the winglets similar in magnitude to the localized enhancement observed for the delta-winglet-pair cases shown in Fig. 4. With the exception of the lowest Reynolds number case, peak local heat transfer coefficients in the vicinity of the winglets are similar to the peak values observed in the cylinder stagnation region. A distinct double peak in local heat transfer coefficient can be seen in the cylinder stagnation region at $Re_H = 670$. This double peak was discussed in some detail in Ref. [7] for a cylinder without winglets. The spanwise streaks evident near the test section inlet for $Re = 1224$ are associated with secondary flows that become established in the flow development section of the rectangular duct.

A direct comparison of local heat transfer distributions for a circular cylinder with and without winglets at $Re_H \sim 1200$ is presented in Fig. 7. The comparison reveals that, for this winglet location, the horseshoe vortex produced by the interaction of the

flow with the circular cylinder is disrupted by the winglets. There is a reduction in the width of the low-heat-transfer wake region, but the heat transfer coefficients directly downstream of the cylinder are actually slightly reduced for the winglet case compared to the no-winglet case. Stagnation-region heat transfer coefficients are slightly higher for the winglet case compared to the no-winglet case.

A plot of the spanwise variation in local wake-region heat transfer coefficient at an axial location just downstream of the winglets is presented in Fig. 8 for the same two data sets presented in Fig. 7. The spanwise variation for the winglet case clearly shows a double peak associated with each winglet. A single peak associated with each horseshoe vortex is evident in the no-winglet curve.

Overall mean fin-surface Nusselt numbers calculated from the heat-transfer-coefficient data files are presented in Fig. 9. For calculation of mean Nusselt numbers, the regions occupied by the winglets and the cylinder (if applicable) were not included. The characteristic dimension used here for both the Reynolds number and the Nusselt number is the channel height, H . This characteristic dimension was chosen for consistency with previous related literature [1–6]. Results from three configurations are included in the figure: delta-winglet pair (no cylinder), circular cylinder without winglets, and circular cylinder with winglets. In addition, a curve representing the Dittus–Boelter correlation for turbulent duct flow is included. Per accepted practice [9], the Dittus–Boelter results were calculated using the duct hydraulic diameter as the characteristic dimension. The Reynolds and Nusselt numbers were then converted to the form based on the duct height, H . It should be noted that since the hydraulic diameter for this duct is almost twice the duct height, transition to turbulence would be expected to occur at a Re_H value of approximately 1250.

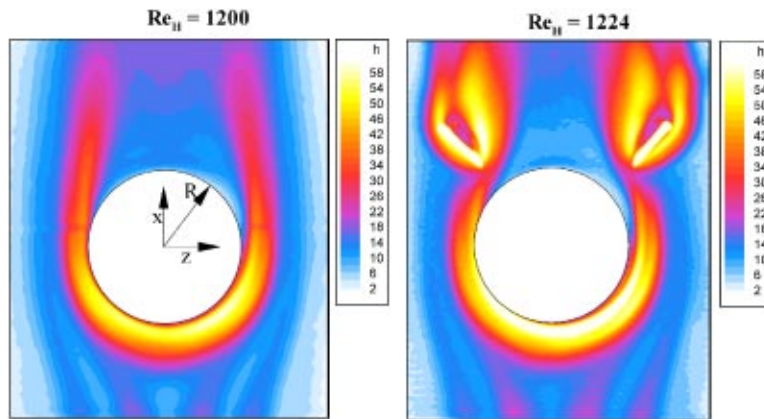


Fig. 7 Direct comparison of local heat transfer distributions for a circular cylinder with and without winglets

Results presented in Fig. 9 indicate a significant level of heat transfer enhancement associated with the deployment of the winglets with the circular cylinder. At the lowest Reynolds numbers (which correspond to the laminar operating conditions of existing geothermal air-cooled condensers), the enhancement level is nearly a factor of 2. At higher Reynolds numbers, the enhancement level is close to 50%. Mean Nusselt numbers for the cylinder-only case and the winglet-only case were very similar to each other and very close to the Dittus–Boelter correlation. The agreement with Dittus–Boelter is surprising since this correlation applies to fully developed turbulent pipe (or duct) flow without any protuberances in the flow. Low heat transfer coefficient values in the corner regions of the duct were included in the calculation of the mean values. Also, when the cylinder is in place, high stagnation-region local heat transfer is offset by the low wake-region values.

A complete evaluation of the usefulness of the addition of winglets to the fin surfaces in a actual heat exchanger must account for the increase in pressure drop associated with the winglets. Work is currently under way on obtaining these measurements.

Summary and Conclusions

An experimental study has been performed on local heat transfer in a narrow rectangular duct fitted with a circular tube, and/or

winglet vortex generators. The duct was designed to simulate a single passage in a fin-tube heat exchanger with a duct height of 1.106 cm and a duct width-to-height ratio, W/H , of 11.25. The test section length yielded $L/H=27.5$ with a flow development length of $L/H=30$. The test cylinder was sized to provide a diameter-to-duct height ratio, D/H of 5.

Heat transfer measurements were obtained using a transient technique in which a heated airflow was suddenly introduced to the ambient-temperature test section. High-resolution local test-surface temperature distributions were obtained at several times after initiation of the transient using an imaging infrared camera. Corresponding local fin-surface heat transfer coefficient distributions were calculated from a locally applied one-dimensional semi-infinite inverse heat conduction model. Heat transfer results were obtained over an airflow rate ranging from 1.51×10^{-3} to 14.0×10^{-3} kg/s. These flow rates correspond to a duct-height Reynolds number range of 670–6300.

Local heat transfer distributions observed for the case of a delta-winglet pair with no tube show the effects of a double-vortex system associated with each winglet. Peak vortex-induced heat transfer coefficients are about 4–5 times larger than corresponding fully developed duct values. However, mean surface heat transfer coefficient values for the delta-winglet pair configuration are just about equal to the corresponding fully developed duct values, as predicted using the Dittus–Boelter correlation, with Reynolds number based on the hydraulic diameter of the

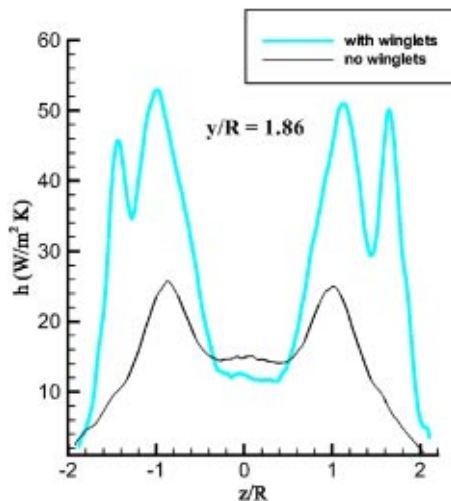


Fig. 8 Spanwise variation in local wake-region heat transfer coefficient, with and without winglets, $Re_H=1200$

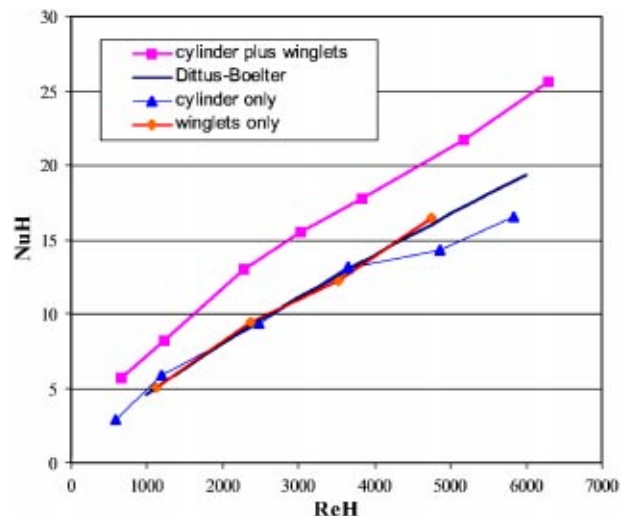


Fig. 9 Mean Nusselt numbers

rectangular duct. The local spanwise variation in heat transfer coefficient at $x/H=3.75$, which is just downstream of the winglets, shows very sharp double peaks in local heat transfer associated with each vortex generator. For all of the Reynolds numbers shown, the highest heat transfer coefficients at each axial location are associated with the primary vortex.

Heat transfer results for the circular-cylinder-plus-winglets configuration indicate that the addition of winglets yields a reduction in the size of the low-heat-transfer wake region and also provides localized heat transfer enhancement in the vicinity of the winglets similar in magnitude to the localized enhancement observed for the delta-winglet-pair-only cases. With the exception of the lowest Reynolds number case, peak local heat transfer coefficients in the vicinity of the winglets are similar to the peak values observed in the cylinder stagnation region.

Overall mean fin-surface Nusselt numbers indicate a significant level of heat transfer enhancement associated with the deployment of the winglets with the circular cylinder. At the lowest Reynolds numbers (which correspond to the laminar operating conditions of existing geothermal air-cooled condensers), the enhancement level is nearly a factor of 2. At higher Reynolds numbers, the enhancement level is close to 50%. Mean Nusselt numbers for the cylinder-only case and the winglet-only case were very similar to each other and very close to the Dittus-Boelter correlation.

Acknowledgments

This work was sponsored by the U.S. Department of Energy, Geothermal Program. The Idaho National Engineering and Environmental Laboratory is operated by Bechtel, Babcock and Wilcox Idaho, LLC under Contract No. DE-AC07-99ID13727.

Nomenclature

| | |
|---------------|--|
| D | = cylinder diameter, cm |
| h | = heat transfer coefficient, $W/m^2 K$ |
| H | = channel height, cm |
| k | = lexan thermal conductivity, $W/m K$ |
| L | = test section length, cm |
| \dot{m} | = air mass flow rate, kg/s |
| $Nu_H = hH/k$ | = Nusselt number based on channel height |

| | |
|--------------------------------------|--|
| R | = cylinder radius, cm |
| $Re_H = \rho UH/\mu$ | = Reynolds number based on channel height |
| t | = time, s |
| T | = temperature, K |
| T_i | = initial temperature, K |
| T_∞ | = flow mean temperature, K |
| U | = mean flow velocity, m/s |
| W | = channel width, cm |
| x | = test section axial coordinate, or semi-infinite solid depth coordinate, cm |
| z | = test section spanwise coordinate |
| α | = lexan thermal diffusivity, m^2/s |
| $\gamma = h\sqrt{x}/\sqrt{\rho c k}$ | = nondimensional heat transfer coefficient |
| $\theta = T(0,t)$ | |
| $-T_i/T_\infty - T_i$ | = nondimensional temperature difference |
| μ | = air absolute viscosity, $N s/m^2$ |

References

- [1] Jacobi, A. M., and Shah, R. K., 1995, "Heat Transfer Surface Enhancement through the Use of Longitudinal Vortices: A Review of Recent Progress," *Exp. Therm. Fluid Sci.*, **11**, 295–309.
- [2] Tiggelbeck, S., Mitra, N. K., and Fiebig, M., 1993, "Experimental Investigations of Heat Transfer Enhancement and Flow Losses in a Channel with Double Rows of Longitudinal Vortex Generators," *Int. J. Heat Mass Transfer*, **36**(9), 2327–2337.
- [3] Torii, K., Nishino, K., and Nakayama, K., 1994, "Mechanism of Heat Transfer Augmentation by Longitudinal Vortices in a Flat Plate Boundary Layer," *Proc. Tenth Int. Heat Transfer Conf.*, Hemisphere, New York, Vol. 6, pp. 123–128.
- [4] Fiebig, M., Valencia, A., and Mitra, N. K., 1993, "Wing-Type Vortex Generators for Fin-and-Tube Heat Exchangers," *Exp. Therm. Fluid Sci.*, **7**, 287–296.
- [5] Chen, Y., Fiebig, M., and Mitra, N. K., 1998, "Conjugate Heat Transfer of a Finned Oval Tube Part B: Heat Transfer Behaviors," *Numer. Heat Transfer, Part A*, **33**, 387–401.
- [6] Chen, Y., Fiebig, M., and Mitra, N. K., 1998, "Heat Transfer Enhancement of a Finned Oval Tube with Punched Longitudinal Vortex Generators In-line," *Int. J. Heat Mass Transfer*, **41**, 4151–4166.
- [7] O'Brien, J. E., and Sohal, M. S., 2000, "Local Heat Transfer for Finned-Tube Heat Exchangers using Oval Tubes," *Proceedings, 2000 ASME National Heat Transfer Conference*, Pittsburgh, August, Paper no. NHTC2000-12093.
- [8] "TIFF revision 6.0," 1992 Adobe Developers Association, Adobe System Incorporated, June.
- [9] Incropera, F. P., and DeWitt, D. P., 1990, *Fundamentals of Heat and Mass Transfer*, 3rd ed., J. Wiley, New York.
- [10] Moffatt, R. J., 1982, "Contributions to the Theory of Single-Sample Uncertainty Analysis," *ASME J. Fluids Eng.*, **104**, 250–260.

An Analytical Study of Heat Transfer in Finite Tissue With Two Blood Vessels and Uniform Dirichlet Boundary Conditions

Devashish Shrivastava

Department of Mechanical Engineering,
University of Utah,
Salt Lake City, UT 84102

Benjamin McKay

Department of Mathematics,
University of Utah,
Salt Lake City, UT 84102

Robert B. Roemer

Department of Mechanical Engineering,
University of Utah,
Salt Lake City, UT 84102
e-mail: bob.roemer@utah.edu

Counter-current (vessel–vessel) heat transfer has been postulated as one of the most important heat transfer mechanisms in living systems. Surprisingly, however, the accurate quantification of the vessel–vessel, and vessel–tissue, heat transfer rates has never been performed in the most general and important case of a finite, unheated/heated tissue domain with noninsulated boundary conditions. To quantify these heat transfer rates, an exact analytical expression for the temperature field is derived by solving the 2-D Poisson equation with uniform Dirichlet boundary conditions. The new results obtained using this solution are as follows: first, the vessel–vessel heat transfer rate can be a large fraction of the total heat transfer rate of each vessel, thus quantitatively demonstrating the need to accurately model the vessel–vessel heat transfer for vessels imbedded in tissues. Second, the vessel–vessel heat transfer rate is shown to be independent of the source term; while the heat transfer rates from the vessels to the tissue show a significant dependence on the source term. Third, while many previous studies have assumed that (1) the total heat transfer rate from vessels to tissue is zero, and/or (2) the heat transfer rates from paired vessels (of different sizes and at different temperatures) to tissue are equal to each other the current analysis shows that neither of these conditions is met. The analytical solution approach used to solve this two vessels problem is general and can be extended for the case of “N” arbitrarily located vessels. [DOI: 10.1115/1.1842788]

Introduction

Many bio-heat transfer applications such as the optimization of thermal therapy related treatment modalities (e.g., high temperature therapy, etc.) require the knowledge of *in vivo* 3-D tissue temperature distributions, and therefore an accurate estimation of heat transfer rates between a complicated 3-D blood vessel network and unheated/heated tissue [1]. Since a considerable fraction of blood vessels are found in pairs (e.g., [2,3]), vessel–vessel heat transfer has generally been postulated as one of the most important heat transfer mechanisms involved in determining the tissue temperature distributions (e.g., [3–7]).

To understand the effect of paired vessels on the tissue temperature distributions, previous researchers have extensively studied the geometry of these vessels in both infinite and finite tissue domains by using several approximations. First, the presence of externally induced heating in the tissue has always been neglected when estimating the heat transfer rates between the vessels and tissue and between the two vessels [6–25]. Since, in many thermal therapy applications, e.g. conventional hyperthermia, high temperature cancer therapies and standard physical therapy, strong source terms are present in tissue, it is important to study the effect of the source terms in the evaluation of the heat transfer rates.

Second, while quantifying the heat transfer rates, one or both of the following two types of assumptions have always been employed; one, the total heat transfer rate from the two vessels to the tissue is zero [8–12] and two, the heat transfer rates from vessels to the tissue are equal to each other regardless of the vessel sizes, locations, and their wall temperatures [13–21]. Since these assumptions limit the applicability of the previous derivations, evaluation of these assumptions is needed. In addition, while a few researchers [22–25] demonstrated the effect of the heat ex-

change between the artery and vein from the axial temperature distribution along the blood vessels, they did not quantify the vessel–vessel heat transfer rates explicitly. Since these axial temperature distributions present the combined effect of the vessel to vessel and vessel to tissue heat transfer rates, the actual amount of the vessel–vessel and vessel to tissue heat transfer rates cannot be explicitly quantified from this information alone.

Third, all of the previous solutions, except DiFelice et al. [8], make significant mathematical approximations in order to obtain solutions for the temperature distribution in tissues with a pair of vessels. For example, several researchers have used the approximate method of sources and sinks to obtain the temperature distribution in both, infinite [9–11] and finite tissue domains [13,16]. This technique implicitly assumes that (1) there exists a source and a sink of equal magnitude in the tissue and (2) the heat flow around the source terms is homogeneous and in the radial direction. Therefore this technique is not appropriate to use in vessel–tissue configurations where vessels may have unequal heat transfer rates from their walls and are close to each other and/or to the outer tissue boundary. Others have used either perturbation methods [15] or have superimposed approximate solutions obtained by considering only one of the paired vessels to develop approximate solutions with two vessels [7,17,18,22,24] in the finite, unheated tissue. It should be noted, however, that these approximate analytical solutions [7,17,18,22,24] are exact when the thermal conductivity of the tissue is equal to that of blood. Also, that the previously developed analytical solutions that are most pertinent to the present study [7,17,24], in their current form, do not allow for specifying the desired temperature boundary conditions independently on all surfaces.

Defilice and Bau [8] used conformal mapping to obtain the exact tissue temperature distribution for a pair of vessels in an infinite tissue medium. However, since it has been shown that approximately 1–3 vessels of the size $50\ \mu\text{m}$ and larger are present in a $1\ \text{mm}^2$ cross section of tissue [2], more vessels are

Manuscript received January 23, 2004; revision received September 1, 2004. Review conducted by: A. F. Emery.

bound to be present in a larger tissue medium ($>1 \text{ mm}^2$). Again, since all of these vessels interact thermally with the tissue and among themselves, any study of the vessel–vessel heat transfer with a pair of vessels in an infinite tissue matrix requires checking of its results against more realistic, finite domain cases.

While the above two vessels studies are most applicable to the present research, there are several single vessel studies that are also pertinent. In particular, the effect of arbitrarily located single vessels in a finite, unheated (e.g., [8,17,22,26]) and heated (e.g., [27–29]) tissue domains with uniform (e.g., [8,17,22,26–28]) and nonuniform boundary conditions [29] has been investigated using two approaches: (1) conformal mapping [8,17,26–29], and (2) the Green's function [22]. However, those single vessels results have not been previously extended to the two vessels case studied herein (i.e., the case of a finite, heated tissue with two arbitrarily located blood vessels), and indeed the conformal mapping technique cannot directly be extended to >1 vessel cases without introducing further approximations [16,17] since it results in more boundary conditions than required. To obtain the exact analytical solution using the conformal mapping technique, the method presented in the present paper would need to be followed. The solution presented using the Green's function can be extended to >1 vessels [22]. This extension, however, will result in the same number of unknowns and related algebraic equations to solve for the tissue temperature distribution as presented in this paper. A more comprehensive review of these single vessel solutions is provided in our earlier work [29].

It is clear from the above discussion that although the vessel–vessel heat transfer has always been postulated as being very important in determining the *in vivo* tissue temperature distributions, there exists neither an appropriate derivation nor an accurate way to quantify the vessel–vessel and vessel–tissue heat transfer rates in finite tissue anatomies of most importance. An accurate and appropriate derivation and quantification are thus needed in order to evaluate the importance of the vessel–vessel heat transfer in such tissues and for use in evaluating the accuracy and applicability of the previously employed approximations. Analytical solutions to such problems are particularly useful in evaluating the effects of all of the variables involved, and providing solutions that can be directly used in developing improved bio-heat transfer equations (e.g. the *TCEBE* [30]). The determination of the tissue temperature distribution with 1–3 blood vessels (typical numbers for perfused tissue control volumes [2]) is of particular importance in such equations. Therefore, the objectives of this study are three fold: (1) to derive an exact analytical solution to obtain the tissue temperature distribution in an unheated/heated, finite, non-insulated tissue with a pair of vessels, (2) to accurately quantify the vessel–vessel and vessel–tissue heat transfer rates, and (3) to study the effects of various geometrical parameters on these heat transfer rates.

Mathematical Model: Solution

As a first step to fulfill the stated goals, an exact series solution is presented of the 2-D energy equation with a uniformly distributed source for a finite, homogeneous, noninsulated tissue with two arbitrarily located circular vessels. Since our work is the first attempt to explicitly define and quantify the vessel–vessel and vessel to tissue heat transfer rates, it has been assumed for simplicity that the temperatures at the vessel walls and outer tissue boundary are uniform [8–10,13,21]. Our assumption is valid when mass flow rates through vessels are high and heating is dominant and uniform in tissue. The effect of variable boundary conditions on the vessel–vessel and vessel to tissue heat transfer rates is under investigation [31]. Further, the applicability of the uniform vessel wall and tissue boundary temperatures to more general cases can be illustrated using the solution presented by Wu et al. 1993 [17] (which is derived for high Peclet numbers) for the blood vessel diameters used in this paper. It can be seen that the temperature oscillations present on the two vessel walls and

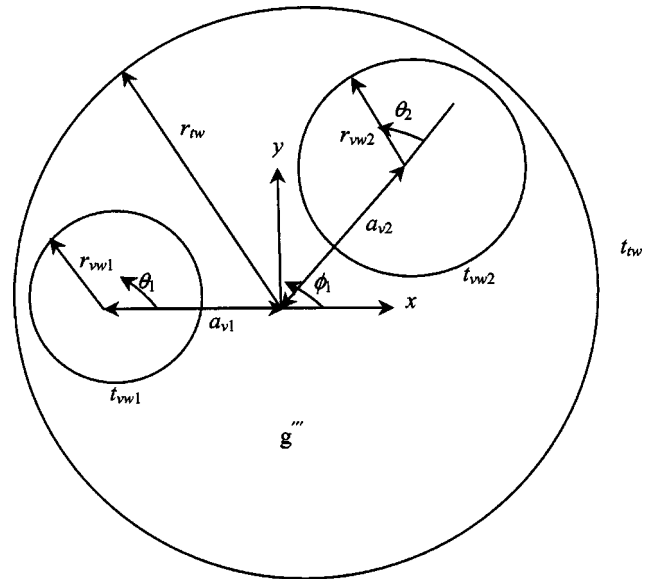


Fig. 1 Schematic of the tissue cylinder with two unequal arbitrarily located vessels

the outer tissue boundary are very small compared to their mean values. A uniform source distribution is assumed both for simplicity, and since the distribution of the source term can be approximated as being uniform over short distances for most heating systems of interest—whose power deposition patterns vary negligibly over distances of the magnitude of the tissue boundary radius. This source term g''' consists of external heating only (the Pennes' [32] BHTE source/sink term is not included in g''' since it represents a method of replacing the effects of the vessels currently under study).

To obtain the temperature field in a 2-D tissue medium with uniform conductivity, a source term and two arbitrarily located circular vessels, we impose a nondimensional equation (1) in the tissue after converting it into a Laplace equation using the change of variable from T to T_1 .

$$\frac{1}{R} \frac{\partial}{\partial R} \left(R \frac{\partial T_1}{\partial R} \right) + \frac{1}{R^2} \frac{\partial^2 T_1}{\partial \psi^2} = 0 \quad (1)$$

The required boundary conditions are presented in Eqs. (2)–(4) (Fig. 1).

$$T_1|_{R_1} = 0 + PR_1^2/4 \quad (2)$$

$$T_1|_{R_2} = T_{vw2} + PR_2^2/4 \quad (3)$$

$$T_1|_1 = 1 + P/4 \quad (4)$$

The problem defined above can be rewritten as the superposition of the following two sub-problems (Fig. 2),

Sub-problem 1:

$$\frac{1}{R} \frac{\partial}{\partial R} \left(R \frac{\partial T_{11}}{\partial R} \right) + \frac{1}{R^2} \frac{\partial^2 T_{11}}{\partial \psi^2} = 0 \quad (5)$$

$$T_{11}|_{R_1} = 0 + PR_1^2/4 - c_{21} \quad (6)$$

$$T_{11}|_{R_2} = c_{12} \quad (7)$$

$$T_{11}|_1 = 1 + P/4 \quad (8)$$

Sub-problem 2:

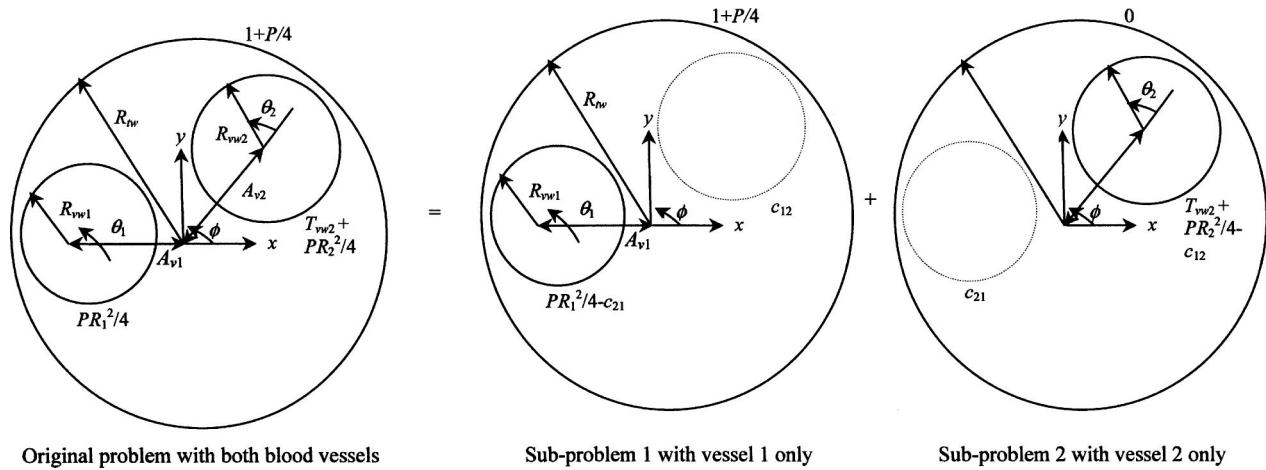


Fig. 2 Dividing the original problem of two vessels in a finite tissue into two sub-problems, each consisting of one vessel only

$$\frac{1}{R} \frac{\partial}{\partial R} \left(R \frac{\partial T_{12}}{\partial R} \right) + \frac{1}{R^2} \frac{\partial^2 T_{12}}{\partial \psi^2} = 0 \quad (9)$$

$$T_{11}|_{R_2=c_{21}} \quad (10)$$

$$T_{12}|_{R_2=R_{vw2}+PR_2^2/4-c_{12}} \quad (11)$$

$$T_{12}|_{\psi=0} = 0 \quad (12)$$

where

$$T_1 = T_{11} + T_{12} \quad (13)$$

This division allows the original problem with two blood vessels to be reformulated as the summation of two sub-problems each consisting of only one of the two vessels (Fig. 2). Here, c_{ij} is the temperature distribution produced on the wall of the j th vessel by the wall of the i th vessel in sub-problem i . Note, however, that the values of the c_{ij} are not known and therefore the boundary conditions (6–7) and (10–11) cannot be used to obtain the complete solution—this issue has been addressed later in the paper. To simplify the problem even further by making vessel and the tissue concentric [33] in both sub-problems, a standard bilinear transformation (w_i) is used. The modified sub-problem 1 with vessel one and tissue concentric and boundary condition equation (8) can be written as

$$\frac{1}{R_1^*} \frac{\partial}{\partial R_1^*} \left(R_1^* \frac{\partial T_{11}}{\partial R_1^*} \right) + \frac{1}{(R_1^*)^2} \frac{\partial^2 T_{11}}{\partial \alpha_1^2} = 0 \quad (14)$$

with

$$T_{11}|_{\alpha_1=1+P/4} \quad (15)$$

The general solution to Eq. (14) is:

$$T_{11} = A_{01} + A'_{01} \ln(R_1^*) + \sum_{n=1}^{\infty} \{A_{n1}(R_1^*)^n + A'_{n1}(R_1^*)^{-n}\} \sin(n\alpha_1) + \sum_{n=1}^{\infty} \{B_{n1}(R_1^*)^n + B'_{n1}(R_1^*)^{-n}\} \cos(n\alpha_1) \quad (16)$$

Using Eqs. (15) and (16) and the orthogonality of sine and cosine functions, the following relations can easily be derived:

$$A_{01} = 1 + P/4 \quad (17)$$

$$A_{n1} = -A'_{n1} \quad (18)$$

$$B_{n1} = -B'_{n1} \quad (19)$$

Using Eqs. (17), (18) and (19), Eq. (16) can be rewritten as follows:

$$T_{11} = 1 + P/4 + A'_{01} \ln(R_1^*) + \sum_{n=1}^{\infty} A_{n1} \{ (R_1^*)^n - (R_1^*)^{-n} \} \sin(n\alpha_1) + \sum_{n=1}^{\infty} B_{n1} \{ (R_1^*)^n - (R_1^*)^{-n} \} \cos(n\alpha_1) \quad (20)$$

Similarly, for sub-problem 2, the following solution can be obtained after applying the transformation w_2 that makes the vessel two and tissue concentric and the boundary condition at the tissue boundary [Eq. (12)] in the transformed plane.

$$T_{12} = A'_{02} \ln(R_2^*) + \sum_{n=1}^{\infty} A_{n2} \{ (R_2^*)^n - (R_2^*)^{-n} \} \sin(n\alpha_2) + \sum_{n=1}^{\infty} B_{n2} \{ (R_2^*)^n - (R_2^*)^{-n} \} \cos(n\alpha_2) \quad (21)$$

Using Eq. (13) and converting variable T_1 back to T , the complete solution to the original nondimensional problem can be written as,

$$T = 1 + P/4 + A'_{01} \ln(R_1^*) + A'_{02} \ln(R_2^*) + \sum_{n=1}^{\infty} A_{n1} \{ (R_1^*)^n - (R_1^*)^{-n} \} \sin(n\alpha_1) + \sum_{n=1}^{\infty} A_{n2} \{ (R_2^*)^n - (R_2^*)^{-n} \} \sin(n\alpha_2) + \sum_{n=1}^{\infty} B_{n1} \{ (R_1^*)^n - (R_1^*)^{-n} \} \cos(n\alpha_1) + \sum_{n=1}^{\infty} B_{n2} \{ (R_2^*)^n - (R_2^*)^{-n} \} \cos(n\alpha_2) - PR^2/4 \quad (22)$$

Since the values of c_{ij} in Eqs. (6–7) and (10–11) are not known, the constants presented in Eq. (22) cannot be evaluated in the transformed plane. Therefore, to evaluate all the constants (A'_{01} , A'_{02} , A_{n1} , A_{n2} , B_{n1} , and B_{n2}), the expression shown in Eq. (22) should be expressed into the original coordinates using relationships presented in the nomenclature section that relate R , R_1^* , α_1 , R_2^* , and α_2 to the original coordinates x_1 and y_1 since the vessel wall boundary conditions are known in the original plane (given temperatures). To evaluate the complete set of $2(2N+1)$ constants where N is the finite number of terms considered in each of the above summation series, a system of $2(2N+1)$ independent linear equations consisting of $2(2N+1)$ constants should be

formed by multiplying the boundary condition equation ($i+1$) and the solution [Eq. (22)] with $\sin(m\theta_i)$ and $\cos(m\theta_i)$ ($m=0 \cdot \cdot \cdot N$), respectively, and integrating over the perimeter of the i th vessel ($i=1,2$) (refer to the Appendix for more details). The obtained system of two $(2N+1)$ linear equations (due to two vessel wall boundary conditions) with $2(2N+1)$ constants can be evaluated using any linear equation solver. It can also be realized from the above description that every other addition of a vessel in the finite tissue medium introduces, in general, another $(2N+1)$ constant, which can be evaluated using the additional vessel wall boundary conditions.

Note that our approach is different from DiFelice et al. [8] who could obtain only $2N$ linear equations for $2N+2$ unknown constants using their boundary conditions (where N was the number of terms considered in their series solution). To obtain two additional equations, they had to define the criteria for convergence of the coefficients. Conversely, in our problem, we do not make such approximations since the partition of the main problem with two vessels into two sub-problems allows us to obtain two additional boundary condition equations.

Using the orthogonality of sine and cosine functions, it is found that for the problem at hand all of the coefficients attached to sine terms are zero. This leaves us a system of $2(N+1)$ equations with the same number of unknowns. The general solution takes the following form.

$$T = 1 + P/4 + A'_{01} \ln(R_1^*) + A'_{02} \ln(R_2^*) + \sum_{n=1}^{\infty} B_{n1} \{(R_1^*)^n - (R_1^*)^{-n}\} \cos(n\alpha_1) + \sum_{n=1}^{\infty} B_{n2} \{(R_2^*)^n - (R_2^*)^{-n}\} \cos(n\alpha_2) - PR^2/4 \quad (23)$$

The obtained system of $2(N+1)$ independent equations can easily be solved for the $2(N+1)$ unknown coefficients using the available numerical linear equation solvers.

Vessel–Vessel Heat Transfer

To meet the second goal of this paper and to accurately quantify the vessel–vessel heat transfer rate it is important to account for the fact that in a finite, noninsulated tissue with two vessels, some of the energy leaving one vessel wall goes to the other vessel wall and the rest goes to the tissue boundary. We can express this physical situation as follows,

$$Q_{total,vw1} = Q_{vw2-vw1} + Q_{tw-vw1} \quad (24)$$

$$Q_{total,vw2} = Q_{vw1-vw2} + Q_{tw-vw2} \quad (25)$$

Again, since the total heat transfer rate leaving each vessel wall can be calculated by using the exact solution for the temperature field presented in the previous section and evaluating and integrating the flux around the vessels, Eqs. (24–25) have four unknown heat fluxes, and only two equations to solve for them. To obtain the other equations, it is hypothesized that the only driving force for the vessel–vessel heat transfer rate is the temperature difference between the two vessel walls in unheated/heated tissues i.e. if the two vessel walls are at the same temperature, the vessel–vessel heat transfer rate is zero. Therefore, if the temperature of one of the vessel walls is set equal to the temperature of the second vessel wall and the total heat transfer rate is calculated on the second vessel wall, it will represent the amount of energy transferred to the tissue boundary only from the second vessel wall. The heat transfer rates from the vessel walls to the tissue wall are thus given as follows.

$$Q_{vw1-tw} = Q_{total,vw1} \Big|_{t_{vw2} \rightarrow t_{vw1}} \quad (26)$$

$$Q_{vw2-tw} = Q_{total,vw2} \Big|_{t_{vw1} \rightarrow t_{vw2}} \quad (27)$$

Equations (24) and (26) and Eqs. (25) and (27) can be used to calculate the vessel–vessel heat transfer rates, $Q_{vw1-vw2}$ and $Q_{vw2-vw1}$, respectively, and the results should be equal in magnitude and opposite in sign if and only if our hypothesis that the vessel wall temperature difference is the only driving force for the vessel–vessel heat transfer rate.

In terms of the situations studied, we have analyzed the effect of the source term and the problems' geometrical parameters on the vessel–vessel and vessel–tissue heat transfer rates for three different cases, namely; one, when the tissue boundary temperature is higher than the two vessel wall temperatures (i.e., the cold vessels case); two, when the tissue boundary temperature is lower than the two vessel wall temperatures (i.e., the warm vessels case); and three, when the tissue boundary temperature lies in between the two vessel wall temperatures (i.e., the mixed case). While results for all of the above cases are presented by Devashish [34], this paper presents results only for the case of both of the vessels cooling the tissue, i.e., the cold vessels case (Figs. 4–8). To study a general case of the unequal vessel wall temperatures it is assumed in our study that the wall temperature of vessel two (simulating a vein) is higher than the wall temperature of vessel one (simulating an artery) and is approximately halfway ($T_{vw2} = 0.6$) in between the wall temperatures of the vessel one and outer tissue boundary. Also, since in high temperature therapy applications the temperature of the vessel wall and the tissue boundary usually varies in between 38°C and 43°C , this gives the vessel 2 wall temperature of 41°C [35,36] which is reasonable since arteries bring in cooler blood to the heated tissues from the rest of the body and veins bring in warmer blood from the heated arteries and veins. Since the average tissue temperature reaches as high as 50°C [35,36], the nondimensional source term P takes the maximum value of 20 in all of the figures so that the average tissue matrix temperature reaches approximately the outer tissue boundary temperature. The total number of terms “ N ” used in the series solution to produce results is 20. This makes the maximum error in the evaluation of boundary temperatures less than 0.5%, which is sufficient [15,22] for bio-heat transfer applications (Fig. 3).

Results

In terms of specific results, first, it is found that the two vessel–vessel heat transfer rate terms, $Q_{vw1-vw2}$ and $Q_{vw2-vw1}$ are always equal to each other in magnitude and opposite in sign for all vessel sizes, eccentricities, and wall temperatures studied, thus verifying our hypothesis about the difference in vessel wall temperatures as the only driving force for the vessel–vessel heat transfer rate, analytical procedure and its numerical implementation. Additionally, Fig. 3 presents for the heated tissue the given and calculated boundary conditions to show that the developed solution satisfies all the boundary conditions and thus validating our solution further.

Next, Fig. 4 presents two sets of curves for the vessel–vessel heat transfer rate ($Q_{vw2-vw1}$) for different values of the nondimensional source term P ($P=0, 10, \text{ and } 20$) and the nondimensional temperature of vessel wall two (T_{vw2}); one set of curves presents the variation in the vessel–vessel heat transfer rate ($Q_{vw2-vw1}$) as a function of the nondimensional radius of vessel two (R_{vw2}) for a fixed nondimensional vessel eccentricity of the two vessels and radius of vessel one. The other set of curves presents the variation in the vessel–vessel heat transfer rate ($Q_{vw1-vw2}$) with the nondimensional eccentricity of vessel two (A_{v2}) for a given nondimensional vessel radius of the two vessels and eccentricity of vessel one. Since it is well known that the vessels of radius $\sim 50\text{--}200 \mu\text{m}$ are thermally significant and make a majority of the counter-current vessel pairs [2,9,10], and the ratio of diameters of veins to arteries in living systems [37,38] varies from $\sim 1\text{--}2$, to study the effect of the vessel radius on the vessel–vessel heat transfer rate, the nondimensional radius of vessel two, R_{vw2} is varied from 0.1–0.5 ($\sim 56.5\text{--}282 \mu\text{m}$) while keeping the nondimensional ra-

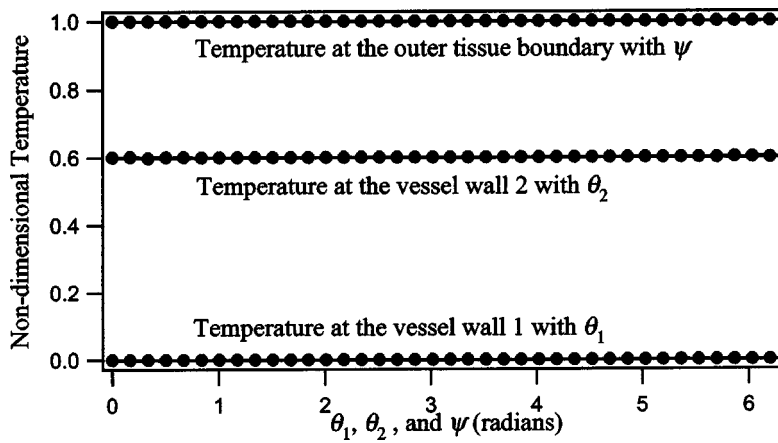


Fig. 3 The validity of the solution is presented for $N=20$, $P=20$, $R_{vw1}=0.2$, $A_{v1}=-0.6$, $R_{vw2}=0.4$, and $A_{v2}=0.4$. Solid lines represent the given nondimensional temperatures at the two vessel walls and the outer tissue boundary. The solution predicted using the solution is presented using markers.

dius of vessel one as 0.2 ($\sim 112 \mu\text{m}$) and assuming that the radius of the tissue matrix is $\sim 564 \mu\text{m}$ (since there are 1–3 vessels in the tissue of the size of 1 mm^2 [2]). The value of the eccentricity of vessel one, A_{v1} , is chosen as -0.6 and the value of vessel two's eccentricity, A_{v2} is chosen as $+0.3$ to be able to put part of the perimeter of the vessels close to the tissue boundary and to include the boundary effects. To study the effect of the vessel eccentricity on the vessel–vessel heat transfer rate in the cases of traditional counter–current vessel pairs [2] (when the smallest distance between the two vessel walls is not greater than the largest diameter of the two vessels), the eccentricity of vessel two is varied from 0.1 to 0.5. The nondimensional eccentricity of vessel one is kept as -0.6 for the aforementioned reasons. The nondimensional radii of vessels one and two are chosen as 0.2 and 0.3, respectively, since, as mentioned before, the ratio of the diameters of the veins to arteries varies in between 1 and 2 in living systems [37,38].

For the purpose of comparing the vessel–vessel heat transfer rates from vessel wall two to vessel wall one that are shown in Fig. 4, with the comparable vessel wall to tissue boundary heat transfer rates, Figs. 5 and 6, present, respectively, for both vessels one and two, the variation in the heat transfer rate from the vessel

wall to the tissue boundary, as functions of the vessel size and eccentricity. Note that all heat transfer rates are nondimensionalized in terms of the conduction heat transfer rate between the vessel wall one and tissue boundary, per unit distance of vessel one perimeter between the two.

To study the importance of vessel–vessel heat transfer, Figs. 7 and 8 present, respectively, for vessels one and two, the vessel–vessel heat transfer rate from vessel two to vessel one, $Q_{vw1-vw2}$ as a percentage of the heat transfer rate from the vessel wall to the tissue boundary as a function of the nondimensional radius and eccentricity of vessel two.

Discussion

Several different observations can be made from this study. First, as seen in Fig. 4, the vessel–vessel heat transfer rate is independent of the source term, while the vessel–tissue heat transfer rates are strong functions of the source terms (Figs. 5–6). This can easily be explained by noticing that the problem investigated can be broken into two sub-problems; sub-problem A, with the given boundary temperatures and no source term and sub-problem B, with the source term and boundary temperatures set at zero.

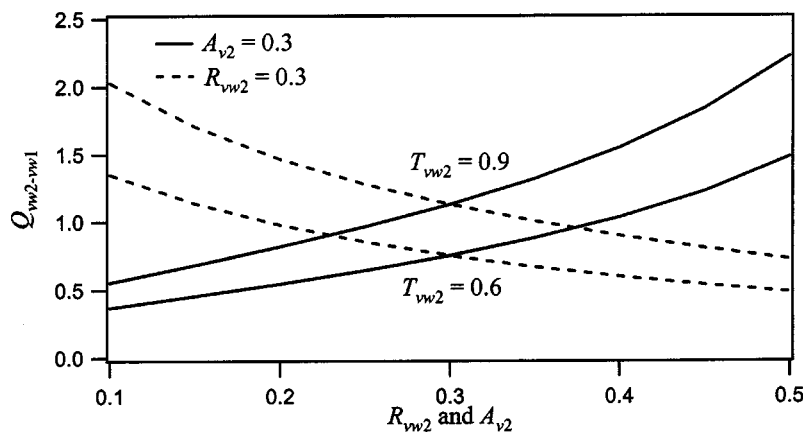


Fig. 4 The variation in the nondimensional vessel–vessel heat transfer rate, $Q_{vw2-vw1}$, as a function of the nondimensional vessel 2 size, R_{vw2} , and eccentricity, A_{v2} , with $R_{vw1}=0.2$, $A_{v1}=-0.6$, $T_{vw1}=0$, $T_{vw2}=0.6$, $T_{tw}=1$, and $P=0, 10, 20$

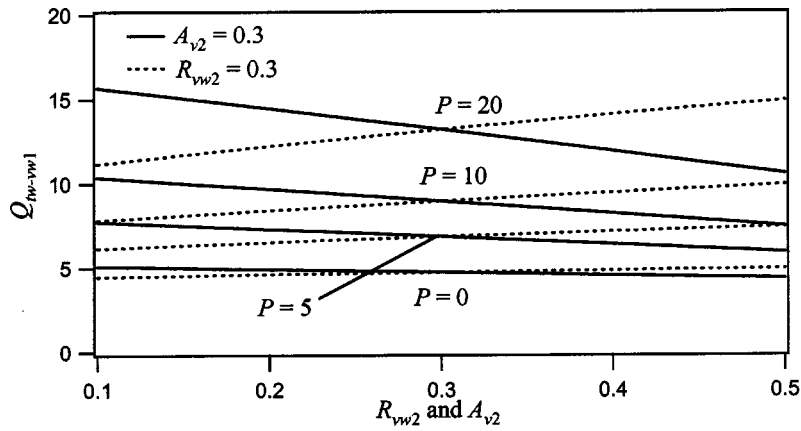


Fig. 5 The variation in the nondimensional heat transfer rate from tissue to vessel 1, Q_{tw-vw1} , as a function of the nondimensional vessel 2 size, R_{vw2} , and eccentricity, A_{v2} , with $R_{vw1}=0.2$, $A_{v1}=-0.6$, $T_{vw1}=0$, $T_{vw2}=0.6$, $T_{tw}=1$

The sub-problem A contains the vessel–vessel and the vessel–tissue heat transfer rates which are dependent on the boundary temperatures and the geometry. In the sub-problem B, there is no vessel–vessel heat transfer rate. It only contains the vessel–tissue heat transfer rates, which are functions of the deposited power.

Second, in cold vessels case in unheated tissues the vessel–vessel heat transfer rate is found to be a significant fraction of the vessel to tissue heat transfer rate for both of the vessels (Figs. 7–8). This is easily explained since the wall temperature difference between the two vessels is on the same order as the tempera-

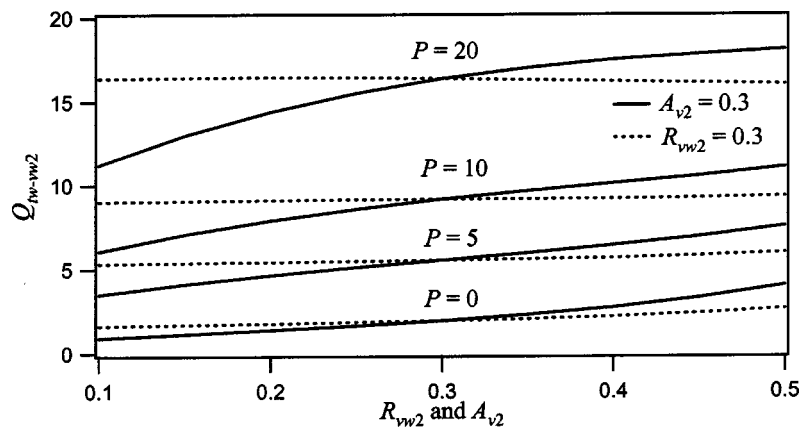


Fig. 6 The variation in the nondimensional heat transfer rate from tissue to vessel 2, Q_{tw-vw2} , as a function of the nondimensional vessel 2 size, R_{vw2} , and eccentricity, A_{v2} , with $R_{vw1}=0.2$, $A_{v1}=-0.6$, $T_{vw1}=0$, $T_{vw2}=0.6$, $T_{tw}=1$

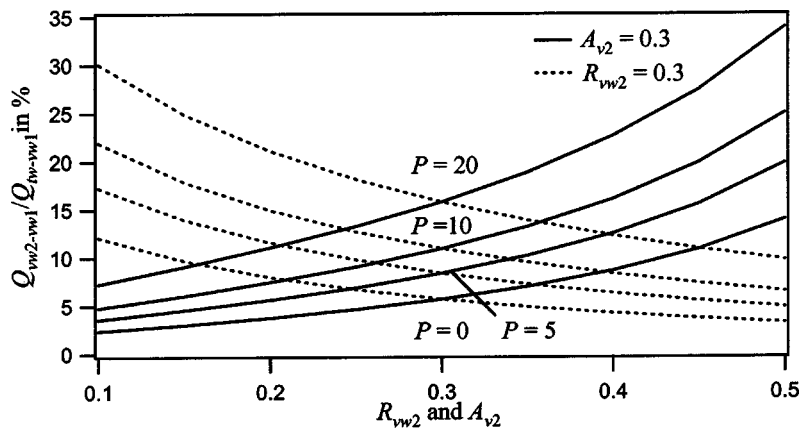


Fig. 7 The variation in the vessel–vessel heat transfer rate, $q_{vw2-vw1}$, as a fraction of the tissue to vessel 1 heat transfer rate, Q_{tw-vw1} , as a function of the nondimensional vessel 2 size, R_{vw2} , and eccentricity, A_{v2} , with $R_{vw1}=0.2$, $A_{v1}=-0.6$, $T_{vw1}=0$, $T_{vw2}=0.6$, $T_{tw}=1$

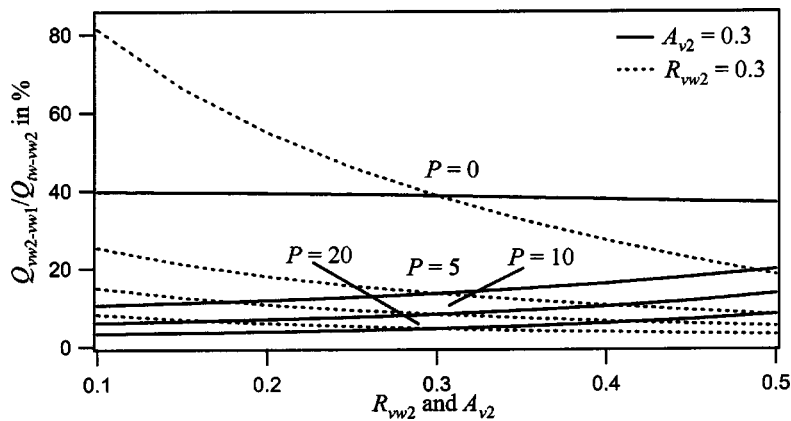


Fig. 8 The variation in the vessel–vessel heat transfer rate, $q_{vw2-vw1}$, as a fraction of the tissue to vessel 2 heat transfer rate, q_{tw-vw2} , as a function of the nondimensional vessel 2 size, R_{vw2} , and eccentricity, A_{v2} , with $R_{vw1} = 0.2$, $A_{v1} = -0.6$, $T_{vw1} = 0$, $T_{vw2} = 0.6$, $T_{tw} = 1$

ture difference between the vessel walls and the tissue boundary. The percentage contribution of the vessel–vessel heat transfer rate decreases compared to the vessel–tissue heat transfer rates as the strength of the source terms increases. The explanation to this result is also intuitive since the vessel–vessel heat transfer rate is a function of the vessel wall temperature difference and geometry only and is independent of the source term (Fig. 4), while the vessel–tissue heat transfer rates are strong functions of the source term (Figs. 5–6). Since the heat transfer is taking place from the tissue wall to the vessel walls (i.e., the vessels are cooling the tissue), an increase in the strength of the source term increases the heat transfer rates from tissue to the vessel walls thereby decreasing the percentage contribution of the vessel–vessel heat transfer rate.

Third, it can be seen from Figs. 5–6 that in the cold vessels case, the summation of the vessel to tissue heat transfer rates is not zero. This summation may become zero only when at least one of the vessel wall temperatures is higher than the tissue boundary temperature and both vessel wall temperatures are not equal to each other. It can also be seen that the two vessel to tissue heat transfer rates are significantly different from each other. Therefore, the vessel–vessel heat transfer analyses with the assumptions that there is no net vessels to tissue heat transfer [8–12] or the vessel to tissue heat transfer rates are equal to each other [13–21], have limited applicability.

Fourth, it is shown in Figs. 5–6 that an increase in the strength of the source term significantly increases the amount of energy transferred from the tissue to the vessel walls. This can be easily explained since an increase in the strength of the source term increases the tissue temperature around the vessels and thus increases the heat flux from tissue to vessels. This result suggests that it is inappropriate to neglect the effect of heating in the evaluation of the vessel to tissue heat transfer rates in applications where significant source terms are present.

Fifth, it is shown in Fig. 5 that as the radius of vessel two increases the amount of energy transferred from the tissue to vessel one decreases. This can easily be explained by noting that in the presented case, the wall temperatures of both of the vessels are lower than the tissue boundary temperature. Therefore, an increase in the radius of vessel two increases its surface area and thus the amount of the energy transferred from the tissue to vessel two (Fig. 6) resulting in a decrease in the amount of energy transferred from the tissue to vessel one. It is also shown that the vessel–vessel heat transfer rate increases as the radius of vessel two increases (Fig. 4) [21]. The explanation of this result is obvious since, as mentioned before, an increase in the radius of vessel two increases the net vessel–vessel heat transfer surface area and

thus the total vessel–vessel heat transfer rate. The behavior of the vessel–vessel, vessel one to tissue and vessel two to tissue heat transfer rates, with the change in the radius of vessel two and source term also explains the curves in Figs. 7–8.

Sixth, it is shown in Figs. 5–6 that as the eccentricity of vessel two increases the amount of energy transferred from the tissue to the vessels increases [21]. An increase in the heat transfer rate from the tissue to vessel one with an increase in the eccentricity of vessel two A_{v2} can be explained since an increase in the eccentricity of vessel two A_{v2} decreases its effect on vessel one and thus allows more energy to flow into vessel one from the tissue around it. An increase in the heat transfer rate from the tissue to vessel two with an increase in the eccentricity of vessel two A_{v2} can be explained since an increase in the eccentricity of vessel two A_{v2} allows part of the perimeter of vessel two to approach the tissue boundary. This results in an increase in the heat transfer rate into the vessel from this thermally more significant part of the vessel, an increase that is larger than the corresponding decrease of the heat transfer rate from the rest of its perimeter. Figure 4 shows that the vessel–vessel heat transfer rate decreases as the eccentricity of vessel two increases [21]. The explanation of this result is obvious since an increase in the eccentricity of vessel two decreases the temperature gradient responsible for the vessel–vessel heat transfer rate. The behavior of the vessel–vessel, vessel one to tissue and vessel two to tissue heat transfer rates with the change in the eccentricity of vessel two and the source term magnitude also explains the curves in Figs. 7–8.

In other cases, i.e., when both vessel wall temperatures are higher than the tissue boundary temperature (the warm vessels case) and when one vessel wall temperature is lower while the other vessel wall temperature is higher than the tissue boundary temperature (the mixed case), all of the previous six findings about the vessel–vessel and vessel–tissue heat transfer rates are found to be valid: the vessel–vessel heat transfer rate is independent of the source term, while the vessel–tissue heat transfer rates are significantly dependent of the source term; the vessel–vessel heat transfer rate is a large fraction of the vessel to tissue heat transfer rate; the sum of the vessel–tissue heat transfer rates from the two vessels to the tissue is not equal to zero, and are indeed significantly different from each other; and, the heat transfer rates from the two vessels to the tissue are functions of the geometry [34].

To address the limitations of the current study, the developed analytical solution method presented herein requires a matrix inversion to evaluate all of the constants to determine the tissue temperature distribution (refer to the Appendix). This makes this solution method slower and relatively difficult to use compared to

the other previous solution techniques (e.g., [7,17,24]) developed for unheated tissues. However, as mentioned before, those analytical solutions [7,17,24], in their current form, do not allow for specifying the desired temperature boundary conditions independently on all surfaces. Therefore, these studies are complementary to one another. Further, future extensions of this work to develop similar expressions for 2-D cases with spatially varying boundary conditions, and three-dimensional situations are necessary to gain insights into, and develop analytical expressions for, the heat transfer rates associated with pairs of vessels eccentrically embedded in finite, heated/unheated tissues.

Conclusions

This paper presents an exact analytical series solution for the tissue temperature distribution in finite, unheated/heated, noninsulated tissue with a pair of arbitrarily located vessels and, for the first time, appropriately quantifies the vessel–vessel and vessel–tissue heat transfer rates for such situations. The analytical solution results show that, in general, it is important to accurately model the vessel–vessel heat transfer in unheated/heated tissues. However, for large values of the source term when vessels are cooling the tissue (the tissue boundary temperature is higher than the vessel wall temperatures), the vessel–vessel heat transfer rate can be neglected in comparison to the vessel to tissue heat transfer rates. It has also been shown that the vessel–vessel heat transfer rate is independent of the magnitude of the source terms, while the heat transfer rate from both of the vessel walls to the tissue boundary is a strong function of the source term. Therefore, it is important to include the effect of the source term to accurately model vessel–tissue heat transfer in applications where strong source terms are present.

Nomenclature

| | |
|-----------------|---|
| a_{vi} | = distance between the centers of the tissue and the i th vessel, $i = 1, 2$ (m) |
| g^m | = uniform source term in the tissue per unit volume (Watts/m ³) |
| k | = tissue conductivity [Watts/(m·K)] |
| $q_{vw2-vw1}$ | = heat transfer rate between vessel wall 2 and vessel wall 1 (Watts/m) |
| q_{tw-vw1} | = heat transfer rate between tissue and vessel wall 1 (Watts/m) |
| q_{tw-vw2} | = heat transfer rate between tissue and vessel wall 2 (Watts/m) |
| $q_{total,vw1}$ | = total heat transfer rate into vessel wall 1 (Watts/m) |
| $q_{total,vw2}$ | = total heat transfer rate into vessel wall 2 (Watts/m) |
| r | = radial distance (m) |
| r_i | = perimeter of vessel ‘ i ’ from the center of outer tissue cylinder $\{(a_{vi} + r_{vwi} \cos \theta_i)^2 + (r_{vwi} \sin \theta_i)^2\}^{1/2}$, $i = 1, 2$ (m) |
| r_{vwi} | = i th vessel radius, $i = 1, 2$ (m) |
| r_{tw} | = outer tissue boundary radius (m) |
| t_{vwi} | = i th vessel wall temperature, $i = 1, 2$ (K) |
| t_{tw} | = outer tissue boundary temperature (K) |

Non-Dimensional Parameters

| | |
|-------------------|---|
| a_{1i} | = constant for i th sub-problem, $A_{vi} - R_{vwi}$, $i = 1, 2$ |
| a_{2i} | = constant for i th sub-problem, $A_{vi} + R_{vwi}$, $i = 1, 2$ |
| A_{0i}, A'_{0i} | = constant associated with the solution of the i th sub-problem, $i = 1, 2$ |
| A_{ni}, A'_{ni} | = constant associated with the solution of the i th sub-problem, $i = 1, 2$ |
| B_{ni}, B'_{ni} | = constant associated with the solution of the i th sub-problem, $i = 1, 2$ |
| A_{vi} | = distance between the centers of tissue cylinder and i th vessel, a_{vi}/r_{tw} , $i = 1, 2$ |

| | |
|-----------------|---|
| P | = power deposition, $g^m r_{tw}^2 / [(t_{tw} - t_{vw1})k]$ |
| $Q_{vw2-vw1}$ | = heat transfer rate between vessel wall 2 and vessel wall 1, $q_{vw2-vw1} / [(t_{tw} - t_{vw1})k]$ |
| Q_{tw-vw1} | = heat transfer rate between outer tissue boundary and vessel wall 1, $q_{tw-vw1} / [(t_{tw} - t_{vw1})k]$ |
| Q_{tw-vw2} | = heat transfer rate between outer tissue boundary and vessel wall 2, $q_{tw-vw2} / [(t_{tw} - t_{vw1})k]$ |
| $Q_{total,vw1}$ | = total heat transfer rate into vessel wall 1, $q_{total-vw1} / [(t_{tw} - t_{vw1})k]$ |
| $Q_{total,vw2}$ | = total heat transfer rate into vessel wall 2, $q_{total-vw2} / [(t_{tw} - t_{vw1})k]$ |
| R | = radius, r/r_{tw} , $(x_1^2 + y_1^2)^{1/2}$ |
| R_i | = perimeter of vessel ‘ i ’ from the center of outer tissue cylinder $\{(A_{vi} + R_{vwi} \cos \theta_i)^2 + (R_{vwi} \sin \theta_i)^2\}^{1/2}$, $i = 1, 2$ |
| R_i^* | = radius in conformally mapped space for i th sub-problem, $(U_i^2 + V_i^2)^{1/2}$, $i = 1, 2$ |
| R_{vwi} | = i th vessel radius, r_{vwi}/r_{tw} , $i = 1, 2$ |
| T | = temperature, $(t - t_{vw1}) / (t_{tw} - t_{vw1})$ |
| T_1 | = temperature, $T + PR^2/4$ |
| U_i | = first of the two coordinates in the conformally mapped space that relates to the x and y coordinates of the original Cartesian coordinate system for i th sub-problem, $\{(x_i - \lambda_i)(1 - \lambda_i x_i) - \lambda_i y_i^2\} / \{(1 - \lambda_i x_i)^2 - (\lambda_i y_i)^2\}$, $i = 1, 2$ |
| V_i | = second of the two coordinates in the conformally mapped space that relates to the x and y coordinates of the original Cartesian coordinate system for i th sub-problem, $\{(1 - \lambda_i^2) y_i\} / \{(1 - \lambda_i x_i)^2 - (\lambda_i y_i)^2\}$, $i = 1, 2$ |
| w_i | = conformal transformation for i th sub-problem, $U_i + jV_i = (x_i + jy_i - \lambda_i) / (1 - \lambda_i(x_i + jy_i))$, $i = 1, 2$ |
| x_i, y_i | = original Cartesian coordinate system in i th sub-problem, $i = 1, 2$ |
| x_2 | = one of the two coordinates of sub-problem 2 related to the original coordinates and the coordinates of sub-problem 1, $x_1 \cos(\phi_1) + y_1 \sin(\phi_1)$ |
| y_2 | = one of the two coordinates of sub-problem 2 related to the original coordinates and the coordinates of sub-problem 1, $y_1 \cos(\phi_1) - x_1 \sin(\phi_1)$ |

Greek Symbols

| | |
|-------------|---|
| θ_i | = angular position from the center of i th vessel in the original coordinate system, $i = 1, 2$ |
| α_i | = angular position from the center of i th vessel in the transformed coordinate system, $\tan^{-1}(V_i/U_i)$, $i = 1, 2$ |
| λ_i | = constant, $\{1 + a_{1i}a_{2i} - ((1 - a_{1i}^2)(1 - a_{2i}^2))^{1/2}\} / (a_{1i} + a_{2i})$, $i = 1, 2$ |
| ψ | = angular position measured from the center of tissue |
| ϕ_i | = angular position of the center of $(i + 1)$ th vessel from the center of tissue |

Appendix:

The purpose of this appendix is to show how $2(2N + 1)$ constants (A'_{01} , A'_{02} , A_{n1} , A_{n2} , B_{n1} , and B_{n2}) of Eq. (22) can be evaluated by constructing a linear system of $2(2N + 1)$ equations:

$$\begin{aligned}
T = & 1 + P/4 + A'_{01} \ln(R_1^*) + A'_{02} \ln(R_2^*) + \sum_{n=1}^{\infty} A_{n1} \{(R_1^*)^n \\
& - (R_1^*)^{-n}\} \sin(n\alpha_1) + \sum_{n=1}^{\infty} A_{n2} \{(R_2^*)^n - (R_2^*)^{-n}\} \sin(n\alpha_2) \\
& + \sum_{n=1}^{\infty} B_{n1} \{(R_1^*)^n - (R_1^*)^{-n}\} \cos(n\alpha_1) + \sum_{n=1}^{\infty} B_{n2} \{(R_2^*)^n \\
& - (R_2^*)^{-n}\} \cos(n\alpha_2) - PR^2/4 \quad (22)
\end{aligned}$$

The following relationships, mentioned in the nomenclature section, relate the variables $(R, R_1^*, \alpha_1, R_2^*, \alpha_2)$ of Eq. (22) to the original coordinates $(x_1, \text{ and } y_1)$:

$$R^2 = x_1^2 + y_1^2 \quad (A1)$$

$$(R_i^*)^2 = (U_i)^2 + (V_i)^2, \quad i = 1, 2 \quad (A2)$$

$$\alpha_i = \tan^{-1}(V_i/U_i), \quad i = 1, 2 \quad (A3)$$

$$U_i = \{(x_i - \lambda_i)(1 - \lambda_i x_i) - \lambda_i y_i^2\} / \{(1 - \lambda_i x_i)^2 - (\lambda_i y_i)^2\}, \quad i = 1, 2 \quad (A4)$$

$$V_i = \{(1 - \lambda_i^2)y_i\} / \{(1 - \lambda_i x_i)^2 - (\lambda_i y_i)^2\}, \quad i = 1, 2 \quad (A5)$$

$$\lambda_i = \{1 + a_{1i}a_{2i} - ((1 - a_{1i}^2)(1 - a_{2i}^2))^{1/2}\} / (a_{1i} + a_{2i}), \quad i = 1, 2 \quad (A6)$$

$$a_{1i} = A_{vi} - R_{vwi}, \quad i = 1, 2 \quad (A7)$$

$$a_{2i} = A_{vi} + R_{vwi}, \quad i = 1, 2 \quad (A8)$$

$$x_2 = x_1 \cos(\phi_1) + y_1 \sin(\phi_1) \quad (A9)$$

$$y_2 = y_1 \cos(\phi_1) - x_1 \sin(\phi_1) \quad (A10)$$

Substituting Eqs. (A1–A10) into Eq. (22), the new equation (22) in the original coordinates (x_1, y_1) can be rewritten as follows:

$$\begin{aligned}
T = & 1 + P/4 + A'_{01} \ln(R_1^*(x_1, y_1)) + A'_{02} \ln(R_2^*(x_1, y_1)) \\
& + \sum_{n=1}^{\infty} A_{n1} \{(R_1^*(x_1, y_1))^n - (R_1^*(x_1, y_1))^{-n}\} \sin(n\alpha_1(x_1, y_1)) \\
& + \sum_{n=1}^{\infty} A_{n2} \{(R_2^*(x_1, y_1))^n - (R_2^*(x_1, y_1))^{-n}\} \sin(n\alpha_2(x_1, y_1)) \\
& + \sum_{n=1}^{\infty} B_{n1} \{(R_1^*(x_1, y_1))^n - (R_1^*(x_1, y_1))^{-n}\} \cos(n\alpha_1(x_1, y_1)) \\
& + \sum_{n=1}^{\infty} B_{n2} \{(R_2^*(x_1, y_1))^n - (R_2^*(x_1, y_1))^{-n}\} \cos(n\alpha_2(x_1, y_1)) \\
& - PR^2(x_1, y_1)/4 \quad (A11)
\end{aligned}$$

The original coordinates (x_1, y_1) relate to the vessel 1 parameters (R_{vw1}, θ_1) and vessel 2 parameters (R_{vw2}, θ_2) as given below.

For vessel 1—

$$x_1 = R_{vw1} \cos \theta_1 + A_{v1} \quad (A12)$$

$$y_1 = R_{vw1} \sin \theta_1 \quad (A13)$$

For vessel 2—

$$x_1 = (R_{vw2} \cos \theta_2 + A_{v2}) \cos(\phi_1) - (R_{vw2} \sin \theta_2) \sin(\phi_1) \quad (A14)$$

$$y_1 = (R_{vw2} \cos \theta_2 + A_{v2}) \sin(\phi_1) + (R_{vw2} \sin \theta_2) \cos(\phi_1) \quad (A15)$$

Substituting Eqs. (A12–A13) and (A14–A15), respectively, into Eq. (A11) and applying the original vessel wall boundary conditions to the resulting equation, gives the following two equations:

$$\begin{aligned}
T_{vw1} = & 1 + P/4 + A'_{01} \ln(R_1^*(R_{vw1}, \theta_1)) + A'_{02} \ln(R_2^*(R_{vw1}, \theta_1)) + \sum_{n=1}^{\infty} A_{n1} \{(R_1^*(R_{vw1}, \theta_1))^n - (R_1^*(R_{vw1}, \theta_1))^{-n}\} \sin(n\alpha_1(R_{vw1}, \theta_1)) \\
& + \sum_{n=1}^{\infty} A_{n2} \{(R_2^*(R_{vw1}, \theta_1))^n - (R_2^*(R_{vw1}, \theta_1))^{-n}\} \sin(n\alpha_2(R_{vw1}, \theta_1)) + \sum_{n=1}^{\infty} B_{n1} \{(R_1^*(R_{vw1}, \theta_1))^n \\
& - (R_1^*(R_{vw1}, \theta_1))^{-n}\} \cos(n\alpha_1(R_{vw1}, \theta_1)) + \sum_{n=1}^{\infty} B_{n2} \{(R_2^*(R_{vw1}, \theta_1))^n - (R_2^*(R_{vw1}, \theta_1))^{-n}\} \cos(n\alpha_2(R_{vw1}, \theta_1)) \\
& - PR^2(R_{vw1}, \theta_1)/4 \quad (A16)
\end{aligned}$$

$$\begin{aligned}
T_{vw2} = & 1 + P/4 + A'_{01} \ln(R_1^*(R_{vw2}, \theta_2)) + A'_{02} \ln(R_2^*(R_{vw2}, \theta_2)) + \sum_{n=1}^{\infty} A_{n1} \{(R_1^*(R_{vw2}, \theta_2))^n - (R_1^*(R_{vw2}, \theta_2))^{-n}\} \sin(n\alpha_1(R_{vw2}, \theta_2)) \\
& + \sum_{n=1}^{\infty} A_{n2} \{(R_2^*(R_{vw2}, \theta_2))^n - (R_2^*(R_{vw2}, \theta_2))^{-n}\} \sin(n\alpha_2(R_{vw2}, \theta_2)) + \sum_{n=1}^{\infty} B_{n1} \{(R_1^*(R_{vw2}, \theta_2))^n \\
& - (R_1^*(R_{vw2}, \theta_2))^{-n}\} \cos(n\alpha_1(R_{vw2}, \theta_2)) + \sum_{n=1}^{\infty} B_{n2} \{(R_2^*(R_{vw2}, \theta_2))^n - (R_2^*(R_{vw2}, \theta_2))^{-n}\} \cos(n\alpha_2(R_{vw2}, \theta_2)) \\
& - PR^2(R_{vw2}, \theta_2)/4 \quad (A17)
\end{aligned}$$

It can be seen from Eqs. (A16) and (A17) that they are only functions of vessel 1 and vessel 2 parameters, respectively. Multiplying both sides of Eq. (A16) with $\sin(m\theta_1)$ and $\cos(m\theta_1)$, respectively (where, $m = 0 \cdots N$), and integrating over the vessel 1

perimeter ($\theta_1 = 0 \cdots 2\pi$) will result in a linear system of $2N + 1$ equations with $2(2N + 1)$ unknowns. Similarly, multiplying both sides of Eq. (A17) with $\sin(m\theta_2)$ and $\cos(m\theta_2)$, respectively (where, $m = 0 \cdots N$), and integrating over the vessel 2 perimeter

($\theta_2=0 \cdots 2\pi$) will result in an additional linear system of $2N + 1$ equations with $2(2N + 1)$ unknowns. This complete set of $2(2N + 1)$ equations with $2(2N + 1)$ unknowns can be solved using any linear equation solver to evaluate the constants.

References

- [1] Hahn, G. M., 1982, *Hyperthermia and Cancer*, Plenum Press, New York.
- [2] Xu, L. X., Holmes, K. R., Moore, B., Chen, M. M., and Arkin, H., 1994, "Microvascular Architecture Within the Pig Kidney Cortex," *Microvasc. Res.*, **47**, pp. 293–307.
- [3] Rommel, S. A., and Caplan, H., 2003, "Vascular Adaptations for Heat Conservation in the Tail of Florida Manatees (*Trichechus Manatus Latiostris*)," *J. Anat.*, **202**, pp. 343–353.
- [4] Pabst, D. A., Rommel, S. A., McLellan, W. A., Williams, T. M., and Rowles, T. K., 1995, "Thermoregulation of the Intra-Abdominal Testes of the Bottlenose Dolphin (*Tursiops Truncatus*) During Exercise," *J. Exp. Biol.*, **198**, pp. 221–226.
- [5] Geist, N. R., 2000, "Nasal Respiratory Turbinate Function in Birds," *Physiol. Biochem. Zool.*, **73**(5), pp. 581–589.
- [6] Mitchell, J. W., and Myers, G. E., 1968, "An Analytical Model of the Counter-Current Heat Exchange Phenomena," *Biophys. J.*, **8**, pp. 897–911.
- [7] Zhu, L., 2000, "Theoretical Evaluation of Contributions of Heat Conduction and Counter-Current Heat Exchange in Selective Brain Cooling in Humans," *Ann. Biomed. Eng.*, **28**, pp. 269–277.
- [8] DiFelice, Jr., R. F., and Bau, H. H., 1983, "Conductive Heat Transfer Between Eccentric Cylinders With Boundary Conditions of the Third Kind," *ASME J. Heat Transfer*, **105**, pp. 678–680.
- [9] Lemons, D. E., Chien, S., Crawshaw, L. I., Weinbaum, S., and Jiji, L. M., 1987, "Significance of Vessel Size and Type in Vascular Heat Transfer," *Am. J. Phys.*, **253**, pp. R128–R135.
- [10] Chato, J. C., 1980, "Heat Transfer to Blood Vessels," *J. Biomech. Eng.*, **102**, pp. 110–118.
- [11] Wissler, E. H., 1988, "An Analytical Solution Countercurrent Heat Transfer Between Parallel Vessels With a Linear Axial Temperature Gradient," *J. Biomech. Eng.*, **110**, pp. 254–256.
- [12] Shitzer, A., Stroschein, L. A., Gonzalez, R. R., and Pandolf, K. B., 1997, "Numerical Analysis of an Extremity in Cold Environment Including Counter-Current Arterio-Venous Heat Exchange," *J. Biomech. Eng.*, **119**, 179–186.
- [13] Baish, J. W., and Ayyaswamy, P. S., 1986, "Small-Scale Temperature Fluctuations in Perfused Tissue During Local Hyperthermia," *J. Biomech. Eng.*, **108**, pp. 246–250.
- [14] Baish, J. W., Ayyaswamy, P. S., and Foster, K. R., 1986, "Heat Transport Mechanisms in Vascular Tissues: A Model Comparison," *J. Biomech. Eng.*, **108**, pp. 324–331.
- [15] Zhu, M., Weinbaum, S., and Jiji, L. M., 1990, "Heat Exchange Between Unequal Countercurrent Vessels Asymmetrically Embedded in a Cylinder With Surface Convection," *Int. J. Heat Mass Transfer*, **33**, pp. 2275–2283.
- [16] Zhu, M., Weinbaum, S., Jiji, L. M., and Lemons, D. E., 1988, "On the Generalization of the Weinbaum–Jiji Bioheat Equation to Microvessels of Unequal Size; The Relation Between the Near Field and Local Average Tissue Temperatures," *J. Biomech. Eng.*, **110**, pp. 74–81.
- [17] Wu, Y. L., Weinbaum, S., and Jiji, L. M., 1993, "A New Analytic Technique for 3-D Heat Transfer From a Cylinder With Two or More Axially Interacting Eccentrically Embedded Vessels With Application to Countercurrent Blood Flow," *Int. J. Heat Mass Transfer*, **36**, pp. 1073–1083.
- [18] Zhu, L., Lemons, D. E., and Weinbaum, S., 1996, "Microvascular Thermal Equilibration in Rat Cremaster Muscle," *Ann. Biomed. Eng.*, **24**, pp. 109–123.
- [19] Song, J., Xu, L. X., Lemons, D. E., and Weinbaum, S., 1997, "Enhancement in the Effective Thermal Conductivity in Rat Spinotrapezius Due to Vasoregulation," *J. Biomech. Eng.*, **119**, pp. 461–468.
- [20] Song, J., Xu, L. X., Lemons, D. E., and Weinbaum, S., 1997, "Microvascular Thermal Equilibration in Rat Spinotrapezius Muscle," *Ann. Biomed. Eng.*, **27**, pp. 56–66.
- [21] Van Leeuwen, G. M. J., Kotte, A. N. T. J., Crezee, J., and Lagendijk, J. J. W., 1997, "Tests of the Geometrical Description of Blood Vessels in a Thermal Model Using Counter-Current Geometries," *Phys. Med. Biol.*, **42**, pp. 1515–1532.
- [22] Zhu, L., and Weinbaum, S., 1995, "A Model for Heat Transfer From Embedded Blood Vessels in 2-D Tissue Preparations," *J. Biomech. Eng.*, **117**, pp. 64–73.
- [23] He, Q., Zhu, L., Lemons, D. E., and Weinbaum, S., 2002, "Experimental Measurements of the Temperature Variation Along Artery–Vein Pairs From 200 to 1000 μm Diameter in Rat Hind Limb," *J. Biomech. Eng.*, **124**, pp. 656–661.
- [24] Zhu, L., Xu, L. X., He, Q., and Weinbaum, S., 2002, "A New Fundamental Bioheat Equation for Muscle Tissue—Part 2: Temperature of SAV Vessels," *J. Biomech. Eng.*, **124**, pp. 121–132.
- [25] He, Q., Zhu, L., and Weinbaum, S., 2003, "Effect of Blood Flow on Thermal Equilibration and Venous Rewarming," *Ann. Biomed. Eng.*, **31**, pp. 659–666.
- [26] Lebedev, N. N., Skalskaya, I. P., and Uflyand, Y. S., 1979, *Worked Problems in Applied Mathematics*, Dover, New York.
- [27] El-Saden, M. R., 1961, "Heat Conduction in an Eccentrically Hollow, Infinitely Long Cylinder With Internal Heat Generation," *ASME J. Heat Transfer*, **83**, pp. 510–512.
- [28] El-Shaarawi, M. A., and Mukheimer, I., 1995, "Unsteady Conduction in Eccentric Annuli," *Heat Mass Transfer*, **30**, pp. 249–257.
- [29] Shrivastava, D., and Roemer, R. B., 2004, "An Analytical Derivation of Source Term Dependent, 2-D Generalized Poisson Conduction Shape Factors," *Int. J. Heat Mass Transfer*, **47**(19–20), pp. 4293–4300.
- [30] Roemer, R. B., and Dutton, A. W., 1998, "A Generic Tissue Convective Energy Balance Equation: Part 1—Theory and Derivation," *J. Biomech. Eng.*, **120**, pp. 395–404.
- [31] Shrivastava, D., and Roemer, R. B., 2004, "An Analytical Study of Heat Transfer in Finite Tissue With Two Blood Vessels and General Dirichlet Boundary Conditions," *Int. J. Heat Mass Transfer*, (accepted).
- [32] Pennes, H. H., 1948, "Analysis of Tissue and Arterial Blood Temperatures in Resting Human Forearm," *J. Appl. Phys.*, **1**, pp. 93–122.
- [33] Brown, J. W., and Churchill, R. V., 1996, *Complex Variables and Applications*, McGraw-Hill, New York.
- [34] Devashish, 2004, "Development and Evaluation of Tissue Convective Energy Balance Equation," Ph.D. dissertation, University of Utah, Salt Lake City, UT.
- [35] Wehner, H., Ardenne, A. V., and Kaltofen, S., 2001, "Whole-Body Hyperthermia With Water-Filtered Infrared Radiation: Technical–Physical Aspects and Clinical Experiences," *Int. J. Hyperthermia*, **17**, pp. 19–30.
- [36] Landry, J., and Marceau, N., 1978, "Rate-Limiting Events in Hyperthermic Cell Killing," *Radiat. Res.*, **75**, pp. 573–585.
- [37] Milnor, W. R., 1990, *Cardiovascular Physiology*, Oxford University Press, New York.
- [38] Gray, H., 1978, *Gray's Anatomy, Descriptive and Surgical*, Barnes and Nobel Inc., New York.

New Interpretation of Non-Fourier Heat Conduction in Processed Meat

Paul J. Antaki

e-mail: antakip@asme.org

Antaki & Associates, Inc., P.O. Box 212, Howell, NJ 07731

This work uses the “dual phase lag” (DPL) model of heat conduction to offer a new interpretation for experimental evidence of non-Fourier conduction in processed meat that was interpreted previously with hyperbolic conduction. Specifically, the DPL model combines the wave features of hyperbolic conduction with a diffusion-like feature of the evidence not captured by the hyperbolic case. In addition, comparing the new interpretation to Fourier-based alternatives suggests that further study of all the interpretations could help advance the understanding of conduction in the processed meat and other biological materials such as human tissue. [DOI: 10.1115/1.1844540]

Keywords: Heat Transfer, Conduction, Non-Equilibrium, Composites, Bioengineering

Introduction

This work uses the “dual phase lag” (DPL) model [1] of heat conduction to offer a new interpretation for the evidence of non-Fourier conduction in the experiments of Mitra et al. [2] with processed meat (bologna). In particular, the DPL model provides a more comprehensive treatment of the heterogeneous nature of the meat compared to the interpretation in [2] that used hyperbolic conduction. Nevertheless, this work does not seek to prove that the DPL model is applicable to the processed meat. Instead, the objective here is to determine if the model merits additional study alongside the alternative interpretations that are summarized later.

Importantly, the evidence in [2] raises the possibility that non-Fourier conduction is relevant to human tissue, as discussed later. Consequently, the motivation for the work here is to extend the analysis of [2] that is aimed at eventually developing better tools to predict transient temperature in human tissue. For example, damage to human tissue from thermal burns is an exponential function of temperature [3] so even small improvements in predicted temperatures can strongly influence predictions of damage.

The approach taken here for the new interpretation with DPL conduction treats the processed meat as a composite material that is a heterogeneous compacted mixture of two different constituents (meat particles and water). A single macroscopic (average) temperature, which is a function of location and time, characterizes the composite. Furthermore, the DPL model accounts approximately for the effects of the different microscopic (individual) thermal behaviors of the constituents on this macroscopic temperature during the period of thermal nonequilibrium that corresponds to the early stages of heating or cooling. That is, before the two constituents closely approach local thermal equilibrium (identical temperatures) at successive locations in the composite.

In contrast to the approach taken here, the classical approach for predicting a single macroscopic temperature of a composite treats it as homogeneous [4]. More specifically, this classical approach uses Fourier conduction and homogenized properties (i.e., effective or average properties) that correspond to local thermal

equilibrium between the different constituents. Consequently, the classical approach does not capture the effects of nonequilibrium on the macroscopic temperature during the early stages of heating or cooling, as observed experimentally (e.g., [1,2,4–7]).

More rigorously, the individual temperatures of the different constituents during nonequilibrium can be close to, or far from, a single macroscopic temperature depending on their thermal properties and modes of heating [8,9]. However, the approach taken here focuses on a single macroscopic temperature because the temperatures measured in [2] appear to be average values for the processed meat, as discussed later.

DPL Model

The DPL model accounts for deviations from the classical approach involving Fourier conduction by introducing the phase lags τ_q and τ_T of heat flux and temperature gradient, respectively. Here, it is convenient to interpret τ_q as a measure of the delay in conduction (e.g., contact resistance between meat particles) that is not captured by the classical approach during nonequilibrium. On the other hand, τ_T is interpreted conveniently here as a measure of the conduction that occurs along microscopic paths (e.g., within meat particles) not captured by the classical approach during nonequilibrium.

For the one-dimensional problems solved later, the DPL relation [1] between heat flux and temperature gradient is

$$q + \tau_q \frac{\partial q}{\partial t} = -k \frac{\partial T}{\partial x} - k \tau_T \frac{\partial^2 T}{\partial t \partial x}, \quad (1)$$

where q and T are the macroscopic (average) heat flux and temperature, x and t are the location and time, and k is the homogenized thermal conductivity of the classical approach described in [4]. These problems are posed with the statement of energy conservation,

$$\rho C \frac{\partial T}{\partial t} = - \frac{\partial q}{\partial x}, \quad (2)$$

where ρ and C are the homogenized density and specific heat of the classical approach [4].

Equation (1) reduces to the corresponding relation for the hyperbolic model in [2] by setting $\tau_T=0$. Also, it reduces to the relation for Fourier conduction of the classical approach by setting $\tau_T=0$ and $\tau_q=0$ (i.e., a homogeneous material). Moreover, for $\tau_T/\tau_q=1$ the solutions to the DPL problems in this work reduce to corresponding Fourier solutions of the classical approach.

Relation to Two-Temperature Model

Reference [1] develops a DPL heat equation for a macroscopic temperature of a two-constituent composite by combining the microscopic (individual) Fourier heat equations of the two constituents. These individual equations comprise a two-temperature model for the composite because they contain the two distinct temperatures of the constituents. Hence, this development in [1] shows that DPL conduction can describe a macroscopic result of microscopic interactions governed by Fourier conduction. Correspondingly, the DPL model adopted here is parabolic (diffusive) in nature similar to the Fourier model. This DPL model, however, can be a more convenient tool for predicting a macroscopic temperature of a composite compared to the two-temperature model because the DPL approach defined earlier solves directly for a macroscopic temperature.

Highlights of Experiments

Reference [2] describes four types of experiments where predictions of transient temperatures obtained with the classical Fourier approach did not reproduce temperatures that were measured in samples of processed meat. However, measurements from only

Contributed by the Heat Transfer Division for publication in the JOURNAL OF HEAT TRANSFER. Manuscript received by the Heat Transfer Division December 10, 2003; revision received October 27, 2004. Review conducted by: G. Chen.

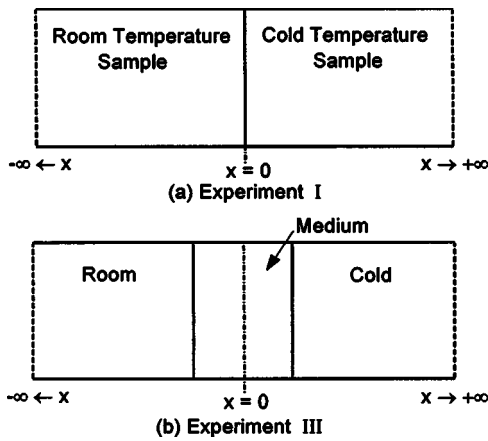


Fig. 1 Schematic of Experiments I and III (after [2])

two of these experiments, Experiments I and III, are needed here to show that DPL conduction can capture their non-Fourier features.

In Experiments I and III, samples of processed meat at uniform but different initial temperatures were placed suddenly into contact at $t=0^+$. The experiments were designed so that the subsequent conduction was one-dimensional, occurring in only the longer-dimension (x -direction) of each sample. Also the samples were sufficiently long so that, for some time after $t=0^+$, each experiment simulated an infinite solid occupying $-\infty < x < +\infty$. Importantly, the temperatures measured with thermocouples at several locations in the samples appear to be macroscopic (average) values because their beads were probably in contact with both constituents (meat particles and water).

For Experiment I a room temperature sample and a cold sample of processed meat were placed into contact along the line $x=0$ corresponding to their interface, as noted in Fig. 1. The initial temperatures were $T_{ri}=23.1^\circ\text{C}$ and $T_{ci}=8.2^\circ\text{C}$ for the “room” and cold samples, respectively. For Experiment III, Fig. 1 shows that a sample (with the thickness of 10.4 mm) at an initial temperature between room and cold values (i.e., a medium temperature) was “sandwiched” between room temperature and cold temperature samples, where $x=0$ was aligned with the center of the medium temperature sample. The initial temperature of the “medium sample,” T_{mi} , was 14.3°C and the initial temperatures of the room and cold samples were 24.1°C and 6.2°C , respectively.

For the meat samples in both experiments [2], $k=0.80\text{ W/mK}$, $\rho=1230\text{ kg/m}^3$, and $C=4.66\text{ kJ/kgK}$. As described shortly, treating k , ρ , C , τ_T , and τ_q as constants, then fitting the DPL predictions made here to the temperatures measured in [2], led to $\tau_T=0.043\text{ s}$ and $\tau_q=16\text{ s}$ for Experiment I, and $\tau_T=0.056\text{ s}$ and $\tau_q=14\text{ s}$ for Experiment III. Similarly, [2] determined that $\tau_q=15.5\text{ s}$ for hyperbolic conduction in each experiment.

The Appendix summarizes the methods underlying the predictions made here for the macroscopic temperatures of the DPL, hyperbolic and classical Fourier cases that accompany the new interpretation discussed next. As described in the Appendix, all of these predictions were performed so that the corresponding temperatures would change by less than 1% with, for example, smaller sizes in time and space steps for the finite-difference solution of the DPL problem posed for Experiment III.

New Interpretation

Figure 2 compares the temperatures predicted here to the measurement in [2] for the room temperature sample of Experiment I at 6.3 mm from its interface with the cold sample. For consistency with [2] the comparison uses the dimensionless temperature θ and dimensionless time $(t/15.5\text{ s})$, where this time incorporates τ_q

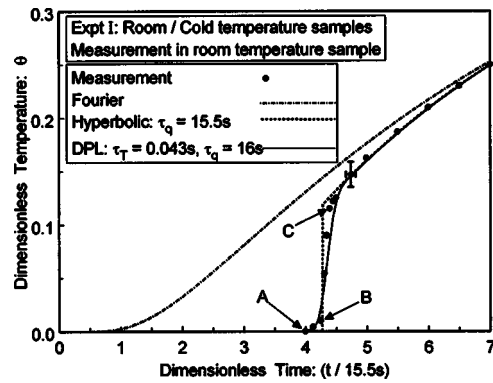


Fig. 2 A comparison of measurement and predictions for Experiment I

$=15.5\text{ s}$ obtained for hyperbolic conduction in [2]. Also, $\theta=(T-T_{ri})/(T_{ref}-T_{ri})$, where the reference temperature, $T_{ref}=15.7^\circ\text{C}$, is the constant value measured at the interface of the cold and room temperature samples after being placed into contact. Importantly, θ is defined so that its value increases even though the actual temperature decreases in the room temperature sample.

The solid circles in Fig. 2 are discrete values of measured temperature that were extracted from the continuous thermocouple record in [2] by enlarging the original figure (Fig. 2(a) in [2]) then noting these values with a caliper and scale. The number of circles was judged sufficient to represent faithfully the continuous record. Also, the vertical range of uncertainty for the extracted values in Fig. 2 is the same as the original range for the continuous record in [2]. This range is the same because the vertical uncertainty associated with the extraction is small relative to the original range. However, the horizontal uncertainty in Fig. 2 is the range associated with the extraction, which is larger than the original range in [2]. Figure 2 shows only one pair of uncertainty bars because this pair is the same at each circle.

For the DPL prediction in Fig. 2 the values of τ_q and τ_T were estimated using a simple method geared toward obtaining quickly a reasonable fit of the prediction to the measurement. Despite its simplicity, this method was deemed adequate for illustrating the overall behavior of the DPL prediction and determining if the DPL model merits additional study. The fit was obtained by noting first that the delayed initial increase in temperature measured within the sample was consistent with the general behavior of DPL conduction in the range of $0 < R < 1$, where $R=\tau_T/\tau_q$ (e.g., see the general behavior in [1]). After that, the value $\tau_q=15.5\text{ s}$, determined for hyperbolic conduction ($R=0$) in [2], was adopted as a first approximation for τ_q of the DPL case here. Then, the values of τ_q and τ_T were adjusted over several cycles of predictions until they provided a reasonable fit to the measurement as judged “by eye.”

The key feature of Fig. 2 is that the DPL prediction (solid line) closely follows the measurement in the room temperature sample. Specifically, this prediction captures the gradual increase in temperature from A to B that is not reproduced by the hyperbolic case (dashed line). Furthermore, the DPL prediction captures the rapid increase in temperature from B to C that the hyperbolic case, in contrast, predicts as an abrupt jump in temperature. Also, the figure shows that at relatively early times the Fourier prediction (dashed-dotted line) of the classical approach deviates significantly from the measurement and non-Fourier (DPL and hyperbolic) predictions.

In more detail, the absence of noticeable increases in the measured temperature and the non-Fourier predictions for times earlier than point A in Fig. 2 is a consequence of the conduction delay induced by the effect of τ_q . With hyperbolic conduction [2]

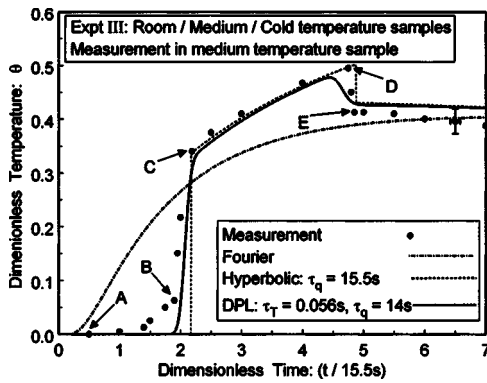


Fig. 3 A comparison of measurement and predictions for Experiment III

this delay leads to the propagation of thermal waves with sharp wave fronts separating heated and unheated zones in the context of the dimensionless temperature θ . Hence, for hyperbolic conduction the abrupt jump in temperature corresponds to a wave front passing this location in the sample. For DPL conduction, however, τ_T accounts for diffusion of heat ahead of the sharp wave fronts that would be induced by τ_q . This diffusion broadens the wave fronts, so the combined effect of τ_q and τ_T appears as the gradual increase in temperature from A to B followed by the rapid (but not abrupt) increase from B to C. Importantly, this diffusion is consistent with the parabolic nature of the DPL model adopted here.

Figure 2 shows also that the Fourier prediction deviates significantly from the measurement at relatively early times because, even though the Fourier model is parabolic, it does not incorporate the combined effect of the phase lags just noted for the DPL case. However, as expected, the Fourier prediction converges to the measurement and non-Fourier predictions as the different constituents of the meat approach thermal equilibrium at this location in the sample.

Before leaving Fig. 2 it is important to note that the vertical uncertainty in measured temperature is larger than the magnitude of the gradual increase in temperature from A to B just attributed to DPL conduction. Thus, even though all the experiments in [2] show this type of gradual increase prior to their rapid increases in temperature, a more detailed study of the gradual increase is postponed until measurements become available with smaller uncertainties that would permit a more definitive discussion. In addition, there is evidence [1] that the phase lags should depend on location so the values of lags listed in Fig. 2 could change after accounting for this dependence. Consequently, using a more sophisticated method to determine the phase lags, such as parameter estimation [10], is postponed until more extensive measurements become available.

Lastly, it is interesting to note that the parabolic nature of the DPL model adopted here means that a thermal disturbance at any point in the meat samples of Experiment I (and in Experiment III) affects instantaneously every other point in the samples, similar to the Fourier case. However, the conduction delay represented by τ_q of the DPL model causes this instantaneous effect to become noticeable at times that are greater than those predicted by the Fourier case.

Next, Fig. 3 shows that the DPL prediction approximately captures the two rapid changes in temperature measured in the medium temperature sample of Experiment III from [2]. The thermocouple was located in this sample at 3.2 and 7.2 mm from its interfaces with the room and cold temperature samples, respectively. In particular, the figure compares the measurement taken from Fig. 4 of [2] to the temperatures predicted here in terms of dimensionless temperature θ versus dimensionless time $(t/15.5s)$,

where $\theta = (T - T_{mi}) / (T_{ref} - T_{mi})$, and $T_{ref} = 19.2^\circ\text{C}$, as calculated with $T_{ref} = (T_{ri} + T_{mi}) / 2$. For this dimensionless temperature, increases and decreases in θ correspond to increases and decreases, respectively, in actual temperature. The solid circles in Fig. 3 are discrete values of measured temperature extracted from the continuous thermocouple record in [2] using the method described earlier. Also, the figure shows only one pair of uncertainty bars because this pair is the same at each circle.

For the DPL prediction in Fig. 3, the values of τ_q and τ_T were estimated using the method described earlier with Fig. 2. However, for Fig. 3 this method was oriented toward obtaining values of the phase lags to approximate only the rapid changes in measured temperature because of its more complex non-Fourier behavior relative to Fig. 2. Accordingly, Fig. 3 shows that the DPL prediction does not follow closely the gradual increase in measured temperature from A to B in the medium temperature sample that would be attributed to DPL conduction. In a future study, a more sophisticated method to estimate the phase lags could provide a DPL prediction that captures closely the entire range of measured temperature in the figure.

Figure 3 does show, however, that the DPL prediction in the medium temperature sample captures the first rapid change in measured temperature (B up to C) that the hyperbolic prediction shows as an abrupt jump in temperature. This abrupt jump is a consequence of the wave front associated with τ_q of the hyperbolic case, similar to the jump discussed previously with Fig. 2. For the DPL case, in comparison, the combined effect of τ_q and τ_T again broadens the wave front, leading to the rapid increase in temperature instead of an abrupt jump. Interestingly, the room temperature sample induces the first rapid change from B to C and subsequent heating from C to D because the thermocouple is located closer to this sample than to the cold sample.

At D the cold sample induces the second rapid change in measured temperature (D down to E). Although the DPL prediction shows a rapid change that begins in the neighborhood of D, this change is significantly less rapid than that of the measurement. Nonetheless, the combined effect of the phase lags permits the DPL prediction to avoid the abrupt decrease in temperature that the hyperbolic case exhibits, starting at about D. In the hyperbolic framework [2], this abrupt decrease is a consequence of destructive interference between heating and cooling waves that originate from the room and cold temperature samples. Figure 3 shows also that the Fourier prediction, which lacks the combined effect of the phase lags, does not capture the two rapid changes in measured temperature.

To complete the discussion of Fig. 3 it is important to note that after the second rapid change in measured temperature (D down to E) the Fourier prediction converges toward the hyperbolic and DPL predictions, as expected. However, the three predictions do not converge to the measured temperature after point E even at the dimensionless time of 15 (not shown), which is the maximum time provided in [2] for the continuous thermocouple record. Additional experiments performed as part of a future study could help explain this lack of convergence.

Finally, DPL predictions made as part of this work, but not shown here, capture the non-Fourier features of the temperatures measured in the other experiments of [2] with processed meat. These DPL predictions avoid the abrupt changes in temperature associated with the hyperbolic model. More generally, the DPL predictions for all the experiments in [2] correspond to the range of $0 < R < 1$, where $R = \tau_T / \tau_q$ (for example, $R \approx 0.003$ with Fig. 2 here). The theoretical study of [11], however, states that DPL predictions for certain heterogeneous materials should be restricted to $R > 1$. It is not yet clear if this restriction should apply to the processed meat of [2], so the potential conflict between the range of R for the DPL predictions here and the restriction of [11] needs to be resolved in a future study. On a related note, [1] and [7] report measurements of temperature and corresponding DPL predictions with $0 < R < 1$ for heterogeneous materials (but not processed meat).

Application to Human Tissue

Figure 7 in [2] shows evidence of non-Fourier behavior for the macroscopic temperature measured in a sample of raw pork (porcine tissue) under conditions analogous to Experiment I. Moreover, this behavior is roughly similar to the DPL prediction shown here in Fig. 2. Hence, this evidence in [2] raises the possibility that non-Fourier conduction is relevant to human tissue in the context of a macroscopic temperature, because there is a close resemblance between human and porcine tissue [12]. In turn, this possibility means that predicting the damage to human tissue from thermal burns might be improved by using the DPL model to calculate macroscopic temperatures during the burn process.

A special note is that the relatively close behaviors of the DPL and hyperbolic predictions in Figs. 2 and 3 appear to suggest that the hyperbolic model could serve as an approximation to the DPL model. In general, however, this approximation should be avoided because solutions to problems governed by this DPL model are diffusive in nature. For example, although not shown here, these DPL solutions do not exhibit the well known abrupt jumps in surface temperature associated with hyperbolic conduction for a solid subjected to a suddenly applied heat flux at that surface. Hence, the artificially high surface temperature of the hyperbolic case could induce large errors in the prediction of damage from thermal burns because the severity of damage is an exponential function of temperature [3].

Alternative Interpretations

In addition to Fourier conduction within the individual constituents (solid and water) of the processed meat, [13] included the motion of water in the meat—and the corresponding convection—to provide an alternative interpretation of the abrupt jumps in temperature measured for the experiments of [2]. In contrast, all of the predictions made here and in [2] corresponded to “pure conduction” because they did not include this convection.

According to [13], convection was induced in the experiments of [2] by pressing the meat samples together at the start of each experiment and by the subsequent development of temperature gradients across the samples. In the context of this convection the temperature jumps were attributed to, for instance, the arrival of warm water at the measurement locations in the colder samples before the effect of “pure conduction” became noticeable at these locations. Interestingly, the temperature predictions in [13] resembled qualitatively the measurement shown, for example, in Fig. 2 here. However, [13] did not directly compare its predictions to the measurement represented in the figure.

Despite the resemblance just noted, interpreting the experiments of [2] in the context of convection might require additional study before it can replace interpretations based on “pure conduction.” In particular, predictions similar to the DPL case in Fig. 2 here can be obtained using the equations of [13] by recasting those equations in the form of a “pure conduction” DPL equation. Specifically, setting the convection term equal to zero in the energy equation for the water (Eq. (1) in [13]) results in a Fourier heat equation that describes “pure conduction” in the water. Then, combining this heat equation with the “pure conduction” Fourier heat equation for the solid (Eq. (2) in [13]) to eliminate either the water or solid temperature leads to a “pure conduction” DPL equation with the form of Eq. (6.17) on p. 158 of [1].

Next, [14] cited the possibility that the measurements in [2] showing evidence of non-Fourier conduction in the processed meat were wrong or misinterpreted. To support this possibility, [14] showed that temperatures measured in its experiment with processed meat did not show non-Fourier behavior. Unfortunately, it was not possible to reconcile the conflicting measurements of [2] and [14] because their experiments were performed differently and there was no information in either study about the internal details of the processed meats.

In contrast to the experiment of [14], the experiment with processed meat in [15] was meant to closely reproduce Experiment I of [2]. Despite this closeness the measurements of [15] did not exhibit non-Fourier behavior. In turn, [15] cited several issues with the experiments of [2] that might have caused the temperature jumps which [2] attributed to hyperbolic conduction. However, [15] left open the possibility that the non-Fourier behavior in [2] could have been a manifestation of the “thermal lag” induced by the different thermal properties for the constituents of the meat.

Finally, it is interesting to note that a classical “thermal penetration time” t_p defined for Fourier conduction does not explain the delays in conduction exhibited by the measurements of [2] with processed meat. In general terms, t_p is the time required for the temperature at a given location in a solid to change by a specified amount after the onset of a thermal disturbance elsewhere in the solid. More specifically, for a semi-infinite solid, [15] cites the expression for penetration time: $t_p = x^2/(10\alpha)$, where x is the given location in the solid relative to its surface at $x=0$ that is subjected to a thermal disturbance and α is its thermal diffusivity. For the processed meat of [2]: $\alpha = 1.4 \times 10^{-7} \text{ m}^2/\text{s}$ using $\alpha = k/(\rho C)$ and the values for k , ρ , and C cited earlier. Importantly the definition of the penetration time is somewhat arbitrary, as noted in [15], so the expression for t_p is treated here as an approximation.

By applying the expression just cited for t_p to, for example, the room temperature sample of processed meat in Experiment I that corresponds to Fig. 2 here, $t_p = 28.4 \text{ s}$ for the sample at 6.3 mm from its interface with the cold sample. Alternatively, in the dimensionless context of Fig. 2, $(t_p/15.5 \text{ s}) = 1.8$. Figure 2 shows that this dimensionless penetration time corresponds approximately to the first noticeable increase in temperature predicted by the classical Fourier model. However, the temperatures for the measurement and the DPL prediction first increase noticeably at the larger dimensionless time of about 4.2. Consequently, this Fourier penetration time does not explain the conduction delay in the measurement of Experiment I.

Conclusion

The existence of several different interpretations for the measurements in [2] with processed meat suggests that additional study is needed to help clarify the nature of conduction in the meat. In particular the parabolic DPL model, as adopted here, merits a role in this study because it accounts for the heterogeneous nature of the meat that is not accommodated by the classical Fourier model. Perhaps more importantly, the additional study could help advance the understanding of conduction in other biological materials such as human tissue.

Acknowledgment

Professor Sunil Kumar of Polytechnic University contributed to this new interpretation and Professor M. Erol Ulucakli of Lafayette College provided advice regarding the revised manuscript.

Appendix: Prediction Methods

The DPL prediction for Experiment I was obtained by applying Eq. (7) from [16] to the cold and room temperature samples in the experiment. This equation is an analytical solution to the DPL problem of a semi-infinite solid with a uniform initial temperature occupying $x > 0$ when, at $t = 0^+$, its surface temperature at $x = 0$ is suddenly raised (or lowered) to a constant value. Hence, this solution applies separately to the cold and room temperature samples of Experiment I after setting the constant surface temperature in the solution to $(T_{ci} + T_{ri})/2$, which is the constant temperature measured at the interface between samples during the experiment. (Also, this interface temperature was derived independently for the Fourier, hyperbolic and DPL predictions in this

work by following the procedure in [17].) Similarly, the Fourier ($\tau_T/\tau_q=1$) and hyperbolic ($\tau_T=0$, $\tau_q=15.5$ s) predictions for Experiment I were obtained using Eqs. (6) and (7) from [16] along with the interface temperature just noted. For all predictions, the integrals in these equations were evaluated numerically using the method described in [16]. During each evaluation, the number of subintervals comprising the ranges of integration was increased until less than a 1% change in temperature would occur with additional subintervals.

For Experiment III, the DPL prediction was obtained by solving numerically the problem posed by Eqs. (1) and (2) cited earlier in this work along with the corresponding initial and boundary conditions for heat flux and temperature. Namely, the heat flux was initially zero everywhere and maintained at zero for $x \rightarrow -\infty$ and $x \rightarrow +\infty$. The initial conditions for temperature were stated earlier and the temperatures were maintained at their initial values for $x \rightarrow -\infty$ and $x \rightarrow +\infty$.

The method of numerical solution for the DPL conduction problem just posed for Experiment III used forward and central difference approximations for the time and space derivatives, respectively, subject to the stability condition given in [18]. For the first time step of the solution, the interface temperatures for the cold, room and medium temperature samples were set equal to the values calculated with the same type of expression noted earlier for the interface temperature in Experiment I. After that, the interface temperatures were determined as part of the solution. The Fourier prediction for Experiment III was obtained with the same numerical method after setting $\tau_T/\tau_q=1$.

To ensure converged numerical solutions for the DPL and Fourier problems of Experiment III, the time and space steps were reduced in size until changes of less than 1% would occur in temperatures predicted with smaller step sizes. For example, the DPL prediction was obtained using $\Delta t=0.01$ s and $\Delta x=5 \times 10^{-6}$ m. Also, using 1×10^4 space steps simulated a solid occupying $-\infty < x < +\infty$ because the temperatures near the first and last space-step locations did not change noticeably from their initial values over the entire time period considered.

Finally, the prediction of hyperbolic conduction for Experiment III was obtained by setting $\tau_T=0$ in Eq. (1), then solving the resulting problem along with Eq. (2) using the method of characteristics and corresponding stability condition described in [19]. For this prediction, $\tau_q=15.5$ s as in [2], and the boundary and initial conditions, convergence criterion, number of space steps, and calculation of the interface temperatures for the first time step were the same as just noted for the DPL prediction of this experiment.

References

- [1] Tzou, D. Y., 1997, *Macro- to Microscale Heat Transfer: The Lagging Behavior*, Taylor & Francis, Washington, DC, Chap. 6.
- [2] Mitra, K., Kumar, S., Vedavaz, A., and Moallemi, M. K., 1995, "Experimental Evidence of Hyperbolic Heat Conduction in Processed Meat," *ASME J. Heat Transfer*, **117**, pp. 568–573.
- [3] Wright, N. T., 2003, "On a Relationship Between the Arrhenius Parameters From Thermal Damage Studies," *ASME J. Biomech. Eng.*, **125**, pp. 300–304.
- [4] Furmanski, P., 1997, "Heat Conduction in Composites: Homogenization and Macroscopic Behavior," *Appl. Mech. Rev.*, **50**, pp. 327–356.
- [5] Nakazawa, K., Asako, Y., Jin, Z. F., and Yamaguchi, Y., 1997, "Transient Thermal Response in Glass Beads Packed Bed," *Fundamental Experimental Techniques in Heat Transfer*, D. E. Beasley et al., eds., ASME, New York, HTD-Vol. 350, pp. 169–174.
- [6] Agwu Nnanna, A. G., Harris, K. T., and Haji-Sheikh, A., 2001, "Experimental Validation of Non-Fourier Thermal Response in Porous Media," *Combustion and Energy Systems*, Y. Jaluria, ed., ASME, New York, NY, HTD-Vol. 369-4, pp. 373–384.
- [7] Jiang, F., Liu, D., and Zhou, J., 2002, "Non-Fourier Heat Conduction Phenomena in Porous Material Heated by Microsecond Laser Pulse," *Micro. Thermophys. Eng.*, **6**, Taylor & Francis, Inc., pp. 331–346.
- [8] Vick, B., and Scott, E. P., 1998, "Heat Transfer in a Matrix With Embedded Particles," *Heat Transfer in Materials Processing*, R. A. Nelson, Jr. and U. Chandra, eds., ASME, New York, HTD-Vol. 361-4, pp. 193–198.
- [9] Minkowycz, W. J., Haji-Sheikh, A., and Vafai, K., 1999, "On Departure From Local Thermal Equilibrium in Porous Media Due to Rapidly Changing Heat Source: the Sparrow Number," *Int. J. Heat Mass Transfer*, **42**, pp. 3373–3385.
- [10] Tang, D. W., and Araki, N., 2000, "An Inverse Analysis to Estimate Relaxation Parameters and Thermal Diffusivity With a Universal Heat Conduction Equation," *Int. J. Thermophys.*, **22**, pp. 553–561.
- [11] Honner, M., and Kunes, J., 1999, "On the Wave Diffusion and Parallel Non-equilibrium Heat Conduction," *ASME J. Heat Transfer*, **121**, pp. 702–707.
- [12] Moritz, A. R., and Henriques, Jr., F. C., 1947, "Studies of Thermal Injury II: The Relative Importance of Time and Surface Temperature in the Causation of Cutaneous Burns," *Am. J. Pathol.*, **23**, pp. 695–720.
- [13] Xu, L. X., and Liu, J., 1998, "Discussion of Non-Equilibrium Heat Transfer in Biological Systems," *Advances in Heat and Mass Transfer in Biotechnology*, S. Clegg, ed., ASME, New York, HTD-Vol. 362/BED-Vol. 40, pp. 13–17.
- [14] Herwig, W., and Beckert, K., 2000, "Fourier Versus Non-Fourier Heat Conduction With a Nonhomogeneous Inner Structure," *ASME J. Heat Transfer*, **122**, pp. 363–365.
- [15] Tilahun, M., Scott, E. P., and Vick, B., 1999, "The Question of Thermal Waves in Heterogeneous and Biological Materials," *Advances in Heat and Mass Transfer in Biotechnology*, E. P. Scott, ed., ASME, New York, HTD-Vol. 363/BED-Vol. 44, pp. 145–152.
- [16] Antaki, P. J., 1998, "Solution for Non-Fourier Dual Phase Lag Heat Conduction in a Semi-Infinite Solid With Surface Heat Flux," *Int. J. Heat Mass Transfer*, **41**, pp. 2253–2258.
- [17] Kazimi, M. S., and Erdman, C. A., 1975, "On the Interface Temperature of Two Suddenly Contacting Materials," *ASME J. Heat Transfer*, **97**, pp. 615–617.
- [18] Tzou, D. Y., and Chiu, K. S., 2001, "Temperature-Dependent Thermal Lagging in Ultrafast Laser Heating," *Int. J. Heat Mass Transfer*, **44**, pp. 1725–1734.
- [19] Antaki, P. J., 1998, "Importance of NonFourier Heat Conduction in Solid-Phase Reactions," *Combust. Flame*, **112**, pp. 329–341.

Transpired Turbulent Boundary Layers Subject to Forced Convection and External Pressure Gradients

Raúl Bayoán Cal, Xia Wang,
Luciano Castillo

Rensselaer Polytechnic Institute, Department of Mechanical, Aerospace and Nuclear Engineering, Troy, NY 12180

*The problem of forced convection transpired turbulent boundary layers with external pressure gradient has been studied by using different scalings proposed by various researchers. Three major results were obtained: First, for adverse pressure gradient boundary layers with suction, the mean deficit profiles collapse with the free stream velocity, U_∞ , but into different curves depending on the strength of the blowing parameter and the upstream conditions. Second, the dependencies on the blowing parameter, the Reynolds number, and the strength of pressure gradient are removed from the outer flow when the mean deficit profiles are normalized by the Zagarola/Smits [Zagarola, M. V., and Smits, A. J., 1998, "Mean-Flow Scaling of Turbulent Pipe Flow," *J. Fluid Mech.*, **373**, 33–79] scaling, $U_\infty \delta_* / \delta$. Third, the temperature profiles collapse into a single curve using the new inner and outer scalings proposed by Wang and Castillo [Wang, X., and Castillo, L., 2003, "Asymptotic Solutions in Forced Convection Turbulent Boundary Layers," *J. Turbulence*, **4**(006)], which produce the true asymptotic profiles even at finite Péclet number. [DOI: 10.1115/1.1842790]*

1 Introduction

In recent years, the field of flow control in turbulent boundary layers has become urgently important due to the wide variety of fundamental and industrial applications, particularly in controlling heat transfer, separation, and drag reduction. In this study, various scalings for both the velocity and temperature profiles will be investigated for the boundary layer subjected to the effects of transpiration, heat transfer and pressure gradient. The similarity analysis of the RANS equations for zero pressure gradient (ZPG) and adverse pressure gradient (APG) developed by George and Castillo [1] and Castillo and George [2], respectively, has been

Manuscript received May 7, 2003; revision received October 8, 2004. Review conducted by: K. S. Ball.

applied to obtain the velocity scales in turbulent boundary layers. The same theory has been developed for thermal turbulent boundary layers by Wang and Castillo [3]. In this investigation, the scales obtained from the similarity analysis of turbulent boundary layers will be applied to analyze the data obtained by Orlando, Kays and Moffat [4], which is subject to transpiration and heat transfer. These similarity scalings will be compared with the classical scalings and scalings obtained by the other investigators, and the advantage and disadvantage of each scaling are clearly observed.

2 Various Velocity and Temperature Scalings

Tables 1 and 2 summarize the available scalings for both the velocity and the temperature profiles, respectively. Table 1 shows the scalings in inner variables from various investigators for both the velocity and temperature profiles. The inner velocity scaling, as shown in row two, is the same for all investigators, which is described by the friction velocity, u_* . In the classical view, this scaling was supposed to collapse both inner and outer parts of the boundary layer as described by Millikan [5], but many measurements predicted the opposite. The inner temperature scaling obtained by the Reynolds analogy shown in the fourth row is different from the scaling by George, Wosnik, and Castillo [6] (known here as GWC) and Wang/Castillo [3] (known here as WC) shown in the last row. The similarity length scale in inner variables is different for all cases in the temperature field. Similarly, Table 2 displayed the scalings in outer variables. The outer velocity scaling obtained from the classical approach (row 2) is different from the scaling obtained by Castillo/George [2] (row 3) (known here as CG), and the Zagarola/Smits [7] (row 4) (known here as ZS). Notice that the outer length scale is the same for all investigators. As for the temperature field, row six shows the scaling used in the Reynolds analogy [8], which again assumed that existence of a single scaling for inner and outer flow. The scaling by GWC using similarity analysis is shown in the seventh row and finally, the results obtained by Wang and Castillo [3] labeled as WC are shown in the eighth row.

3 Velocity and Temperature Profiles

Figure 1 shows the velocity profile normalized by the scalings listed in Tables 1 and 2. Figure 1(a) shows the velocity profiles in a semi-log scale normalized with the friction velocity, u_* , and the length scale, ν/u_* . Using the inner scaling, u_* , the profiles collapse in the inner region, but fail to collapse in the outer region for this particular low Reynolds number data ($834 \leq Re_\theta \leq 3144$). Although the profiles have a similar range of Reynolds number, the profiles move towards the wall as the magnitude of the blowing parameter is increased. Also, notice the overlap region

Table 1 The inner velocity and temperature scalings

| 1 | Investigator | Scaling: U_{si} | Length Scale: y^+ |
|---|--|--|--|
| 2 | Classical and other investigators $\frac{U}{U_{si}}$ | $U_{si} = u_*$ | $y^+ = \frac{y u_*}{\nu}$ |
| 3 | Investigator | Scaling: T_{si} | Length Scale: y_T^+ |
| 4 | Reynolds Analogy $\frac{T - T_\infty}{T_{si}}$ | $T_{si} = T_\tau = \frac{q_w}{\rho C_p u_*}$ | $y_T^+ = y^+ = \frac{y u_*}{\nu}$ |
| 5 | George/Wosnik/Castillo $\frac{T - T_\infty}{T_{si}}$ | $T_{si} = T_w - T_\infty$ | $y_T^+ = \frac{y q_w / \rho C_p}{\alpha (T_w - T_\infty)}$ |
| 6 | Wang/Castillo $\frac{T_w - T}{T_{si}}$ | $T_{si} = Pr (T_w - T_\infty) \sqrt{St}$ | $y_T^+ = \frac{y U_\infty}{\nu} \sqrt{St}$ |

Table 2 The outer velocity and temperature scalings

| 1 | Investigator | Scaling: U_{so} | Length Scale: \bar{y} |
|---|--|---|-----------------------------------|
| 2 | Classical Scaling $\frac{U_\infty - U}{U_{so}}$ | $U_{so} = u_*$ | $\bar{y} = \frac{y}{\delta_{99}}$ |
| 3 | Castillo/George $\frac{U_\infty - U}{U_{so}}$ | $U_{so} = U_\infty$ | $\bar{y} = \frac{y}{\delta_{99}}$ |
| 4 | Zaragola/Smits $\frac{U_\infty - U}{U_{so}}$ | $U_{so} = U_\infty(\delta_* / \delta)$ | $\bar{y} = \frac{y}{\delta_{99}}$ |
| 5 | Investigator | Scaling: T_{so} | Length Scale: \bar{y}_T |
| 6 | Reynolds Analogy $\frac{T - T_\infty}{T_{so}}$ | $T_{so} = T_\tau = \frac{q_w}{\rho C_p u_*}$ | $\bar{y}_T = \frac{y}{\delta_T}$ |
| 7 | George/Wosnik/Castillo $\frac{T - T_\infty}{T_{so}}$ | $T_{so} = (T_w - T_\infty) \frac{St}{C_f/2}$ | $\bar{y}_T = \frac{y}{\delta_T}$ |
| 8 | Wang/Castillo $\frac{T - T_\infty}{T_{so}}$ | $T_{so} = (T_w - T_\infty) \frac{\delta_T^*}{\delta_T}$ | $\bar{y}_T = \frac{y}{\delta_T}$ |

increases with increasing value of V_0^+ while the wake region decreases. The blowing parameter V_0^+ was determined from the similarity analysis and was given as $V_0^+ = V_0 / U_\infty d \delta / dx$ according to Cal [9].

Figures 1(b), 1(c), and 1(d) show the normalized velocity deficit profiles. Figure 1(b) shows the profiles normalized using the classical scaling, u_* , and δ_{99} . Notice that in the classical view, the profiles should collapse as a single curve. Clearly, this figure

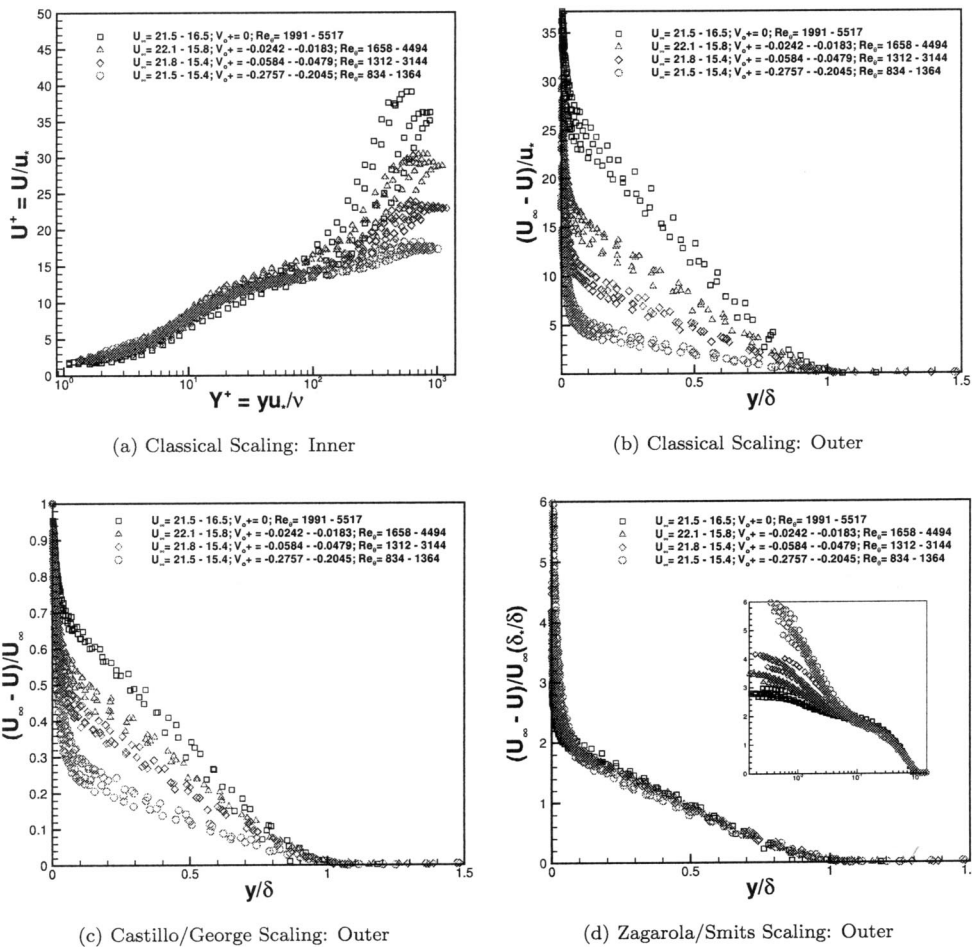


Fig. 1 Velocity profiles in APG normalized by different outer scalings and δ_{99} subject to suction and forced convection using the data of Orlando et al. [4]

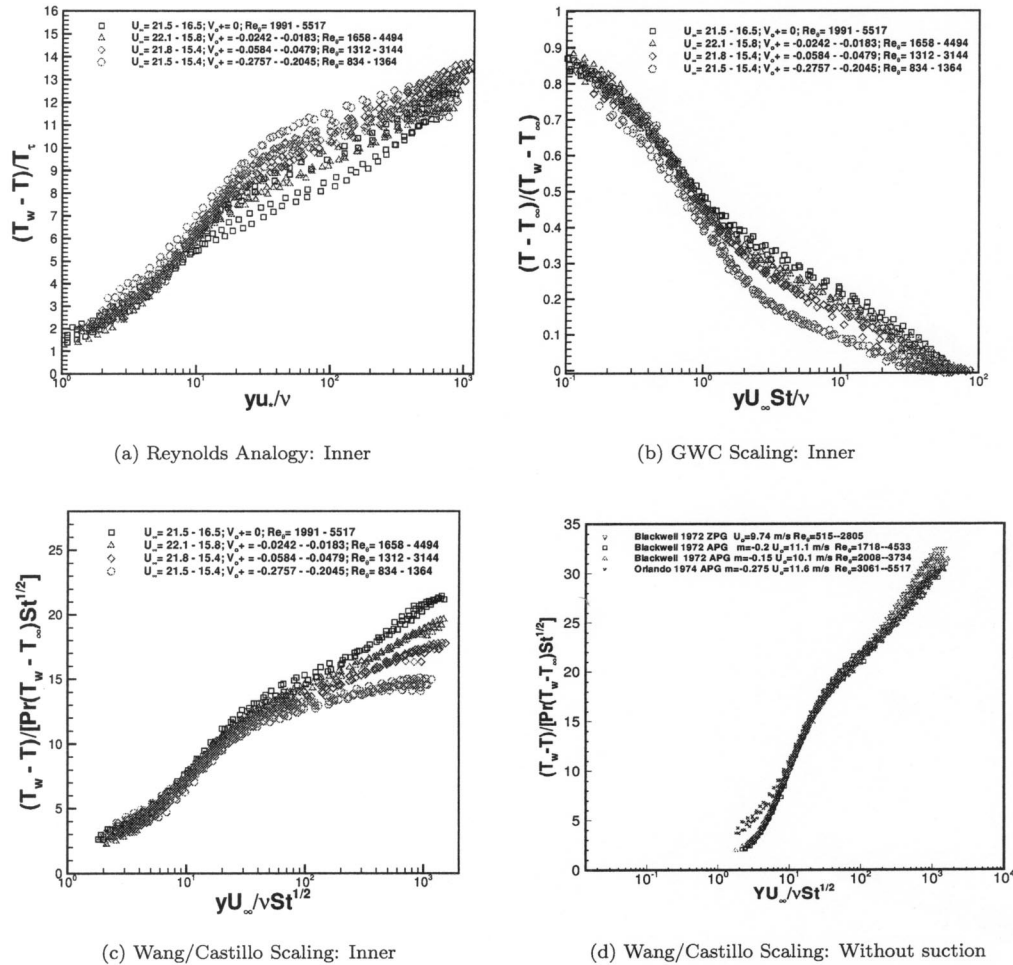


Fig. 2 Comparison of different inner temperature scalings in APG subject to suction and forced convection using the data of Orlando et al. [4]

shows the opposite effect. In Fig. 1(c), the profiles are now normalized by the CG scaling, U_∞ . It can be seen that the profiles collapse, but to different curves showing the effect of the blowing parameter. Notice that as the magnitude of V_0^+ increases, the profiles move closer to the wall; thus increasing the skin friction coefficient. This scaling is obtained by means of the similarity analysis proposed by Castillo and George [2], which is contrary to the classical view that the scaling is chosen before any type of analysis. Finally when the ZS scaling is used as shown in Fig. 1(d), the profiles collapse to one single curve. More importantly, this scaling successfully removes all effects including the pressure gradient, the upstream conditions and the blowing parameter from the outer flow. Also, notice that the slope in the overlap region is close to 1/2, which is consistent with the 1/2 power theory of Perry [10]. In addition, the blowing parameter influences the outer flow and the inner flow, but mostly in the inner region.

Figure 2 displays the temperature profiles scaled in inner variables in a semi-log scale. Figure 2(a) shows the APG temperature profiles with suction using the Reynolds analogy scaling, T_r . Notice that the classical scaling fails to collapse the profiles in the overlap region and near the wall. However, the GWC profiles shown in Fig. 2(b) show a better collapse than the classical scaling. However, the profiles with strong suction (i.e., $V_0^+ = -0.2757 \rightarrow -0.2045$) are far away from other profiles. The more negative the parameter (increase in suction) the closer the profiles move toward to the wall. The WC inner temperature scaling collapses the profiles very well as shown in Fig. 2(c). Interestingly,

the effects of the blowing parameter are nearly removed from the inner flow, but the blowing parameter has an effect on the overlap region. However, Fig. 2(d) shows various APG and ZPG flows without suction normalized with the new scaling proposed by Wang and Castillo [3]. Notice the remarkable collapse of these profiles even with APG over the entire boundary layer. Therefore, Fig. 2(c) shows that suction effects do have a significant influence in the inner flow. Therefore, this inner scaling related to the heat transfer coefficient only is not enough to remove the effect of suction on the inner flow, and a scaling which includes the mass transfer information may do a better job.

Figure 3(a) shows the outer temperature profiles normalized using the Reynolds analogy. Notice that the profiles do not collapse as expected from the classical theory; consequently they show a Péclet number and blowing parameter dependence. The same experimental data scaled using GWC scaling is shown in Fig. 3(b). Clearly, the outer temperature profiles with suction collapse into a single curve, but different from the profile without suction, which means that GWC scaling cannot remove the effects of suction. In Fig. 3(c), the profiles are now normalized using the new proposed outer temperature scaling found by Wang and Castillo [3]. Evidently, the profiles collapse into one curve regardless different Péclet number and effects of suction, specially for the outer region as shown in the semi-log scale figure. Thus, the asymptotic profiles are found at finite Péclet number. Notice that these profiles collapse better than the profiles normalized using the GWC scaling even near the wall region.

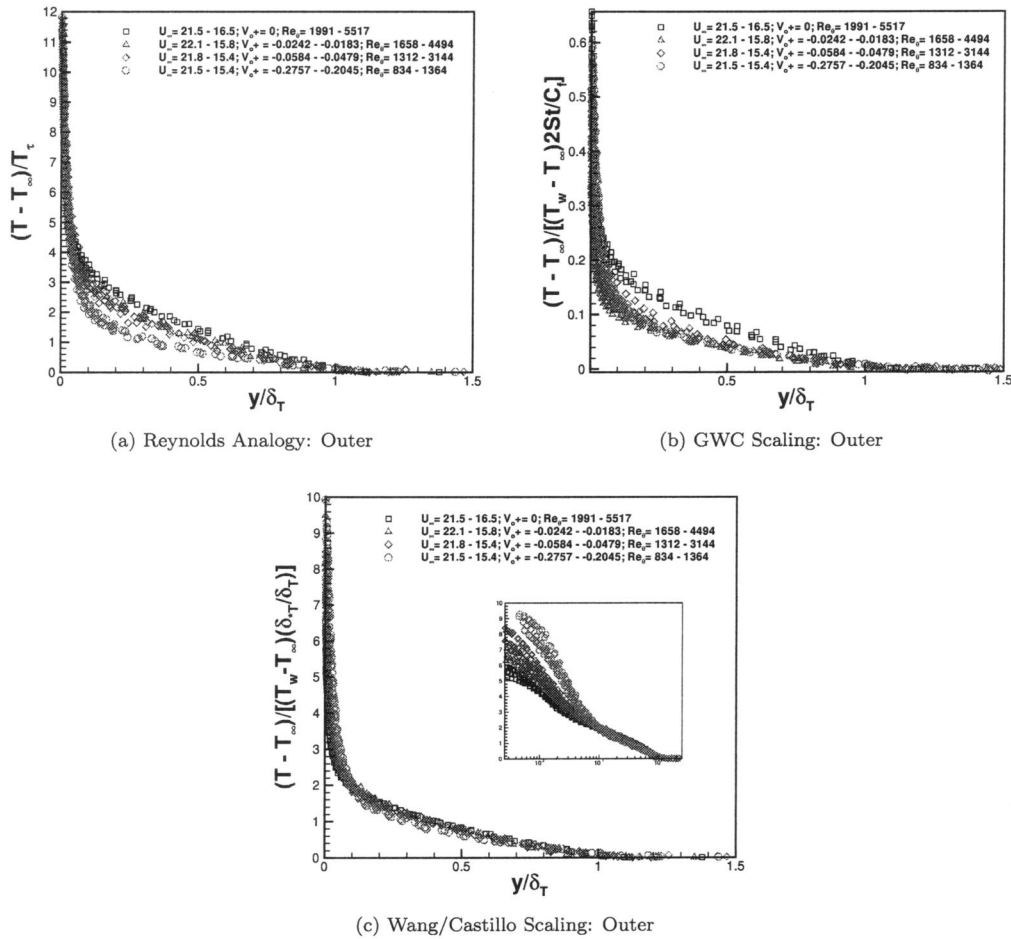


Fig. 3 Comparison of different outer temperature scalings in APG subject to suction and forced convection using the data of Orlando et al. [4]

4 Summary and Conclusions

Both velocity scalings and temperature scalings have been tested for forced convected turbulent boundary layer subject to suction and pressure gradients. The mean deficit profiles collapse with the free-stream velocity, but to different curves depending on the blowing parameter. This is true as long as the upstream conditions are kept fixed, such as the wind-tunnel speed. The dependencies on the upstream conditions, strength of pressure gradient, the Reynolds number and the blowing parameter are removed from the mean deficit profiles when normalized by the Zagarola/Smits scaling, $U_\infty \delta_*^*/\delta$. It was also shown that the velocity profiles normalized in inner variables are affected by the blowing parameter in the overlap region and in the wake region. Increasing the blowing parameter, increases the overlap region, and decreases the wake region.

The effects of the blowing parameter are completely removed from the outer temperature profiles when normalized with the outer scaling $T_{so} = (T_w - T_\infty) \delta_T^*/\delta_T$; thus the profiles collapse into a single curve. However, the profiles in inner variables using the scaling, $T_{si} = Pr(T_w - T_\infty) \sqrt{St}$, exhibit a dependence on the blowing parameter V_0^+ .

Acknowledgments

The authors are very thankful to Dr. Ramona Travis from NASA Stennis Space Center for her continuous support of many of our projects.

Nomenclature

- δ = boundary layer thickness, δ_{99}
- St = Stanton number, $St = q_w / \rho C_p U_\infty (T_w - T_\infty)$
- T_∞ = free stream temperature
- δ_T^* = thermal displacement thickness
- δ_*^* = displacement thickness, $\delta_*^* = \int_0^\infty (1 - U/U_\infty) dy$
- δ^+ = local Reynolds number dependence, $\delta^+ = \delta u_*^+ / \nu$
- $*$ = dependence on upstream conditions
- V_0^+ = blowing parameter, $V_0^+ = V_0 / U_\infty d / dx$
- δ_T = thermal boundary layer thickness
- T_τ = friction temperature, $T_\tau = q_w / \rho C_p u_*^*$
- T_w = wall temperature
- Pr = Prandtl number
- U_∞ = free-stream velocity
- $U_\infty - U$ = velocity deficit
- $U_\infty \delta_*^* / \delta$ = Zagarola/Smits scaling
- u_*^* = friction velocity, $u_*^2 = \tau_w / \rho$

References

- [1] George, W. K., and Castillo, L., 1997, "Zero-Pressure Gradient Turbulent Boundary Layer," *Appl. Mech. Rev.*, **50**(11), pp. 689-729.
- [2] Castillo, L., and George, W. K., 2001, "Similarity Analysis for Turbulent Boundary Layer With Pressure Gradient: Outer Flow," *AIAA J.*, **39**(1), pp. 41-47.
- [3] Wang, X., and Castillo, L., 2003, "Asymptotic Solutions in Forced Convection Turbulent Boundary Layers," *J. Turbulence*, **4**(006).
- [4] Orlando, A. F., Kays, W. M., and Moffat, R. J., 1974, "Turbulent Transport of

- Heat and Momentum in a Boundary Layer Subject to Deceleration, Suction, and Variable Wall Temperature," Report No. HMT-17, Dept. of Mech. Eng., Stanford University, Stanford, CA.
- [5] Millikan, C. M., 1938, "Critical Discussion of Turbulent Flows in Channels and Circular Tubes," *Proc. 5th Int. Congr. Applied Mech.*, Wiley, New York, pp. 386–392.
- [6] George, W. K., Wosnik, M., and Castillo, L., 1997, "Similarity Analysis for Forced Convection Thermal Boundary Layer," *Transp. Phenomena Thermal Sci. Process Eng.*, **1**, pp. 239–244.
- [7] Zagarola, M. V., and Smits, A. J., 1998, "Mean-Flow Scaling of Turbulent Pipe Flow," *J. Fluid Mech.*, **373**, pp. 33–79.
- [8] Monin, A. S., and Yaglom, A. M., 1971, *Statistic Fluid Mechanics*, MIT Press, Cambridge, MA.
- [9] Cal, R. B., 2003, "Similarity Analysis of Transpired Turbulent Boundary Layers," M.S. thesis, Rensselaer Polytechnic Institute.
- [10] Perry, A. E., Bell, J. B., and Joubert, P. N., 1966, "Velocity and Temperature Profiles in Adverse Pressure Gradient Turbulent Boundary Layers," *J. Fluid Mech.*, **25**, pp. 299–320.

A Semi-Analytical Model for Evaporating Fuel Droplets

Achintya Mukhopadhyay¹ and Dipankar Sanyal

Department of Mechanical Engineering, Jadavpur University Kolkata—700 032 India
e-mail: a_mukho@vsnl.net

An algorithm for solution of a model for heating and evaporation of a fuel droplet has been developed. The objective of the work is to develop a computationally economic solution module for simulating droplet evaporation that can be incorporated in spray combustion CFD model that handles a large number of droplets. The liquid-phase transient diffusive equation has been solved semi-analytically, which involves a spatially closed-form and temporally discretized solution procedure. The model takes into account droplet surface regression, nonunity gas-phase Lewis number and variation of latent heat with temperature. The accuracy of the model is identical to a Finite Volume solution obtained on a very fine nonuniform grid, but the computational cost is significantly less, making this approach suitable for use in a spray combustion code. The evaporation of isolated heptane droplet in a quiescent ambient has been investigated for ambient pressures of 1 to 5 bar. [DOI: 10.1115/1.1842791]

Introduction

The combustion of liquid fuels has been widely studied owing to its importance in various power and propulsion systems. The design of advanced combustors is increasingly relying on CFD techniques. A crucial component of the spray combustion CFD codes is the module for computing evaporation of individual droplets, which forms the core of spray evaporation and combustion. Since thousands of droplets have to be handled in a spray combustion code, computationally efficient droplet evaporation models and solution algorithms that capture the essential physics are necessary. The droplet model predicts heat transfer to the droplet and evaporation rate, and provides a distributed mass source and heat sink to the transport equations in the spray combustion model.

Considerable effort has been directed in the past towards development of efficient but accurate droplet models. Tong and Sirignano [1,2] developed an approximate solution technique for vaporizing pure and binary fuel droplets with internal circulation. In their model, they eliminated the spatial dependence by transforming the one-dimensional transient equation in the droplet core to a set of coupled first order differential equations, which were solved numerically using piecewise constant droplet regression rates.

Mandal et al. [3] developed a semi-analytical model for the diffusion-limit liquid-phase transport for spherically symmetric combustion of a multicomponent droplet. They solved the liquid phase equations using separation of variables technique. However, they did not take the droplet surface regression into account, which introduces a significant error, particularly in the later stages. Zeng and Lee [4] developed a model for multicomponent droplet evaporation that takes into account the spatial variation of concentration and temperature within the droplet and used the separation of variables to obtain closed form expressions for the droplet surface and center parameters. The computational requirement for this method was similar to that of infinite diffusion models while

taking into account the spatial variation of properties. However, like Mandal et al. [3], the model did not consider the droplet regression effect. Zeng and Lee [5] modified their analysis by incorporating the high pressure and radius regression effects. However, the radius regression effects were considered only at later times when a quasi-steady state was reached.

Mukhopadhyay and Sanyal [6] developed a model for multi-component droplet burning in which the effects of radius regression and gas phase Lewis number were considered. In their model, the liquid phase transient diffusive equations were solved numerically using Finite Volume Method. Torres et al. [7] also developed a liquid phase model that accounted for droplet regression and solved the equations numerically. In addition, they considered the convective field in the droplet, induced by the thermal expansion of the droplet. However, they did not compare the predictions of this comprehensive model with those of simpler models. Both these models, moreover, required numerical solution of the liquid phase transport equations over the entire liquid domain.

Objective

The above discussion reveals the necessity of developing physically accurate and computationally simple droplet models. The objective of the present work is to develop a solution technique for liquid phase transport for droplet evaporation using a model that takes into account both transient diffusive heating and radius regression. In the larger context of simulation of spray combustion, this provides a cheaper alternative to the full numerical solution procedures [6,7] that capture both these effects. On the other hand, closed form solutions [3,4], though computationally economic, do not address the effect of droplet surface regression satisfactorily, while the predictions of infinite diffusion model are significantly erroneous, especially at increasing ambient pressures [8]. The liquid phase equations are solved analytically leading to a significant reduction in computational time. Aggarwal and Mongia [8] observed that liquid phase modeling with a surrogate single-component fuel is adequate even for multicomponent droplets, especially at higher pressures when the droplet heating effect becomes significant. Accordingly, we demonstrate the solution method with an isolated droplet of heptane vaporizing in a heated ambient. The pressure range investigated extends from 1 bar to 5 bar, where ideal gas models have been shown to be adequate, especially at high ambient temperatures [9,10].

Analysis

The mathematical model of the problem consists of quasi-steady vapor phase transport processes and transient-diffusive liquid phase transport. The two sets of equations are coupled by a set of interface relations obtained by applying Reynolds Transport Theorem to an infinitesimal control volume containing the interface. The phase equilibrium relation incorporates variation of boiling point and the latent heat with pressure. The liquid phase properties are assumed constant while constant values have been used for thermal conductivity, specific heat and product of density and mass diffusivity in the vapor phase. The transient diffusive liquid phase equations have been non-dimensionalised using the initial droplet radius and the gas phase mass diffusion time as the length scale and time scale, respectively. The use of an initial radius as the length scale gives a solution domain that changes with time. The heat flux boundary condition, used at the droplet surface, is obtained by an energy balance at the interface involving the heat flux at the interface on the liquid and the vapor sides and the latent heat of evaporation. The use of instantaneous values of vapor side temperature gradient and evaporation rate give a time-dependent boundary condition at the interface. The vapor phase and interface equations have been detailed in Mukhopadhyay and Sanyal [6].

The liquid phase energy equation in dimensionless form can be written as:

¹Corresponding author. Fax: +91-33-24146532; Phone: +91-33-24146177.

Manuscript received March 31, 2004; revision received August 11, 2004. Review conducted by: R. P. Roy.

$$\frac{\partial \theta}{\partial \tau} = \frac{\text{Le}D^*}{R^2} \frac{\partial}{\partial R} \left(R^2 \frac{\partial \theta}{\partial R} \right), \quad 0 \leq R \leq R_d(\tau), \quad \tau > 0 \quad (1)$$

The initial and the boundary conditions are as follows:

$$\left. \frac{\partial \theta}{\partial R} \right|_{R=0} = \left. \frac{\partial \theta}{\partial R} \right|_{R=R_d(\tau)} - f(\tau) = 0, \quad \tau > 0 \quad (2)$$

$$\theta(R, \tau=0) = \theta_{\text{in}}, \quad 0 \leq R \leq R_d(\tau=0) \quad (3)$$

The above system of equations are transformed by change of variables, $U(R, \tau) = R\theta(R, \tau)$ to the following form:

$$\frac{\partial U}{\partial \tau} = \text{Le}D^* \frac{\partial^2 U}{\partial R^2}, \quad 0 \leq R \leq R_d(\tau), \quad \tau > 0, \quad (4)$$

$$U(R=0, \tau) = \left. \frac{\partial U}{\partial R} \right|_{R=R_d(\tau)} - g(\tau) = 0, \quad \tau > 0, \quad (5a)$$

$$g(\tau) = \theta_s + R_d f(\tau) \quad (5b)$$

$$U(R, \tau=0) = R\theta_{\text{in}}, \quad 0 \leq R \leq R_d(\tau=0) \quad (6)$$

The time-varying solution domain and time-varying boundary conditions are the two aspects of the above system of equations, Eqs. (4)–(6), which render closed form solution difficult. In the present work, the time domain is discretized into finite number of steps. Within each time step, $R_d(\tau)$ and $g(\tau)$ are assumed constant. However, these values are updated at each time step from the corresponding vapor phase and interface solutions. Within each time step, the problem can thus be solved by separation of variables as follows.

$$\theta^{(k)}(R, \tau) = \bar{g}^{(k)} + \frac{1}{R} \sum_{n=0}^{\infty} C_n^{(k)} \exp(-\lambda_n^{(k)2} \text{Le}D^* \tau) \sin(\lambda_n^{(k)} R), \quad \tau^{(k-1)} \leq \tau \leq \tau^{(k)}, \quad (7)$$

where $\tau^{(k)} = \sum_{i=1}^k \Delta \tau^{(i)}$ and $\lambda_n^{(k)} = (2n+1)\pi/2R_d^{(k)}$. The function $\bar{g}^{(k)}$ represents the average (constant) value of $g(\tau)$ over the interval. The updating of eigenvalues at each time step, resulting from changing domain size, is a significant contribution of the present approach that enables proper treatment of surface regression effects. The constants $C_n^{(k)}$ are evaluated by matching the piecewise closed-form solutions of successive time-steps as follows.

$$\theta(R, \tau = \tau^{(k)}) = \theta^{(k)}(R, \tau^{(k)} = 0) = \theta^{(k-1)}(R, \tau^{(k-1)} = \Delta \tau^{(k-1)}); \tau^{(k)} = \tau - \tau^{(k-1)} \quad (8)$$

From Eq. (8) that implies temperature equality at the same physical time, namely the final time of the preceding time step and the initial time of the current time step, the constants are evaluated as

$$C_n^{(k)} = \frac{(-1)^n 8R_d^{(k)}}{(2n+1)^2 \pi^2} (\bar{g}^{(k-1)} - \bar{g}^{(k)}) + \frac{(-1)^{n+1} 4}{\pi} \times \sum_{m=1}^{\infty} C_m^{(k-1)} \exp(-\lambda_m^{(k-1)2} \text{Le}D^* \Delta \tau^{(k-1)}) \times \left\{ \frac{(2m+1)}{(2m+1)^2 \frac{R_d^{(k)}}{R_d^{(k-1)}} - (2n+1)^2 \frac{R_d^{(k-1)}}{R_d^{(k)}}} \right\} \times \cos \left[\frac{(2m+1)\pi}{2} \frac{R_d^{(k)}}{R_d^{(k-1)}} \right], \quad k > 1 \quad (9)$$

and

$$C_n^{(1)} = \frac{(-1)^n 8R_d^{(1)}}{(2n+1)^2 \pi^2} (\theta_{\text{in}} - \bar{g}^{(1)}) \quad (10)$$

The method has the advantage that the quantity of specific interest to spray computations, namely, surface temperature can be computed without calculating the temperature at the interior points. The surface temperature at discrete intervals can be expressed as

$$\theta_s |_{\tau=\tau_k} = \bar{g}^{(k)} + \frac{1}{R_d^{(k)}} \sum_{n=0}^{\infty} (-1)^n C_n^{(k)} \exp(-\lambda_n^{(k)2} \text{Le}D^* \Delta \tau^{(k)}) \quad (11)$$

In the limit of very small time steps, as is normally used in such computations, $R_d^{(k)}/R_d^{(k-1)} \rightarrow 1$. For this limiting case, $\int_0^{R_d^{(k)}} \cos(\lambda_m^{(k-1)} R) \cos(\lambda_n^{(k)} R) \rightarrow 0$ for $m \neq n$. This simplifies Eq. (9) to the following form:

$$C_n^{(k)} = \frac{(-1)^n 8R_d^{(k)}}{(2n+1)^2 \pi^2} (\bar{g}^{(k-1)} - \bar{g}^{(k)}) + \frac{(-1)^{n+1} 4}{\pi} C_n^{(k-1)} \times \exp(-\lambda_n^{(k-1)2} \text{Le}D^* \Delta \tau^{(k-1)}) \times \left\{ \frac{\cos \left[\frac{(2n+1)\pi}{2} \frac{R_d^{(k)}}{R_d^{(k-1)}} \right]}{(2n+1) \left(\frac{R_d^{(k)}}{R_d^{(k-1)}} - \frac{R_d^{(k-1)}}{R_d^{(k)}} \right)} \right\}, \quad k > 1 \quad (12)$$

We compare the predictions with C_n evaluated using Eqs. (9) and (12) and refer to them as full semi-analytical or ‘‘FSA’’ and truncated semi-analytical or ‘‘TSA’’ models.

Results and Discussions

Figure 1 compares the predictions of the present solution procedure for evaporation of an isolated heptane droplet in a quiescent ambient with the experimental results of Nomura et al. [11]. The ambient conditions investigated correspond to 1 bar and 471 K and 5 bar and 468 K, respectively. The results obtained for both the cases are in excellent agreement with the experimental observations, clearly indicating the initial heat-up period and the subsequent d^2 -law period. From the figure, it is observed that over a significant period of droplet life, the droplet heating and evaporation are both significant and this trend is increasingly apparent at

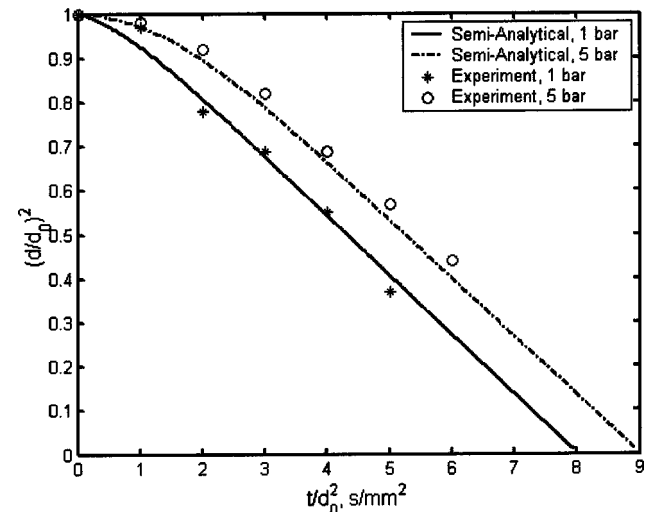


Fig. 1 A comparison of the prediction of the present model with experimental observations of Nomura et al. [11]

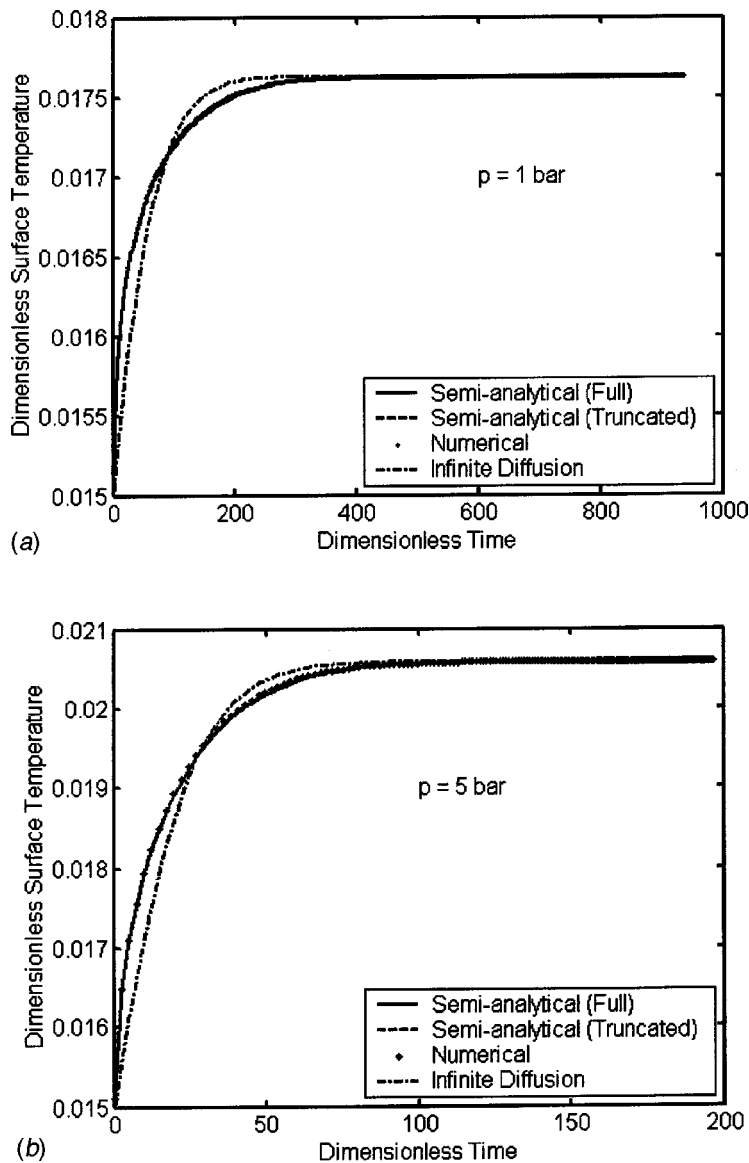


Fig. 2 Temporal variation of droplet surface temperature at (a) 1 bar and (b) 5 bar

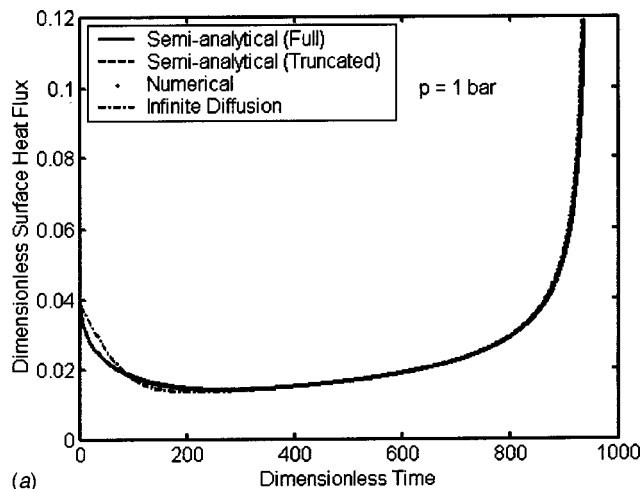
higher ambient pressures. This observation puts into question the procedure adopted in commercial CFD packages like Fluent [12], where droplet heating and evaporation are treated separately.

In Figs. 2 and 3, the predictions of the present semi-analytical models have been compared with the results obtained from numerical simulation of the liquid phase transport. The code with numerical solution module (FVM) for the liquid phase has been validated earlier [6] for both single and multicomponent droplets. For the numerical solution, 150 grids with clustering near the droplet surface and a dimensionless time step of 0.0125 have been used. Simulation with substantially finer grid and time step (250 grids and 0.00125) resulted in an improvement of about 0.01% for both droplet surface temperature and droplet radius. The results presented here are for an isolated heptane droplet evaporating in a quiescent ambient at 1500 K in terms of the droplet surface temperature and droplet surface heat flux. These are the quantities, which are of primary importance to spray computation. For comparison, the predictions of the infinite diffusivity model, which uses lumped models for liquid phase transport, have also been included.

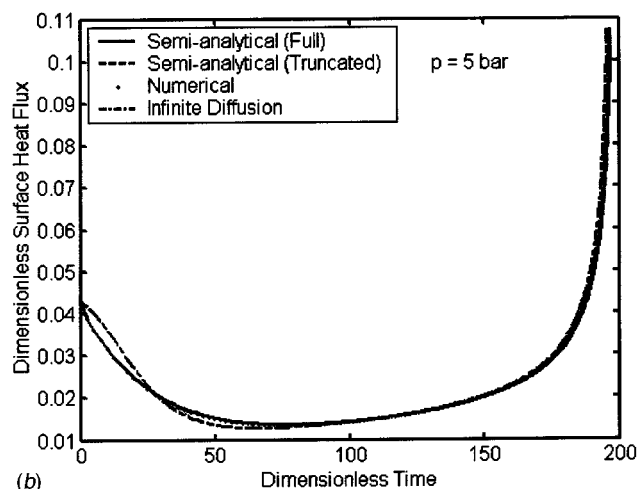
The temporal variation of droplet surface temperature (θ_s) shows the initial heat up period followed by the quasi-steady

phase when the droplet attains the “wet-bulb” temperature. Since this final surface temperature is unaffected by the liquid phase transport, all the models including the infinite diffusivity model show identical values. However, during the heat-up period the prediction of the infinite diffusivity model significantly differs from the other models. The infinite diffusivity model considers the thermal capacity of the entire droplet whereas the diffusion-limit model is limited to a thin thermal layer due to the diffusional resistance. This leads to an underprediction of the droplet surface temperature in the initial stages. On the other hand, towards the later stages of the heat-up period, when the thermal layer for the diffusion limit model is of the same order as the droplet radius, the higher thermal diffusivity for the infinite diffusion limit leads to overprediction of the droplet surface temperature. The other three models give identical predictions throughout the droplet life. We also observe that the prediction of the infinite diffusivity model differs from those of the other models for a greater fraction of the droplet life at higher pressures. This is expected, since at higher pressures, the droplet heat-up period is extended.

Figure 3 shows the temporal variation of droplet surface heat flux. Initially the surface heat flux decreases with time due to increase in the droplet surface temperature, which decreases the



(a)



(b)

Fig. 3 Temporal variation of droplet surface heat flux at (a) 1 bar and (b) 5 bar

temperature difference between the ambient and the droplet surface. At later times, however, the surface heat flux starts to increase again as the droplet surface area decreases due to evaporation. As in the case of droplet surface temperature, the prediction of the infinite diffusivity model differs significantly from the other models at the initial stages, while the other three models give identical predictions throughout the droplet life. Initially, the infinite diffusivity model overpredicts and subsequently underpredicts the heat flux. This difference is consistent with the initially lower and subsequently higher prediction of the droplet surface temperature, as discussed in the context of Fig. 2. As in the case of droplet surface temperature, the difference in predictions is significant over a greater portion of the droplet life at higher pressures.

Table 1 lists the computation time required for simulating the evaporation of an isolated heptane droplet in a stationary ambient of 1500 K on a Pentium III 1 GHz processor using a Compaq Visual Fortran compiler. The time required for the “truncated” semi-analytical model is of the same order as the infinite diffusivity model, while its accuracy is comparable to that of the numerically simulated diffusion limit model. Considering the large number of droplets involved in a spray computation, both the truncated semi-analytical and infinite-diffusion models imply significant reduction in overall computational time. Since the predicted deviation of the surface heat-flux between the infinite-diffusion model and the truncated semi-analytical model tend to

Table 1 A comparison of the computation times for different models

| Solution model | Simulation time (seconds) |
|---------------------------|---------------------------|
| Infinite diffusion | 1.07 |
| Present model (full) | 8.03 |
| Present model (truncated) | 2.42 |
| Numerical | 14.18 |

increase with increase in ambient pressure, the present truncated semi-analytical model appears to be a good candidate to be interfaced in a full-scale spray code. This procedure can also be used for convecting droplets using “effective diffusivity” concept introduced by Abramzon and Sirignano [13].

Conclusions

A model for heating and evaporation of a fuel droplet has been developed. The liquid-phase transient diffusive equation has been solved semi-analytically, which involves a spatially closed-form and temporally discretized solution procedure. The model takes into account droplet surface regression, nonunity gas-phase Lewis number and the variation of latent heat with temperature. The accuracy of the model is identical to a Finite Volume solution obtained on a very fine nonuniform grid, but the computational time is nearly one-tenth and comparable to that of infinite diffusivity model. The difference between the present model and the infinite diffusivity model increases with increase in ambient pressure. The present approach combines the accuracy of finite diffusion models with the computational economy of infinite diffusivity model. Hence, it is an attractive alternative to the infinite diffusivity model for use in spray combustion codes to obtain droplet parameters, especially at elevated pressures, where the droplet heating is significant.

Nomenclature

- C_p = Gas phase specific heat at constant pressure (kJ/kg K)
- d = Instantaneous droplet diameter (m)
- d_0 = Initial droplet diameter (m)
- D^* = Ratio of liquid to gas phase mass diffusivity (dimensionless)
- $f(\tau)$ = Liquid side instantaneous temperature gradient (dimensionless)
- $g(\tau)$ = Defined in Eq. (5b)
- Le = Liquid phase Lewis number (ratio of thermal to mass diffusivity)
- Q_{cv} = Heating value of fuel (kJ/kg)
- R = Radial coordinate (dimensionless)
- R_d = Instantaneous droplet radius (dimensionless)
- t = Time (s)
- T = Dimensional temperature (K)

Greek Symbols

- θ = Dimensionless temperature ($C_p T / Q_{cv}$)
- λ = Eigenvalue
- τ = Dimensionless time
- $\Delta\tau$ = Dimensionless time step

Subscripts

- in = Initial
- s = Droplet surface

Superscripts

- (k) = Time step

References

- [1] Tong, A. Y., and Sirignano, W. A., 1982, “Analytical Solution for Diffusion and Circulation in a Vaporizing Droplet,” *Proc. 19th Symp. (Int.) on Combustion*, pp. 1007–1020.

- [2] Tong, A. Y., and Sirignano, W. A., 1986, "Multicomponent Transient Droplet Vaporization with Internal Circulation: Integral Equation Formulation and Approximate Solution," *Numer. Heat Transfer*, **10**, pp. 253–278.
- [3] Mandal, S., Kant, K., and Sundararajan, T., 2000, "Multicomponent Fuel Droplet Combustion: An Alternative Method of Solution," *Proc. 4th ISHMT-ASME Heat and Mass Transfer Conference*, pp. 1087–1092.
- [4] Zeng, Y., and Lee, C.-F., 2002, "A Preferential Vaporization Model for Multicomponent Droplets and Sprays," *Atomization Sprays*, **12**, pp. 163–186.
- [5] Zeng, Y., and Lee, C.-F., 2002, "A Model For Multicomponent Spray Vaporization in a High-Pressure and High-Temperature Environment," *ASME J. Eng. Gas Turbines Power*, **124**, pp. 717–724.
- [6] Mukhopadhyay, A., and Sanyal, D., 1999, "A Study of Thin-Flame Quasi-steady Sphericallysymmetric Combustion of Multicomponent Fuel Droplets: Part-I. Modelling for Droplet Surface Regression and Non-unity Gas-Phase Lewis Number," *Int. J. Energy Res.*, **23**, pp. 963–977.
- [7] Torres, D. J., O'Rourke, P. J., and Amsden, A. A., 2003, "Efficient Multicomponent Fuel Algorithm," *Combust. Theory Modell.*, **7**, pp. 67–86.
- [8] Aggarwal, S. K., and Mongia, S. K., 2002, "Multicomponent and High Pressure Effects on Droplet Vaporization," *ASME J. Eng. Gas Turbines Power*, **124**, pp. 248–255.
- [9] Jia, H., and Gogos, G., 1992, "Investigation of Liquid Droplet Evaporation in Subcritical and Supercritical Gaseous Environment," *J. Thermophys. Heat Transfer*, **6**, pp. 738–745.
- [10] Zhu, G.-S., Reitz, R. D., and Aggarwal, S. K., 2001, "Gas-Phase Unsteadiness and its Influence on Droplet Vaporization in Sub- and Super-Critical Environments," *Int. J. Heat Mass Transfer*, **44**, pp. 3081–3093.
- [11] Nomura, H., Ujiie, Y., Rath, H. J., Sato, J., and Kono, M., 1996, "Experimental Study on High Pressure Droplet Evaporation Using Microgravity Conditions," *Proc. 26th Symposium (International) on Combustion*, pp. 1267–1273.
- [12] *Fluent Users Guide*, Version 5.4, Fluent Incorporated, New Hampshire, 1998.
- [13] Abramzon, B., and Sirignano, W. A., 1989, "Droplet Vaporization Model For Spray Combustion Calculations," *Int. J. Heat Mass Transfer*, **32**, pp. 1605–1618.

Errata: “Mie Scattering Theory for Phonon Transport”
[ASME J. Heat Transfer, 2004, 126, pp. 793–804]

The paper appeared under the section on *Radiative Transport* whereas it should have appeared under the section on *Nan/Micro Scale Heat Transfer*.